University of Bath

PHD

Ionospheric Irregularities and their Impact on Global Navigation Satellite Systems (GNSS)

John, Habila Mormi

Award date:
2021

Awarding institution:
University of Bath

Link to publication

Alternative formats
If you require this document in an alternative format, please contact:
openaccess@bath.ac.uk

Copyright of this thesis rests with the author. Access is subject to the above licence, if given. If no licence is specified above, original content in this thesis is licensed under the terms of the Creative Commons Attribution-NonCommercial 4.0 International (CC BY-NC-ND 4.0) Licence (https://creativecommons.org/licenses/by-nc-nd/4.0/). Any third-party copyright material present remains the property of its respective owner(s) and is licensed under its existing terms.

Take down policy
If you consider content within Bath's Research Portal to be in breach of UK law, please contact: openaccess@bath.ac.uk with the details. Your claim will be investigated and, where appropriate, the item will be removed from public view as soon as possible.

Download date: 04. May. 2023

University of Bath

Ionospheric Irregularities and their Impact on Global Navigation Satellite Systems (GNSS)

Habila Mormi John

A thesis submitted for the degree of Doctor of Philosophy

University of Bath

Department of Electronic and Electrical Engineering

August 2021

COPYRIGHT

Attention is drawn to the fact that copyright of this thesis rests with the author and copyright of any previously published materials included may rest with third parties. A copy of this thesis/portfolio has been supplied on condition that anyone who consults it understands that they must not copy it or use material from it except as licenced, permitted by law or with the consent of the author or other copyright owners, as applicable.

Access to this thesis in print or electronically is restricted until ……. (date). Signed on behalf of the Doctoral College.....(print name) ……

Abstract

Drifting ionospheric irregularities in the form of inhomogeneities in the electron density distribution can affect the propagation of Global Navigation Satellite System (GNSS) signals causing fluctuations in amplitude and phase. Such fluctuations in amplitude and phase of the signals with shorter periods arise from small-scale irregularities and are known as scintillation. Typically, scintillation is accompanied by temporal fluctuations in Total Electron Content (TEC): that is, fluctuations in the phase of the signals with longer periods arising from large-scale irregularities. Large-scale irregularities tend to cascade into small-scale irregularities owing to instability mechanisms.

Whilst this is the case for the equatorial ionosphere, at high-latitudes, such energy cascade does not seem to be as developed. Consequently, mainly phase scintillation tends to be detected on GNSS at auroral and polar latitudes. TEC fluctuations can be used as a proxy to indicate the presence of phase fluctuations induced by large-scale irregularities at high-latitudes. Scintillation and TEC fluctuations can significantly impact the performance of GNSS particularly in equatorial latitudes and high-latitudes ionosphere. Scintillation can be modelled by means of propagation through phase-changing screens which are thin irregular layers across a propagation path used to approximate a stochastic medium between a transmitter and a receiver.

The thesis aims to characterise the spatial distribution of electron density irregularities along profiles in the E and F layer transverse to GPS ray paths and their impact on GPS signals at high-latitudes. To achieve this, in 2018 and 2019, multi-instrument experimental campaigns were designed and conducted involving the European Incoherent SCATter (EISCAT)/EISCAT Svalbard Radar (ESR) UHF radars and geodetic GNSS receiver stations of relevance at the auroral and polar latitudes. It is worthy to clearly mention here that the data collected from these experiments were utilised in the research.

EISCAT UHF/ESR radar beams were used to infer the distribution of electron density irregularities along hypothetical phase screens in which EISCAT UHF/ESR electron density profiles were measured along hypothetical phase screens

alternately intersecting GNSS ray paths at different ionospheric shell heights. In this investigation, representative case studies were considered in the auroral and polar ionospheres. Whilst auroral irregularities seemed to be originated mainly by particle precipitation, polar irregularities could arise from polar patches and/or particle precipitation.

The effects of electron density irregularities distributed along phase screens across GNSS ray paths of relevance were investigated in terms of temporal fluctuations in TEC and positioning performance. These experiments provide information about the outer scale of the phase screens and the likely spatial distance over which auroral and polar irregularities distribute. The electron density distribution along a given phase screen, that is whether it is symmetrical or not, and the origin of the phase screens were also considered. The results provide insight into the impact of adverse space weather conditions on real-time and post-processing positioning applications at auroral and polar latitudes.

Acknowledgements

My special thanks to the Almighty God for His grace and mercy over the years without whom I am nothing. To my beloved wife (Chongdah) and adorable children (Helsa, Haviva, and Hanana), many thanks for your support, love, and understanding during the course of my PhD. To my beloved parents late Mrs. Maryamu John Mormi and Cpl John Ndaken Mormi (retd), many thanks for being my parents despite my shortcoming. My dearest mother, I believe you are resting in the LORD Jesus Christ, all that I could ever achieve in life is dedicated to honour your loving memories. To my dear siblings, inspiring cousins, esteemed In-laws, and wonderful friends, I cannot appreciate you enough for being part of this remarkable success story.

To my lead supervisor Biagio Forte, thank you so much. Your patience, willingness to support and help, and constructive criticism have enabled me to be a critical thinker and developed skills needed to become a competent researcher.

I wish to express my gratitude to the Petroleum Technology Development Fund (PTDF), Nigeria, for sponsoring my PhD research and to my home country employer, the Department of Electrical and Electronic Engineering, University of Abuja, Nigeria for allowing my paid study-leave. I also acknowledge the Rt. Hon. Dr. Yakubu Dogara who personally provided me the opportunity for the PhD research. My gratitude to Professor Suleiman Bogoro who showed special interest in supporting my academic and professional career. To a beloved friend and brother James Habila Komo, I cannot forget your being there for me at all times. My dear elder brother Godiya Adamson, your prayers and support mean a lot to me. My good friend Yahaya Enefola, you being there for me and my family is well appreciated. I say a big thank you to Mrs. Folasade Gbadegesin for your kindness and compassion toward my family.

I also wish to extend my appreciation to my second supervisor, Cathryn Mitchell, for your support and kind advice, which had been of immense help. To Ben Witvliet, I cannot thank you enough for your personal sacrifice when I was faced with financial stress. I cannot forget the invaluable support of my colleagues from the INVERT

Group: Karl Bolmgren, Jon Bruno, Sam Lo, Nikola Rankov, and Talini Pinto Jayawardena. Thank you, also, for the kind support of Ivan Astin, Tom Allbrook, Alex Arnold (for also proofreading of the thesis), and Bruno C. Vani.

I wish to thank TREASURE for the award of TREASURE Bursary to attend the 2nd TREASURE Workshop on “A response to user needs in PPP and RTK” in Toulouse, France on 21-22 May 2019. Many thanks to the following Societies who supported me during the research when I was under financial stress: The Royal Society of St George Bath and District Branch, United Kingdom and the Royal Commonwealth Society (RCS) Bath and District Branch, United Kingdom.

The European Incoherent SCATter (EISCAT) experimental campaigns were supported through the EISCAT UK time allocation and the Natural Environment Research Council (NERC).

The data used in this thesis were provided by EISCAT, the International GNSS Service (IGS), the GNSS Calendar and Utility product, the German Aerospace Centre (DLR), the National Institute of Polar Research (NIPR), the International Monitor for Auroral Geomagnetic Effects (IMAGE), the Super Dual Auroral Radar Network (SuperDARN), CALSKY (GPS satellites predicted azimuth and elevation) courtesy of calsky.com, and Spirent GPS Simulator (GPS satellites predicted azimuth and elevation) courtesy of Spirent Communications.

In addition, the software used in this study were the Grand Unified Incoherent Scatter Design and Analysis Program (GUISDAP) courtesy of EISCAT, the GNSS Laboratory (gLAB, interactive educational multipurpose package to process and analyse GNSS data) courtesy of European Space Agency (ESA), the Real-Time Kinematic Library (RTKLIB) open source program package for GNSS positioning courtesy of RTK, and the Matrix Laboratory (MATLAB) courtesy of MathWorks.

Table of Contents

List of Figures

List of Tables

List of Abbreviations

ABAS	Aircraft-Based Augmentation System
AEJ	Auroral Electrojet
AFREF	African geodetic Reference Frame
ALOS-2	Advanced Land Observing Satellite-2
AMBER	African Meridional B-field Education and Research
AMISR	Advanced Modular Incoherent Scatter Radar
ANTEX	Antenna Exchange Format
ASC	All-Sky Camera
ASCs	All-Sky Cameras
ATC	Air Traffic Control
ATM	Air Traffic Management
BDS	BeiDou Navigation Satellite System
BOC	Binary Offset Carrier
BPSK	Binary Phase Shift Keying
C/A	Coarse/Acquisition
CADIs	Canadian Advanced Digital Ionosondes
CDDIS	Crustal Dynamics Data Information System
CDMA	Code Division Multiple Access
CGSM	Canadian GeoSpace Monitoring
CHAIN	Canadian High Arctic Ionospheric Network
CME	Coronal Mass Ejection
CMEs	Coronal Mass Ejections
C/NOFS	Communication/Navigation Outage Forecast System
COSMIC	Constellation Observing System Meteorology, Ionosphere, and Climate
CSR	Coherent Scatter Radar
2-D	2-Dimensional
3-D	3-Dimensional

4-D	4-Dimensional
DA	Data Analytics
DASI2	Digital All Sky Imager 2
DF	Dual-Frequency
DLR	Deutsches Zentrum für Luft-und Raumfahrt (German Aerospace Centre)
DMSP	Defence Meteorological Satellite Program
Doc	Document
DOP	Dilution of Precision
DPS-4	Digisonde Portable Sounder-4
ECMWF	European Centre for Medium Range Weather Forecasts
EEJ	Equatorial Electrojet
EGNOS	European Geostationary Navigation Overlay Service
EIA	Equatorial Ionisation Anomaly
EISCAT	European Incoherent SCATtar
EPB	Equatorial Plasma Bubble
EPBs	Equatorial Plasma Bubbles
EPS	EUMETSAT Polar System
ESA	European Space Agency
ESE	Equatorial Sporadic-E
ESF	Equatorial Spread-F
ESOC	European Space Operation Centre
ESR	EISCAT Svalbard Radar
EU	European Union
EUMETSAT	European Organisation for the Exploitation of Meteorological Satellites
EUV	Extreme Ultraviolet
FBI	Farley-Buneman Instability
FDMA	Frequency Division Multiple Access
FMI	Finnish Meteorological Institute
FOC	Full Operational Capability

FORMOSAT	Formosa and Satellite
FPI	Fabry-Perot Interferometer
GAGAN	GPS Aided GEO Augmented Navigation
gAGE	research group of Astronomy and Geomatics
GBAS	Ground-Based Augmentation System
GDI	Gradient Drift Instability
GDOP	Geometric Dilution of Precision
GDP	Gross Domestic Product
GEO	Geostationary Earth Orbit
GEOSS	Global Earth Observation System of Systems
GHz	Giga Hertz
GIC	Ground Induced Currents
GIPSY	GPS-Inferred Positioning System
GIS	Geographic Information System
GISM	GPS Ionospheric Scintillation and TEC Monitor
gLAB	GNSS-Laboratory
GLONASS	Globalnaya Navigatsionnaya Sputnikovaya Sistema (Global Navigation Satellite System)
GLONASS-M	Second generation of GLONASS
GLONAS-K	Third generation of GLONASS
GNSS	Global Navigation Satellite System
GNSSs	Global Navigation Satellite Systems
GOLD	Global-scale Observation of the Limb and Disk
GOV	Government
GPS	Global Positioning System
GRACE	Gravity Recovery and Climate Experiment
GRAS	GNSS Receiver for Atmospheric Sounding
GSO	Geosynchronous Orbit
GSV	GPS Silicon Valley
GUISDAP	Grand Unified Incoherent Scatter Design and Analysis Program
GW	Gravity Waves

HAARP	High Frequency Active Auroral Research Program
HMB	Heppner–Maynard Boundary
HDF5	Hierarchical Data Format 5
HF	High Frequency
HK	Hong Kong
ICAO	International Civil Aviation Organisation
ICON	Ionospheric Connection Explorer
ICT	Information and Communication Technology
IGS	International GNSS Service
IGSO	Inclined Geosynchronous Orbit
IISR	Irkutsk Incoherent Scatter Radar
IMAGE	International Monitor for Auroral Geomagnetic Effects
IMF	Interplanetary Magnetic Field
IMPC	Ionospheric Monitoring and Prediction Centre
IONO	Ionosphere
IoT	Internet of Things
IPI	Ionospheric Plasma Instabilities
IPP	Ionospheric Pierce Point
IPS	Interplanetary Scintillation
IRNSS	Indian Regional Navigation Satellite System
IRF	Swedish Institute of Space Physics (Swedish: Institutet för rymdfysik, IRF)
ISMR	Ionospheric Scintillation Monitor Receiver
ISR	Incoherent Scatter Radar
ISRs	Incoherent Scatter Radars
ISTP SB RAS	Institute of Solar-Terrestrial Physics of the Siberian Branch of the Russian Academy of Sciences
ITU	International Telecommunication Union
JPL	Jet Propulsion Laboratory
KHI	Kelvin-Helmholtz Instability

L_{110}	Spatial distances calculated in the auroral ionosphere between consecutive IPPs of GPS PRNs ray paths at $110\,km$ shell height at $1\,s$ or $30\,s$
L_{300}	Spatial distances calculated in the polar ionosphere between consecutive IPPs of GPS PRNs ray paths at $300\,km$ shell height at $1\,s$ or $30\,s$
LAAS	Local Area Augmentation System
LOFAR	Low Frequency Array
LoS	Line-of-sight
LT	Local Time
MA	Massachusetts
MATLAB	Matrix Laboratory
MEO	Medium Earth Orbit
MIRACLE	Magnetometers - Ionospheric Radars - All sky Cameras Large Experiment
MLT	Magnetic Local Time
MPS	Multiple Phase Screen
MSAS	MTSAT Satellite Augmentation System
MSP	Meridian Scanning Photometer
MTSAT	Multifunctional Transport SATellites
MWA	Murchison Widefield Array
NASA	National Aeronautics and Space Administration
NBASS	National BDS Augmentation System Service
NIPR	National Institute of Polar Research
NMA	Norwegian Mapping Authority
NNSS	Navy Navigation Satellite System
NOAA	National Oceanic and Atmospheric Administration
NRL	National Research Laboratory (NRL)
NSAS	Nigerian Satellite Augmentation System
PANDA	Position And Navigation system Data Analyst
PBN	Performance-Based Navigation
PDOP	Position Dilution of Precision

PFISR	Poker Flat ISR
PLASLIFE	PLASma LIFEtime
PPP	Precise Point Positioning
PPS	Precise Positioning Service
PRN	Pseudorandom Noise
PRNs	Pseudorandom Noises
PNT	Positioning, Navigation, and Timing
PVT	Position, Velocity, and Time
QZSS	Quasi-Zenith Satellite System
RAIM	Receiver Autonomous Integrity Monitoring
RF	Radio Frequency
RINEX	Receiver Independent Exchange Format
RISR	Resolute Bay ISR
RISR-C	RISR Canada
RO	Radio Occultation
ROT	Rate of change of TEC
ROTI	Rate of change of TEC Index
RSAS	Regional Satellite Augmentation System
RT	Real-Time
RTI	Rayleigh-Taylor Instability
RTK	Real-Time Kinematic
RTKLIB	Real-Time Kinematic Library
SANAE	South African National Antarctic Expedition
SAR	Search and Rescue or Synthetic Aperture Radar
SatRef	Hong Kong Satellite Positioning Reference Station Network
SBAS	Satellite-Based Augmentation System
SCINDA	Scintillation Network Decision Aid
SDCM	System for Differential Correction and Monitoring
SEP	Solar Energetic Particles
SF	Single-Frequency

SJC	São José dos Campos
SNAS	Satellite Navigation Augmentation System
SNR	Signal-to-Noise Ratio
SoL	Safety of Life
SP3	Standard Product 3
SPS	Standard Positioning Service
SRI	Stanford Research Institute
SSC	Sudden Storm Commencement
STEC	Slant Total Electron Content
STFC	Science and Technology Facilities Council
SuperDARN	Super Dual Auroral Radar Network
SW	Space Weather
T_e	Electron Temperature
T_i	Ion Temperature
T_n	Neutral Temperature
TACSat4	Tactical Satellite-4
TEC	Total Electron Content
TECU	TEC Unit
TIDs	Travelling Ionospheric Disturbances
TOI	Tongues of Ionisation
UAV	Unmanned Aerial Vehicle
UHF	Ultra High Frequency
UK	United Kingdom
UN	United Nations
UNESP	Universidade Estadual Paulista Júlio de Mesquita Filho (Paulista State University Júlio de Mesquita Filho)
UNOOSA	United Nations Office for Outer Space Affairs
UPC	Universitat Politecnica de Catalunya (Polytechnic University of Catalonia)
URSI	International Union of Radio Science
U.S.	United States

USA	United States of America
USAID	United States Agency for International Development
UT	Universal Time
VHF	Very High Frequency
VLF	Very Low Frequency
VTEC	Vertical TEC
WAAS	Wide Area Augmentation System
WBMOD	WideBand MODel
WGS	World Geodetic Survey
WMO	World Meteorological Organisation

List of Symbols

%	Percent
°	Degree
< >	Average
ε_0	Permittivity of free space (F/m)
$\langle H \rangle$, $\langle D \rangle$, $\langle Z \rangle$	Temporal averages of H, D, and Z (nT)
$\pm$	Plus-minus sign
λ	Wavelength (m)
Θ	Angle between the ray path and the Earth's magnetic field induction B (°)
∇	Gradient
χ	Zenith angle of solar radiation (°) with respect to the normal
$\int$	Integral sign
ζ	Zenith angle (90° - elevation angle) (°)
λ_1	Wavelength corresponding to f_1 (m)
λ_2	Wavelength corresponding to f_2 (m)
$>$	Greater than
$\geq$	Greater than or equal to
$<$	Less than
Φ	Detrended carrier phase signal (cycles)
dh	Small change in h (m)
dP_s	Small change in P_s (m)
∂t	Small change in t (s)
P_r^s	Pseudorange between satellite and receiver (m)
ρ_r^s	Measured range between satellite and receiver (m)
dt_r, dt^s	Receiver and satellite clock offsets, respectively (s)
T_r^s	Tropospheric propagation delay between satellite and receiver (m)
I_r^s	Ionospheric propagation delay between satellite and receiver (m)

e_r^s	Unmodelled range errors including receiver noise, multipath, and other small effects (m)
ϵ_r^s	Unmodelled phase errors including receiver noise, multipath, and other small effects (cycles)
M_r^s	Sum of integer phase ambiguity, receiver, and satellite phase delay (cycles)
N_r^s	Integer carrier phase ambiguity between satellite and receiver (cycles)
$\delta_r,\ \delta^s$	Receiver and satellite phase delay, respectively (cycles)
Δt	Change in time (s)
ΔH, ΔD, ΔZ	Geomagnetic variations obtained by subtracting the calculated averages from geomagnetic field components $H,\ D,$ and Z (nT)
ΔTEC	Change in TEC ($TECU$)
$\Delta TEC/\Delta t$	Temporal TEC fluctuations ($TECU/\Delta t$)
σ_ϕ	Phase scintillation index
dB	Decibels
A	Amplitude of a GPS signal
Ar	Argon
B	Magnetic intensity or magnetic flux density (T)
B1	BeiDou carrier phase at $1561.10\ MHz$ (cycles)
B2	BeiDou carrier phase at $1207.14\ MHz$ (cycles)
B3	BeiDou carrier phase at $1268.52\ MHz$ (cycles)
B_y	The east-west direction of the interplanetary magnetic field (i.e. y-component in solar magnetic coordinates) (T)
B_z	The north-south direction of the interplanetary magnetic field (i.e. z-component in solar magnetic coordinates) (T)
c	Speed of light in a vacuum ($2.99792458\ \times\ 10^8\ m/s$)
C/N_0	Carrier to noise ratio ($dB-Hz$)
CO_2	Carbon dioxide
D	Angle of declination of B between X and H components
$d_1,\ d_2$	Distances from a transmitter and receiver, respectively (m)
D_{st}	Disturbance Storm Time Index (nT)

e	Electron
ê	Charge of electron (C)
E	East
$\mathbb{E}$	Elevation angle (°)
E	Energy (J)
E1	Galileo carrier phase at $1575.42\ MHz$ (cycles)
E5a	Galileo carrier phase at $1176.45\ MHz$ (cycles)
E5b	Galileo carrier phase at $1207.14\ MHz$ (cycles)
E6	Galileo carrier phase at $1278.75\ MHz$ (cycles)
$E \times B$	Charged particle drift experienced due to perpendicular external electric and magnetic fields (E and B, respectively)
E_{3D}	3-D positioning error (m)
eV	Electron volt
f	Radio wave frequency (Hz)
f_0	GPS fundamental frequency ($10.23\ MHz$)
f_1	GPS frequency at $154 f_0$ (Hz)
f_2	GPS frequency at $120 f_0$ (Hz)
F_1	Fresnel radius (m)
f_g	Gyrofrequency (Hz)
f_p	Plasma frequency (Hz)
$f0E, f0F1, f0F2$	Critical frequencies at ionospheric E, F1, and F2 layers, respectively (MHz)
G1	GLONASS carrier phase between $1593\ MHz\ and\ 1610\ MHz$ (cycles)
G2	GLONASS carrier phase between $1237\ MHz\ and\ 1254\ MHz$ (cycles)
G3	GLONASS carrier phase at $1207.14\ MHz$ (cycles)
GHz	Gigahertz
H	Pressure scale height of a neutral gas in the background ionosphere (N/m^2)
h	Planck's constant [6.62607015 × $10^{-34}\ J \cdot s$]
$\hbar$	Height above the Earth's surface (km)

$\hbar_1$	Height of the thin shell representing the ionosphere (km)
$\hbar_o$	Peak electron density height (km)
H^+	Atomic hydrogen positive ion
H_2O	Water
$H,\ Z$	Local geomagnetic field components of B in the horizontal (north-south) and vertical directions, respectively (nT)
He	Helium
$hmE, hmF1, hmF2$	Peak heights at ionospheric E, F1, and F2 layers, respectively (km)
Hz	Hertz
i	Ion
I	Detrended GPS signal intensity ($dB - Hz$)
J	Joule
K	Kelvin
K_p	Global geomagnetic storm (Planetary K) index
keV	Kiloelectron volt
Kg	Kilogram
km	Kilometre
km/s	kilometre per second
kW	Kilowatt
L1	GPS carrier phase at $154f_0$ (cycles)
L2	GPS carrier phase at $120f_0$ (cycles)
L5	GPS carrier phase at $115f_0$ (cycles)
L_e	Rate of electron loss ($\mathrm{electrons/m^3/s}$)
m	Metre
$M(E)$	Mapping function which is a ratio of STEC to VTEC
m_e	Mass of electron (kg)
m^2	Square metre
m^3	Cubic metre
m^{-3}	Per cubic metre
MHz	Megahertz

min	Minute
ms	Millisecond
m/s	Metre per second
MHz	Megahertz
MW	Megawatts
n	Neutral
$\mathcal{n}$	Refractive index
N	North
N_2	Molecular nitrogen
N_e	Electron density ($electrons/m^3$)
N_o	Peak electron density of the layer ($electrons/m^3$)
$NmE, NmF1, NmF2$	Peak densities at ionospheric E, F1, and F2 layers, respectively ($electrons/m^3$)
nm	Nanometre
NO^+	Nitrogen oxide positive ion
nT	Nanotesla
O^+	Atomic oxygen positive ion
O_2	Molecular oxygen
O_2^+	Molecular oxygen positive ion
O_3	Ozone
P_s	Slant range path between satellite and receiver (km)
pW	Picowatt
Q_e	Rate of electron production ($\mathrm{electrons/m^3/s}$)
R	Range delay (m)
$R_\oplus$	Earth's radius ($6378.14\ km$)
rad	Radian
s	Second
S_4	Amplitude scintillation index
S_{4corr}	Corrected S_4
S_{4tot}	Total S_4

sec	$1/cos$
S/N_0	Signal to noise ratio (dB)
t	Time (s)
T	Tesla
$TEC(k)$	TEC at epoch k $(TECU)$
$TEC(k-1)$	TEC at epoch $k-1$ $(TECU)$
$TECU/s$	TEC Unit per second
$TECU/30\ s$	TEC Unit per 30 seconds
$TECU/min$	TEC Unit per minute
v_e	Mean velocity of electron (m/s)
X, Y, Z	Cartesian components of B in the northward, eastward, and downward directions, respectively collected from the IMAGE magnetometer network (nT)
X_0, Y_0, Z_0	Geodetic GNSS station *a-priori* ECEF coordinates courtesy of IGS (m)
$X(t)$, $Y(t)$, $Z(t)$	Geodetic GNSS station coordinates in ECEF reference frame at each epoch t (m)
z	constant whose value depends on $\hbar$, $\hbar_o$, and H

1 Introduction

Our planet's atmosphere is strongly influenced by the dynamics of the Sun. Solar emissions from explosive eruptions on the surface of the Sun can find their way into our planet's atmosphere by means of the solar wind – a continuous stream of charged particles originating from the Sun that sweeps across the solar system. It also carries along with it the Interplanetary Magnetic Field (IMF) 'frozen-in' with the solar wind, whose source is the solar magnetic field. The emissions carried by the solar wind influence physical processes in the Earth's magnetosphere, which is the region surrounding the Earth that is dominated by its magnetic field. It also impacts the Earth's atmosphere, both neutral and ionised, which lies within the inner magnetosphere. Dynamics in this solar-terrestrial (near-Earth space) environment is referred to as space weather.

Solar Extreme Ultraviolet (EUV) and X-ray emissions together with charged particles carried in the solar wind interact with the Earth's atmosphere to create the ionosphere. The ionosphere is an electrically neutral plasma in the upper atmosphere that connects the near-Earth space environment with the neutral atmosphere. EUV and X-rays ionise atoms and molecules of the neutral atmosphere in a process called photoionisation. In the high-latitude ionosphere, the magnetic field lines connecting the region with magnetosphere are almost vertical. Energetic charged particles are injected into the high-latitude ionosphere through these magnetic field lines causing the formation of positive ions and free electrons in a process referred to as impact ionisation. The auroral and polar regions are therefore highly dynamic and complex due to a combination of ionisation and particle precipitation owing to interaction with magnetosphere. These physical processes result in large-scale electron density irregularities, which are localised fluctuations of the ionospheric electron density over the region. In this region, dynamic and drifting large-scale irregularities of longer duration can cascade into small-scale irregularities of shorter duration owing to instability mechanisms causing scintillation. This is, however, a common feature of the equatorial ionosphere.

The ionosphere acts as a dispersive medium to electromagnetic waves in which the refractive index depends on frequency. Free electrons in the ionosphere interact

with and refract the incident waves resulting in delay of propagation. Where ionospheric irregularities are present, the gradient in electron density also can distort the electromagnetic signals transversing these structures through diffractive and additional refractive processes causing rapid fluctuations of the amplitude and phase of the signals. This is known as ionospheric scintillation. For GNSS signals travelling from satellite to receiver, operating in the $1-2\,GHz$ range, these effects are seen as a delay in the received GNSS signal and scintillation of the signal, respectively. Typically, ionospheric irregularities cause GNSS signals to experience mainly amplitude scintillation in the equatorial ionosphere, while auroral and polar ionospheres see predominantly phase scintillation. Phase fluctuations can cause interruptions or degradations of GNSS signals leading to a reduced signal amplitude or losses of lock due to cycle slips. Scintillation and phase fluctuations can impact on the performance of GNSS positioning for receivers operating at auroral and polar latitudes.

Given the impact of ionospheric irregularities on GNSS signals, they can be characterised by measuring their effects on the amplitude and phase of the received GNSS signals. Scintillation indices (S_4 and σ_ϕ) and fluctuations in Total Electron Content (TEC), the total number of electrons in a one-metre square area perpendicular to signal path, can be used as convenient proxies to investigate and characterise the presence of small-scale (10's m to 100's m) and large-scale (10's km to 100's km) irregularities, respectively. Characterisation of ionospheric irregularities at auroral and polar ionospheres is performed by measuring the fluctuations in TEC, which is often used as a convenient proxy to indicate the presence of phase scintillation. While in the equatorial ionosphere, ionospheric irregularities are characterised by the Rate of change of TEC Index (ROTI) which is strongly associated with amplitude scintillation.

This thesis aims to investigate the spatial distribution of electron density irregularities in the E and F layers and their impact on received GNSS signals operating at the auroral and polar latitudes. A simultaneous multi-instrument experimental campaigns involving the European Incoherent SCATter (EISCAT)/EISCAT Svalbard Radar (ESR) and geodetic GNSS receiver stations in 2018 and 2019 were designed and conducted. It is important to note that the data collected from these experiments are used in this research. The uniqueness in this

aim of the thesis is the new method used in the study. In the new method, EISCAT UHF/ESR beams were designed to theoretically intersect GPS ray paths at ionospheric heights. This is so because phase screens, which are observation planes characterised by irregularities, are transverse to the propagation direction of GPS signals. EISCAT UHF/ESR are incoherent scatter radars with $32\ m$ parabolic steerable antennas operating at $930\ MHz$ and $500\ MHz$ (UHF) respectively used to determine the conditions in the background European high-latitude ionosphere. The EISCAT facility located at Tromsø is used to study the auroral irregularities while the ESR facility located at Longyearbyen is employed to investigate the polar irregularities.

To achieve this aim, the research objectives are to:

a) Review literature to provide insight into the thesis.
b) Design and simulate the experimental geometry as well as conduct the 2018 and 2019 EISCAT UHF/ESR campaigns at the auroral and polar latitudes, respectively.
c) Simultaneously collect the EISCAT UHF/ESR experimental data combined with geodetic GNSS data courtesy of IGS. In addition, ASC, IMAGE magnetometers, and SuperDARN data for 2018 and 2019 experiments are collected for the purpose of interpretations and validations. The research data collected in this context are referred to as ionospheric data.
d) Read, process, and analyse raw EISCAT UHF/ESR and GNSS data (GUISDAP/gLAB/MATLAB).
e) Discuss the results obtained to infer the impact of ionospheric electron density irregularities on the performance of GNSS positioning using 30-s and 1-s observables at the auroral and polar latitudes.
f) Draft peer-reviewed journal papers for the purpose of publication in GPS Solutions, Sensors, Radio Science, etc.
g) Present summary and conclusions.
h) Finally, future work. The future work is divided into parts. Firstly, to give a new design geometry of November 2019 EISCAT UHF/ESR campaigns. Secondly, to conduct a background study on the potentials of GNSS in Sub-Saharan Africa with a view to use the experience acquired from the research to examine the socio-economic impact of ionospheric irregularities on

applications of precise GNSS in the region. Apart from this, the experience acquired can support the deployment of AMISR and other ground-based ionospheric instruments at the Department of Electrical and Electronic Engineering, University of Abuja, Nigeria. This can facilitate education, training, and research on upper atmospheric studies and GNSS applications.

In this work, EISCAT UHF/ESR incoherent scatter radars were used to infer the spatial and temporal distribution of electron density irregularities along specific ionospheric shell heights in the E and F layers. EISCAT UHF/ESR beams are directed across Global Positioning System (GPS) ray paths of relevance alternating in space and time along these selected ionospheric shell heights. This is so because the irregularities are distributed across the radio signal path. The presence and spatial scale of irregularities can be inferred from EISCAT UHF/ESR profiles of electron density measured transverse to GNSS ray paths of relevance. Previous methods sampled profiles of electron density by means of EISCAT UHF/ESR where the radar beams and GNSS ray paths have the same line-of-sight (LoS). This means the EISCAT UHF/ESR facility is collocated with the GNSS receiver.

Phase changes imposed on GNSS signals transversing these irregularities are characterised using TEC fluctuations and or scintillation. The impact of phase fluctuations caused by irregularities in the high-latitude ionosphere on GNSS positioning was investigated during the 2018 and 2019 campaigns in the presence of quiet-to-moderately disturbed geomagnetic conditions. In this work, the impact of auroral and polar irregularities was studied in terms of TEC fluctuations and positioning performance.

The high-latitude ionospheric conditions, as well as the likely origin of the observed structures are further investigated using the following ionospheric instruments: All-Sky Camera (ASC) courtesy of the National Institute of Polar Research (NIPR), Magnetometers courtesy of the International Monitor for Auroral Geomagnetic Effects (IMAGE), and Super Dual Auroral Radar Network (SuperDARN) courtesy of VirginiaTech.

The impact of high-latitudes ionospheric irregularities on GPS positioning is investigated using geodetic GNSS receivers located at auroral and polar latitudes (near EISCAT UHF/ESR). The data courtesy of the International GNSS Service

(IGS) are used to infer the presence of large-scale electron density irregularities obtained from fluctuations of TEC derived from carrier phase signals. The corresponding impact of the observed irregularities on GPS positioning is studied using positioning performance. In this research, 30-s and 1-s RINEX observation data combined with Antenna Exchange Format (ANTEX) file as well as orbit and clock sources were used to process GPS-only positioning solution by means of gLAB software.

1.1 Structure of Thesis

To provide an insight on the content of the thesis, Chapter 2 presents an overview of the ionosphere. To achieve this; space weather events, the ionosphere, ionospheric plasma instabilities, and ionospheric irregularities at equatorial, middle, and high-latitudes are discussed.

Chapter 3 presents a review of ionospheric irregularities and their impact on GNSS applications at equatorial, middle, and high-latitudes. Techniques for characterisation of these irregularities in terms of scintillation and TEC measurements were investigated by means of ground-based and in situ instrumentation. The effects of irregularities on the performance of GNSS positioning using RTK and PPP solutions are also reviewed.

Chapter 4 discusses the effects of the ionosphere on propagation of GNSS radio signals. These effects were studied in terms of scintillation and TEC fluctuations using theoretical equations to understand how these ionospheric metrics were calculated. Further discussion on the influence of the ionosphere on GNSS radio signals propagation in the various ionospheric regions is included.

Chapter 5 gives the ionospheric instrumentations and measurements utilised (or with a potential to be used in future) in the report. These include EISCAT UHF/ESR incoherent scatter radars, GNSS receivers, IMAGE magnetometers, SuperDARN HF radars, ASCs, and Spirent GPS Simulator. In this chapter, software utilised during the investigation were listed as well as the challenges encountered while using GNSS data and keograms obtained from Kiruna courtesy of DLR and NIPR, respectively.

Chapter 6 presents the report of a multi-instrument experimental campaign involving EISCAT UHF/ESR and geodetic GNSS receivers at the auroral and polar latitudes in March 2018. The purpose was to understand how ionospheric irregularities originate GPS phase fluctuations expressed in terms of TEC fluctuations in the regions. The spatial distribution as well as the origin of auroral and polar irregularities inferred from EISCAT UHF/ESR profiles of electron density measured traverse to GNSS ray paths were studied. The results of this experimental investigation has been submitted to Radio Science.

Like Chapter 6, Chapter 7 reports the results of March 2018 experimental campaigns designed and conducted to provide insight on the performance of GPS positioning in the presence of phase fluctuations caused by auroral and polar irregularities. The presence and type of irregularities was deduced from EISCAT UHF/ESR profiles of electron density. Other measurements were collected and analysed to validate as well as support the interpretation of results. Here, the results of this investigation will be submitted to a peer-reviewed journal for the purpose of publication.

Lastly, Chapter 8 summarises the results of the research and the conclusions as well as future work. The first part of the future work presents a new design geometry of November 2019 experimental campaigns using EISCAT UHF/ESR beams along hypothetical phase screens at several ionospheric heights to intersect GNSS radio ray paths of relevance in the northern European ionosphere. This campaign was a follow-up on 2011, 2013, 2016, and 2018 experimental investigations. In this case, SGS was utilised to simulate the experimental geometry in advance using azimuth and elevation measurements for given positions of IGS geodetic GNSS receivers stations at the auroral and polar latitudes. To increase confidence of the SGS measurements, the accuracy of the design geometry was validated and confirmed to show a strong association with SP3 satellites orbital data. In this research, only the new design geometry of EISCAT UHF/ESR experiments are presented. The results of the November 2019 campaigns will be submitted for publication. The second part gives a background study on the potentials of GNSS in Sub-Saharan Africa leading to a proposed research on the “Socio-economic assessment of the impact of irregularities on applications of precise GNSS (e.g. oil and gas, precision agriculture, civil aviation) in Sub-Saharan Africa.”

2 Overview of the Ionosphere

2.1 Introduction

To enable understanding of how irregularities originate in the ionosphere, a brief overview on Space Weather (SW) events is presented. Adverse SW conditions are closely associated with disturbed ionospheric conditions. SW events such as solar wind, solar radiations, solar flares, Solar Energetic Particles (SEPs), and Coronal Mass Ejection (CME) can cause disturbances in the Earth's magnetic field – magnetosphere - and this, in turn, influence the morphology and dynamics of the Earth's ionosphere [*Eastwood, 2008*]. The origin of ionospheric plasma instabilities and subsequently irregularities are traceable to the Sun. These SW events are good indicators of ionospheric perturbation [*Ghafoori and Skone, 2015*]. In this report, to provide insight into ionospheric irregularities, a brief discussion on SW and Ionospheric Plasma Instabilities (IPIs) originating ionospheric irregularities is considered.

2.2 Effects of SW on Systems

SW variability has been reported to influence the performance of space-based and ground-based technological infrastructure [*Moen et al., 2013; Denardini et al., 2016; Correia et al., 2018*] as shown in Figure 2.1. Adverse SW conditions can trigger Ground Induced Currents (GIC) affecting electric power grid while Gravity Waves (GW) associated with ionospheric scintillation can severely degrade the performance and reliability of GNSS-based technologies [*Eastwood, 2008*]. SW events can cause disturbances in the ionosphere, thereby affecting GNSS services and operations [*Doherty et al., 2004*]. Economists have pointed out that these adverse SW conditions can impact large losses on technological systems supporting our modern life, for example, in applications including geodetic positioning, navigation, and timing [*Correia et al., 2018*]. Such losses can account to up to hundreds of million dollars per annum [*Horne, 2003; Oxford Economics, 2012*]. Several definitions have been given to the term SW but, for the benefit of this report, the definition attributed to the World Meteorological Organisation (WMO) is adopted. Here, the term SW is defined as ‘‘Conditions and processes occurring in

space, including on the Sun, in the magnetosphere, ionosphere, and thermosphere, which have the potential to affect the near-Earth environment" [*Denardini, 2016*]. In view of this, ionospheric SW can be correlated with ionospheric instabilities and these ionospheric instabilities are regarded as primary candidates inducing ionospheric irregularities. One of the signatures of adverse SW is amplitude and phase scintillation often used to characterise ionospheric irregularities [*Kintner et al., 2007*].

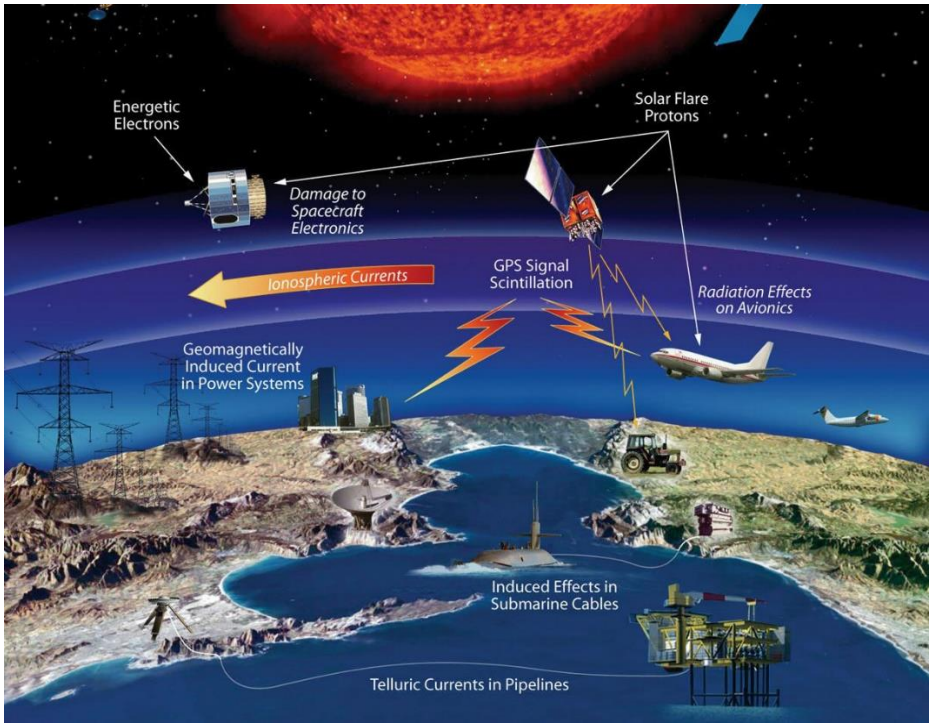

Figure 2.1: Space Weather effects on technological infrastructure. Courtesy of NASA.
Source: https://www.nasa.gov/mission_pages/sunearth/spaceweather/index.html

2.2.1 Solar wind

Parker, [1958] proved that the solar corona is in a hydrostatic non-equilibrium state, which expands continuously. Matters leave the Sun from corona and stream out into space and this is called solar wind. In the early 1960s, space-borne probes proved the existence of solar wind as a permanent event of the solar system. Solar wind can be characterised in terms of its density, velocity, and the direction of IMF. Space-based devices have observed velocity of around $500\,km/s$. Solar wind of velocity greater than $800\,km/s$ is regarded as fast-moving solar wind, or slow-moving solar wind otherwise. The speed of the solar wind also determines the

magnitude of a geomagnetic storm. In other words, solar wind velocity is directly proportional to the magnitude of a geomagnetic storm. The solar wind is one of the mechanisms through which solar events are transported to the Earth environment, which is vital to the solar-terrestrial interactions. As the solar wind flows out almost radially from the surface of the Sun, called the corona, it carries along with it a very weak magnetic field, IMF. Due to solar rotation, the magnetic field tends to form a spiral formation as it travels with the solar wind. As the solar wind moves outwards from the Sun, it then interacts with the magnetosphere thereby causing disturbances. These disturbances, supported by irregular events originating from the Sun, can induce geomagnetic storms which have adverse effects on the electrodynamic state of the ionosphere. Details on the solar wind are contained in *Hargreaves*, [1992].

2.2.2 Solar flares

Solar flares, as one of the major problems in SW, occur due to eruptions from active regions of the Sun. They are sudden brightening of a small section of the photosphere lasting for few minutes to several hours [*Schunk and Nagy, 2009*]. Solar flares are important sources of sporadic particles and electromagnetic radiation. The presence of enhanced X-ray and EUV radiations are associated with flares. Like CMEs (Section 2.2.3), flares are important sources of energetic particles, which can affect the performance of space-based and ground-based navigation and communication infrastructure. As geomagnetic storms are often classified based on G-Scale which can be access online (https://spaceweather.sansa.org.za/space-weather-information/definitions/noaa-scales/297-geomagnetic-storm-scale), flares are categorised according to R-Scale (https://www.swpc.noaa.gov/noaa-scales-explanation). Measurements revealed that flares consist of both cold and hot plasma. A cold plasma from a solar flare has a temperature of about $1000\,K$ whereas as hot plasma portion of flares can be as high as 10^7 to 10^8 K. Observations showed that a typical flare releases 10^{25} J of electromagnetic energy and sometimes emits multiples of this energy as particles. The large amount of energy is stored in the magnetic fields and are released when the fields break up [*Hargreaves, 1992*].

2.2.3 Coronal Mass Ejections (CMEs)

CMEs are forms of mass release from the Sun's corona and these are magnetised plasma, which consist of primarily of electrons and protons. As these streams of high-energy particles are released from the surface of the Sun, they tend to expand and sometimes attain a speed of about $1000\,\mathrm{km/s}$. CMEs are consequence of eruptions from active regions of the Sun. CMEs are known as sources of intense geomagnetic storms and energetic particles. Large CME is observed to contain about $10^{13}\ kg$ of plasma [*Hargreaves, 1992*]. CMEs are considered as one of the transient phenomena induced by the Sun that are related to erupting prominences and solar flares. They have been observed to follow solar flares and are often released into the solar wind. CMEs depend on solar activity, for example, near solar maximum, the Sun produces multiples of CMEs per day, whereas near solar minimum, the Sun produces a single CME every five days. The largest recorded geomagnetic perturbation was the solar storm of 1859 (the Carrington Event) associated with a solar flare and possibly CMEs as they tend to follow flares [*Baker et al., 2013 and references therein*].

2.3 The Ionosphere

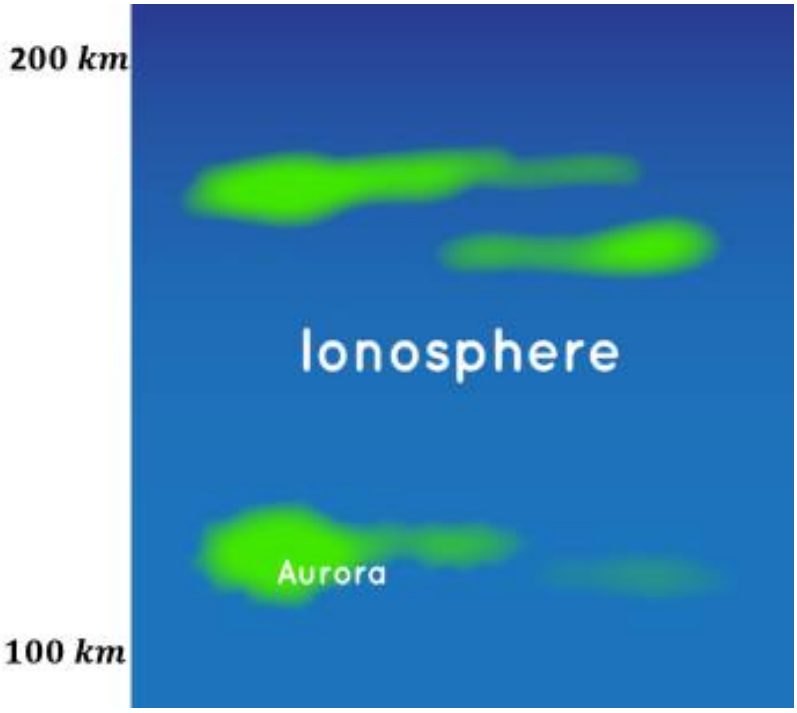

Figure 2.2: Shows aurora in the ionosphere (green colour).
Source: https://spaceplace.nasa.gov/ionosphere/en/

The ionosphere is the portion of the atmosphere where free electrons and ions of electrodynamic properties are governed by gravity and magnetospheric mechanisms [*Zolesi and Cander, 2014*]. Watson-Watt coined the name ionosphere several years ago, but it was used in 1932 according to *Hunsucker and Hargreaves*, [2007]. The ionosphere extends from about $50\,km$ to above $1000\,km$ altitude *[Klobuchar, 1991; Hargreaves, 1992; Doherty, 2009*]. It overlaps the neutral-atmospheric mesosphere, thermosphere, and exosphere. Plasma properties in the ionosphere show variation with geographic location, local time, season, solar activity, and geomagnetic conditions. According to studies, the principal sources of plasma and energy in the region are the Extreme Ultraviolet (EUV), Ultraviolet (UV), X-ray, and particle precipitation [*Doherty, 2009, Cannon et al., 2013; Barona et al., 2017*]. Magnetospheric electric field and energetic (energies $\geq 1\,keV$) charged particles have significant effects on the ionosphere especially in high-latitudes [*Kivelson, 1995; Schunk and Nagy, 2009*]. The ionosphere's chemical composition includes $O, O_2, N, N_2, and\ NO$ from which positive charge ions and negative charge electrons are produced.

As a requirement, the ionising photons and particles must possess energies (energy $E = hc/\lambda$ in the case of photons and kinetic energy in the case of particles) greater than the ionisation potential or binding energy of atomic or molecular constituents of the ionosphere. Interaction of charged particles with atomic or molecular constituents of the ionosphere can produce aurora as indicated in Figure 2.2. Free electrons are formed during photoionisation (or particle ionisation) process and neutrals are regenerated during the recombination process. SW variabilities, mostly controlled by the Sun, determine the structure and dynamics of the ionosphere [*Cannon et al., 2013*]. These variabilities can affect the performance and reliability of space-based and ground-based communication and navigation systems [*National Science Foundation, 2012*]. *Zolesi and Cander*, [2014] discussed in detail the general structure of the ionosphere and the primary causes of ionisation.

2.3.1 Ionospheric Layers

The ionosphere can be classified based on layers which are the D, E, and F layers. The D layer extends between an altitude of $50\,km$ and $90\,km$ and has electron

density between 10^8 and 10^{10} m^{-3}. Similarly, the E layer extends between an altitude of 90 km and 150 km and electron density between 10^{10} and 10^{11} m^{-3} with ionisation peak at 105 $km - 110$ km [*Hunsucker and Hargreaves, 2007*]. In addition, the F layer extends between an altitude of 150 km and 1000 km and has an electron density between 10^{11} and 10^{12} $electrons/m^3$ [*Aikio et al., 2011*]. The E layer was the first to be discovered, followed by the F and D layers. Critical frequencies ($f0E, f0F1, and\ f0F2$), peak heights ($hmE, hmF1, and\ hmF2$) and peak densities ($NmE, NmF1, and\ NmF2$) represent the E and F layers [*Schunk and Nagy, 2009*]. Critical frequency is the maximum value of frequency in a given layer at a peak height and a peak density above which a radio wave penetrates the ionosphere and below which the wave is reflected back from the ionosphere.

The E layer consists of Sporadic-E (Es) layer, which affects the propagation of radio waves because of enhanced electron density irregularities, and the E layer is strongest at daytime [*Aylward, 2012*]. Furthermore, the F layer is broken into F1 and F2 layers. Most ionospheric scintillation activities occur in the F layer [*Hargreaves, 1992*]. During the day, the D, E, F1, and F2 layers are present. However, at night-time, the D, E, and F1 layers disappear [*Anderson and Fuller-Rowell, 1999*] while F1 and F2 layers combine to form F layer [*Klobuchar, 1991*]. The F2 layer lies between an altitude of 250 km and 400 km and its altitude is higher at daytime than night-time as well as during solar maximum [*Aylward, 2012*]. Among the ionospheric layers, the F2 layer has the greatest concentration of free electrons which decreases during night-time due to recombination as indicated in Figure 2.3. The F2 layer is the most variable and least predictable. This layer has the greatest impact on GNSS signals including radio telecommunication infrastructure [*Anderson and Fuller-Rowell, 1999; SBAS-IONO Working Group, 2012*], and its ionisation density peaks between 200 km and 400 km altitude on average [*Hunsucker and Hargreaves, 2007*].

In terms of composition, around the peak of the F layer, O^+ dominates and H^+ starts to increase considerably above 300 km. In the E and upper D layers, NO^+ and O_2^+ are dominant. In addition, the D layer consists of neutrals, which include $N_2, O_2, Ar, CO_2, He, O_3, and\ H_2O$ and both positive and negative ions [*Aylward, 2012*]. The height of each layer of the ionosphere depends on solar zenith angle, time of

day, season of year, 11-year solar cycle, and geomagnetic conditions *[Zolesi and Cander, 2014*].

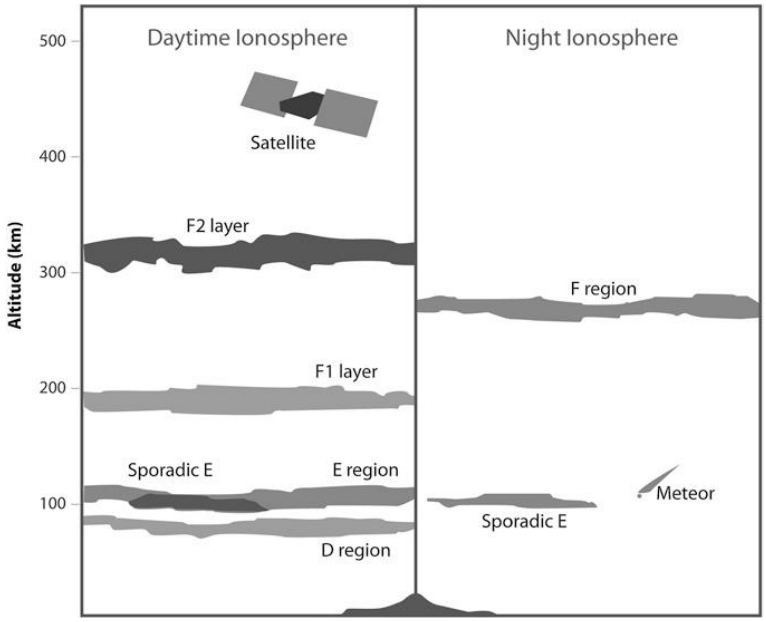

Figure 2.3: Ionospheric layers at daytime and night-time. The light grey shaded electron density is around $10^{10}\ electrons\ m^{-3}$ and the dark grey shaded electron density is around $10^{11}\ electron\ m^{-3}$ [*Zolesi and Cander, 2014*].

2.4 Ionospheric Plasma Instabilities (IPIs)

Instabilities can occur in a medium when there is a positive feedback process. For instance, a medium can be unstable due to internal or external factors. In the presence of free energy, waves can be self-excited and a state of unstable equilibrium is attained. A state of instability is a motion with a potential to decrease the free energy and then cause the plasma into a dynamic equilibrium manifesting as perturbations [*Chen, 1984*]. The perturbation may induce disturbances in some constituents of the medium and these effects, in turn, can enhance the original perturbation thereby causing the resultant perturbation to rise. In the same medium, there may exist other consequences tending to damp the perturbation. However, if the consequences tending to reduce the perturbation are in a minority to those enhancing the perturbation as well as inducing positive feedback, this is termed instability. Instability has the potential to develop if it grows in a rapid and fast procession and when the seeding factors, in this case positive or negative, produce

an effect greater than a specific threshold, then the instability grows [*Hargreaves, 1992*].

IPI is explained based on ionospheric region. Instabilities in the high-latitudes, mid-latitudes, and equatorial latitudes ionosphere are unique and distinct. In the high-latitudes ionosphere are Gradient Drift Instability (GDI) ("$E \times B$" or cross-field instability), Kelvin-Helmholtz Instability (KHI), Auroral Electrojet (AEJ), and Farley-Buneman (two-stream) Instability (FBI) [*Fejer and Kelly 1980; Keskinen and Ossakow, 1983; Moen et al., 2013*]. In the equatorial ionosphere, Rayleigh-Taylor Instability (RTI), Equatorial Plasma Bubbles (EPBs), Equatorial Sporadic-E (ESE), Equatorial Spread-F (ESF), and Equatorial Electrojet (EEJ) have been considered as types of instabilities associated with the region [*Fejer and Kelly, 1980*]. For the benefit of this thesis, only three high-latitudes IPI are discussed (GDI, FBI, and KHI).

2.4.1 Gradient Drift Instability (GDI)

Under certain conditions, as ionospheric plasma cloud convect, they become unstable leading to GDI expressed as $E \times B$ plasma drift [*Keskinen and Ossakow, 1983*]. As an example of Rayleigh-Taylor Instability, GDI is described by when a heavier fluid is placed upon a lighter one [*Chen, 1984*]. This mechanism is illustrated in Figure 2.4. GDI is often associated with instabilities in the high-latitudes ionosphere while RTI is used to describe the physics of plasma bubbles in the equatorial ionosphere.

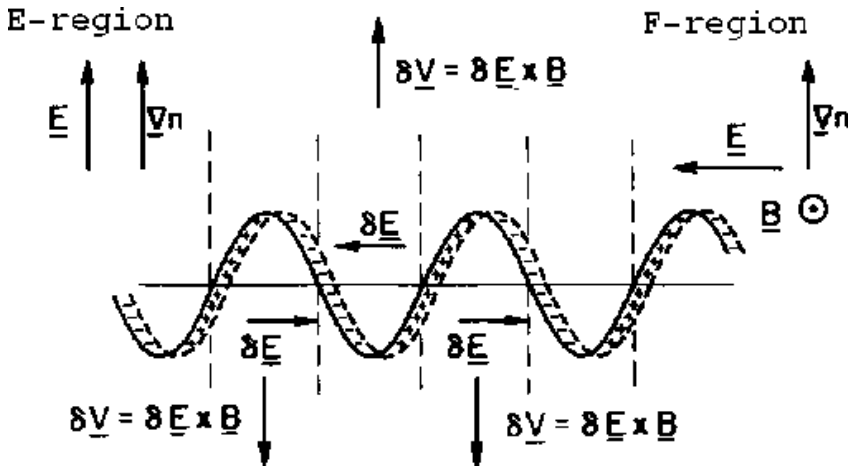

Figure 2.4: Gradient Drift Instability (GDI) in the E and F region of the High-Latitude ionosphere.
Source: http://www.ferzkopp.net/Personal/Thesis/node11.html

As the collision frequency of electrons and ions becomes less than gyrofrequency, the positive ions and the negative electrons become separated due to a force acting perpendicular to the magnetic field (B). Variation of plasma density and convection of plasma creates a net positive and negative charge separation which consequently produces a measurable polarisation electric field δE. In the presence of magnetic field (B), the third force at right angles to E and B is generated given by $E \times B$. In the ionospheric F layer, the GDI has been considered as a mechanism causing irregular plasma structures to cascade into smaller structures [*Hargreaves, 1992*]. Plasma structuring in the high-latitude ionospheric polar cap patches is associated with GDI mechanism [*Gondarenko and Guzdar, 2004*].

2.4.2 Farley-Buneman Instability (FBI)

As one of the likely causes of high-latitude E layer irregularities, the FBI also known as two-stream instability is propelled by auroral electrojet current. FBI produces electrostatic waves in the E layer due to variations of electrons and ions velocity above a certain threshold [*Hunsucker and Hargreaves, 2007*]. Separation of positive ions and negative electrons create electric fields, which in turn produce electrojet currents leading to the development of plasma instabilities. This mechanism has been used to explain the generation of small-scale irregularities in both auroral and polar cap ionospheric E layer [*Keskinen and Ossakow, 1983; and references therein*]. FBI creates unstable waves in the ionospheric E layer resulting in plasma heating and this is connected to irregular electron temperature.

2.4.3 Kelvin-Helmholtz Instability (KHI)

Another type of instability common to the high-latitudes ionosphere is the KHI (see Figure 2.5). Changes in velocity across the interface of two fluids create KHI, which manifests as waves on the surface of the fluids [*Hunsucker and Hargreaves, 2007*]. In the auroral latitudes, for instance, KHI has been observed to develop in the region of a strong velocity shear. Velocity shear is when two different ionospheric layers are moving at different velocities. As these velocities interact with each other, the resultant effect is the wake-like structure indicated in Figure 2.5. Inhomogeneous

structures are developed from relatively smooth plasma because of the effects of KHI and other instabilities phenomena occurring in the region. These structures created by velocity shear are magnetic field-aligned and can span in a spatial scale between $0.1\ km$ and $10\ km$ through which ionospheric scintillation is developed. This typical high-latitudes scintillation can originate amplitude fading and phase modulation degrading operations and services in the VHF and few GHz [*Kivelson, 1995*].

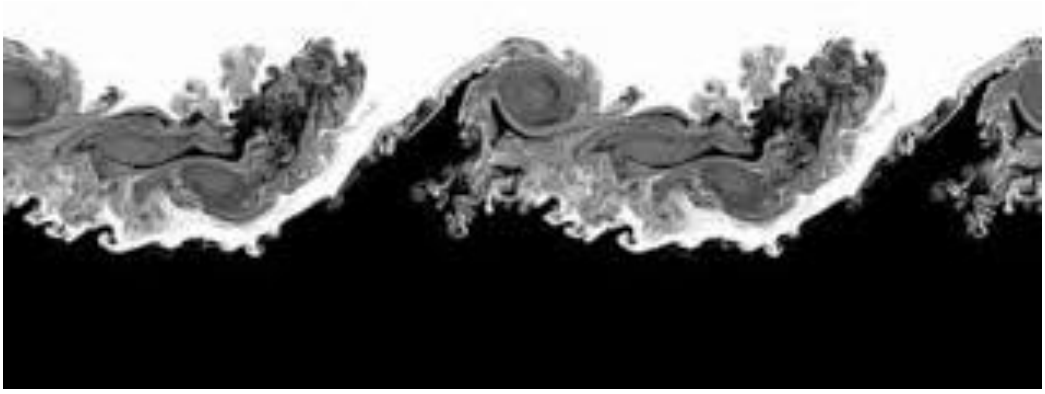

Figure 2.5: Example of Kelvin-Helmholtz Instability caused by a strong velocity shear. The shaded grey embedded in white background is instability manifesting as wave-like structures.
Source: https://www.globalweatherclimatecenter.com/weather-education/weather-phenomena-what-is-kelvin-helmholtz-instability-credit-met-office#

2.5 Ionospheric Irregularities

Several ground-based and in situ experiments as well as theoretical research were conducted to investigate ionospheric irregularities. Results of the investigation suggest a positive correlation between ionospheric plasma instabilities and ionospheric irregularities [*Fejer and Kelly, 1980; Teunissen and Montenbruck, 2017*]. Plasma instabilities mechanisms acting on plasma structures can produce ionospheric irregularities [*Keskinen and Ossakow, 1983*]. Ionospheric irregularities can be characterised by using TEC fluctuations and scintillation. Scintillation-producing irregularities have a typical spatial scale of $10's\ m$ to $100's\ m$. To the GNSS user community, the presence of irregularities as GNSS signals transverse plasma structures can cause losses of lock due to cycle slips on the received GNSS signals as indicated in Figure 2.6. Figure 2.6 shows GPS ray path from GPS satellite to a ground-based GNSS receiver. The ray path passes across three different

ionospheric shell heights ($350\ km$, $250\ km$, and $150\ km$, respectively) containing ionisation structures to the receiver. These given ionospheric shell heights were chosen to investigate the contribution of E and F layers irregularities to GNSS positioning at the auroral and polar latitudes during 2018 experimental campaigns.

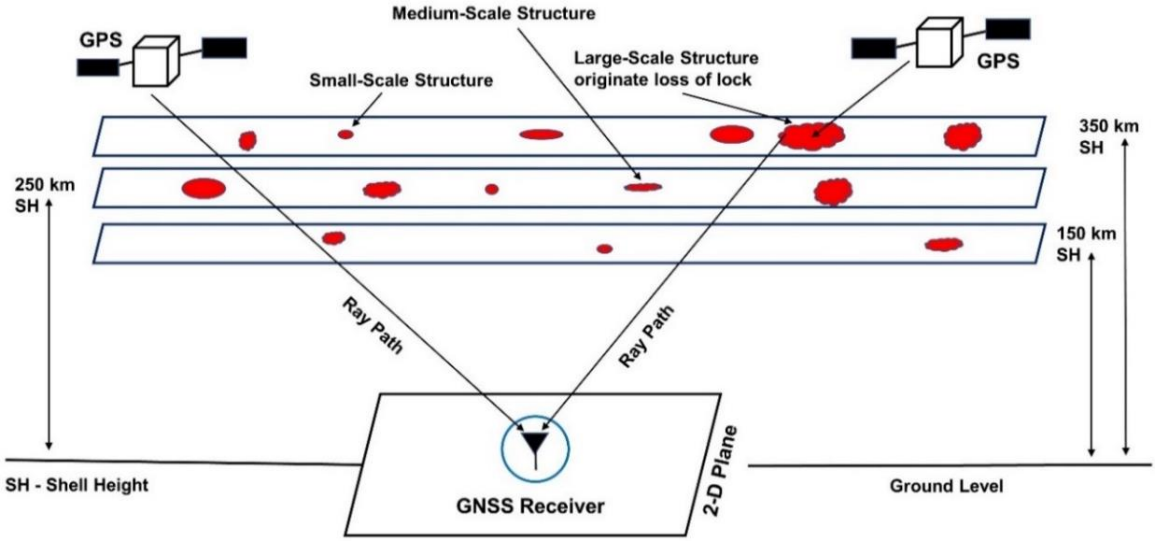

Figure 2.6: Example of the impact of electron density irregularities on GPS signals at $150\ km$, $250\ km$, and $350\ km$ ionospheric shell heights observed from a ground-based GNSS receiver. Ionospheric shell height is the altitude from the ground-based GNSS receiver to a given ionospheric layer which is defined by the ellipsoidal shape of the Earth.

Irregularities have been studied for over 80 years to understand their evolution, morphology, and dynamics and to mitigate their effects on GNSS and telecommunication technologies [*Booker and Wells, 1938; Yokoyama, 2017; and references therein*]. In the equatorial and high-latitudes ionosphere, for example, different geophysical mechanisms originate irregularities. In the case of the equatorial ionosphere, equatorial electrojet has been considered as a likely candidate inducing equatorial irregularities. However, in the high-latitudes ionosphere, particle precipitation and convecting plasma patches are likely sources of ionospheric irregularities in the region [*Hargreaves, 1979; Keskinen and Ossakow, 1983*]. Ionospheric irregularities in electron density distribution manifesting in the form of ionospheric density gradient can affect the operations and services of GNSS. The morphology and dynamics of these irregularities have the potential to distort the propagation of RF signals, for example, L-band, inducing cycle slips, losses of lock, and sometimes outages on received GNSS signals [*Correia et al., 2018*]. As RF signals traverse the ionosphere, ionospheric

irregularities can scatter radio waves inducing refraction (from large-scale irregularities) effects and diffraction (from small-scale irregularities) effects [*Rishbeth and Garriott, 1969*]. These phenomena both have the potential to degrade the quality of GNSS signals [*Eastwood, 2008*].

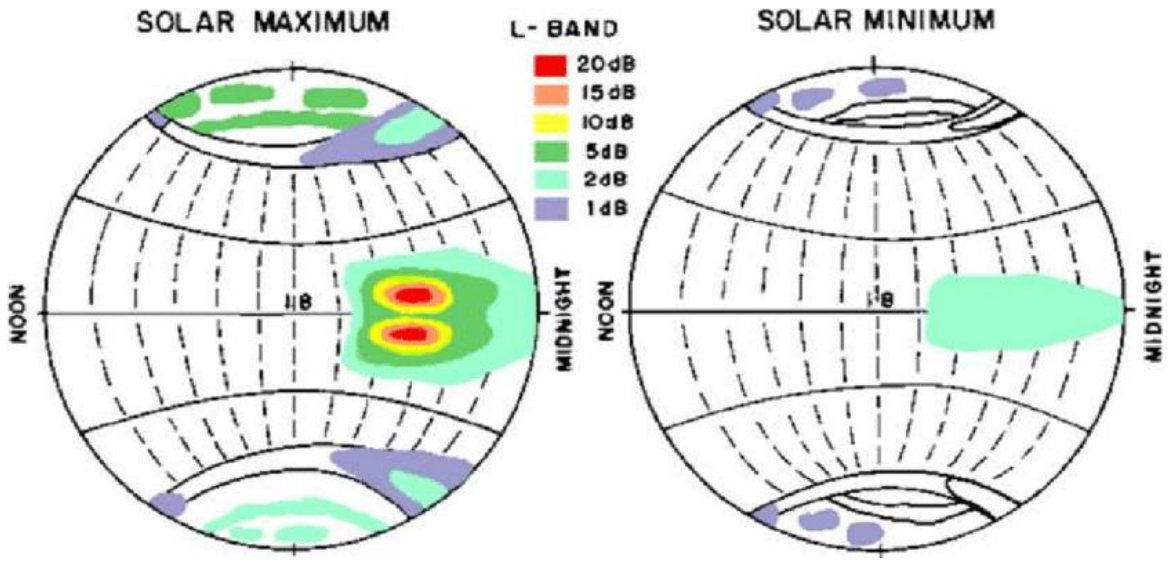

Figure 2.7: Global distribution of ionospheric irregularities in the equatorial, auroral, and polar ionosphere at L-band during solar maximum and solar minimum [*Basu et al., 1988a, b*].

Figure 2.7 shows a global distribution of ionospheric irregularities in the equatorial and high-latitudes at L-band during solar maximum and solar minimum. Ground-based and in situ satellite observations revealed that ionospheric irregularities are symmetrically distributed in the north-south near the geomagnetic equator and are observed between post-sunset and pre-midnight. These are localised in the equatorial anomaly region where the background ionisation is enhanced. In the auroral ionosphere, ionospheric irregularities are observed during night-time while in the polar ionosphere, they occur at all local times [*Wernik et al., 2004*].

2.5.1 Equatorial Irregularities

The equatorial ionosphere is located between 30° on either side of the geomagnetic equator. It behaves differently from the ionospheres at the middle and high-latitudes. At the magnetic equator the Earth's magnetic field is horizontal on average. Because of the orientation of the Earth's magnetic field, charged particles move freely along the magnetic field lines than across. This implies ionisation can move orthogonal to the magnetic field lines when orthogonal electric field is set up [*Beer,*

1973]. Thus, electric field enables the flow of ionisation irregularities occurring in the ionosphere [*Hargreaves, 1979*]. It is understood that electric fields are generated by neutral wind influencing ionisation across the magnetic field lines in the dynamo region ($100\ km - 110\ km$). In this report, the D layer in the equatorial ionosphere is not discussed because of its negligible effects on GNSS radio signals.

During the day, the E layer electron density profile can have value of the order of $10^{11}\ electrons/m^3$ and the value drops at night due to recombination. Above the geomagnetic equator, electric current flows in the dynamo region and this current is called electrojet. This electrojet current is eastward during the day and westward with a smaller magnitude at night. Equatorial electrojet is known as a likely source of atmospheric waves. Irregularities in the equatorial E layer are identified as Sporadic-E (E_s) by means of ionosondes [*Hargreaves, 1992*]. E_s is a random layer of enhanced ionisation with a width between $0.6\ km$ and $2\ km$ and a horizontal spatial scale between $10\ km$ and $1000\ km$ [*Tsai et al., 2018*]. This layer enables long distance communications. Majority of the equatorial E_s irregularities are produced by a plasma instability mechanism known as two-stream instability. Two-stream instability is caused by large relative motion between electrons and ions in the electrojet. In the equatorial F layer, the peak electron density is of the order of $10^{12}\ electrons/m^3$ during the day and drops at night. At night, thermal equilibrium exists in the equatorial ionosphere such that $T_e = T_i = T_n$ (where $e = electron, i = ion, and\ n = neutral$). While during the day, above $400\ km$, thermal equilibrium exists but not between $200\ km$ and $400\ km$ ($T_e > T_i > T_n$). Ionisation in the equatorial ionosphere shows depleted electron density at the geomagnetic equator with two crests on either side below 20° latitudes [*Sastri, 1990*]. This is called the Equatorial Ionisation Anomaly (EIA) a common feature of the F2 layer [*Dabas and Dabas, 2000; Henderson and Swenson, 2005*]. The equatorial anomaly is caused by diffusion of ionisation along magnetic field lines and the vertical motion of ionisation owing to $E \times B$ plasma drift. Hence, the vertical flow of ionisation is caused by the $E \times B$ plasma drift. The EIA is responsible for equatorial F layer night-time irregularities known as Equatorial Plasma Bubbles (EPBs) which can cause ionospheric scintillation as indicated in Figure 2.8. In Figure 2.8, result of numerical simulation show EPBs localised in the F layer between altitude of $350\ km$ and $800\ km$ with electron density of around 10^6 electrons cm^{-3}.

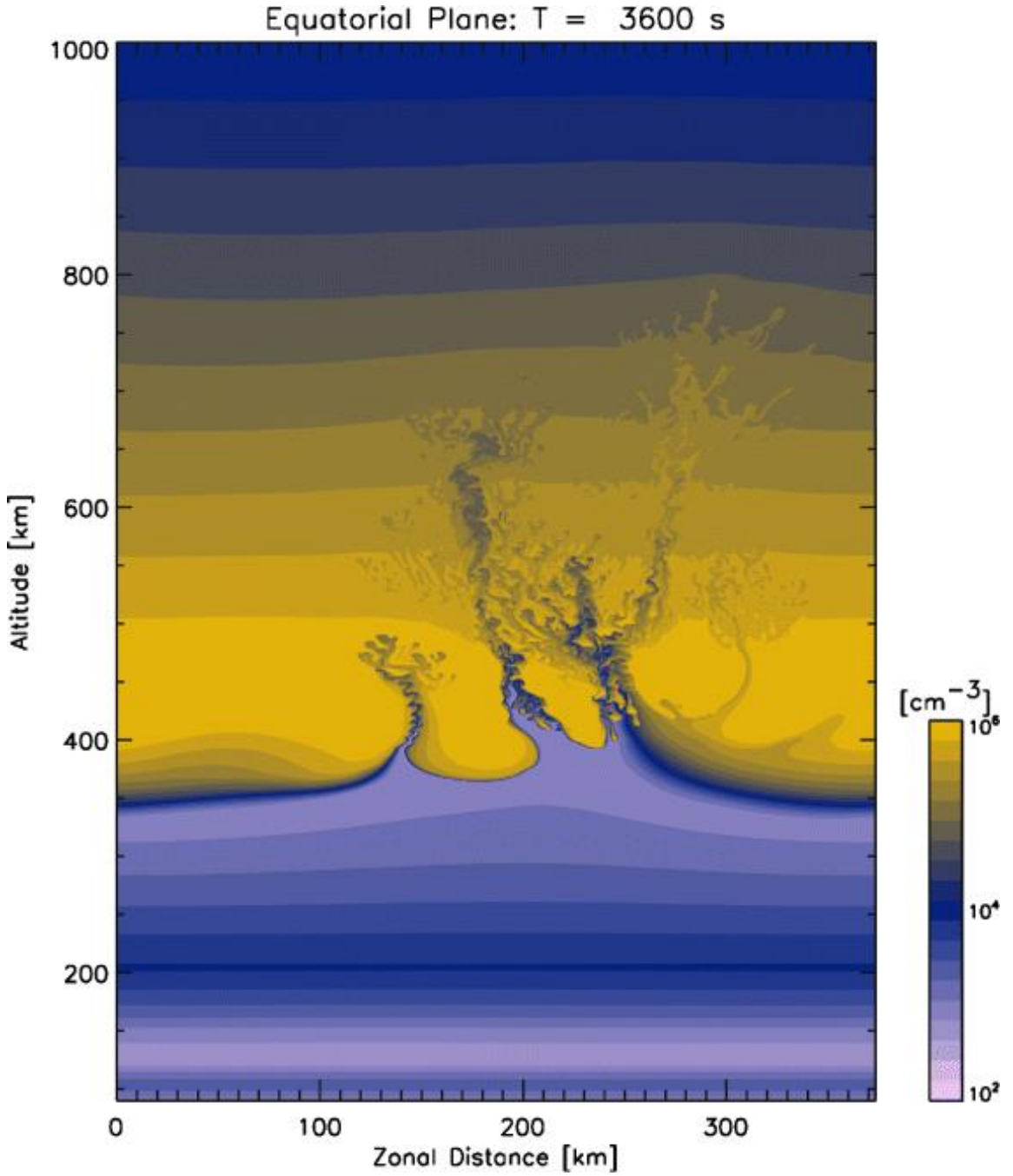

Figure 2.8: Study of nonlinear evolution of EPBs observed to be localised in the F layer using numerical simulation [*Yokoyama, 2017*].

2.5.2 Middle Latitude Irregularities

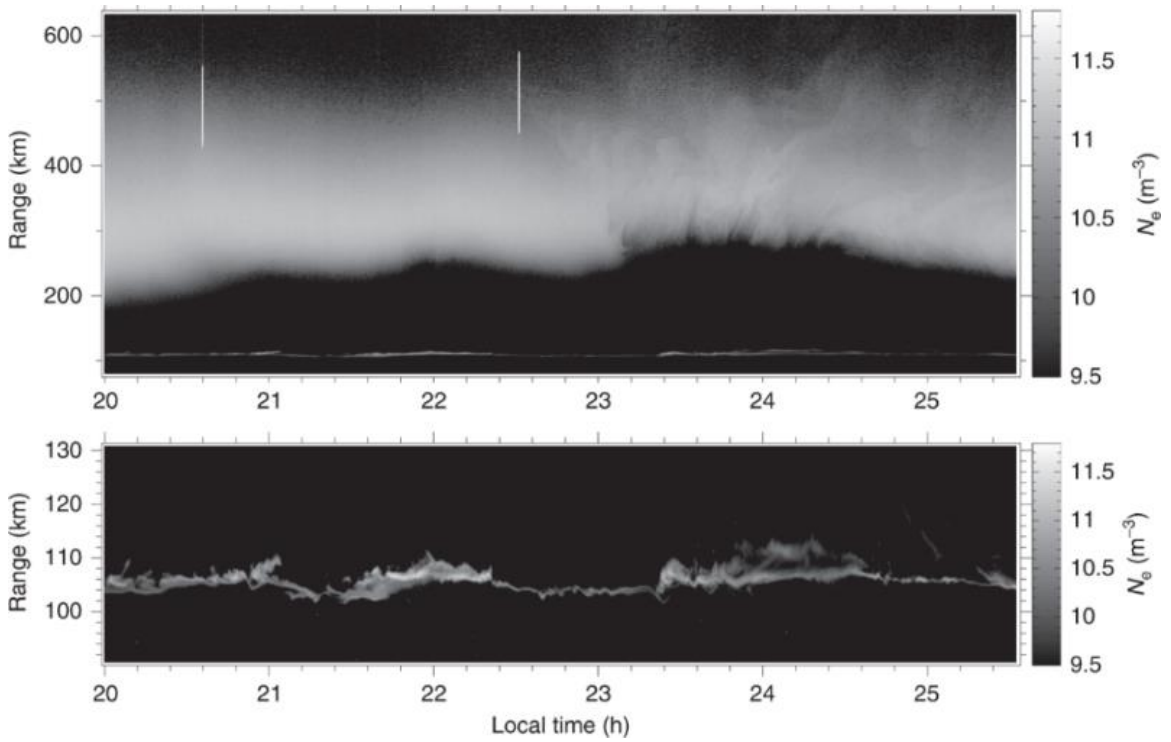

Figure 2.9: Profiles of electron density temporal variations in the E and F layer mid-latitude ionosphere on 30 July 2016 from Arecibo observatory, Puerto Rico [*Hysell et al., 2018*]. N_e is given in logarithmic scale.

Hysell et al., [2018] reported evidence of plasma irregularities observed in the middle latitude ionosphere (Figure 2.9). The values of electron density N_e are expressed in logarithmic scale ($log_{10}(N_e)$) for simplicity. Plasma density distribution and electrodynamics in the region are quite different from the case as observed in the equatorial and high-latitudes ionosphere. In this region, the plasma density can be severe during disturbed geomagnetic conditions and increased solar activity. Because of boundary layer interface and coupling of this region with other latitudes, plasma conditions in the region can be altered and therefore perturbed enough to generate plasma irregularities. *Bowman*, [1990], in a reviewed article, studied Spread-F occurrence at a chain of stations in the American sector. This Spread-F is a signature on ionograms (measured through ionosondes) caused by the presence of electron density irregularities. From experimental results of night-time plasma irregularities during the occurrence of Spread-F in the middle latitude ionosphere measured from ionosonde data, four different types were identified. These are classified in terms of spatial scale size known as macroscale, large-scale, medium-scale, and small-scale ionisation structures. It is proposed that large-scale and

medium-scale ionospheric irregularities are the major ionisation structures in the production of extra traces termed middle latitude ionosphere Spread-F traces [*Bowman, 1990*].

2.5.3 High-Latitude Irregularities

In the high-latitudes ionosphere, ionospheric irregularities are likely originated by energetic precipitating electrons, currents parallel and perpendicular to the geomagnetic field, plasma transport, and thermospheric heating [*Hargreaves, 1979; Keskinen and Ossakow, 1983*]. Like in other regions of the ionosphere, different physics are used to describe E and F layer irregularities at high-latitudes. In the high-latitudes F layer, particle precipitation, plasma processes and instabilities, and dynamics of neutral fluids have been projected as irregularities source mechanisms. Particle precipitation is considered to play a key role in plasma structuring of the F layer high-latitude ionosphere where particles with low ionisation energies (10^2 to 10^3 eV) deposit most of their energies. Structured low-energy precipitation is proposed as a source of large-scale ($\geq 10\,km$) F layer plasma irregularities. Unstable convecting ionospheric plasma, under required condition, have the potential to produce irregularities which are driven by $E \times B$ drift instability. Another source of plasma free energy in the F layer high-latitudes ionosphere is velocity sheared plasma flows. For example, auroral arcs can induce small-scale and large-scale irregularities. Another feature of the high-latitudes F layer is plasma density gradient manifesting as sharp and smooth. These density gradients can drive a drift wave type of plasma instabilities.

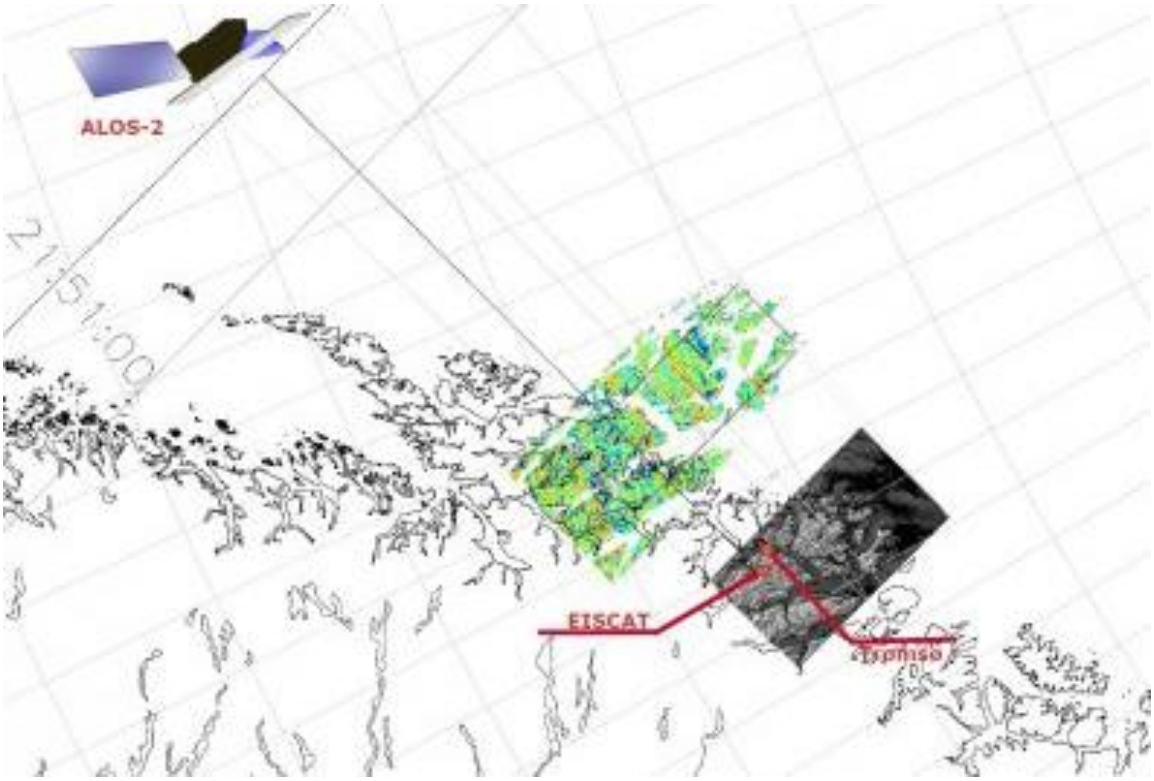

Figure 2.10: Imaging high-latitudes ionosphere small-scale electron density irregularities originating from particle precipitation under a high level of ionisation at ionospheric pierce point $300\ km$ using a combination of a space-based (Synthetic Aperture Radar [SA SAR] on-board a Japanese Advanced Land Observing Satellite [ALOS-2]) and ground-based (EISCAT) measurements over Tromsø, Norway [*Sato et al., 2018*].

In the high-latitudes E layer ionosphere, plasma density irregularities are strongly correlated with AEJ. Backscattered power received from ISR (See Figure 2.10) has been used to capture small-scale electron density irregularities originating from particle precipitation under a high level of ionisation at ionospheric pierce point $300\ km$ using a combination of a space-based (Synthetic Aperture Radar [SAR] on-board a Japanese Advanced Land Observing Satellite [ALOS-2]) and ground-based (EISCAT) measurements over Tromsø. The linear theory of these irregularities in the high-latitudes E layer is explained using the FBI. Similarly, ion cyclotron instability originating from magnetic field-aligned currents in the E layer high-latitudes ionosphere is considered as a source of both small-scale and large-scale electron density irregularities [*D'Angelo, 1973*].

Large-scale structures are the common features observed in the auroral and polar ionospheres. They are as follows:

a) Polar cap plasma patches, which are enhanced electron density about 2 to 10 times greater than the background ionisation [*Hunsucker and Hargreaves, 2007; Jin et al., 2014*]. The patches are estimated to be circular with a spatial scale size between $200\ km$ and $1000\ km$ and are observed when the IMF B_z component is southward.
b) Enhanced electron and ion temperatures caused by thermal heating occurring during energetic electron precipitation [*Schunk and Nagy, 2009*]. Electron precipitation can be inferred from auroral/polar optical emissions as well as the presence of auroral substorms. Substorm is a localised disturbance of the magnetosphere in high-latitudes which manifest as aurora.
c) Enhanced auroral ionisation. For example, in the auroral zone, such enhancements are called blobs [*Hunsucker and Hargreaves, 2007*]. Auroral blobs are smaller than polar cap patches in horizontal spatial scale (tens of km)
d) Ionisation trough (a region of depleted ionisation density) are extended in the east-west direction but enhanced in the north-south direction [*Hunsucker and Hargreaves, 2007*].
e) Polar holes (F layer depleted ionisation).
f) Tongues of ionisation (TOI). Convecting electric field drives plasma structures from middle latitudes into high-latitudes. These structures in the polar cap are observed to have a storm enhanced electron density about 2 to 10 times the background but at low electron temperatures [*Foster et al., 2005; Liu et al., 2015; and references therein*]. Hence, TOI is a cold dense plasma structure in the F layer polar cap and extends from the dayside to the nightside and this can be observed by ISR.
g) Auroral filaments, arcs, and inverted-V are regions of enhanced electron densities. These are features observed in the auroral oval identified by their spatial scale sizes [*Dahlgren and Whiter, 2007; Jin et al., 2014*].

2.6 Summary

This chapter presents an overview of the ionosphere starting from adverse SW events. Adverse SW events originate perturbations in the magnetosphere which can

manifest in the form of storms and substorms. Because of the orientation of magnetic field lines in the high-latitudes ionosphere, energetic particles are injected into high-latitudes inducing ionospheric plasma instabilities. Consequent to IPIs, auroral and polar structures are acted upon to produce ionospheric irregularities. This implies, adverse SW events originate IPIs; these IPIs subsequently induce ionospheric irregularities. Each region of the ionosphere shows different types of IPIs responsible for irregularities as discussed in this chapter. In general, auroral and polar irregularities in the E and F layer can originate from particle precipitation and drifting polar cap patches.

3 Literature Review

This chapter reviews the effects of ionospheric irregularities on GNSS systems operating in the equatorial, middle, and high-latitudes (auroral and polar). Ionospheric measurements from orbiting satellites and ground-based instrumentations were collected and analysed to understand their impact on GNSS navigation and positioning applications.

3.1 Equatorial Latitudes

Susnik and Forte, [2011] obtained scintillation data for 12 days derived from dual-frequency GPS receiver stationed in the African equatorial latitudes on 4-15 November 2014. Parameters monitored were scintillation indices and TEC. These were derived from the GPS receiver. The results obtained validate that scintillation is a function of local time, season, solar, and geomagnetic activity. Further, the investigation concludes that scintillation in the African equatorial latitude occurs post-sunset between 21:00 and 03:00 UT. When compared to Latin America, African equatorial latitude scintillation occurs before the former. The objective of measurements, analysis, modelling, and prediction is perhaps to add to the existing knowledge on ionospheric scintillation. Or to support mitigation of the effects using robust GNSS-based receivers and radio telecommunication systems.

Scintillation shows a daily occurrence in the equatorial latitudes and may persist for a few hours. The case is quite different in other latitudes. However, the impact of scintillation on GNSS and communication infrastructure can be a degradation of signal quality. GISM discussed here uses the Multiple Phase Screen (MPS) method. Parameters acquired into the GISM are spectral density of the electron density distribution, velocity, displacement direction, and correlation distance. In this campaign [*Béniguel and Hamel, 2011*], equatorial scintillation occurrence per year was about 40% and between 20:00 and 02:00 UT. Its probability of occurrence is high during high sunspot number. The NeQuick model and parabolic equation are used to investigate the mean scintillation and mean error. The Helmholtz equation was employed to calculate the radio signal propagation supported by a developed algorithm; and monitoring stations are spread across Asia, Africa, and Europe to

obtain measurements. The data obtained was analysed and the results utilised to compare with GISM results: a sort of validation all within the equatorial and high-latitudes. A different approach would be used to study or characterise the ionospheric phenomenon. The African equatorial latitudes region with a long-term data experimental campaign might be considered.

In another study, *Basu et al.,* [1996] investigates the neutral wind and plasma dynamics for 13 days in the equatorial ionosphere to understand the existence of equatorial Spread-F after sunset. Measurement centres were spread across Jicamarca, Peru, and Chile (Latin America) equatorial regions. Measurement instruments such as digisonde, Fabry-Perot Interferometer (FPI), ISR, all-sky imager, and space-antenna satellite scintillation were employed. Results of the analysis performed with ISR reveals that equatorial Spread-F in the equatorial ionosphere during minimum solar activity ($10 - 20\, m/s$) is due to post-sunset dynamo of upward plasma drift. The occurrence of equatorial Spread-F varies with frequency, time of day, season of year, latitude and longitude, geomagnetic condition, and solar activity. The study explores the behaviour and features of neutral wind and plasma mobility linked to equatorial Spread-F. The work establishes the contribution of neutral wind, not only plasma dynamics, to the determination of the occurrence of ionospheric scintillation. Inferring from the investigation, when studying the ionosphere and the physical processes within the region, it is recommended to consider the aggregate impact of boundary layers associated with the region.

Priyadarshi and Singh, [2011] studied the impact of geomagnetic storm on ionospheric scintillation in the equatorial latitude of Varanasi, India. The research reports that gravitational Rayleigh-Taylor Instability (RTI), as the cause of plasma bubbles in this region and this produces a phenomenon known as equatorial Spread-F (ESF). The study confirms this as the cause of scintillation in equatorial latitudes. The ionospheric mechanism is characterised by a noticeable upward plasma drifts in the bottom F layer following irregularities at post-sunset. GSV4004 GPS receiver was used to measure scintillation data. Amplitude scintillation index derived from experimental analysis and magnetic indices were used to investigate ionospheric irregularities in the representative region. Interplanetary Magnetic Field (IMF), D_{st}, K_p, and B_z magnetic parameters were used to categorise geomagnetic

storms. The data was obtained from the Coordinated Data Analysis Web. The finding is that geomagnetic storm does not mean disruptive scintillation. Scintillation can occur during geomagnetic quiet days. The reason is scintillation occurs a few hours post geomagnetic storm period. In the future, multi-instrument experimental technique would be used to provide insight into scintillation events for GNSS users by means of measurements from observatories at different locations in the African ionospheric sector.

Mungufeni et al., [2016] investigates ionospheric fluctuations trends in the African equatorial latitudes during quiet geomagnetic conditions. TEC measurements from GNSS stations observed from 2001 to 2012 were utilised. The observatories are in Gabon, Uganda, and Kenya; East and West Africa. The study disregards the rate of change of TEC index values greater than or equal to $0.5\,TECU/min$ in the estimation. Such values are considered as severe ionospheric irregularities. Scintillation data was collected from IGS stations using GNSS receivers located at the 3 stations. Attention was on the assessment of longitudinal variations in the intensity of ionospheric irregularities and asymmetries observed in the intensity of the ionospheric irregularities during equinoxes. The finding records enhanced intensity of ionospheric irregularities during March equinox over East Africa while West Africa records less. However, September equinox presented greater intensity of ionospheric irregularities over West Africa compared to East Africa. The campaign agreed with previous research. Thus, the report validates longitudinal differences and equinoctial asymmetry in the intensity of ionospheric irregularities using past studies. One technique of data collection over 3 stations may not be sufficient to generalise the observed phenomena over the African equatorial latitudes region. The question that remains unanswered is the evaluation of ionospheric irregularities trends over this region during moderate or strong geomagnetic conditions. Further research will attempt to answer this question. Since the study observes a long-term data of 12 years, relating the findings to 11-year solar cycle can provide valuable insight into ionospheric patterns in the region.

In *Seo et al.,* [2007], scintillation shows mild effects in the middle latitudes but posed a potential threat to availability and continuity of radio signals at the equatorial latitudes. The work describes the impact of scintillation on GPS receivers in the equatorial region during minimum solar activity. In the campaign, 4 GPS receivers

were identified for collection of data in Brazil but approved WAAS receivers utilised for aircraft navigation were studied for scintillation. The study evaluates observables obtained from Ascension Island observatory during solar maximum. Investigation reveals that more satellite signals are degraded by scintillation, but the frequency of occurrence was the same compared to the solar minimum period. According to the report, the frequency of occurrence of simultaneous loss of lock in both minimum and maximum solar activity can be minimised by having fast GPS receiver reacquisition time. The finding was a reduction in the reacquisition time of GPS receivers increased the number of satellites being tracked. The campaign uses measurements from a single station over Brazil and a single method of data collection from a Garmin WAAS receiver for a duration of 36 days. More stations and different data collection techniques would be attempted.

GNSS multivariate data, which were obtained, computed, or derived from GNSS measurements were investigated for quality. The chain flow of data acquisition, processing, and results depend partly on the data quality. The data processing during GNSS positioning can utilised RINEX data in Standard Positioning Service (SPS), for example, positioning based on GPS L1 or PPP mode. The contribution reviewed data quality using the computation of 3-D positioning errors between a known position and a surveyed position. Data visualisation was used to present data quality using several methods. In the study, positioning accuracy and attribute accuracy were processed using the Ionospheric Scintillation Monitor Receiver (ISMR) Query Tool. RINEX data was obtained from the Brazilian Network of Continuous Monitoring of GNSS Receivers. The data were processed from the Precise Positioning Service (PPS) online software that performed GPS positioning. The study processed data obtained from CIGALA/CALIBRA network of 11 receivers distributed in the Brazilian region to investigate the definition, management, and visualisation of uncertainty in attributes. The data quality was investigated using scintillation indices in the Brazilian ionosphere. This investigation can be extended to the African ionosphere when such data are available and evenly distributed through a strategic deployment of ionospheric monitoring equipment [*Vani et al., 2014*].

Luo et al., [2018] investigates the effects of ionospheric scintillation on BeiDou Navigation Satellite System (BDS) PPP in equatorial latitudes region. Data was

obtained from a newly installed ionospheric scintillation monitoring receiver located at Sha Tin, Hong Kong and 15 Hong Kong Satellite Positioning Reference Station Network (SatRef) from 6 October to 17 November 2015. The reference stations received real-time GNSS signals from GLONASS, GPS, and BDS. The PPP solution was performed using the Position And Navigation system Data Analyst (PANDA) software developed by Wuhan University, China. ROTI derived from BDS signals was observed to be a convenient indicator of ionospheric scintillation. In the contribution, the correlation between ROTI and the ratio of amplitude to phase scintillation indices was about 0.7 on average. Under scintillation and non-scintillation conditions, the 3-D root-mean-squares of BDS PPP are $1.842\ m$ and $0.155\ m$, respectively. Different positioning software can be used in both RTK and PPP solutions to investigate the effects of ionisation structures on navigation and positioning systems.

GPS availability and positioning solutions as signal paths are aligned with plasma bubbles in the ionosphere are reported. For example, 32-day scintillation data was obtained from São José dos Campos (SJC) on 15-30 November 2014 and 4-18 February 2015. GPS DF PPP was performed using a Real-Time RT-PPP software courtesy of the Universidade Estadual Paulista Júlio de Mesquita Filho (UNESP). The results obtained show scintillation enhancement events are correlated with GPS signals traversing through plasma bubbles aligned along the direction of the magnetic field. Severe scintillation events and elevated losses of phase lock are directly proportional to the length of propagation path through plasma bubbles. The PPP analysis shows that this condition corresponds to the observed enhanced positioning errors [*Marques et al., 2016*]. The performance of GPS positioning in the presence of TEC fluctuations would be investigated at the high-latitudes [*Moraes et al., 2018*].

Yue et al., [2014] reports an investigation on SW observation by means of GNSS Radio Occultation (RO). A joint research project embarked by Taiwan and the United States FORMOSAT-3/COSMIC (Constellation Observing System for Meteorology, Ionosphere, and Climate) designed and launched the first low earth orbit satellites as a remote sensing tool for atmospheric and ionospheric observations using GPS RO. Apart from providing atmospheric measurements, the constellation of 6 satellites in 2006 provides ionospheric measurements

(ionospheric electron density profiles, TEC arcs profiles, and S_4 index profiles) as well. The constellation supplies a global coverage and a high vertical resolution data. This has enabled the system to be useful for ionospheric data assimilation models as well as the construction of a global 4-D (space and time) ionospheric electron density reanalysis. COSMIC can provide about 1000-1500 occultations per day. As a follow up to FORMOSAT-3/COSMIC due to its functional limitations, FORMOSAT-7/COSMIC-2 was designed and launched in 2016 (6 satellites) into low-inclined orbits and 2019 (6 satellites) into high-inclined orbit: a total of 12 satellites with a capacity to measure 12000 ionospheric profiles per day. COSMIC-2 compared to COSMIC will provide a higher quality and quantity of data. COSMIC-2 RO measurements would have the potential to support SW middle-and large-scale nowcasting and forecasting. Being a low orbiting satellite carrying on-board GNSS receiver for RO, the dynamic motion of the satellite can influence the integrity of measurement. Again, since the minimum altitude of a COSMIC satellite is about $160\ km$ on average, this implies E layer ionospheric measurements are not likely feasible. Hence, the use of ground-based ionospheric instrumentations in a fixed position will be employed to study ionospheric irregularities at the European high-latitudes.

On GNSS radio occultation, *Von Engeln et al.,* [2010] reports GNSS Receiver for Atmospheric Sounding (GRAS) occultation on-board of the Meteorological Operational (METOP) satellites. METOP is the European Organisation for the Exploitation of Meteorological Satellites (EUMETSAT) also called EUMETSAT Polar System (EPS) which flies the sun-synchronous orbit at $820\ km$ altitude. The satellites were launched in 2006 with an expected life-time of 5 years. GRAS is a radio occultation system that utilises the GPS satellites constellation to determine the METOP orbital data for the purpose of occultations. Each occultation provides a vertical sampling of atmospheric temperature, pressure, and water vapour profiles. Apart from GRAS, COSMIC and Gravity Recovery and Climate Experiment (GRACE) are other forms of RO. Based on the study, GRAS bending angle data as against collocated European Centre for Medium Range Weather Forecasts (ECMWF) and COSMIC were validated. The results of the investigation reveal that GRAS bending angle biases agree to within 0.5% against ECMWF and to within 0.1% against COSMIC for altitudes between $8\ km$ and $40\ km$. With the growing

number of operational GNSS constellation such as GLONASS, Galileo, and Beidou, the RO community would greatly benefit in terms of increased occultations and opportunity to validate measurements. METOP satellites are low orbiting meteorological satellites. METOP has the potential to carry on-board GNSS receivers for ionospheric studies. Like its counterpart COSMIC, the movements of GNSS satellites and METOP as well as ionospheric irregularities (METOP is embedded in the ionosphere given its altitude) can affect the accuracy of measurements. Ground-based ionospheric measurements can be used to validate METOP measurements.

Zuo and Wang, [2009] conducted a study on GPS scintillations using measurements collected from a dual-frequency GPS receiver GSV4004 located at Guilin, China near the northern crest of the equatorial anomaly region. Temporal variations in amplitude and phase of the received GPS signals are produced by the movement of the GPS satellites and or ionospheric irregularities. These are called amplitude and phase scintillations. The data was collected from January 2007 to December 2008. The results obtained revealed a night-time amplitude scintillation observed at a greater proportion towards south of Guilin and this was correlated with phase scintillation, TEC depletions, and TEC fluctuations. The investigation presented results obtained from COSMIC satellites (amplitude scintillation calculated from detrended SNR) to validate measurements from the ground-based scintillation receiver. According to the report, GPS scintillation/TEC measurements obtained from the scintillation receiver at Guilin and SNR calculated from the GPS-COSMIC radio occultation indicated daytime and night-time scintillation are caused by likely Sporadic-E and ionospheric F layer irregularities, respectively. Study of ionospheric irregularities would be designed and conducted at auroral and polar latitudes using multiple-instruments approach.

Luo et al., [2020] reported a new amplitude scintillation metric (S_{4c}) derived from C/N_0 measurements at 1-s sampling collected from a geodetic GNSS receiver. The purpose was to determine the suitability of the new amplitude scintillation index in place of the usual amplitude scintillation (S_4) data collected from Ionospheric Scintillation Monitoring Receivers (ISMRs) at 50-Hz. Because of the regional and global sparsity of this specialised scintillation receivers, the availability and evenly distributed network of geodetic GNSS receivers can support ionospheric

irregularities and scintillation studies. Scintillation and C/N_0 data were collected from 3 low-latitudes ISMR receivers to validate the correlation between S_4 and S_{4c}. Data was also collected from 16 Hong Kong (HK) Continuously Operating Reference Stations (CORS) used to analyse the availability of S_{4c}. To validate the accuracy of S_{4c} index to be used for the study of ionospheric irregularities, C/N_0 from IGS station KOUR located in South America, C/N_0 from 117 National BDS Augmentation System Service (NBASS) stations, and electron density data from Swarm (A and C) satellites. The S_{4c} was calculated at 1-minute interval to agree with traditional way of computing S_4 at 1-minute. In this way, the reliability of S_{4c} index was validated both at the Brazilian and Hong Kong low-latitudes. The results obtained revealed that S_{4c} and S_4 had a correlation coefficient above 0.9 during scintillation activity. During non-scintillation activity, the correlation coefficient between the 2 metrics was improved. The accuracy of S_{4c} was further validated using a 1-year measurements from 2 adjacent GNSS receivers (geodetic and scintillation) located at HK. Both indices were considered at a threshold above 0.2 and the results obtained showed a good correlation. However, in this report, ionospheric irregularities will be investigated using ISR as well.

3.2 Middle Latitudes

Fallows et al., [2016] reveals that ionospheric scintillation does not only affect the operation of GNSS and other ground-based measurements in terms of accuracy but also interplanetary scintillation (IPS) monitoring. IPS was monitored through low frequency array (LOFAR) in conformity with Murchison Widefield Array (MWA). Research questions were raised, and the models used to provide answers. Therefore, the study of scintillation and ionospheric irregularities in the Earth's ionosphere can assist researchers in other fields.

Yasyukevich et al., [2020] reported small-scale ionospheric irregularities originating from auroral ionosphere at mid-latitudes during the 22 June 2015 geomagnetic storm and how they impact on GPS positioning. The study uses experimental facilities located at the Institute of Solar-Terrestrial Physics of the Siberian Branch of the Russian Academy of Sciences (ISTP SB RAS) Irkutsk, Russia. To study ionospheric irregularities, Spread-F width was measured by means of a Digisonde

Portable Sounder-4 (DPS-4) ionosonde located at Irkutsk. To measure amplitude scintillation, receivers of the Irkutsk ISR (IISR) which observed signals from a radio galaxy Cygnus A at $150\ MHz$ were used. Amplitude and phase scintillations were measured by GPStation-6 specialised GPS/GLONASS receivers while TEC fluctuations were calculated by using the dual-frequency GPS/GLONASS phase measurements. On the other hand, the expansion of auroral oval to around 50° magnetic latitudes was observed using SuperDARN radars. The results provide insight into enhanced Spread-F, Cygnus A amplitude scintillation. In the report, by means of TEC maps it was inferred that small-scale irregularities were caused by the expansion of auroral oval. In the region of the small-scale irregularities, the observed PPP error was increased. Thus, in the middle latitude, the mean PPP error was at least 5 times more than the quiet level. Ionospheric irregularities and their impact on GNSS would be studied using EISCAT UHF/ESR measurements combined with L-band signals from GNSS.

3.3 High-Latitudes

Forte et al., [2013] compares experimental TEC derived from EISCAT and GPS observatory. Both monitors were collocated and having the same line of sight. For instance, a day measurement for PRN23 between 16:00 and 18:00 UT was obtained. The parameters were analysed and validation of variation in TEC values as captured by the two techniques was done. The campaign was conducted at a station in Europe (Tromsø, Norway). The results obtained from EISCAT and GPS TEC variations were strongly associated. Further, the study observes that EISCAT in the future can provide gains for 3-D study. The knowledge acquired herein can be used to conduct a multi-instrument campaign at high-latitudes with measurements of ionospheric electron density irregularities using EISCAT.

Jacobsen and Dähnn, [2014] conducted a statistical study of ionospheric disturbances and their correlation with GNSS positioning errors in the high-latitude ionosphere. In the year 2012, GNSS data from 10 dual-frequency GNSS receivers with a sampling rate of 1-Hz located in the auroral and polar ionospheres were collected and analysed. Rate of change of TEC Index (ROTI) was used as a measure of ionospheric activity. The investigation observed ROTI to be stronger in

the auroral oval compared to the cusp. To investigate the causal relationship between positioning error and ROTI, the receiver coordinates were calculated using GIPSY software. From the study, there was a strong correlation between PPP error and ROTI and that 3-D positioning error increases significantly with increasing ROTI. Apart from using GNSS data to investigate the relationship between the selected measure of ionospheric activity and PPP errors, a multi-instrument experimental approach could be designed and conducted to validate the results obtained from a single ionospheric instrumentation. A different GNSS positioning software can be explored to perform the investigation.

An overview of the 2015 St. Patrick's Day storm and its impact on RTK and PPP in Norway was presented. A daily solar wind (https://omniweb.gsfc.nasa.gov/), equivalent ionospheric currents (IMAGE network), and GNSS data from Norwegian Mapping Authority (NMA) were obtained for 17 and 18 March 2015. The Norwegian GNSS receivers are located between the middle latitude and high-latitude regions. The positioning was performed using GNSS-Inferred Positioning System (GIPSY) software courtesy of the National Aeronautics and Space Administration (NASA) Jet Propulsion Laboratory (JPL). Strong GNSS disturbances were observed at all latitudes and in all days. Phase scintillation was correlated with ROTI (a measure of GNSS disturbances) as well as enhanced positioning errors (both RTK and PPP modes). PPP was more precise than RTK irrespective of the level of ionospheric disturbance [*Jacobsen and Andalsvik, 2016*]. These findings will be extended to the polar ionosphere using a powerful ionospheric instrumentation (the ISR).

Dabove et al., [2019] investigates the performance of multi-constellation GNSS PPP solutions in the presence of phase scintillations at high-latitudes. The PPP performance was assessed using accuracy and convergence time which is about 30 minutes or more required to achieve centimetre- to decimetre level accuracy. GNSS/scintillation data was obtained from the South African National Antarctic Expedition (SANAE IV) research station for several days in 2016. Bernese GNSS software was used to analyse the data to obtain the reference antenna coordinates while RTKLIB was used to analyse the PPP solutions. The receiver is capable of receiving signals from GPS, GLONASS, and Galileo constellations. GPS satellites coverage was low compared to GLONASS or Galileo satellites over the receiver station. In the report, the use of multi-constellation solutions did not only improve

the accuracy but the convergence time as well. Different approach will be employed to study GNSS PPP performance in the Northern European sector using EISCAT facilities.

Kersley et al., [1988] presented small-scale irregularities associated with a high-latitude electron density gradient: scintillation and EISCAT measurements. A simultaneous experiment involving scintillation observations by means of the Navy Navigation Satellite System (NNSS) receiver located at Kiruna and EISCAT measurements using receivers from Kiruna and Sodankylä was described. NNSS is a constellation of about 6 low earth orbit ($1100\ km$ altitude) satellites which transmits signals between $150\ MHz$ and $400\ MHz$. The presence of small-scale electron density irregularities was inferred from scintillation measurements while ionospheric conditions were inferred from EISCAT electron density profiles. The EISCAT antenna and the NNSS receiver antenna were collocated to have the same line-of-sight. Based on the results, the existence of sub-kilometre scale irregularities was observed in the boundary of long-lived steep anti-poleward electron density gradients. Further, southward flow of plasma would cause the formation of irregularities through gradient drift instability mechanism. The origin of the observed irregularities was far from soft particle precipitation owing to the synchronous occurrence of cooler electron temperature with enhancement in electron density. The potentials of current GNSS and EISCAT in the studies of ionospheric irregularities would be exploited.

Kelley et al., [1982] reported on the origin and spatial extent of F layer ionospheric irregularities occurring at high-latitudes. Structured soft-electron precipitation is reported to be the primary cause of large-scale ($\lambda \geq 10\ km$) high-latitude F layer irregularities. Plasma structures of tens of kilometres are observed both in the dayside and nightside of the auroral oval. According to the study, plasma convection serves as a means of distribution of F layer plasma irregularities in the polar ionosphere. Plasma instability mechanism must operate on larger-scale structures of longer duration to produce smaller-scale structures of shorter duration. Small-scale structures are of the order of $10\ m < \lambda < 100\ m$ while intermediate-scale structures are structures between large-scale and small-scale structures ($100\ m < \lambda < 10\ km$). The findings in this report can be validated by means of incoherent scatter radar measurements.

Wood et al., [2009] conducted a multi-instrument experiment to investigate the effects of geomagnetic substorm activity on the spatial distribution of plasma patches in the nightside F layer ionosphere. Ionospheric measurements were collected from meridian scanning photometer (MSP), magnetometer, Hankasalmi SuperDARN radar, EISCAT Svalbard Radar (ESR), and ionospheric radio tomography experiment of Aberystwyth University located in northern Scandinavia on the evening of 12 December 2001. There was evidence of moderately disturbed geomagnetic condition as indicated by $K_p = 3$. Patches of ionisation were formed under the conditions of IMF B_z (north-south) and B_y (east-west) components both negative. These patches are correlated with dayside photoionisation in the sub-polar latitude and transported by the high-latitude convection pattern through the polar cap to the nightside ionosphere. The results indicate that patches on the nightside were separated by 5° and 2° from the expansion and contraction of the high-latitude convection pattern as a consequence of substorm activity. The spatial distribution of polar structures and their influence on GNSS signals will be investigated using a multi-instrument experimental campaign.

Wood and Pryse, [2009] studied seasonal influence of polar cap patches in the high-latitude nightside ionosphere above northern Scandinavia during solar maximum (1999-2001). EISCAT Svalbard Radar was used to observed nightside high-latitude F layer polar structures on the conditions suitable for the existence of patches. These conditions are plasma convection, interplanetary magnetic field, and absence of in situ precipitation. To model the observed seasonal trends in the patch-to-background ratio, a computer simulation by means of Aberystwyth University's PLASLIFE (PLASma LIFEtime) was performed. By means of the PLASLIFE tool, the reason for the observed difference between winter and summer patch-to-background ratio was established. According to the report, winter patch-to-background ratio was above 2. In summer there was evidence of enhancement in electron density in the nightside, however, the ratio was below 2. It was established that high-latitude convection pattern was responsible for transporting electron density enhancement into the nightside ionosphere. One of the reasons for a lower patch-to-background ratio in summer was the chemical composition of the atmosphere which causes a reduction in the electron density of the plasma

convected into the polar cap due to recombination. The other reason was the maintenance of the background polar ionosphere by means of photoionisation.

Bernhardt et al., [2016] reported the results of an investigation on large ionospheric disturbances generated by the High frequency Active Auroral Research Program (HAARP). The new ionospheric modification shows the production of an unprecedented ionospheric disturbances in Alaska by means of HAARP owing to its large transmitter power, fully programmable antenna array, and robust frequency generation. The experiment used pencil and conical beam transmissions to produce artificial ionisation cloud near the second to sixth harmonics of the electron gyrofrequency. With the use of the conical beams, the ionisation cloud has been sustained for about 5 hours as opposed to the pencil beams which last for about 30 minutes. The largest plasma density cloud was produced at the highest harmonic. To investigate the influence of the artificial ionospheric disturbances on radio propagation, satellite radio transmission at $253\ MHz$ from the National Research Laboratory (NRL) Tactical Satellite-4 (TACSat4) was allowed to traverse the region. The satellite signal was severely affected by the region. Study of ionospheric irregularities from natural sources can validate the results obtained from ionospheric modification by means of HAARP facility.

Prikryl et al., [2010] reported GPS TEC, scintillation, and cycle slips at high-latitudes during solar minimum in 2008-2009. GPS TEC and scintillation data were collected from the Canadian High Arctic Ionospheric Network (CHAIN). CHAIN comprises of 10 specialised GPS receivers and 6 ionosondes also referred to as the Canadian Advanced Digital Ionosondes (CADIs) distributed between the auroral oval and polar cap. Apart from CHAIN, optical, radar, and magnetometer data were collected from the Canadian GeoSpace Monitoring (CGSM). In the solar minimum, the observed amplitude scintillation was lower than phase scintillation at high-latitudes. Auroral arcs, substorm enhancement, and cusp region dynamics were correlated with the observed phase scintillation and possibly cycle slips. CHAIN observations were compared to CGSM which suggest polar cap scintillation and TEC fluctuations are correlated with polar cap patches which are inferred to originate polar irregularities. The impact of auroral and polar structures on GNSS would be investigated in terms of TEC fluctuations and positioning performance.

3.4 Equatorial, Middle, and High-Latitudes

Kintner et al., [2007] reports GPS and ionospheric scintillation at low, middle, and high-latitudes. Scintillation is described as fluctuation in the amplitude and phase of a signal. This may lead to degradation in the quality of GPS received signal or losses of lock. The investigation provides insight into how scintillation occurs at different layers of the ionosphere using a theoretical technique only. The findings were GPS received signals are more affected by scintillation at equatorial and high-latitudes; the former having temporal and seasonal variations while the latter occurs at all seasons. The report further supports that scintillation studies would attract researchers because of its impact on GNSS-based technologies. Knowledge of its effects on GNSS can assist to mitigate the impact on GNSS applications worldwide. The research, however, did not use other GNSS constellations like the GLONASS, Galileo, etc. to give a wider understanding of the impact on GNSS.

In *Oxford Economics*, [2012], today's society depends on the services of GNSS in an increasing degree. The research projected that the global demand for GNSS products and services would increase by 10% from 2011 to 2020. This provides an opportunity for Europe to key in through the Galileo project. The existing augmentation systems are regionally based. This, therefore, suggests that some parts of the world are not covered. Since aviation is a global business, there is henceforth the need to ensure continents like Africa are not left behind. Given this background, the study of ionospheric irregularities at the African equatorial latitudes sector is a potential research area. This is because of its potential to enhance the accuracy, integrity, continuity, and availability of GNSS navigation and positioning systems.

According to *SBAS-IONO Working Group*, [2012], ionospheric scintillation is a danger to GNSS especially at the low and high-latitudes. Scintillation phenomena are more severe at the equatorial latitudes compared to high-latitudes whose severity is associated with severe solar activity. Further discussions were put forward to explain scintillation at low, middle, and high-latitudes. Ionospheric scintillation data (GPS stations) were obtained from Ascension Island, Greenland, and Japan. The study presents three empirical scintillation models and the impact of ionospheric scintillation on GPS and SBAS equipment. In the report, to reduce

the impact of scintillation will mean to increase the availability of GPS satellites. There was no form of validation of the results and the ionospheric data did not include data from the African ionosphere.

Béniguel et al., [2004] presents a modelling method capable of communicating changes in propagation fields across the ionosphere due to scintillation. Measurements of GPS data obtained from equatorial and high-latitudes were analysed and the results present the effects of scintillation on GPS receivers. The campaign uses experimental data obtained from GPS station to assess GISM and WBMOD (theoretical scintillation models). It reviews the two models as well as the GPS receiver and how scintillation is analysed at the receiver. GPS derived experimental data measured and analysed from stations in Finland and Norway (high-latitudes) describes the occurrence of a high phase scintillation index but a low amplitude scintillation index. While empirical results due to measurements from Tucuman, Argentina and Naha, Japan present a high amplitude scintillation index but showing a low phase scintillation index in the equatorial latitudes region. The studies recommend further research in the forecasting of scintillation owing to SW influence on the ionosphere.

Over the years [*Aarons, 1982*], there has been gains recorded in the field of morphology and physics of the ionosphere. However, the investigation observes questions yet unanswered. Questions bordering around irregularities development in various layers of the ionosphere. The review paper explains the contribution of frequency, time of day, season of year, geomagnetic, and solar activity to plasma irregularities in the ionosphere, which can cause traversing radio waves to undergo amplitude fading and phase variation. According to the report, satellite signal entering a region of ionospheric irregularities develops spatial phase changes. Amplitude scintillation occurs as the wave passes through the anomaly and attains its peak value in the far-field. The finding is that knowledge of the characteristics of scintillation can support the design of models to mitigate scintillation problems associated with satellite to Earth link. Knowledge of ionospheric morphology can assist GNSS users to understand scintillation signatures originating from ionospheric and non-ionospheric sources.

Shanmugam and MacLeod, [2013] described the use of GNSS signals in ionospheric studies. The campaign reviewed ionospheric scintillation, TEC, and limitations of past methods of ionospheric measurements using dual-frequency GPS receivers. GPS L1 and L2 frequencies were utilised. The previous techniques of monitoring the ionosphere have proved to be inadequate in scintillation and TEC monitoring, particularly on the L2 frequency. The study presents a modern and robust multi-constellation and multi-frequency GNSS receiver, NovAtel GPStation-6. According to the research, the specialised GNSS receiver can track all present and upcoming GNSS constellation and satellite signals including GPS, Galileo, GLONASS, BeiDou, QZSS, and SBAS. The report compares GPStation-6 and GSV4004B receivers' performance for ionospheric monitoring. GNSS observables were measured in 2012 during scintillation and non-scintillation conditions. GPStation-6 has demonstrated to be a good replacement for GSV4004B receivers because of its ability to measure TEC and ionospheric scintillation real-time and other comparative advantages such as expanded measurement. However, the method of probing the ionosphere using GNSS monitors has its limitations compared to other available techniques. Over the years, ISR has demonstrated to be the most suitable means of monitoring the ionosphere. Instead of conducting an investigation using GNSS instruments only, other measurement techniques would offer an invaluable means of probing the ionosphere and validation of the physical mechanisms therein.

The performance of GPS PPP solutions under varying geomagnetic storm conditions during Solar Cycle 24 by using a large data obtained from about 500 IGS stations was evaluated. To evaluate the performance of GPS Single-Frequency (SF) and Dual-Frequency (DF) PPP in the presence of geomagnetic storms: moderate storm (27 March 2017), intense storm (20 December 2015), and super storm (17 March 2015) data were obtained. The results show that for high-latitudes (60° - 90° north/south), the 3-D root-mean-square errors during the moderate, intense, and super storms are $0.393\,m$, $0.680\,m$, and $1.051\,m$, respectively. In the mid-latitudes (30° - 60° north/south) and low-latitudes (0° - 30° north/south), the performance of GPS DF PPP are not correlated with moderate and intense storm. However, when compared to GPS DF PPP, the performance of GPS SF PPP was inferior irrespective of quiet or disturbed ionospheric condition. Nonetheless, few stations

were degraded during super storm condition. Thus, during geomagnetic storm periods, the deteriorated performance of GPS positioning (regardless of DF or SF) was strongly correlated with enhanced ionospheric disturbances. The results obtained herein can be validated [*Luo et al., 2018*].

Fejer and Kelley, [1980] report substantial theoretical and experiment research has been conducted in the last few decades to describe ionospheric irregularities. These investigations provide insight into how plasma instabilities contribute to the production of irregularities. The work revealed recent experimental investigations of the E and F layers' irregularities and the development of plasma instability theories to support understanding of the physical mechanism. The investigation provides the primary experimental techniques used to study ionospheric irregularities. In the report, the experimental methods such as radio and radar techniques as well as in situ probes were discussed. One of the findings was that most techniques used in the studies of irregularities are in favour of measurements of plasma density. The work described radio wave and spacecraft-borne experimental techniques used in the studies of irregularities to allow an understanding of measurements from ground-based and in situ experiments. In this thesis, electron density measurements will be used to study ionospheric irregularities at auroral and polar latitudes by radio (GNSS) and radar (EISCAT UHF/ESR) experimental techniques.

Wernik et al., [2003] reviewed ionospheric scintillation and irregularities. The report reviewed the correlation between scintillation and ionospheric irregularities as well as characterisation of equatorial and high-latitude irregularities in view of SW and scintillation models. The presence of random fluctuations in electron density can cause scintillation of GNSS radio signals. Equatorial and high-latitude ionospheric irregularities are caused by different plasma instability mechanisms. Motion of plasma structures in high-latitudes is controlled by IMF and large-scale structures have been observed to have a long lifetime as they convect away from their places of origin. In the report, WBMOD scintillation model can be improved by using GNSS and in situ measurements. The origin of auroral and polar latitudes ionospheric irregularities would be investigated using a multi-instrument technique.

In summary, this chapter reviews several contributions relating to ionospheric irregularities in the equatorial, middle, and high-latitudes ionospheres by means of

ground-based and in situ measurements. The presence of ionospheric irregularities between satellite to satellite/ground receivers can influence the performance and operations of GNSS infrastructures. Theoretical and experimental techniques by means of, for example, EISCAT and GNSS were presented. In each contribution, the methods and results obtained were studied to inform the approach/method adopted in this research.

4 Ionospheric Effects on Propagation of GNSS Signals

4.1 Introduction

The ionosphere affects radio waves propagation from Very Low Frequency (VLF) to above Super High Frequency (SHF) [*Dabas and Dabas, 2000*]. It can support long-distance communications in the High Frequency (HF) but disrupts radio communications beginning from Very High Frequency (VHF) and above. For example, GNSS radio signals operate in the Ultra High Frequency (UHF) band between $300\,MHz$ and $3\,GHz$ band. To provide a good understanding of transionospheric radio wave propagation and the corresponding effects on GNSS signals, certain properties of the ionosphere are presented and discussed. Ionospheric processes produced in the ionosphere including electron density, TEC, and temporal TEC fluctuations with governing equations; the refraction of transionospheric radio waves; diffraction and scattering of GNSS radio signals; and ionospheric scintillation. In this chapter, the ionospheric metrics TEC fluctuations and scintillation were considered.

4.2 Ionospheric Processes

The ionospheric plasma is produced mainly by solar radiation, which causes excitation and ionisation of atomic and molecular constituents. These constituents of the ionosphere are ionised by the far and extreme ultraviolet (EUV) wavelength ($\lambda < 130\,nm$) and particle precipitation from processes originating from the Sun [*Rana and Yadav, 2014*]. Consequently, the ionospheric plasma consists of atomic and molecular ions interact with each other in complex chemical reactions. The ionosphere is considered as a quasi-neutral medium in which the total number of electrons is equal to the total number of ions described by continuity and energy equations, as well as equations of motion for the individual charged particles. The fundamental continuity equation, for example, for the electrons is expressed as

$$\frac{\partial N_e}{\partial t} = Q_e - L_e - \nabla(N_e v_e)\ [electrons/m^3/s] \qquad (4.1)$$

Where N_e is the electron density, t is the time, Q_e $[electrons/m^3/s]$ is the rate of electron production, L_e $[electrons/m^3/s]$ is the rate of electron loss, and v_e is the mean velocity of electrons.

Similarly, the continuity equation for the ions is given by

$$\frac{\partial N_i}{\partial t} = Q_i - L_i - \nabla(N_i v_i) \quad [ions/m^3/s] \tag{4.2}$$

All terms in equation (4.1) are unchanged except that instead of e for electron, the e here is replaced with i which stands for ion.

The complex dynamics of production, loss, and motion of the ionospheric plasma including electrodynamic coupling with the thermosphere and magnetosphere leads to structuring of ionospheric electron density according to altitude variation [*Rana and Yadav, 2014*]. Different ionospheric layers ($D, E, F_1, and\ F_2$) define regions in which specific ionospheric processes dominate [*Schunk and Nagy, 2009; Rana and Yadav, 2014*]. Electrical conductivity and electric currents peak in the E layer where the ionisation at about $110\ km$ on average are strongly associated with energetic particle precipitation and X-rays driven by solar flares.

Chapman's theory is used to describe the vertical electron density distribution, which depends on the height, given by

$$N_e = N_o exp\left(\frac{1}{2}[1 - z - sec\,\chi\, exp(-z)]\right) \quad [electrons/m^3] \tag{4.3}$$

And

$$z = \frac{\hbar - \hbar_0}{H} \quad [dimensionless] \tag{4.4}$$

Where χ is the zenith angle of the solar radiation with respect to the normal, N_0 is the peak electron density of the layer, $\hbar$ is the height above the Earth surface, $\hbar_0$ is the peak electron density height, z is dimensionless, and H is the pressure scale height of the neutral gas in the background. Electron density is normally given in $electrons/m^3$.

To characterise the refractive index for transionospheric radio waves, the electron density is being considered as the most significant metric. This is also valid for the integral of the vertical electron density, referred to as TEC. TEC is defined as the

total number of electrons in a columnar cylinder of unit area. Therefore, the Vertical TEC (VTEC) is expressed as [*Kaplan and Hegarty, 2005; Norsuzila et al., 2010; Correia et al, 2018*]

$$VTEC = \int N_e d\hbar \quad [electrons/m^2] \tag{4.5}$$

Whereas the Slant TEC (STEC) as indicated in Figure 4.1, measured along a slant ray path P_s is expressed as [*Rao and Dutt, 2017*].

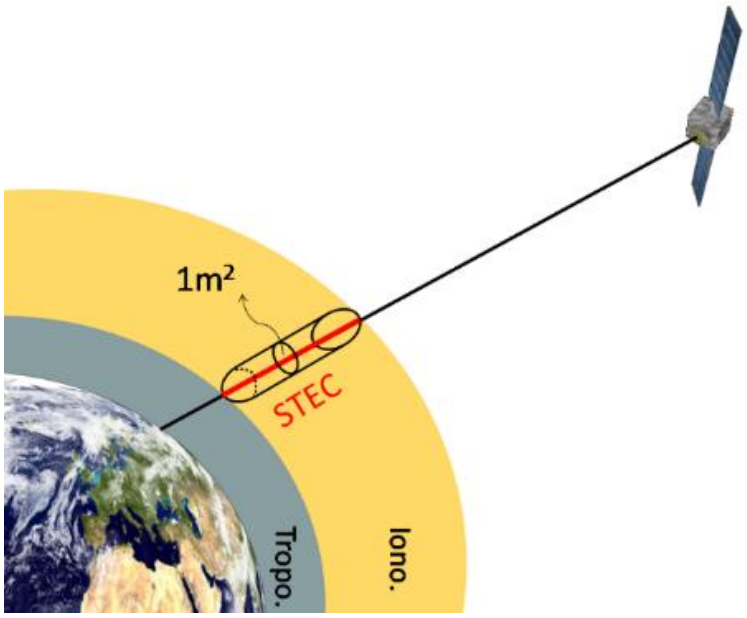

Figure 4.1: STEC obtained from a GPS ray path between satellite to GPS receiver located on the ground.
Source: http://gnss.be/ionosphere_tutorial.php

$$STEC = \int N_e dP_s \quad [electrons/m^2] \tag{4.6}$$

VTEC and STEC are related by a so-called obliquity factor mapping function $M(E)$ which depends only on ray path elevation angle $\mathbb{E}$ [*Rao and Dutt, 2017*].

$$M(\mathbb{E}) = \frac{STEC}{VTEC} = \frac{1}{cos\zeta} \quad [dimensionless]$$

$$= \left[1 - \left(\frac{R_\oplus cos\,\mathbb{E}}{R_\oplus + \hbar_1}\right)^2\right]^{-1/2} \quad [dimensionless] \tag{4.7}$$

Where $R_\oplus$ is the radius of the Earth, $\hbar_1$ is the height of the thin shell representing the ionosphere, ζ is the zenith angle, and $\mathbb{E}$ is the angle of elevation. To measure ionospheric variability, VTEC can be used to image electron density distribution at ionospheric pierce point (IPP) $350\ km$ [*Rao and Dutt 2017*].

TEC is directly proportional to range delay in a transionospheric radio wave propagation [*Nava et al., 2005*]. To first order, the magnitude of range delay and carrier phase advance is the same except for the signs. This range delay, R, expressed in metres is given by

$$R = 40.3\frac{TEC}{f^2} \quad [m] \tag{4.8}$$

Where TEC is given in $electrons/m^2$, and f is frequency in Hz. TEC is commonly expressed in TECU (1 $TECU = 10^{16}\ electrons/m^2$) [*Kaplan and Hegarty, 2005; Rao and Dutt, 2017; Correia, et al., 2018*].

Similarly, TEC (STEC) can be computed by measuring the difference in ionospheric delay between L1 and L2 GNSS (GPS) signals expressed as [*Rao and Dutt, 2017*]

$$TEC(t) = \frac{1}{40.3}\frac{f_1^2 f_2^2}{f_1^2 - f_2^2}(L1 - L2)\ [electrons/m^2] \tag{4.9}$$

Where f_1 and f_2 are high (L1 signal) and low (L2 signal) frequencies respectively obtained from a dual-frequency GNSS (GPS) receiver expressed in Hz ($f_1 = 154f_0$, $f_2 = 120f_0$, and fundamental frequency $f_0 = 10.23\,MHz$). L1 and L2 are carrier phase signals expressed in cycles.

To convert TEC from $electrons/m^2$ to TECU, L1 and L2 carrier phase signals equation (4.9) must be converted to metres and the result divided by 10^{16}. Given that, $c = 2.99792458 \times 10^8\ m/s$ (c is the speed of light in a vacuum), $\lambda_1 = c/f_1$, and $\lambda_2 = c/f_2$, therefore, $L1\ [m] = \lambda_1 \times L1$ and $L2\ [m] = \lambda_2 \times L2$. This implies that equation (4.9) can now be written as

$$TEC(t) = \frac{1}{40.3}\frac{f_1^2 f_2^2}{(f_1^2 - f_2^2) \times 10^{16}}(L1\ [m] - L2\ [m])\ [TECU] \tag{4.10}$$

Temporal TEC fluctuations ($\frac{\Delta TEC}{\Delta t}$) for each specific PRN is given by

$$\frac{\Delta TEC}{\Delta t} = \frac{TEC(k) - TEC(k-1)}{\Delta t} \quad [TECU/\Delta t] \tag{4.11}$$

$TEC(k)$ is TEC at epoch k, $TEC(k-1)$ is TEC at $k-1$, and Δt is the change in time (assuming unit of time is second) [*Forte et al., 2013; Carrano and Groves 2007; Luo et al., 2018*]. In this report, TEC fluctuations is used as a convenient proxy to infer the presence of large-scale ionospheric irregularities.

4.3 Refraction of Transionospheric Radio Waves

Refraction of electromagnetic waves is caused by sudden changes in the velocity of a propagating radio wave as it enters into a different medium [*Rana and Yadav, 2014*]. The refraction of electromagnetic waves is a function of the following:

a) The magnitude of the ionisation density of the ionospheric layer.
b) The angle at which the electromagnetic wave makes with the ionospheric layer (angle of incidence).
c) Frequency of the electromagnetic wave.

The electromagnetic field of radio waves interacts with charged particles in the ionosphere whose motion are governed by the Earth's magnetic field. In the presence of geomagnetic field, the ionosphere is an anisotropic medium and the collision between charged particles are allowed. The refractive index can be defined by the Appleton-Hartree equation. Ignoring collision terms, the refractive index n [dimensionless] is given by the equation

$$n^2 = 1 - \frac{2X(1-X)}{2(1-X) - Y^2 \sin^2\Theta \pm [Y^4 \sin^4\Theta + 4(1-X)^2 Y^2 \cos^2\Theta]^{\frac{1}{2}}} \quad [dimensionless] \quad (4.12)$$

Where

$$X = \frac{f_p^2}{f^2} \quad [dimensionless] \quad (4.13)$$

$$Y = \frac{f_g}{f} \quad [dimensionless] \quad (4.14)$$

And Θ is the angle between the ray path and the Earth's magnetic field induction B, f is the radio wave frequency, f_p is the plasma frequency, X and Y are dimensionless quantities, and f_g is the gyrofrequency of electrons that gyrate clockwise around the geomagnetic field line in the field direction [*Teunissen and Montenbruck, 2017*].

In addition, the plasma frequency f_p of electron density n_e excited by a radio wave at two frequencies f_1 and f_2 in the presence of a geomagnetic field B is given by the equation

$$f_p^2 = \frac{N_e \hat{e}^2}{4\pi^2 \varepsilon_0 m_e} \quad [Hz^2] \quad (4.15)$$

Where ê is the charge of electron, m_e is the mass of electron, ε_0 is the permittivity of free space [*Beynon and Williams, 1978; Teunissen and Montenbruck, 2017*].

The gyrofrequency (synchrotron) f_g which is dependent on the geomagnetic field B is given by the equation

$$f_g = \frac{\hat{e}\, B}{2\pi m_e} \quad [Hz] \tag{4.16}$$

4.4 Diffraction and Scattering of L-band Signals

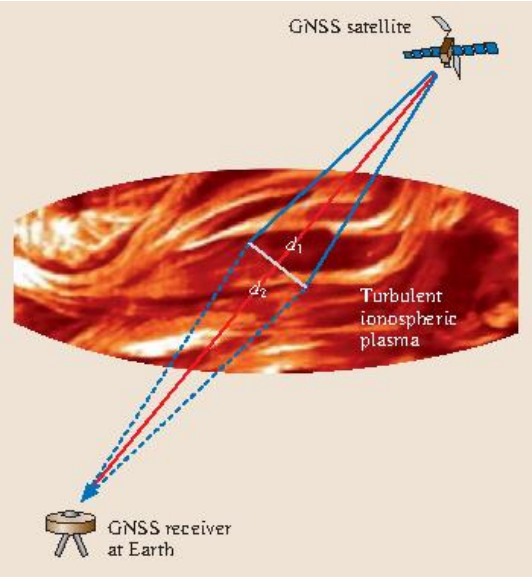

Figure 4.2: Superposition of diffracted and scattered GNSS signals at the GNSS receiver located on the ground due to disturbed ionospheric condition [*Teunissen and Montenbruck, 2017*].

Supposing the spatial scale of ionospheric density fluctuations are comparable to the wavelength of a radio wave transversing the ionosphere, the propagation of the wave can be explained by diffraction and scattering theories. Small-scale ionospheric irregularities can diffract radio waves. These small-scale ionospheric irregularities can induce rapid variations in the amplitude and/or phase of RF signals referred to as scintillation. During scintillation, the ionosphere does not absorb radio waves. However, ionospheric irregularities in the index of refraction scatter the radio waves about the propagation direction [*SBAS-IONO Working Group, 2012*]. In Figure 4.2, both the satellites and irregularities are moving. At ionospheric heights corresponding to E and F layers, the movement of satellites is far less than the movement of irregularities. Hence, movement of irregularities is mostly considered.

Scintillation can affect satellite signals from VHF ($30\,MHz$ to $300\,MHz$) to SHF ($3\,GHz$ to $30\,GHz$) bands. Severe scintillation can last up to about several hours on average [*Teunissen and Montenbruck, 2017*].

The first Fresnel zone can be used to estimate the spatial scale of ionospheric irregularities inducing scintillations at RF signals of wavelength λ. The corresponding Fresnel radius F_1 is given by the equation

$$F_1 = \sqrt{\frac{\lambda d_1 d_2}{d_1 + d_2}} \quad [m] \tag{4.17}$$

Where d_1 and d_2 are the distances from the transmitter to the receiver, respectively (Figure 4.2).

In GNSS applications, the first Fresnel radius F_1 is about $300\,m$ on average. Here, ionospheric irregularities of this spatial scale or smaller can cause multiple diffracted and scattered RF signals at the GNSS receiver due to electron density variations.

4.5 Ionospheric Scintillation

The ionosphere is reported to have two main effects on GNSS radio signals called range delay and scintillation [*Doherty, 2009*]. Among the effects posed by the ionosphere on GNSS signals (circularly polarised), Faraday rotation is ignored because it only affects linearly polarised signals. Ionospheric scintillation is responsible for refraction and diffraction of transionospheric signals [*Aaron, 1982; Yeh and Liu, 1982, Dabas and Dabas, 2000; and references therein*]. Small-scale irregularities in the medium scatter electromagnetic waves causing range delay and phase advance. Scintillation activity depends on operating frequency, time of day, season of year, longitude and latitude, geomagnetic activity, and 11-year solar cycle [*Susnik and Forte, 2011*]. Geomagnetic field of the Earth plays an important role in determining scintillation. Figure 4.3 shows the effects of ionospheric scintillation on GPS signals originating from ionospheric electron density irregularities. Scintillation activity varies in equatorial latitudes, middle latitudes, and high-latitudes. Unlike equatorial and high-latitudes ionosphere, middle latitudes region is characterised by mild scintillation except in disturbed geomagnetic conditions when its effects on

GNSS-based applications can degrade the performance and reliability of such technological systems in the region [*Dabas and Dabas, 2000*].

Scintillation may be treated as amplitude scintillation and phase scintillation. Amplitude scintillation explains what happens to the amplitude of the carrier signal when it passes from one plasma medium to another with a varying index of refraction. It can cause deep signal fade challenging the ability of the GNSS receiver to acquire or track the signal. Such fading may cause the received signal to come short of the estimated threshold value. The overall effect of amplitude scintillation will be a threat to availability of service [*SBAS-IONO Working Group, 2012*]. Phase scintillation refers to rapid variations in the carrier phase are observed in the phase lock loop. Depending on the severity of the irregularities, phase scintillation may result into increased phase noise, cycle slips or sometimes losses of lock where the receiver is unable to track the received signal [*SBAS-IONO Working Group, 2012*]. The widely used indices to characterise the two types of scintillation are S_4 and σ_Φ [*Hargreaves, 1992 ; ICAO, 2012*]. The amplitude scintillation index S_4 is the standard deviation of the normalised signal intensity while the phase scintillation index σ_Φ is defined as the standard deviation of the normalised signal phase [*Jiao and Morton, 2015; Guo et al., 2017; Luo et al., 2018*]. These indices are given by equations (4.18) and (4.21) respectively [*Briggs and Parkin, 1963; Van and Klobuchar, 1993; Van, 2009*].

$$S_4 = \sqrt{\frac{<I^2> - <I>^2}{<I>^2}} \ [dimensionless] \tag{4.18}$$

Where I is the detrended signal intensity (power) and is given by $I = A^2$. A is the amplitude of the signal, and $< >$ stands for the average over a certain time interval.

The part of $S4$ value that originates from ambient noise is given by the equation [*Van Dierendonck et al., 1993; Andalsvik and Jacobsen, 2014*]

$$S_{4corr} = \sqrt{\frac{100}{S/N_0}\left[1 + \frac{500}{19S/N_0}\right]} \ [dimensionless] \tag{4.19}$$

Where S/N_0 is the signal-to-noise ratio $[dB - Hz]$

Hence, if a 60-s approximation of the S/N_0 is used, this corrected S_4 value (S_{4corr}) can then be subtracted from the total S_4 value (S_{4tot}) to obtain the S_4 value without the noise effects [*Andalsvik and Jacobsen, 2014*]

$$S_4 = \sqrt{[S_{4tot}^2 - S_{4corr}^2]} \quad [dimensionless] \tag{4.20}$$

$$\sigma_\Phi = \sqrt{<\Phi^2> - <\Phi>^2} \quad [rad] \tag{4.21}$$

Where Φ is the detrended carrier phase signal [*Andalsvik and Jacobsen, 2014*]. Phase scintillation (σ_Φ) cannot be directly computed from GNSS data but is obtained from detrended phase observation. Amplitude and phase scintillation indices are used to categorise the level of scintillation severity as weak, moderate, and strong scintillation as indicated in Table 4.1.

Table 4. 1: Categorisation of ionospheric scintillation severity

Category	**Magnitude of index**
Weak	$0.1 < S_4 < 0.25$ or $0.1 < \sigma_\Phi < 0.25$
Moderate	$0.25 < S_4 < 0.7$ or $0.25 < \sigma_\Phi < 0.7$
Strong	$S_4 \geq 0.7$ or $\sigma_\Phi \geq 0.7$

Both scintillation indices are computed over 60-s (1-minute) with a typical value between 0 and 1 and are inversely proportional to the critical frequency of L-band signal [*ICAO, 2012*]. Ionospheric scintillation indices are obtained from a special GNSS dual-frequency receiver able to record data at a high data rate at a sampling frequency of 50-Hz. The receiver can compute the TEC from which other ionospheric metrics can be computed. For example, TEC fluctuations (ΔTEC), and Rate of change of TEC Index (ROTI). Amplitude scintillation (S_4) indicates the presence of small-scale electron density irregularities while phase scintillation suggests the presence of large-scale electron density irregularities [*Correia et al., 2018*].

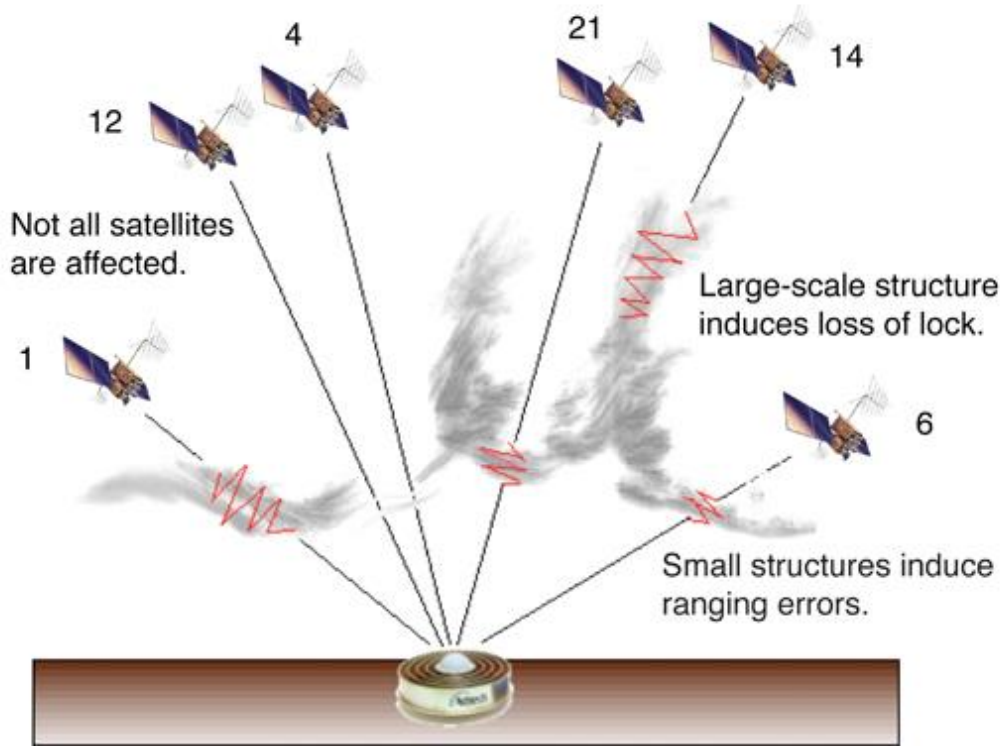

Figure 4.3: Effects of ionospheric scintillation on GPS signals originating from ionospheric electron density irregularities [*SBAS-IONO Working Group, 2012*].

4.5.1 Scintillation at Equatorial Latitudes

The largest ionospheric region is the equatorial ionosphere. Host to EIA, complex electrodynamic processes [*Fejer, 2015*], and where plasma bubbles are deep and intense. This region has strong and most frequent [*Basu et al., 1988 and National Science Foundation, 2012*] effects on GNSS-based, High Frequency (HF) radio communications, and associated telecommunication facilities. Scintillation and plasma bubbles are limited to post-sunset and pre-midnight [*Doherty, 2009*] at equatorial latitudes happening above 40% of the year between 20:00 and 02:00 Local Time (LT) [*Béniguel and Hamel, 2011*]. Scintillation depends on the season and can occur during quiet geomagnetic conditions [*Priyadarshi and Singh, 2011*]. However, the frequency and severity of scintillation are high during disturbed geomagnetic conditions. Figure 4.4 shows scintillation effects on L1 and L2 GPS signals observed in 2002 near peak of the solar cycle. The GPS receivers are located at Ascension Island. Scintillation causes a signal fade of about 20 dB on L1 and 60 dB on L2 on average. Signal fluctuations shown in red colour are indications of scintillations occurring between 21:00 and 22:00 UT. This result agrees with

previous studies [*Klobuchar, 1991; Doherty, 2009; Béniguel and Hamel, 2011; Susnik and Forte, 2011; SBAS-IONO Working Group, 2012*]. It is important to point here that in this region, amplitude scintillation is dominant compared to phase scintillation [*Béniguel et al., 2004*].

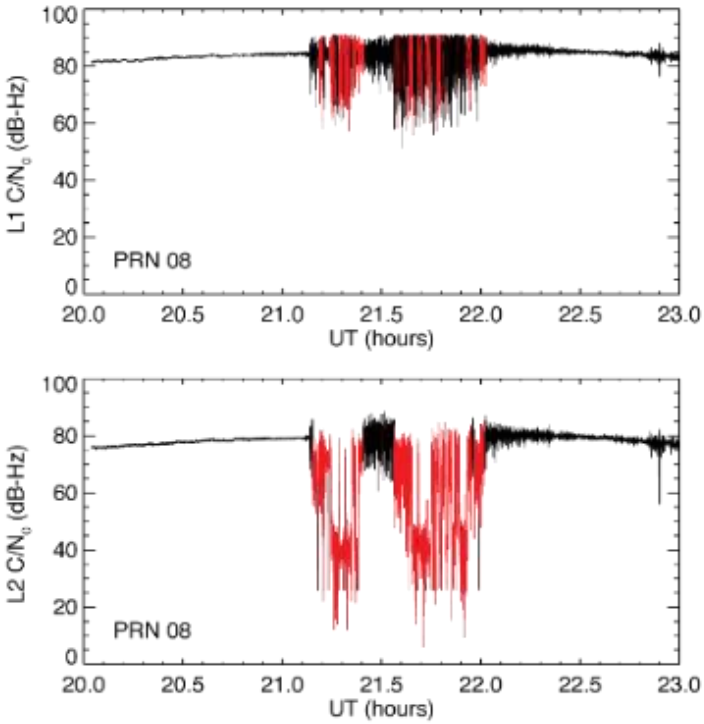

Figure 4.4: From top to bottom shows the fading of L1 and L2 signals from a GPS satellite recorded from Ascension Island on 16 March 2002, respectively. Absolute power levels are arbitrary [*Carrano et al., 2009*].

4.5.2 Scintillation at Middle Latitudes

Middle latitudes ionosphere lies between the equatorial and high-latitudes. Ionospheric behaviour in the region tends to be favourable to GNSS and associated telecommunication systems. There are times during geomagnetic storm where activities in the equatorial and high-latitudes regions impact on middle latitudes [*SBAS-IONO Working Group, 2012*]. SuperDARN ionospheric convection maps or electric potential patterns are utilised to deduce plasma motion, for instance, from auroral magnetic latitudes to middle latitudes. In middle latitudes, scintillation is rare but occurs only during extreme geomagnetic conditions [*Doherty, 2009*]. Geomagnetic and ionospheric storms can cause electron density irregularities and these disturbances affect GNSS and associated RF applications [*Romano et al., 2013*]. For instance, scintillation may interfere with the ability of a GNSS receiver to

track a GNSS continuously. Thus, the availability of GNSS service is impaired [*SBAS-IONO Working Group, 2012*]. Figure 4.5 shows a scintillation signature in the middle latitude during geomagnetic storms observed on 26 September 2001 in the United States. Aurora activities moved equatorward causing plasma disturbances in the middle latitudes producing impairments on GPS signals. The power fade observed was about $20\ dB$ on average and this level of signal fade has potential to cause losses of lock on GPS L1 signal. This magnitude of signal fade can cause a more significant impact on L2 signals because they are more susceptible to disruption due to scintillation during severe geomagnetic storm. Scintillation has been observed to have greater limiting effects on lower frequencies. That is, L2 ($1227.60\ MHz$) signals are more degraded than L1 ($1575.42\ MHz$) signals. Hence, L5 ($1176.45\ MHz$) signals fading is worst under the same ionospheric condition compared to L1 and L2 signals.

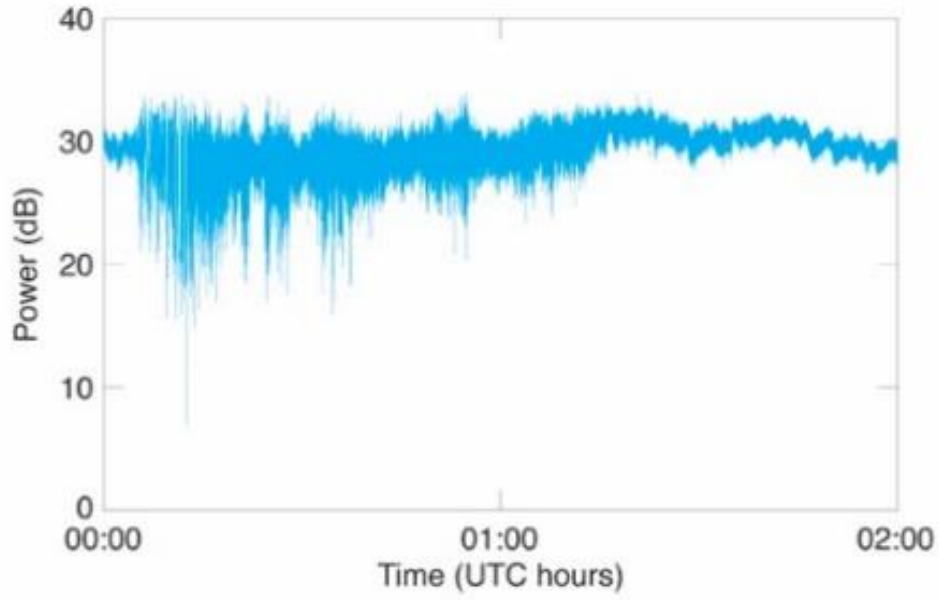

Figure 4.5: GPS scintillations observed at a middle latitude location between 00:00 and 02:00 UT during the intense magnetic storm of 26 September 2001 [*Ledvina et al., 2002*].

4.5.3 Scintillation at Auroral Latitudes

Aurora is the most widely observed consequences of the coupling between the magnetosphere and ionosphere and the dominant characteristics of the high-latitudes ionosphere [*Hargreaves, 1992*]. Aurora latitude scintillation is related to geomagnetic activity and has fewer effects when compared to equatorial latitudes

[*Doherty, 2009*]. Post-sunset, magnetic field lines which are almost vertical at high-latitudes trap solar energetic particles (e.g. electrons and protons). These particles are injected into the auroral oval leading to the formation of electron density irregularities responsible for scintillation of GNSS radio signals [*SBAS-IONO Working Group, 2012*]. According to *Rino et al.,* [1978], field-aligned irregularities can cause enhancement of localised scintillation at auroral latitudes when the propagation path occurs simultaneously with the magnetic zenith. These scintillation enhancements occurring in the presence of east-west elongation of diffraction patterns, originate from sheet-like irregularities [*Martin and Aarons, 1977*]. To add to this, these sheet-like irregularity structures occur mainly in night-time diffuse or discrete particle precipitation region. Further, the intensity of scintillation is interrelated with local geomagnetic activity. On the other hand, irregularities causing scintillation in the polar latitudes are plasma patches [*Klobuchar, 1991; Schunk and Nagy, 2009*]. At high-latitudes, phase scintillation is reported to be high with low amplitude scintillation [*Chartier et al., 2016; Béniguel, 2017*] as shown in Figure 4.6.

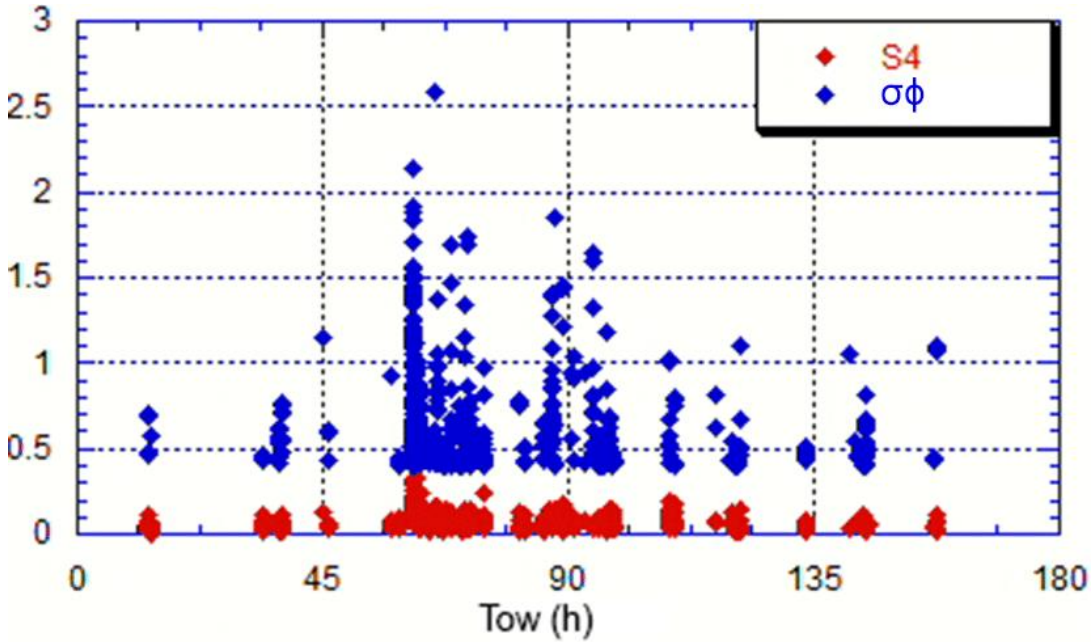

Figure 4.6: Amplitude and phase scintillation on L1 during St. Patrick's Day storm over Sodankylä, Finland in the auroral latitude for days 75-82 (16-23 March) 2015 [*Béniguel et al., 2017*].

In view of 2018 and 2019 EISCAT UHF/ESR experimental campaigns, ionospheric plasma gradients as well as irregularities can adversely affect GNSS signals propagation as indicated in Figure 4.7. Figure 4.7 provides insight into investigation

of the performance of GNSS positioning in the presence of high-latitudes irregularities by means of EISCAT UHF/ESR. A multi-instrument approach was required using case studies (auroral and polar ionospheres) to investigate the effects of large-scale irregularities on GNSS positioning applications.

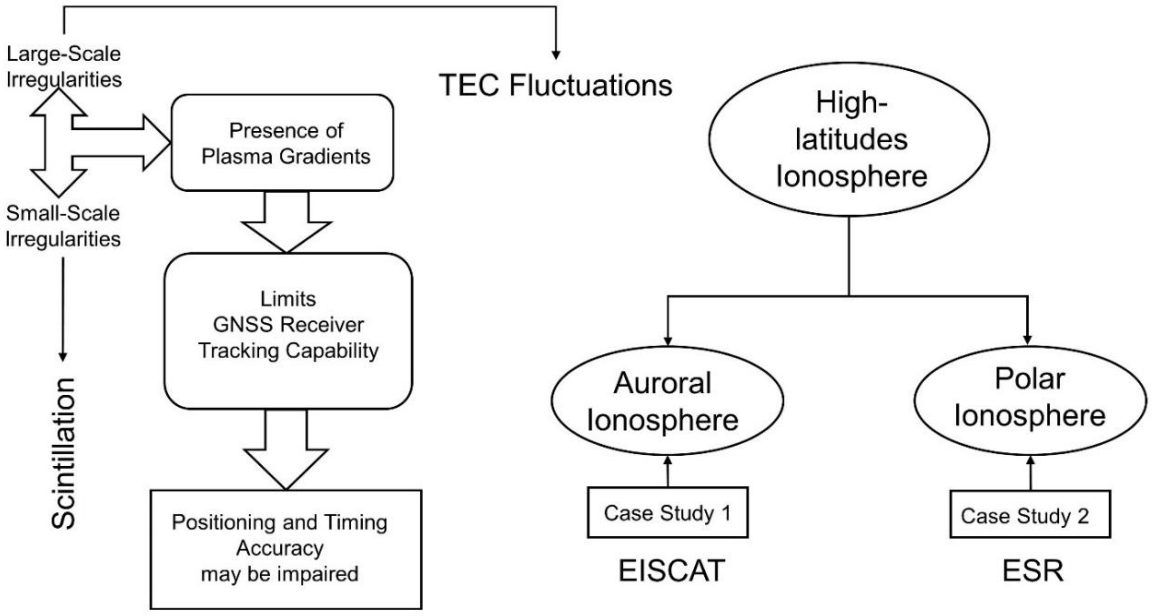

Figure 4.7: Description of the performance of GNSS positioning in the presence of ionospheric plasma gradients as well as irregularities at auroral and polar latitudes using EISCAT (Case Study 1)/ESR (Case Study 2), respectively. High-latitudes ionosphere is divided into auroral and polar ionospheres. The impact of large-scale irregularities on GNSS signals at high-latitudes is quantified in terms of TEC fluctuations.

4.6 Summary

This chapter discusses the influence of the ionosphere on propagation of GNSS signals. Ionospheric irregularities presented in Chapters 2 and 3 occurring between a satellite and receiver are responsible for degradation and interruption of GNSS signals used in navigation, positioning, and communication systems. These irregularities, depending on their spatial scale, were characterised by means of TEC fluctuations and scintillation. Scintillation in the different regions of the ionosphere were presented. In the high-latitude ionosphere, scintillation activity is closely associated with geomagnetic activity. Theoretical equations required to support the understanding of this research are also presented.

5 Instrumentations and Measurements

5.1 Introduction

This chapter presents the instrumentations and measurements used to study ionospheric irregularities and their impact on GNSS in this research. Instrumentations used herein refer to sources of measurements through which the experiments were designed and conducted. Because the study was simultaneous multi-instrument experimental campaigns involving the incoherent scatter radars (EISCAT UHF/ESR) combined with geodetic GNSS receivers, these instrumentations are discussed together with other instrumentations used for the purpose of elucidation and validation. A section on the software used in the investigation as well as the observed challenges encountered with the use of 50-Hz GNSS data and keograms was included to support understanding. In addition, the reasons for the use of measurements from geodetic GNSS receivers at the auroral and polar latitudes to overcome these challenges were stated.

In view of this, the ionospheric instrumentations and their corresponding measurements are presented as follows:

a) Incoherent Scatter Radars (ISRs). For example, EISCAT, ESR, and Advanced Modular Incoherent Scatter Radar (AMISR).
b) GNSS constellation/GNSS receivers.
c) International Monitor for Auroral Geomagnetic Effects (IMAGE) magnetometer network.
d) Super Dual Auroral Radar Network (SuperDARN).
e) All-Sky Cameras (ASCs).
f) Spirent GPS Simulator (SGS).

5.2 Incoherent Scatter Radars (ISRs)

The incoherent scatter radar is a powerful ground-based upper atmospheric equipment used to measure the various properties of the ionosphere. Radio waves transmitted from the radar are scattered incoherently by free electrons in the ionosphere causing them to accelerate in response to the incident waves and

reradiate the signal. The incoherent scatter theory, as applicable to radar, to measure the received electromagnetic waves was first proposed by Professor William E. Gordon in 1958 [*Gordon, 1958*]. A typical transmitted wave power is in megawatt (MW) while the received waves (much weaker waves) are in picowatt (pW). Because of the very weak backscattered signal, ISR requires a transmitter with strong power, a large antenna, a very sensitive receiver, and a sophisticated data processing system, which altogether make ISR very expensive [*Hargreaves, 1992*]. The incoherent scatter returns originate from these free electrons usually with a strong influence on the ions. This picture of incoherent scatter returns assumes that electrons are independent in which the intensity of the scattered signal provides insight into the electron density. This simple picture is not however adequate: the width of the returned spectrum is directly proportional approximately to the thermal velocities of ions. Theoretical investigations validate that the spectral width is controlled by ion motions [*Rishbeth and Williams, 1985*]. Valuable ionospheric parameters can be measured from the spectrum of the returned echo, which includes electron density, electron temperature, ion temperature, and ion drift velocity [*National Science Foundation, 2012*]. From these parameters, other parameters such as electric field, neutral wind, neutral temperature, vertical fluxes of particles and heat, photoelectron energy, and composition of the atmosphere are derived [*Beynon and Williams, 1978*]. These ionospheric parameters are used to deduce the ionospheric activity in the region under observation.

According to *Beynon and Williams*, [1978], the International Union of Radio Science (URSI) in 1968 constituted an expert Working Group to evaluate the whole scope of electromagnetic probing of the atmosphere. The Group reports that ISR appears to provide the most accurate and convenient way of measuring electron density, electron temperature, ion temperature, and ion drift velocity between $100\ km$ and several $100\ km$ in the ionosphere. These features have made ISR the most powerful tool for bottomside and topside ionospheric research. These radar instrumentations have made invaluable contributions to the understanding of the morphology and dynamics of the upper and lower atmosphere.

ISRs can be used to verify several aspects of the behaviour of plasma in the ionosphere, including plasma instabilities created naturally or artificially through HF radar modification. Unlike ionosonde, ISR can measure both the lower and upper

atmosphere with a better spatial resolution [*Hargreaves, 1992*]. Details on ISR principles can be found in the literature cited herein [*Gordon, 1958; Beynon and Williams, 1978; Hargreaves, 1992; Hunsucker and Hargreaves, 2007*]. There are ISR observatories located at Arecibo, Puerto Rico; Jicamarca, Lima, Peru; Millstone Hill, Boston, MA; Sondrestrom, Greenland; EISCAT Tromsø, Norway; ESR, Longyearbyen, Norway [*Bob, 2001*]. Figure 5.1 shows the global network of ISRs using parabolic antennas courtesy of URSI ISR Working Group. In this report, the ISRs used were EISCAT UHF/ESR.

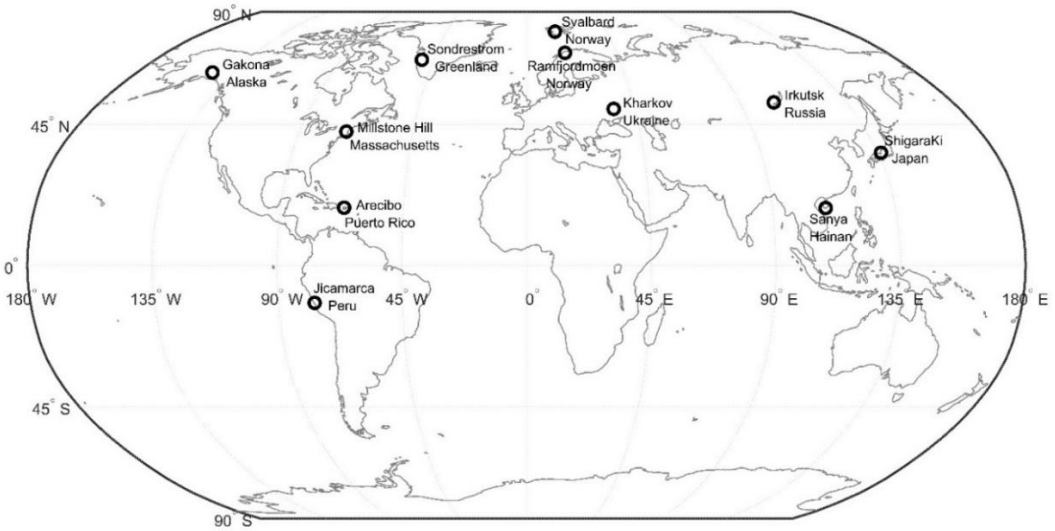

Figure 5.1: Global network of Incoherent Scatter Radars (ISRs) using parabolic antennas.

EISCAT facilities operating four radar antenna sites located at Kiruna, Sweden; Tromsø, Norway; Longyearbyen, Norway; and Sodankylä, Finland are presented in Figure 5.2.

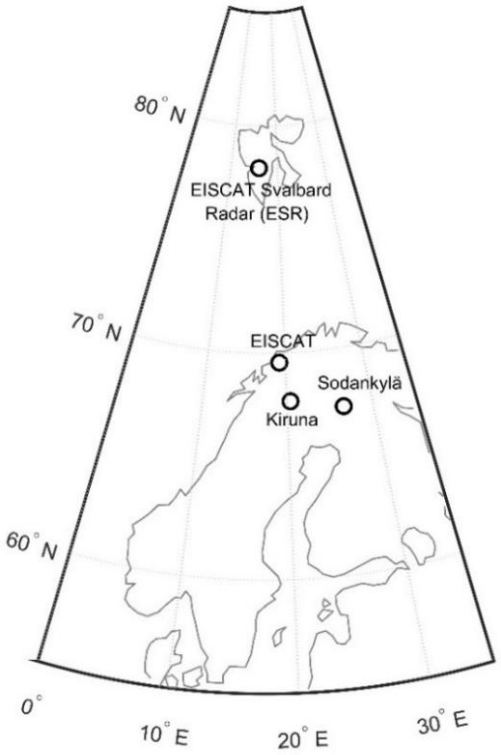

Figure 5.2: Geographic location of EISCAT facilities in terms of latitude and longitude with main transmitters located at Tromsø (receivers at Tromsø, Kiruna, and Sodankylä) and Longyearbyen (receiver at Longyearbyen) in the Northern Hemisphere.

5.2.1 EISCAT

The EISCAT (69.58° N, 19.23° E) radar facility at Tromsø, Norway is the heart of the mainland system. It is a tristate system with the main transmitter at Tromsø and two receivers located at Kiruna and Sodankylä. The site consists of a parabolic steerable antenna, the rectangular VHF antenna, the heating facility for ionospheric modification, several buildings, and the site for the EISCAT3-D system. The EISCAT UHF radar used during the 2018 and 2019 experimental campaigns operating frequency is $930\ MHz$ at a peak power of $2.0\ MW$ and a duty cycle of 12.5%. The antenna has a $32\ m$ diameter fully mechanically steerable parabolic dish as indicated in Figure 5.3. Details of EISCAT facility are obtainable online through the website https://www.eiscat.se/about/sites/eiscat-tromso-site/.

Figure 5.3: EISCAT UHF radar located at Tromsø, Norway [Photo by Mike Zawadzki].
Source: https://imgur.com/gallery/xxKx9Ua

5.2.2 ESR

ESR (78.15° N, 16.02° E) located at Longyearbyen, Svalbard is the most recent EISCAT facility for scientific research. Its location provides great potential for polar ionospheric research. Northern Lights in this region are mostly observed starting from mid-October preferably at night-time. The ESR operates in the $500\ MHz$ band with a peak power of $1\ MW$ at a duty cycle of 25%. The facility consists of two antennas, one is a $32\ m$ fully mechanically steerable parabolic antenna and the other a $42\ m$ fixed parabolic antenna aligned along the direction of the local geomagnetic field. Details of ESR facility can be obtained online through the website https://www.eiscat.se/about/sites/eiscat-svalbard-radar/. The ESR facility is shown in Figure 5.4 where the $32\ m$ and $42\ m$ dish antennas are located on the left and right-hand side of the figure, respectively.

Figure 5.4: EISCAT Svalbard Radar (ESR) located at Longyearbyen [Photo by Craig Heinselman].
Source: https://www.eiscat.se/about/sites/eiscat-svalbard-radar/

5.2.3 AMISR

Before the invention of AMISR, there were other radar facilities used for solar-terrestrial environment research. Radars operating between Medium Frequency (MF) and Ultra High Frequency (UHF) are used to study the structure and dynamics of the lower and upper atmosphere [*Roettger, 1989*]. Ionosondes (HF Radar), for instance, are used for ionospheric studies but have limitations. Many important ionospheric mechanisms occur below the F2 peak but the ionosphere extends beyond the F2 peak. Two-thirds of the total ionisation happens in the topside ionosphere that is above the F2 peak [*Beynon and Williams, 1978*]. However, the ionosonde is limited to bottomside ionosphere and there is a full range of information provided by ISR that ionosonde is unable to provide. Thus, the need for another type of radar that can bridge the gap in the field of aeronomy.

AMISR is a latest generation solid-state phase-array ISR, designed and operated by the Stanford Research Institute (SRI) and funded by the National Science Foundation (NSF), the United States [*Bob, 2001; Varney, 2016*]. AMISR is modular, transportable, and reconfigurable with a 10% duty cycle, operating frequency between $430\ MHz$ and $450\ MHz$ and peak power of $2\ MW$ [*Kelley, 2005*]. Examples of AMISR are Resolute Bay ISR (RISR-C) in Canada and Poker Flat ISR (PFISR)

in Alaska, U.S. [*Butler et al., 2010*]. RISR-N antennas are pointing north while RISR-C antennas are directed towards south. Scientists and students, from around the world, use the AMISR for upper atmospheric studies and to monitor SW events [*Valentic et al., 2013; Nicolls, 2014*]. A major advantage of AMISR technology is that its beam can be steered electronically unlike EISCAT UHF/ESR [*Hickey et al., 2015*]. For AMISR, the number of panels is directly proportional to transmitter power and antenna aperture [*Hickey et al., 2015*]. The first AMISR observatory built in Alaska is shown in Figure 5.5. The architecture and specifications of a typical AMISR are detailed in [*Nicolls, 2014; Valentic et al., 2013; Varney, 2016*].

Figure 5.5: Shows AMISR located at Poker Flat (PFISR), Alaska. [*Valentic et al., 2013*].

In this research, the ISR facilities utilised are EISCAT UHF/ESR UHF $32\,m$ dish antennas presented and discussed as two separate case studies. EISCAT UHF/ESR provide the opportunity to measure profiles of electron density, electron temperature, ion temperature, and ion drift velocity. These ionospheric properties measured by the radars enabled the study of ionospheric activity at the high-latitudes region. The high-latitude locations of EISCAT UHF/ESR support the studies of the spatial and temporal distribution of auroral and polar irregularities, respectively.

5.3 GNSS

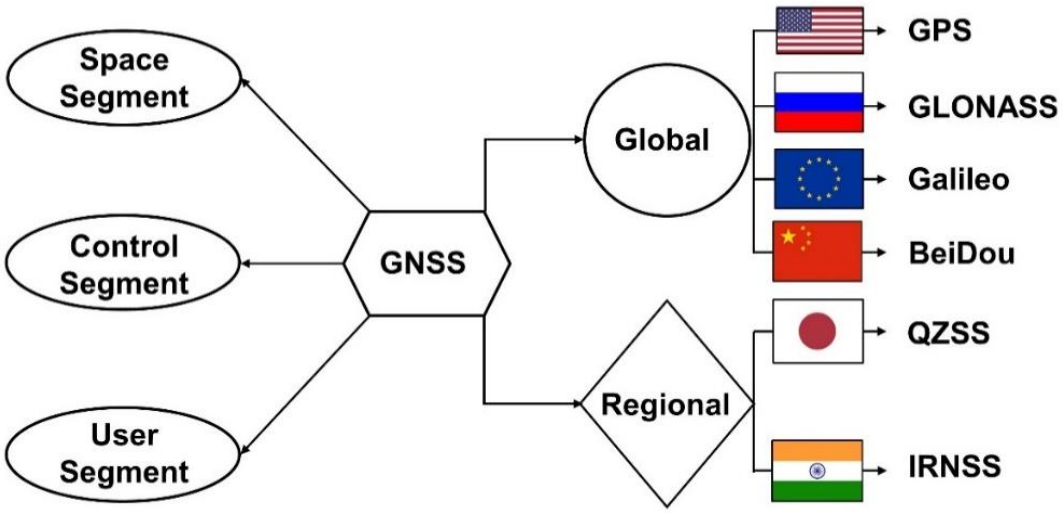

Figure 5.6: GNSS constellation with global and regional coverage as well as space, control, and user segments. The flags, from top to bottom of right-hand side of figure, show the country or region which own the satellite constellation: US, Russia, Europe, China, Japan, and India, respectively.

GNSS is a navigation system based on the use of satellites: a space-based or ground-based infrastructure that can provide positioning solution regardless of user location in the world. GNSS is currently used as a collective term for the Global Positioning System (GPS), Globalnaya Navigatsionnaya Sputnikovaya Sistema (GLONASS), Galileo, and BeiDou systems. Other GNSS constellation with regional coverage are the Quasi-Zenith Satellite System (QZSS) and Indian Regional Navigation Satellite System (IRNSS). Figure 5.6 shows GNSS with global and regional coverage including the different segments: space, control, and user. Refer to *Teunissen and Montenbruck*, [2017] for details. GNSS technology was pioneered in the late 1950s and has since transitioned into a global system providing positioning, navigation, and timing (PNT) solutions. It consists of three components which are referred to as the space segment (constellation of satellites orbiting above the Earth's surface), the control segment (maintains the health of the system), and the user segment (GNSS receivers both civil and military). The system uses a coded satellite signal sent to a space-based or ground-based electronic receiver to accurately determine position (e.g. latitude, longitude, and altitude or X, Y, and Z in the ECEF reference frame) velocity, and time [*Oxford Economics, 2012*].

Furthermore, the satellite navigation industry is broken into the upstream and downstream sector. The upstream sector provides satellite technology while

downstream exploit the technology. For over four decades, GNSS has proved to be an enabling technology with applications in almost every area of life and providing significant economic and social benefits to the users of the technology worldwide. At present, there are three fully operational GNSS. They are GPS designed and operated by the United States, GLONASS designed and operated by the Russian Federation, and BeiDou designed and operated by China. Galileo (Europe) is to be fully operational in 2020 [*Someswar et al., 2013*]. GNSS operates within the L-band ($1 - 2\ GHz$) frequency range. The choice of L-band for GNSS signals was due to the following reasons:

a) Frequency is required to be below $2\ GHz$ because frequency above $2\ GHz$ will normally require a directional or beam antenna for signal reception.
b) Ionospheric delays are significant for RF signals less than $1\ GHz$ and greater than $10\ GHz$.
c) The Pseudorandom Noise (PRN) codes require a wide bandwidth for code modulation on the carrier frequency signal.
d) L-band frequencies do not suffer attenuation in the atmosphere due to rain, snow, or cloud.
e) Allows for simple and reasonable antenna size.

Generally, GNSS signals allow measurements of three basic observables namely: pseudorange, carrier phase, and Doppler. These observables allow for calculation of position, velocity, and time (PVT).

GNSS signals, pseudorange and carrier phase, are given by equations (5.1) and (5.2), respectively

$$P_r^s = \rho_r^s + c(dt_r - dt^s) + T_r^s + I_r^s + e_r^s \ [m] \qquad (5.1)$$

where $dt_r \ and \ dt^s$ are the receiver and satellite clock offset, T_r^s is the tropospheric propagation delay, I_r^s is the ionospheric propagation delay, ρ_r^s is the measured range between satellite and receiver, e_r^s stands for the unmodelled errors including receiver noise, multipath, and other small effects [*Teunissen and Montenbruck, 2017*].

Furthermore, the carrier phase equation is similar to the pseudorange equation, expressed as

$$\varphi_r^s = \rho_r^s + c(dt_r - dt^s) + T_r^s - I_r^s + \lambda M_r^s + \epsilon_r^s \ [m] \quad (5.2)$$

where λ is the carrier wavelength, $M_r^s = N_r^s + \delta_r - \delta^s$ is the sum of the integer carrier phase ambiguity N_r^s (cycles) and the instrumental receiver and satellite phase delay $\delta_r - \delta^s$ (cycles), ϵ_r^s stands for unmodelled phase errors including receiver noise, multipath, and other small effects. The magnitude of the ionospheric terms in equations (5.1) and (5.2) is the same but of a different sign. This is because the phase of the carrier signal is advanced during transionospheric propagation, as opposed to pseudorange, which suffers phase delay [*Teunissen and Montenbruck, 2017*].

To achieve GNSS performance requirements in terms of accuracy, integrity, availability, and continuity in safety-critical applications such as civil aviation, augmentation systems are designed and implemented. They are Satellite-Based Augmentation System (SBAS), Aircraft-Based Augmentation System (ABAS), and Ground-Based Augmentation System (GBAS) [*ICAO, 2012; ICAO Doc 9849, 2012*]. The following are examples of SBAS:

a) Wide Area Augmentation System (WAAS, USA).
b) European Geostationary Navigation Overlay Service (EGNOS, European Union).
c) MTSAT Satellite Augmentation System (MSAS, Japan). MTSAT stands for Multi-functional Transport SATellites.
d) GPS Aided Geo Augmented Navigation (GAGAN, India).
e) System for Differential Correction and Monitoring (SDCM, Russia).
f) Satellite Navigation Augmentation System (SNAS, China).
g) Nigerian Satellite Augmentation System (NSAS, Nigeria) with PRN code 147 [*Lasisi, 2018; Lawal et al., 2018*].

Whereas example of ABAS is the Receiver Autonomous Integrity Monitoring (RAIM) and GBAS is the Local Area Augmentation System (LAAS) as indicated in Figure 5.7. The name denotes where the main system is located. Currently, these augmentation systems have regional coverage and are associated with regions such as America, Europe, Japan, India, Russia, and China.

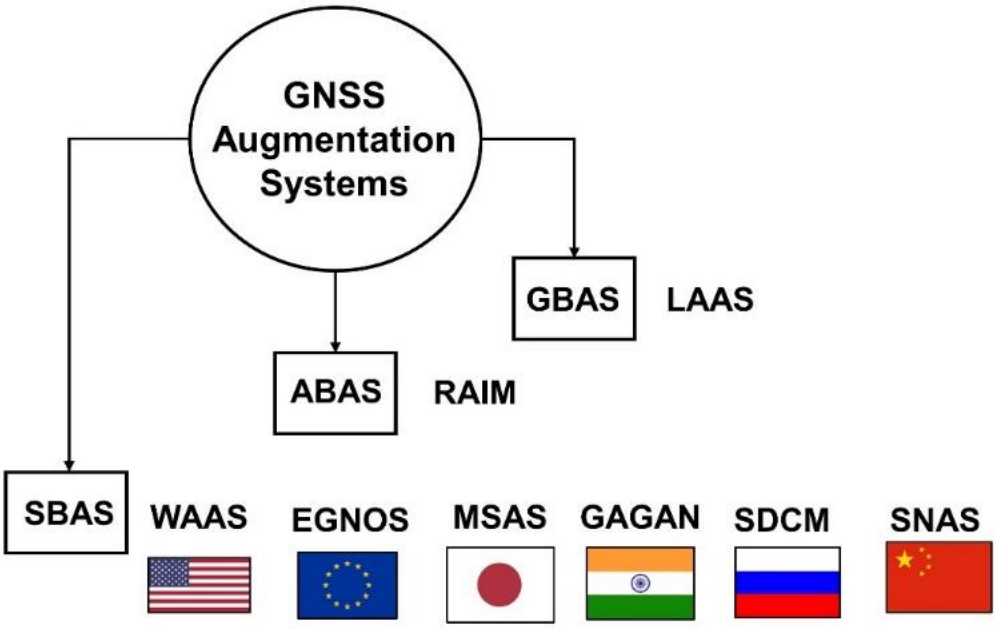

Figure 5.7: GNSS augmentation systems and their examples indicating the country (see flag) of ownership.

5.3.1 GPS

GPS is the first GNSS launched in the late 1970s with full operational capability in June 1995. It uses a constellation between 24 and 32 satellites positioned in six earth-centred orbital planes having four satellites and a spare satellite slot in each plane with an orbital radius of $26559\,km$ [*Jeffery, 2010; Teunissen and Montenbruck, 2017*], Figure 5.8. Spare satellites are placed in locations adjacent to the satellites closed to their end of life (expected to be replaced). Whenever a GPS satellite has reached its end of life, its navigation signals are switched off and is disposed at an altitude of around $500\,km$ higher than its altitude. The satellites' orbits are inclined 56° to the equatorial plane. GPS coding scheme is Code Division Multiple Access (CDMA) to multiplex several satellites signals onto the same frequency and the modulation technique is Binary Phase Shift Keying (BPSK). The concept of CDMA is to assign to each satellite a PRN code that modulates the transmitted signal. While BPSK is a two-phase modulation where the binary states (0's and 1's) in a message are represented by two phase states. GPS frequencies of operation are L1 ($1575.42\,MHz$), L2 ($1227.60\,MHz$), and L5 ($1176.45\,MHz$). GPS provides two positioning services, which are the Precise Positioning Service (PPS) utilising both L1 and L2 carrier phase signals and the Standard Positioning Service

(SPS) utilising only L1 carrier phase signal. There are other frequencies that are not mentioned here. GPS provides military and civil services. GPS is a Medium Earth Orbit (MEO) satellite with an orbital height of about $20180\ km$ at a speed of $3.9\ km/s$ and an orbital period of about 11 hours 58 minutes on average.

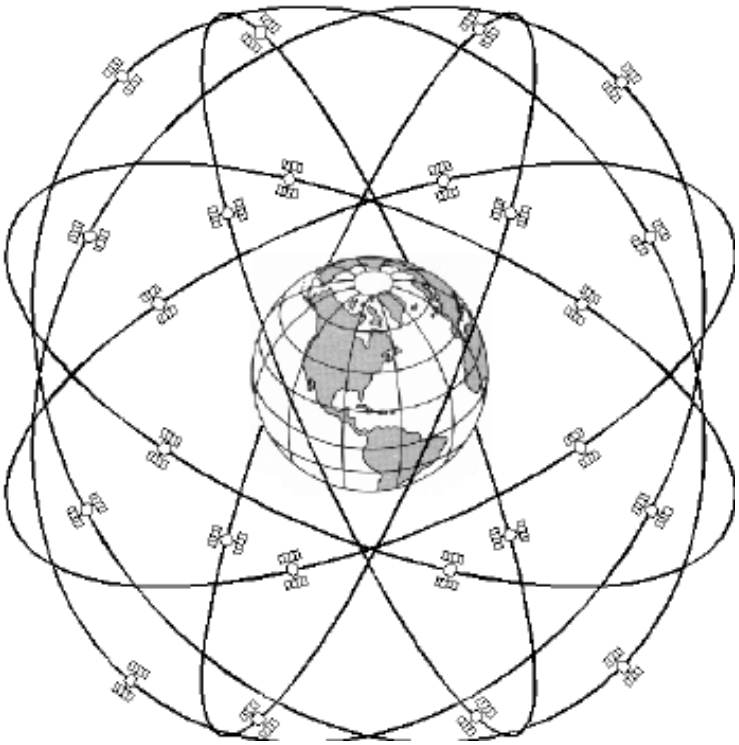

Figure 5.8: GPS constellation [*Rizos, 2003*].

5.3.2 GLONASS

The first GLONASS satellite was launched in 1982 and operated a full constellation of 24 satellites in 1996. However, the full constellation of 24 satellites was short-lived but later gained full operational capability in December 2011 [*Teunissen and Montenbruck, 2017*]. GLONASS full constellation consists of 24 satellites [Jeffery, 2010] in three orbital planes inclined at 64.8° with eight satellites in each orbital plane as indicated in Figure 5.9. The coding scheme is Frequency Division Multiple Access (FDMA). In FDMA, all users transmit and receive at different frequency but share the same frequency channel. GLONASS uses BPSK modulation technique. It has an altitude of about $19140\ km$ and an orbital period of 11 hours 15 minutes on average. Frequencies are G1 ($1593\ MHz - 1610\ MHz$), G2 ($1237\ MHz - 1254\ MHz$), and G3 ($1207.14\ MHz$). Applications are for military and civil purposes. A typical MEO satellite system. GLONASS is categorised into three generations

which are (a) first-generation GLONASS I/II (started in 1982), (b) second-generation GLONASS-M (started in 2003), and (c) third-generation GLONASS-K (started in 2011). GLONASS-K satellites, apart from FDMA coding scheme, include CDMA as well as the latest GLONASS-M satellites, which also transmit a CDMA signal [*Teunissen and Montenbruck, 2017*].

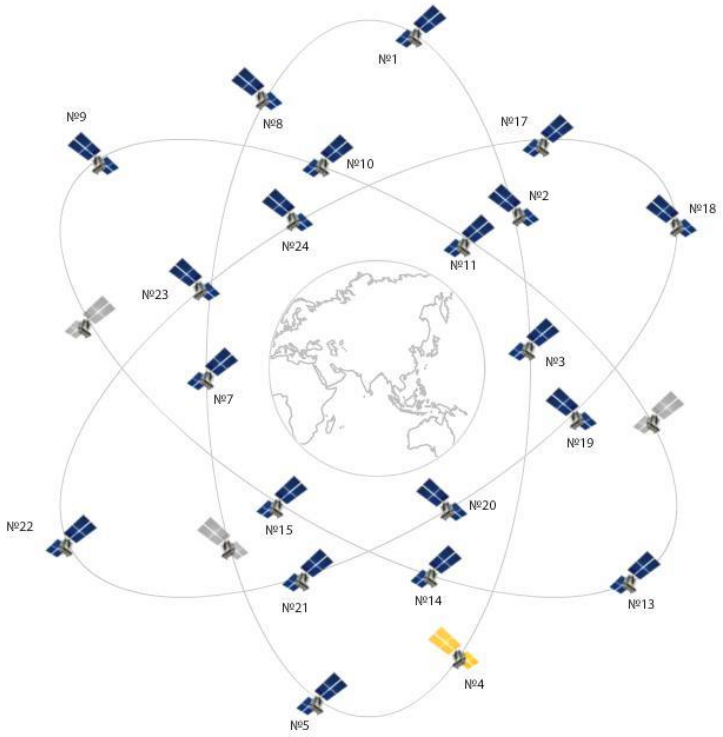

Figure 5.9: Shows GLONASS constellation.
Source: https://gssc.esa.int/navipedia/index.php/GLONASS_Space_Segment

5.3.3 Galileo

Galileo is a joint project between the European Union (EU) and the European Space Agency (ESA) [*Teunissen and Montenbruck, 2017*]. It is the first satellite navigation system designed to meet civil and commercial purposes [*Oxford Economics, 2012*] launched in 2011. It will consist of 30 satellites and 3 orbital planes inclined at 56° with 10 satellites in each orbital plane as shown in Figure 5.10. Out of the 30 satellites, 24 are designated as primary while 6 are spares. The coding scheme is CDMA. Galileo uses Binary Offset Carrier (BOC) modulation technique. Galileo RF signals are E1 ($1575.42\ MHz$), E5a ($1176.45\ MHz$), E5b ($1207.14\ MHz$), and E6 ($1278.75\ MHz$). Galileo is a MEO satellite with an orbital height of about $23222\ km$ and an orbital period of about 11 hours 22 minutes on average. Galileo satellites are

deorbited after they have reached their end of life. The satellites are moved to a graveyard orbit that is at least $300\,km$ higher than their nominal orbital altitude [*Teunissen and Montenbruck, 2017*]. Galileo is projected to provide a global coverage by 2020. However, the system is yet to have a global coverage.

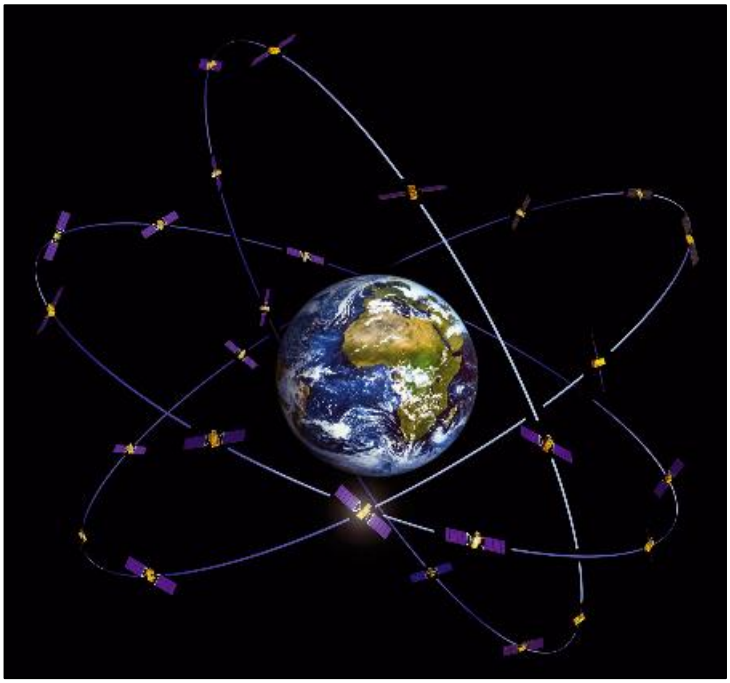

Figure 5.10: Shows Galileo constellation.
Source: https://gssc.esa.int/navipedia/index.php/Galileo_Space_Segment

5.3.4 BeiDou

China began with a demonstration regional satellite-based navigation system called BeiDou following a research and development satellite technology programme that started in 1980. Its English name used in the system's official filing to the International Telecommunication Union (ITU) is COMPASS. BeiDou consists of 35 satellites, which include 5 geostationary orbits (GEO), and 30 non-GSO satellites; 27 in Medium Earth Orbit (MEO) and 3 in Inclined Geosynchronous Orbit (IGSO) with an orbital inclination of 55° as indicated in Figure 5.11. Regional coverage was achieved in 2010 [*Jeffery, 2010*]. BeiDou uses CDMA coding scheme. It utilises the Quadrature Phase Shift Keying (QPSK) modulation type. Its RF signals are B1 ($1561.10\,MHz$), B2 ($1207.14\,MHz$), and B3 ($1268.52\,MHz$). BeiDou is operated by the Chinese National Space Agency (CNSA) and launched in 2000. It provides military and commercial services. Unlike GPS, GLONASS, and Galileo launched in MEO, BeiDou-1 uses Geostationary Earth Orbit (GEO). The satellites have a

lifespan of eight years. BeiDou-2 consists of 27 satellites in MEO and 3 in inclined GEO. BDS-3 required to complete full operational capability (FOC) with a global coverage was launched on 23 June 2020 (http://en.beidou.gov.cn/). BeiDou orbits the Earth at an altitude of $21528\ km$ at an orbital period of 12 hours 53 minutes.

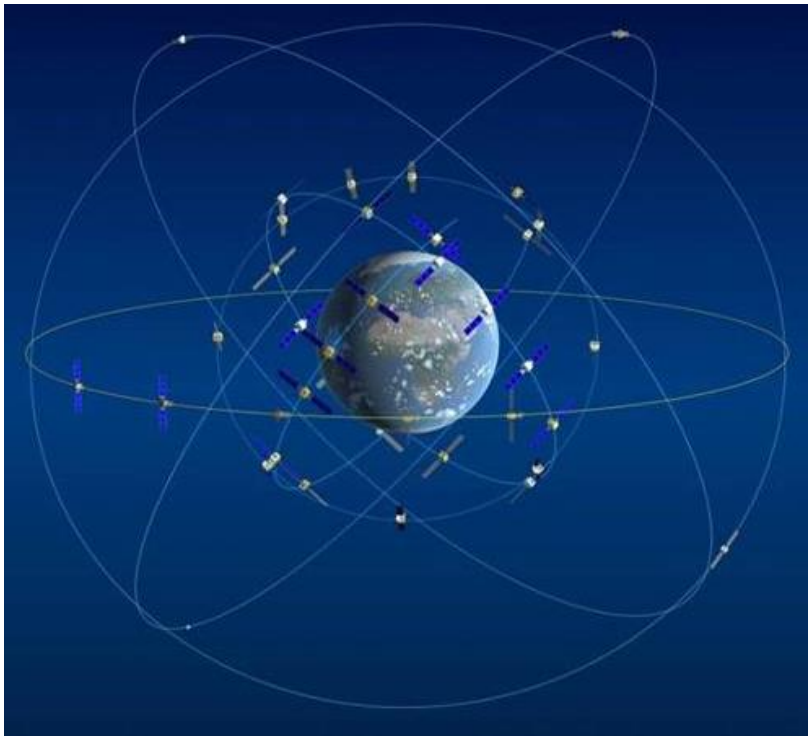

Figure 5.11: Shows BeiDou constellation.
Source: https://gssc.esa.int/navipedia/index.php/BeiDou_Space_Segment

5.4 GNSS Receivers

GNSS receivers using multi-constellation (GPS, GLONASS, Galileo, BeiDou, etc.) are used in different applications. A GNSS receiver is L-band radio signal processor capable of solving the navigation equations to determine user position, velocity, and time (PVT) through the processing of the signals provided by GNSS satellites. The earliest single constellation satellite receiver in this category is the GPS receiver, which according to the GNSS Market Report, Issue 3; made available by European GNSS Agency estimated the number of GPS enabled devices in 2012 to around 2 billion. GNSS receivers can provide navigation solution (PVT) through a calculation of their distances to a set of satellites. For this to happen, the satellite signal must be acquired and tracked. The functional units in the GNSS receiver that perform these tasks are the antenna, the RF front-end, and the baseband signal processing [*Borre et al., 2007; Teunissen and Montenbruck, 2017*]. In modern GNSS receivers,

the RF unit is the most critical because it determines the size, power, and cost of the entire device [*Teunissen and Montenbruck, 2017*]. These receivers can be located on-board or on the ground surface depending on application. To provide a user position, the GNSS signal (navigation) must be acquired and tracked. The navigation message consists of the following parameters:

a) Ephemeris to calculate satellite coordinates
b) Time and clock corrections
c) Service with satellite health
d) Ionospheric model for single frequency receivers
e) Almanac to calculate satellites position

Based on this research, only geodetic and scintillation GNSS receivers are considered.

5.4.1 Geodetic GNSS Receivers (Courtesy of IGS)

Geodetic GNSS receivers are GNSS receivers operated and maintained by several organisations around the world whose data are made available to the public courtesy of IGS. The GNSS receivers are permanently installed which have the advantage of monitoring changes in the position of the station. GNSS data, for example, observation and navigation, can be downloaded before, during, and after geophysical events. This can provide scientists and researchers data to study the Earth and atmospheric processes. A list of permanent and continuously operating geodetic GNSS receiver stations courtesy of IGS is presented in Figure 5.12. This research utilises GNSS data from permanent geodetic GNSS receiver stations courtesy of IGS located at, for example, Kiruna (KIRU: 67.86° N, 20.97° E), Tromsø (TRO1: 69.66° N, 18.94° E), Ny-Ålesund (NYA1: 78.93° N, 11.87° E), and Ny-Ålesund (NYA2: 78.93° N, 11.86° E).

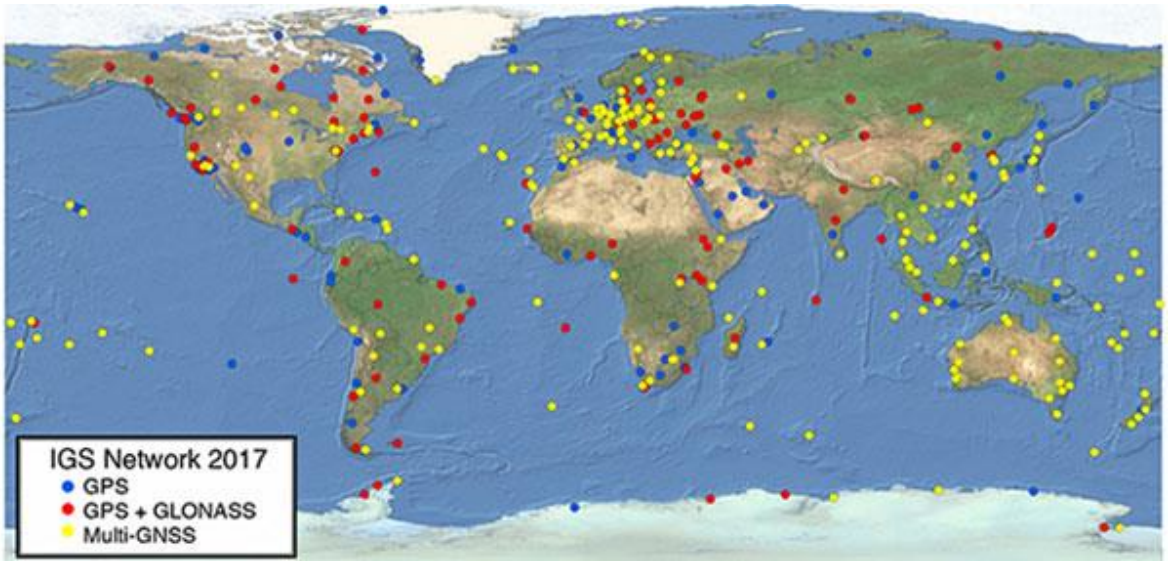

Figure 5.12: List of permanent and continuously operating GNSS receivers indicating GPS only (blue dots), GPS + GLONASS (red dots), and multi-GNSS (yellow dots) from IGS network in 2017.
Source: https://www.gpsworld.com/the-international-gnss-service-25-years-on-the-path-to-multi-gnss/

Depending on the geodetic GNSS receiver (30-s or 1-s), the data can be stored as RINEX observation (RINEX version 2.11, 3.01, 3.02, 3.03 etc.). The type of receiver used in this work is multi-frequency and multi-constellation. However, for the benefit of this report, only GPS constellation was considered. RINEX 2.11 allows the measurements of carrier phase, pseudorange, and signal strength (or raw SNR) observables [*Pestana, 2015*]. The positioning mode (RTK or PPP) informs the type of orbit and clock source (navigation or SP3 file) to be used alongside ANTEX file. From the navigation file, position, velocity, and clock information of satellites in ECEF reference frame are obtained. SP3 file provides, satellites position (X, Y, and Z) as well as the clock information in terms of ECEF reference frame. In this report, TEC (in units of TECU) is calculated from GPS L1 and L2 carrier phases from which instantaneous (epoch by epoch) TEC fluctuations ($TECU/\Delta t$, e.g. $TECU/30\,s$ or $TECU/s$) were computed. Where Δt is in seconds. See Chapter 4 for details. The presence of large-scale irregularities can be inferred from fluctuations in TEC. How ionospheric irregularities impact on GNSS positioning performance is stated in this chapter under software (gLAB).

5.4.2 GSV4004B GPS Ionospheric Scintillation and TEC Monitor

The GPS Silicon Valley's GPS Ionospheric Scintillation and TEC Monitor (GISTM) system model GSV4004B consists of L1/L2 GPS antenna (NovAtel's Model 532, 533 or GPS702), a GPS receiver (NovAtel's EuroPak-3M), and a power supply with several interconnecting cables. The GPS receiver, with firmware, can track up to 11 GPS signals at L1 and L2 frequencies. For each satellite tracked on L1, the receiver can measure phase and amplitude (at $20-\mathrm{ms}$) and code/carrier divergence (at $1-s$) and calculates TEC from combined L1 and L2 pseudorange and carrier phase measurements. Channels 11 and 12th are configured as SBAS satellites tracking channels, and to measure a noise floor for carrier-to-noise ratio (C/N_0) and amplitude scintillation index (S_4) correction. Figure 5.13 shows GSV4004B scintillation receiver. Details of GSV4004B scintillation receiver are available online (http://indico.ictp.it/event/a08148/session/90/contribution/56/material/0/0.pdf).

Figure 5.13: GSV4004B GPS ionospheric scintillation and TEC monitor courtesy of NovAtel.
Source:
http://indico.ictp.it/event/a08148/session/90/contribution/56/material/0/0.pdf

Through GNSS scintillation receivers, scintillation indices (S_4 and σ_ϕ) are derived from 50-Hz measurements. By means of these indices, the presence of small-scale irregularities can be inferred. But as at the time of writing, scintillation data was not used owing to reasons explained later in section 5.10.

5.5 IMAGE Magnetomer Network

IMAGE consists of 81 magnetometer observatories maintained by 8 institutes in Germany, Norway, Russia, Sweden, Poland, and Finland. The main objective of the IMAGE magnetometer network is to study auroral electrojets and moving current systems (2-D). The stations are located from geographic latitude 51° to 79° to observe and study auroral electrojets. Combined with other ground-based space science instrumentations, IMAGE provides a critical part in the investigation of the physics of high-latitude magnetosphere-ionosphere interactions. IMAGE data can support the study of local geomagnetic activity in the high-latitudes ionosphere (https://space.fmi.fi/image/www/index.php?#). Figure 5.14 shows the spatial distribution of IMAGE magnetometer observatories in 2018 courtesy of the IMAGE magnetometer network (https://space.fmi.fi/image/www/index.php?page=maps).

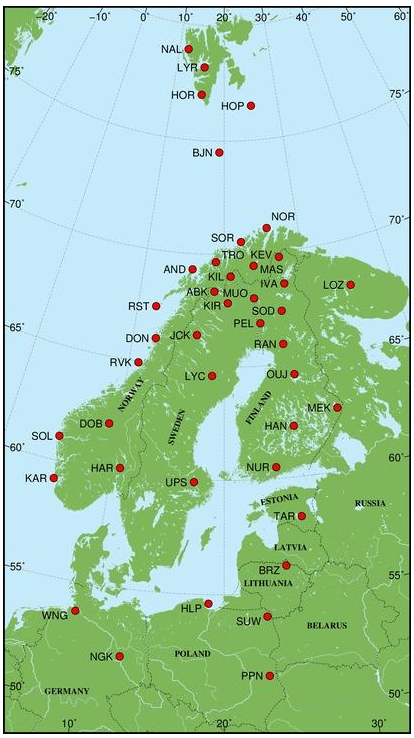

Figure 5.14: A geographic map that shows IMAGE Magnetomer observatories courtesy of IMAGE.

The IMAGE magnetometer measures temporal variations of local geographic components of a station in terms of (X, Y, and Z (nT)). Magnetograms measured in X, Y, and Z components are then converted to temporal variations of local geomagnetic components in terms of H, D, and Z (nT). In the high-latitudes ionosphere, ionospheric activity is influenced by geomagnetic activity. This geomagnetic activity can be characterised by means of measurements from IMAGE

magnetometer stations. The H, D, and Z components provide understanding of the local strength and direction of the geomagnetic field. For example, negative H component (southward) indicates auroral substorm onset which is correlated with particle precipitation in the E layer [*Forte et al., 2017*]. Particle precipitation is often regarded as a mechanism originating auroral and or polar structures observed by means of EISCAT UHF/ESR, respectively.

5.6 SuperDARN

Figure 5.15: Shows SuperDARN HF radar located at Japan. Courtesy of NIPR, Japan.
Source: http://polaris.nipr.ac.jp/~SD/sdjapan/

Figure 5.15 shows a typical antenna structure of SuperDARN HF radar located in Japan as one of the stations of the SuperDARN network courtesy of NIPR. SuperDARN consists of over 30 low-power HF radars to monitor the upper atmosphere between the middle and polar latitudes. The radars operate continuously and observe plasma convection in the ionosphere. SuperDARN operates between $8\,MHz$ and $22\,MHz$ at a peak power of $9.6\,kW$. In standard operating mode, each radar scans through 16 beams covering 52° in azimuth over $3000\,km$ in range. Each beam is divided into 75 range gates each $45\,km$ in distance. SuperDARN pulse range is between 100 and 300 microseconds while the range resolution is between $15\,km$ and $45\,km$. The primary targets of the radar beams are field-aligned plasma density irregularities in the E and F layers of the ionosphere. The plasma density irregularities spatially diffuse along magnetic field lines. The knowledge gain from this network of radars can provide insight into SW hazards including radiation exposures for space vehicles and travellers, disruptions to communications, navigation, and positioning infrastructure. Figure 5.16 shows a list of SuperDARN Northern Hemisphere HF radars operating at middle latitudes (pink),

high-latitudes (blue), and the polar cap (green) courtesy of VirginiaTech. Apart from the Northern Hemisphere, SuperDARN also has facilities in the Southern Hemisphere. SuperDARN can be used to study middle and auroral latitude irregularities [*Nishitani et al., 2019*]. Details of SuperDARN can be obtained online through the website http://vt.superdarn.org/tiki-index.php.

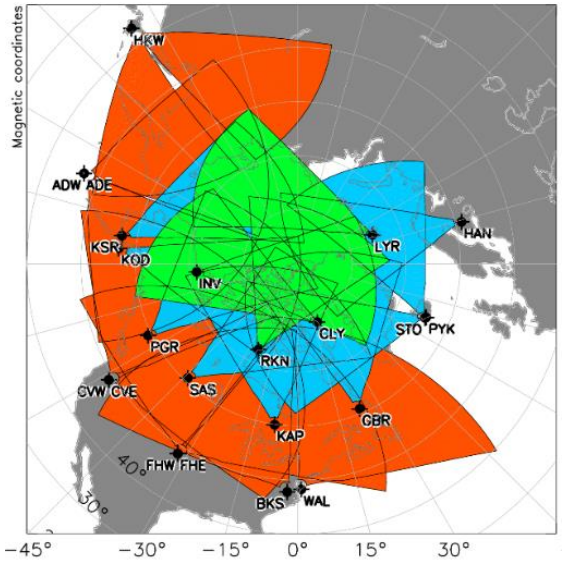

Figure 5.16: Shows SuperDARN northern hemisphere HF radars operating in the middle latitudes (pink), high-latitudes (blue), and the polar cap (green) Courtesy of VirginiaTech.
Source: http://vt.superdarn.org/tiki-index.php?page=Radar+Overview

SuperDARN HF radars located in the Northern Hemisphere are used to study the presence of auroral and polar E and F layer irregularities. Electric potential pattern measured in terms of azimuth and elevation angles can be used to infer the presence of ionospheric convection over a particular station at the high-latitudes region. In this work, SuperDARN measurements were used to identify the presence and direction of ionospheric convection in the auroral and polar ionospheres. The expansion or contraction of auroral oval owing to ionospheric convection can be deduced from SuperDARN. These measurements are used to interpret and validate EISCAT UHF/ESR measurements and likewise the ionospheric mechanism inducing the observed ionisation structures can be inferred.

5.7 ASC

A typical ASC is an optical imager with a transparent hemispherical dome mounted on a rooftop or on an unobscured platform for an unhindered wide view of the

ionosphere as shown in Figure 5.17. Its images are used to study auroral activity in the high-latitudes region due to majorly atomic or molecular oxygen optical emissions. The optical colour obtained depends on the wavelength of the particle in the high-latitude ionosphere. At above $95\ km$ altitude nitrogen emission at $427.8\ nm$ (blue-violet) is recorded. Oxygen emission at $557.7\ nm$ (green) above $100\ km$ altitude can be recorded. While above $200\ km$ altitude, oxygen emission at $630\ nm$ (red) is recorded. Auroral signatures, for example, auroral arcs, auroral inverted-V, diffuse aurora, omega bands, westward travelling surge, ovals, pulsating auroras, black auroras, and substorm onset can be monitored and recorded [*DASI2*]. The geographical locations of ASCs courtesy of MIRACLE are shown in Figure 5.18.

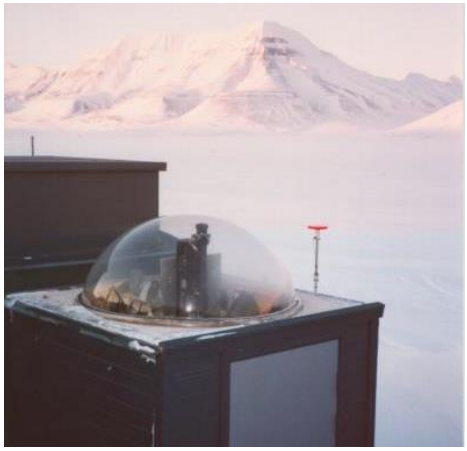

Figure 5.17: All-Sky Camera (ASC) courtesy of Magnetometers Ionospheric Radars All-sky Cameras Large Experiment (MIRACLE).
Source: https://space.fmi.fi/MIRACLE/ASC/?page=stations

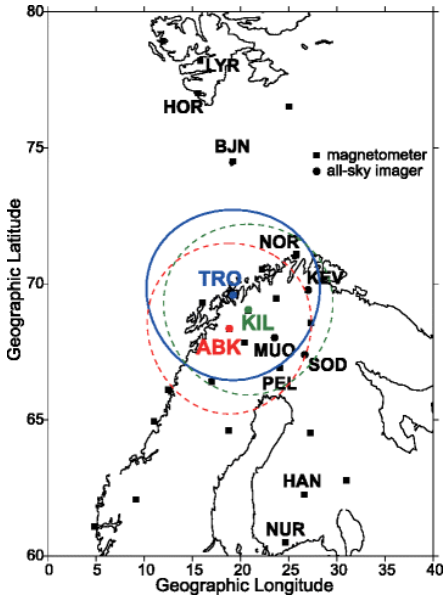

Figure 5.18: Geographical locations of ASCs stations in terms of latitude and longitude with Tromsø (TRO: blue circle) and their corresponding circular area. [*Tanaka et al., 2015*].

ASCs are used at high-latitudes for imaging the Northern and Southern Lights. At $110\ km$ altitude, one ASC extends to a circular area of diameter at about $600\ km$ on average (http://www.space.fmi.fi/MIRACLE/ASC/). Coupling of the magnetosphere-ionosphere results in the precipitation of energetic electron particles into the region. These particles collide with the ionospheric constituents thereby losing energy in the form of heat. The energy lost results into excitation and ionisation of plasma particles thereby emitting lights of varying colours and complexity. For this experiment, ASC images were obtained from Tromsø, Norway observatory to further interpret and validate EISCAT profiles of electron density with TEC fluctuations in the regions under investigation. The orientation of ASC axes at Tromsø are north (up), south (down), east (left), and west (right). The ASC can provide information on the morphology and dynamic of the auroral and polar ionosphere originating from particles precipitation.

A keogram is produced from ASC images. Keograms are important images used to evaluate aurora activity, especially in the high-latitude ionosphere. The name keograms may sometimes mean aurora borealis or Northern Lights [*FMI All-Sky Camera*]. Data used to generate keograms are from vertical pixels' columns of individual ASC images. They are produced by taking north-south vertical columns of ASC images and placing the columns side-by-side. The horizontal axis is the time (UT) whereas the vertical axis is the geographical/geomagnetic latitude/longitude. This is another method of investigating the electrodynamics of the high-latitudes region.

Auroral and polar activity can be investigated by means of ASC images (or keograms). ASCs measure auroral or polar optical emissions caused by ionisation. Green emissions at $557.7\ nm$ above $100\ km$ altitude and $630.0\ nm$ (red emissions) above $200\ km$ latitude occurring at the auroral and polar latitudes, respectively suggest the presence of particle precipitation. ASC images can provide insight into the type of aurora in the region (e.g. arcs or diffuse aurora). Inhomogeneous and intermittent variation of optical emission over high-latitude station observed through keograms in terms of time series of geomagnetic latitude/longitude are indications of particle precipitation mechanism.

5.8 Spirent GPS Simulator (SGS)

SGS was used to obtain azimuth, elevation, and X, Y, and Z coordinates of GPS satellites from a given GNSS receiver stations. The receiver geodetic position is provided in terms of latitude, longitude, and height (these are obtained after transformation from ECEF (X, Y, and Z) coordinates to geodetic coordinates (latitude, longitude, and height). From RINEX observation files, the corresponding GNSS receiver geodetic coordinates (X, Y, and Z) are obtained. SGS utilises the position of a given GNSS receiver in terms of latitude, longitude, and height. GPS ephemerides, date, and time of the satellites positions to be simulated are also required. In this report, EISCAT UHF/ESR experimental campaigns of November 2019 utilised GPS satellites azimuth and elevation data collected from SGS for satellites orbital prediction purpose. The new design geometry of November 2019 campaigns was performed by means of SGS measurements.

5.9 Software

The software used in this research are listed as follows and the details can be found online through the references stated herein:

a) MATLAB (Matrix Laboratory).
   Source: https://uk.mathworks.com/help/matlab/
b) GUISDAP (Grand Unified Incoherent Scatter Design and Analysis Program).
   Source: https://www.eiscat.rl.ac.uk/intro/step-by-step/analysing.html
c) gLAB (GNSS-Lab).
   Source: https://gage.upc.es/gLAB/
   The GNSS positioning tool utilised in this research is gLAB. Based on applications, the positioning solutions utilised were RTK (Broadcast Kinematic, BK) and PPP (Precise Static, PS). BK uses broadcast ephemerides (navigation files) while PS utilises precise products (SP3 and clock) during processing of positioning solution by means of gLAB tool. To assess the performance of GPS positioning in the presence of auroral or polar irregularities, 3-D positioning solution from X, Y, and Z ground stations coordinates were calculated by gLAB. Satellites geometries in terms of Time, Position, and Geometric Dilution of Precision (TDOP, PDOP, GDOP),

respectively were also calculated by gLAB. Time series of 3-D positioning error are used to infer the accuracy and availability performance of GPS positioning at the auroral and polar latitudes.

d) RTKLIB (Real-Time Kinematic Library).
   Source: http://www.rtklib.com/prog/manual_2.4.2.pdf

e) CalSKY (Source: Arnold Barmettler, www.calsky.com).
   CalSKY is an online utility used for assessing the constellation geometry (orbital parameters: azimuth and elevation) of navigation satellites (GNSS). CalSKY supports GPS, GLONASS, and Galileo constellations. This online utility allows proper planning to predict navigation satellites orbital data in terms of azimuth, elevation, and height. It can support the planning of remote sensing flight campaigns or terrestrial surveys.
   Details on CalSKY software utility are available online through the website https://www.calsky.com/cs.cgi/Satellites/12?

5.10 Results of 50-Hz GNSS Phase and SNR Data and Keograms

This section presence the results of 50-Hz GNSS phase observation obtained from both RINEX and Hierarchical Data Format 5 (HDF5) files from JAVAD scintillation receiver. The receiver is own by the German Aerospace Centre, DLR (Deutsches Zentrum für Luft-und Raumfahrt). The receiver is located on geographic coordinate 67.8° N and 20.4° E at the Ionospheric Monitoring and Prediction Centre (IMPC) Kiruna, Sweden. The experimental campaign of March 2018 was designed and conducted using GPS PRNs of relevance. The PRNs ray paths were intersected by EISCAT beams at $350\ km$, $250\ km$, and $150\ km$ shell heights between 20:00 and 24:00 UT corresponding to night-time because ionospheric irregularities have a high probability of occurrence at the high-latitudes. For the benefit of this investigation, more GPS PRNs (8, 10, and 20) located in the proximity of PRNs of relevance were considered as indicated in Figure 5.19.

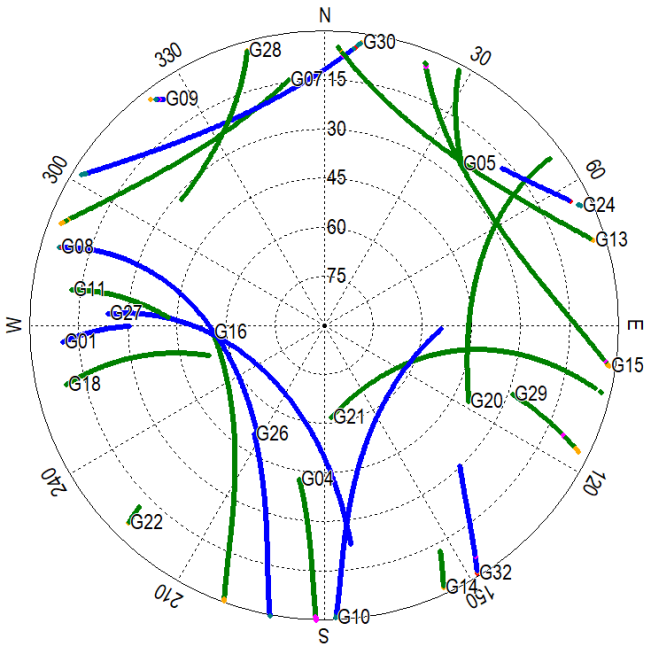

Figure 5.19: GPS PRNs orbital trajectory from azimuth and elevation data over Kiruna geodetic GNSS receiver station located at the centre between 20:00 and 24:00 UT on 15 March 2018 from 30-s RINEX observation and navigation data courtesy of RTKLIB. The visible GPS PRNs represented by solid green line have L1C/A, L1P, and L2P signals while PRNs represented by solid blue line have L1C/A, L1P, L2P, L2C, and L5 signals.

In addition, the signals obtained from a GNSS data depend on the block a given PRN belongs. PRNs 16 and 21 were launched between 1997 and 2004 and belong to GPS Block IIR (Replenishment). Block IIR PRNs signals are L1C/A, L1P, and L2P (legacy signals). Whereas PRNs 26 and 27 belong to GPS Block IIF (2010 – 2016) and were launched in 2015 and 2013, respectively. GPS Block IIF (Follow-on) signals are L1C/A, L1P, L2P, L2C, and L5 and the details are obtained online (https://www.gps.gov/systems/gps/space/).

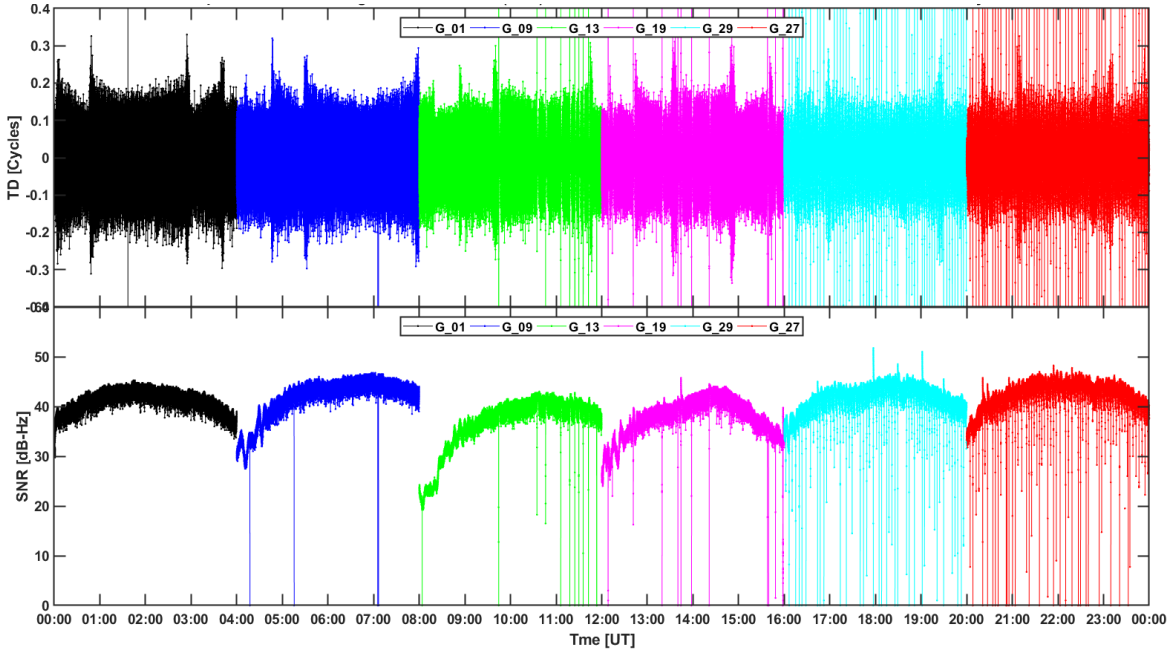

Figure 5.20: From top to bottom shows L1 carrier phase triple difference (TD) and SNR of GPS PRNs 1 (black line), 9 (blue line), 13 (green line), 19 (magenta line), 29 (cyan line), and 27 (red line) 4-hour time of measurements for each PRN obtained from a 50-Hz RINEX observation file between 00:00 and 24:00 UT on 12 March 2018.

Both the 50-Hz HDF5 and RINEX data obtained from the JAVAD receiver were characterised by cycle slips leading to likely data gaps. The multi-instrument experimental campaign (EISCAT/Kiruna experiment) was performed between 20:00 and 24:00 UT for several days in March 2018.

In Figure 5.20, from top to bottom, shows the triple difference (TD) of L1 carrier phase signal and SNR of GPS PRNs 1, 9, 13, 19, 29, and 27 obtained from 50-Hz RINEX observation file between 00:00 and 24:00 UT on 12 March 2018 courtesy of DLR. TD of L1 calculates the difference between adjacent elements of L1 three (3) times. L1 carrier phase is used because L2 carrier phase is more susceptible to interference than L1. If L1 is a matrix of size 10 by 10, then the TD of L1 will be a matrix of size 10 by 7. Here, the 6 PRNs visible for 4 hours between the time of measurements were selected and their corresponding carrier phase triple difference and SNR presented to understand the data quality with respect to the GNSS receiver. The observed spikes commenced at about 1 hour before midday (11:00 UT) on average up to midnight on 12 March 2018. From the National Oceanic and Atmospheric Administration (NOAA) Space Weather Prediction Centre online utility, the K_p index corresponding to this day was between 0 and 1

(ftp://ftp.swpc.noaa.gov/pub/indices/old_indices/). The changes in the values of the K_p index is inconsistent with the spikes. For example, between 00:00 and 03:00 UT ($K_p = 1$) fewer spikes were observed on PRN 1 carrier phase TD and SNR. However, between 21:00 and 24:00 UT ($K_p = 0$) spikes were observed on PRN 27 carrier phase TD and SNR in the entire 3 hours. This suggests the spikes are not caused by external interference. These spikes are indicators of the presence of cycle slips caused by the degradation of the L1 carrier phase signal.

Figure 5.21, from top to bottom, shows the carrier phase triple difference of GPS PRNs 1, 9, 13, 29, and 27 (4-hour time of measurements each PRN) obtained from a 50-Hz RINEX observation data between 00:00 and 24:00 UT on 15 March 2018 at Kiruna courtesy of DLR. The essence was to verify the data quality and to understand the origin of the observed spikes. As indicated in the figure, the spikes appeared throughout the 24-hour time of measurement. In view of this, the possibility that interference in the form of spikes was externally induced by the experiment is essentially ruled out. It can be inferred that the observed cycle slips were possibly caused by noise in the GNSS receiver.

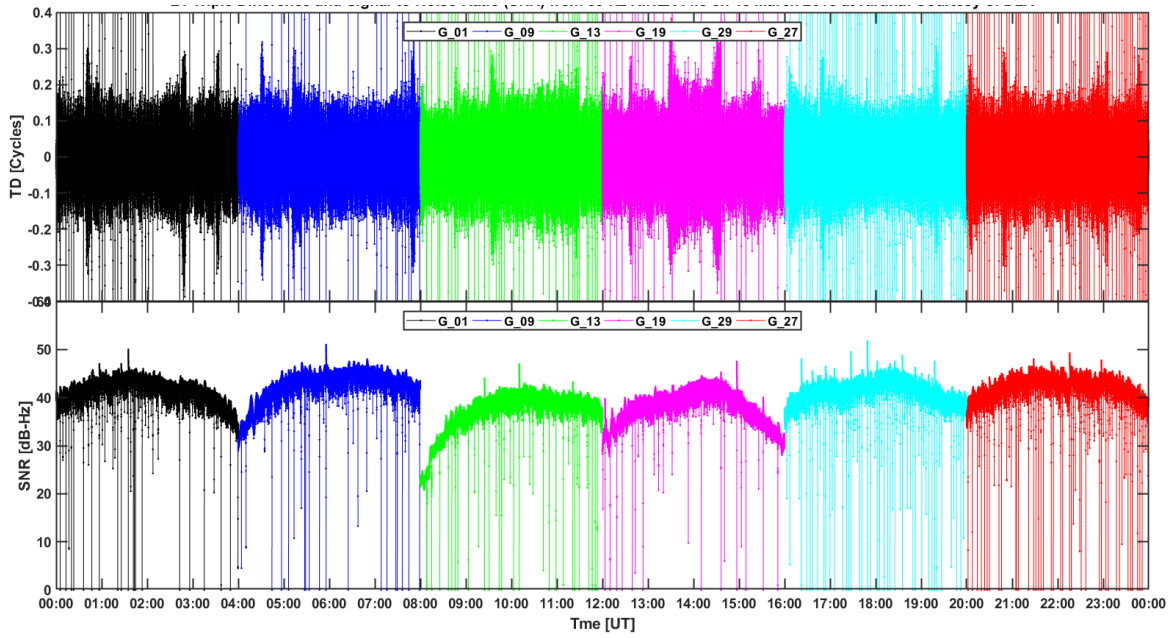

Figure 5.21: From top to bottom shows L1 carrier phase triple difference and SNR of GPS PRNs 1 (black line), 9 (blue line), 13 (green line), 19 (magenta line), 29 (cyan line), and 27 (red line) 4-hour time of measurements for each PRN obtained from 50-Hz RINEX observation file between 00:00 and 24:00 UT on 15 March 2018, respectively.

Figure 5.22 showed the L1 signal strength of GPS PRNs 26, 16, 21, and 27 between 20:00 and 24:00 UT during the 12, 15, 16, 19, and 20 March 2018 experiments from 50-Hz HDF5 files respectively at Kiruna, Sweden. Unlike the results of Figures 5.20 and 5.21, the results of the data analysis obtained from the HDF5 file was only for 4 hours because of the size of the data. The irregular increase and decrease unique patterns observed below 55 dB-Hz and around 5 minutes in Figure 5.22 are spikes due to cycle slips which are random as typical of noise. The spikes were observed on all the selected PRNs throughout the time of observation. However, this is not the case in the 1-s RINEX data (Figure 5.24). Thus, external interference as the possible cause of spikes (cycle slips) in the 50-Hz GNSS data is eliminated and therefore not considered. Further, comparing Figures 5.20 and 5.21, the spikes observed have no spatial and temporal relation in the 2-day measurements. The inconsistency in the spikes observed in the figures removed the possibility of multipath interference near the independent receivers at the same location and time.

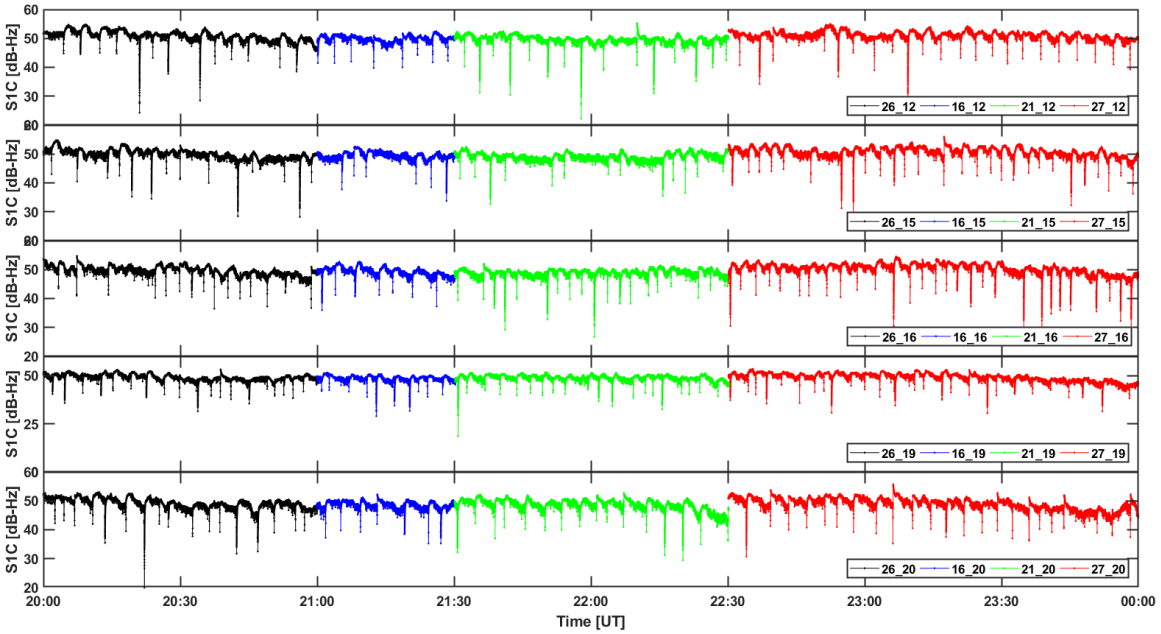

Figure 5.22: From top to bottom shows L1 signal strength of GPS PRNs 26 (20:00 and 21:00 UT, black line), 16 (21:00 and 21:30 UT, blue line), 21 (21:30 and 22:30 UT, green line), and 27 (22:30 and 24:00 UT, red line) obtained from a 50-Hz HDF5 observation file between 00:00 and 24:00 UT on 12, 15, 16, 19, and 20 March 2018, respectively.

Figure 5.23, from top to bottom, shows the L1 triple difference of GPS PRNs 1, 9, 13, 19, 29, and 27 (4-hour time of measurements for each PRN) obtained from 20-ms RINEX observation files on 12, 15, 16, 19, and 20 March 2018 at Kiruna, Sweden courtesy of DLR. In the figures, it can be inferred that the spikes observed in the 5

days showed no day-to-day repeatability. Thus, external interference due to multipath is ruled out as a likely candidate originating the spikes. Similarly, the spikes as indicated in Figure 5.24 did not originate from the ionosphere because of the observed difference between the two results. This further suggests that the spikes were unsynchronised with ionospheric irregularities (such as scintillation events).

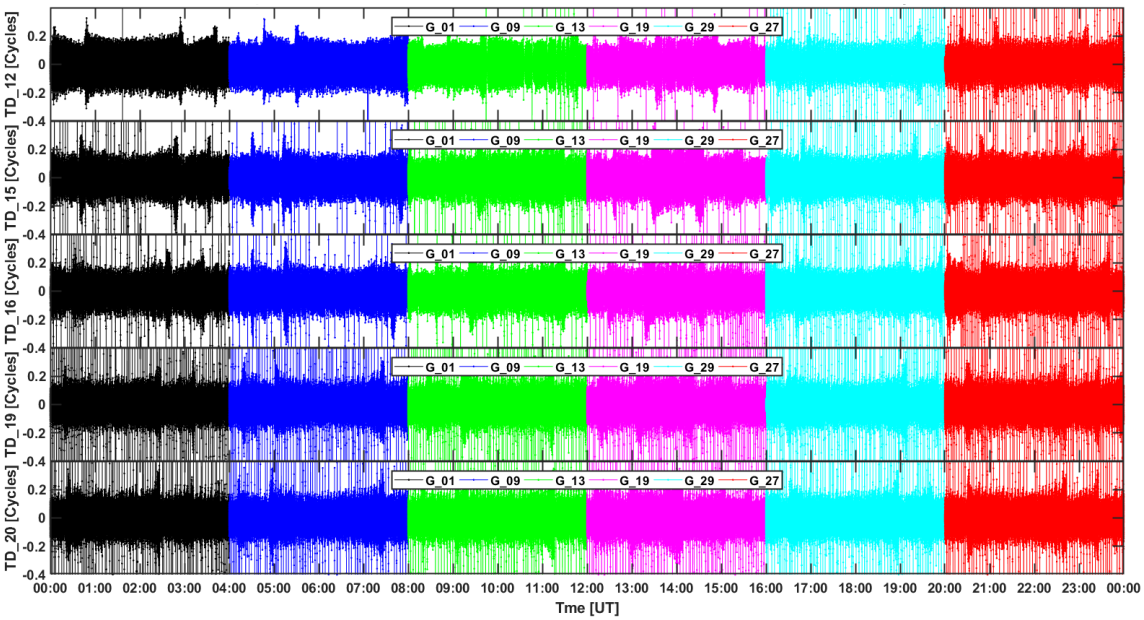

Figure 5.23: From top to bottom shows L1 carrier phase triple difference of GPS PRNs 1 (black line), 9 (blue line), 13 (green line), 19 (magenta line), 29 (cyan line), and 27 (red line) 4-hour observation time each obtained from 50-Hz RINEX observation file between 00:00 and 24:00 UT on 12, 15, 16, 19, and 20 March 2018, respectively.

Figure 5.24, from top to bottom, shows L1 triple difference of GPS PRNs 1, 9, 13, 19, 29, and 27 (4-hour time of measurements for each PRN) obtained from 1-s RINEX observation data between 00:00 and 24:00 UT on 12, 15, 16, 19, and 20 March 2018 at Kiruna at elevation mask of 20°. The observed data gap was caused by the elevation threshold, which removed measurements from PRNs with elevation angle below 20°. One fundamental observation was the observed spikes likely due to cycle slips were fewer compared to the results of Figure 5.23 and there was no day-to-day repeatability in the 5 days. Looking at the results of Figure 5.24, interference originating from external environment is removed when compared to Figure 5.23. Furthermore, the results obtained from Figure 5.24 appeared to have better data quality compared to the results in Figure 5.23. The geodetic GNSS

receiver, Septentrio POLARX4, was a property of ESA/ESOC, which forms part of the IGS network.

The observed spikes in Figures 5.20 - 5.23 obtained from both the 50-Hz RINEX and HDF5 observation data remained when an algorithm was developed to remove the presence of spikes. Further iteration created unnecessary data gaps where significant data points were lost. With this presence of spikes, the data collected from the JAVAD GNSS scintillation receiver located at Kiruna during the time of measurements were unused because of poor data quality. To overcome the challenge, 30-s and 1-s RINEX data were used to calculate, for example, GPS TEC fluctuations (phase fluctuations) as convenient indicators of the likely presence of large-scale irregularities ($10's\ km$ to $100's\ km$) at the auroral and polar latitudes [*Keskinen and Ossakow, 1983*].

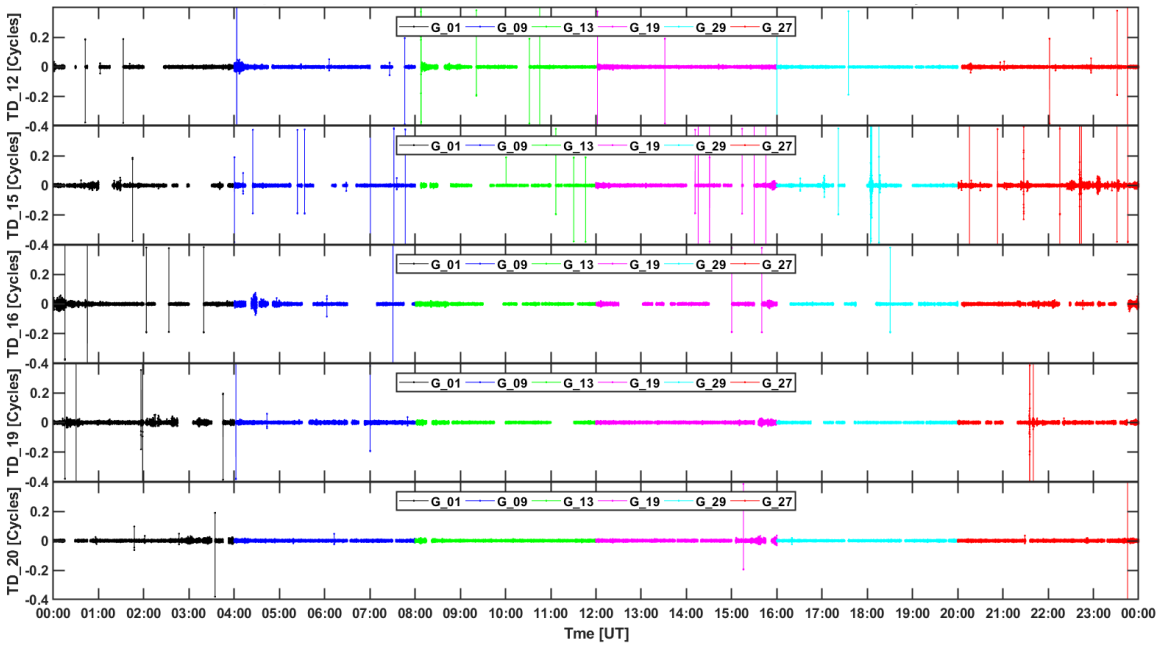

Figure 5.24: From top to bottom shows L1 carrier phase triple difference of GPS PRNs 1 (black line), 9 (blue line), 13 (green line), 19 (magenta line), 29 (cyan line), and 27 (red line) 4-hour observation time each obtained from 1-s RINEX observation file between 00:00 and 24:00 UT on 12, 15, 16, 19, and 20 March 2018, respectively.

Other challenges observed during the March 2018 experimental campaign were the absence of ASC images/keograms from stations of relevance. For example, the ASC data was unavailable from Ny-Ålesund, Norway or the data was available but cloudy as indicated in Figure 5.25. Keograms were used herein as examples since they are normally extracted from ASC images. Figure 5.25, from left to right, shows a time series keograms indicating (a) north-south and (b) east-west geomagnetic

latitude/longitude distribution of aurora from the zenith (Tromsø) between 20:00 and 24:00 UT on 20 March 2018. The data was accessed online courtesy of NIPR.

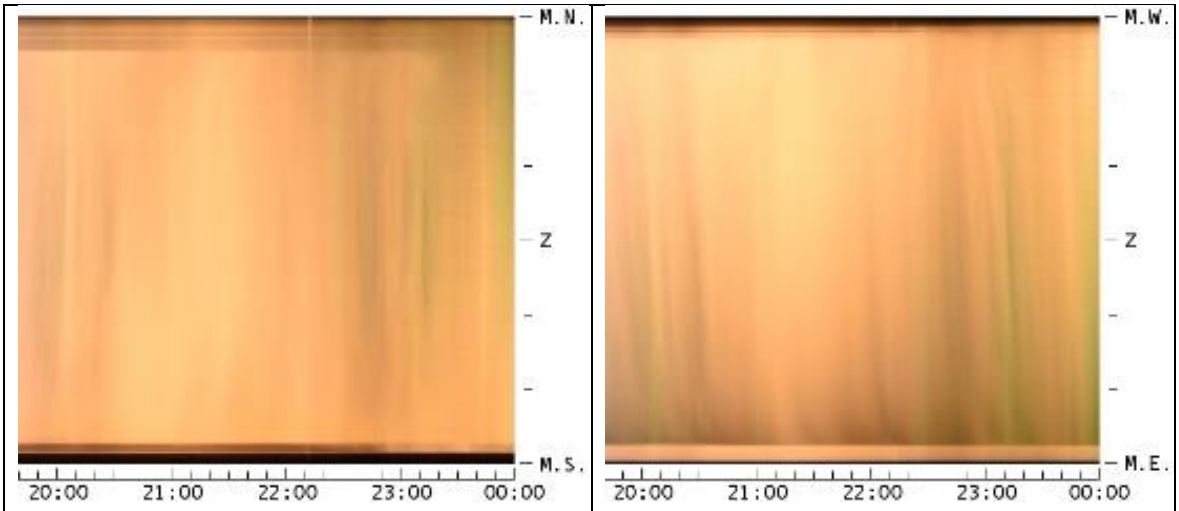

(a) North-south geomagnetic field variations (b) East-west geomagnetic field variations

Figure 5.25: keograms indicating (a) north-south and (b) east-west geomagnetic latitude/longitude distribution of aurora from the zenith (Tromsø) respectively between 20:00 and 24:00 UT on 20 March 2018, respectively courtesy of NIPR, Japan.
Source:
ttp://nordlys.nipr.ac.jp/acaurora/Tromso/html/wrap.php?html=20180319.html

Though scintillation data obtained courtesy of DLR could not be used due to reasons which were inferred to be non-ionospheric, TEC fluctuations were used as a convenient proxy to infer the presence of ionospheric irregularities. TEC fluctuations were calculated from 30-s and 1-s RINEX observation data collected from permanent geodetic GNSS receiver stations courtesy of IGS. Characterisation of ionospheric irregularities at the auroral and polar latitudes using fluctuations in TEC was performed because of the predominance of phase scintillation over amplitude scintillation in the regions. In the event where ASC images could not be used to infer the presence of particle precipitation, keograms and or magnetograms were utilised. Hence, measurements from other ionospheric instruments (apart from the primary instruments – EISCAT UHF/ESR UHF $32\ m$ dish and geodetic GNSS receivers), in this case, ASC, magnetograms, and SuperDARN HF radars were used for the purpose of elucidation and validation of results.

5.11 Summary

This chapter presented ionospheric instrumentations and measurements used in this research. Ionospheric instrumentations discussed here were ISRs (EISCAT, ESR, and IMISR), GNSS/GNSS receivers (geodetic and specialised), IMAGE magnetometers, SuperDARN HF radars, ASC, and SGS, respectively. The measurements collected from each of these instrumentations and the purpose thereof were discussed. Apart from the instrumentations, software used to download data, read, process, and analyse raw ISRs and GNSS data were presented. While using 50-Hz GNSS data from Kiruna location courtesy of DLR as well as Kiruna keograms, specific challenges were observed and reported. For instance, the 50-Hz GNSS data (both RINEX and HDF5 files) were characterised by noise and cycle slips identified in the form of spikes. Quality checks were performed on the data to understand the originating of the observed spikes. The overall results presented in section 5.10 ruled out the ionosphere as the source. Multipath interference was also ruled out because of the absence of day-to-day repeatability of spikes. Hence, it was inferred here that the spikes likely originate from the GNSS receiver. In view of this, the data could not be used but 30-s and 1-s GNSS observables were used instead to quantify the presence of ionospheric irregularities by means of TEC fluctuations.

6 Investigation of GPS Phase Fluctuations originating from Ionospheric Irregularities by means of Incoherent Scatter Radars at the Auroral and Polar Latitudes

6.1 Introduction

This chapter investigates how auroral and polar irregularities originate phase fluctuations on GPS signals during transionospheric propagation by using incoherent scatter radars. As GNSS signal traverses the ionosphere, electron density irregularities can cause fluctuations in its amplitude and phase [*Yeh and Liu, 1982*]. Irregularities are localised random fluctuations in the electron density distribution in the ionosphere. Fluctuations in the amplitude and phase of the received GNSS signal are known as amplitude and phase scintillation [*Aarons, 1982*], respectively. Scintillation activity is largely influenced by the carrier frequency, time of day, the season of a year, location, solar activity, and geomagnetic conditions [*Basu and Basu, 1981; Prikryl et al., 2011*]. A wide network of ground-based GNSS stations courtesy of IGS have been used to measure ionospheric TEC. TEC measurements are integrated over a long distance (at about $20200\ km$) which may include contributions from different regions of the ionised atmosphere [*Forte et al., 2013*]. However, its measurements can provide approximate insight into background ionospheric electron density distribution. Fluctuations in TEC are often used to indicate the presence of irregularities as GNSS signals travel through the ionosphere [*Coker et al., 1995*]. Hence, scintillation and TEC fluctuations on GNSS signals can provide insight into auroral and polar irregularities.

To measure signatures of ionospheric irregularities on GNSS signals propagation, scintillation and temporal fluctuations in TEC are often used as convenient proxies. The intensity and presence of scintillation and TEC fluctuations depend on the ionospheric region. At auroral and polar latitudes, phase fluctuations caused by large-scale irregularities are higher than amplitude fluctuations originating from small-scale irregularities and the intensity thereof is largely controlled by geomagnetic condition [*Forte and Radicella, 2004; Forte et al., 2017; Keskinen and Ossakow, 1983*]. Geomagnetic condition can be inferred by means of K_p value. In

general, the K_p value may suggest a quiet or disturbed geomagnetic conditions. Because the auroral and polar ionospheres are largely influenced by geomagnetic condition, therefore, disturbed geomagnetic conditions are associated with disturbed ionospheric conditions. The presence of irregularities is a consequence of disturbed ionospheric conditions. As GNSS signals propagate in the presence of irregularities, the effects on GNSS receivers are interruptions and degradation of observables. Phase fluctuations can induce phase noise or cycle slips thereby degrading the performance of GNSS services and applications [*Forte et al., 2017; Jiao et al., 2013; Luo et al., 2018; Walter, 2010; Wernik et al., 2003*].

The experiments aimed to investigate the spatial distribution and type of auroral and polar irregularities which originate temporal phase fluctuations on GPS signals, by measuring electron density profiles transverse to GPS ray paths of relevance. This is so because ionospheric irregularities are distributed across the signal paths. In this chapter, temporal phase fluctuations were identified by means of temporal TEC fluctuations which are used herein to deduce the presence and distribution of auroral and polar irregularities.

To measure auroral and polar irregularities, two representative experimental studies involving EISCAT UHF/ESR incoherent scatter radars and surrounding geodetic IGS stations were considered. The design geometry of 2018 campaigns was a follow up on experiments presented in *Forte et al.,* [2013, 2017]. In *Forte et al.,* [2013, 2017], EISCAT UHF ($32\,m$ dish antenna) measurements were collected along the same line of sight with GPS ray paths at a ground receiver located in Tromsø. Thus, the previous experiments provide insight into auroral irregularities signatures. In these experiments (for the first time), EISCAT UHF/ESR beams were directed transverse to GPS ray paths of relevance and alternately intersecting the ionosphere at several shell heights corresponding to E and F layer heights. EISCAT UHF/ESR beams scanning between the E and F layers reveal information on the contribution of irregularities in the layers to the observed temporal TEC fluctuations. EISCAT UHF/ESR electron density profiles measured transverse to GPS ray paths provide insight into the type and distribution of the irregularities whereas GPS observations are used to deduce the spatial scale over which irregularities are distributed.

The results of the experiments provide insight into the type and distribution of the ionisation structures, and the spatial ionospheric distances over which the structures are distributed, using the correlation between electron density profiles and temporal TEC fluctuations. Apart from this, the results also provide insight into the mechanisms originating temporal phase fluctuations on the received GNSS signals.

6.2 Data and Methodology

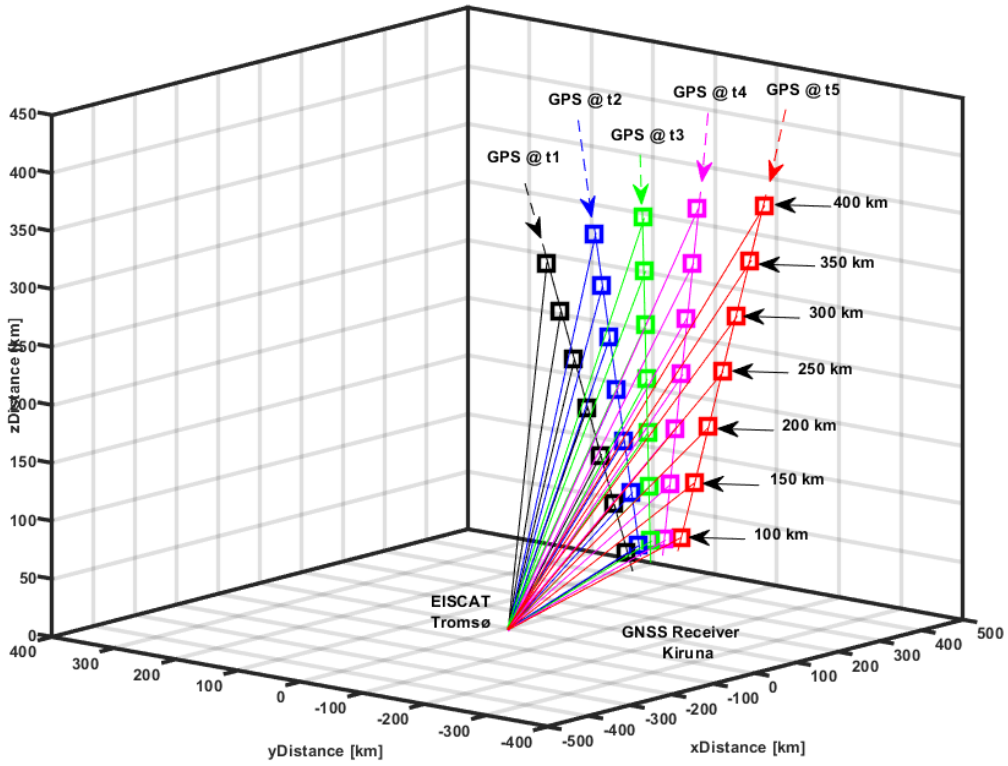

Figure 6.1: 3-D simulation of EISCAT beams scanning and following GPS ray paths (black, blue, green, magenta, and red lines) from t1-t5 at $100\ km$, $150\ km$, $200\ km$, $250\ km$, $300\ km$, $350\ km$, and $400\ km$ ionospheric shell heights over Kiruna on 12 March 2018.

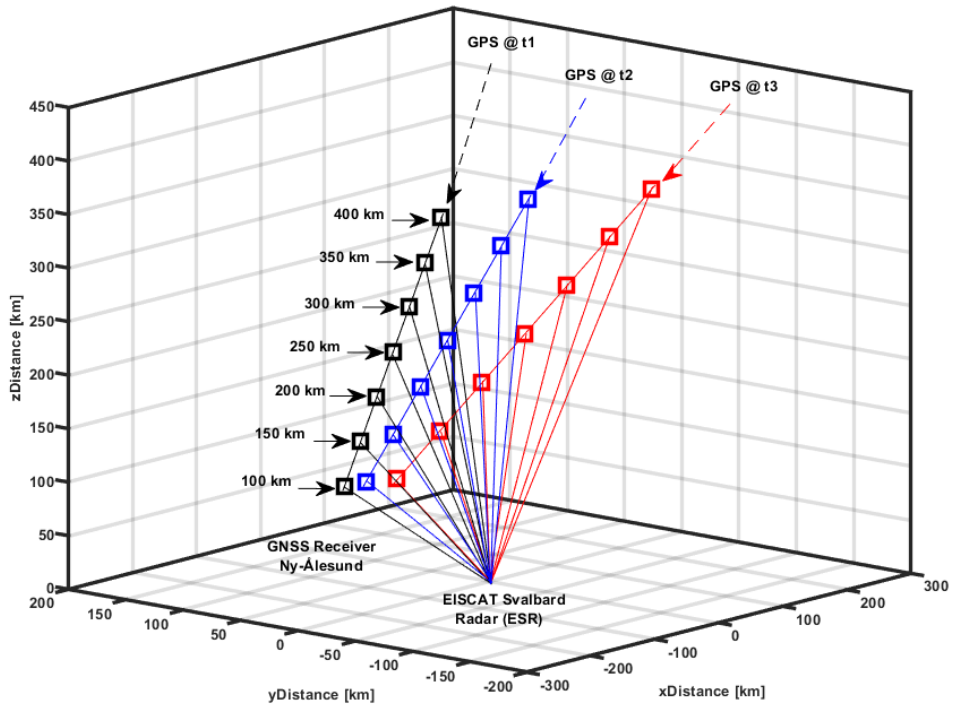

Figure 6.2: 3-D simulation of ESR beams scanning and following GPS ray paths (black, blue, and red lines) from t1-t3 at $100\ km$, $150\ km$, $200\ km$, $250\ km$, $300\ km$, $350\ km$, and $400\ km$ ionospheric shell heights over Ny-Ålesund on 12 March 2018.

To achieve the aim of the investigation, the geometry of the experiments involving EISCAT UHF/ESR and GPS satellite to GNSS receiver ray paths was designed and simulated at three shell heights as shown in Figures 6.1 and 6.2. The reason for these shell heights was to understand the contribution of E and/or F layer structures to the induced TEC fluctuations. Azimuth and elevation data of GPS satellites from known locations at Kiruna (KIRU) and Ny-Ålesund (NYA2) collected through CalSKY (https://calsky.com) were used to simulate the geometry of the experiments. Figure 6.1 shows the 3-D simulation of the design geometry of EISCAT experiment from t1 to t5 over Kiruna during 12 March 2018. The EISCAT beams directions in terms of azimuth and elevation angles intersecting GPS ray paths were calculated using the CalSKY derived azimuth and elevation angles. Similarly, Figure 6.2 illustrates the 3-D simulation of the design geometry of ESR experiment from t1 to t3 over Ny-Ålesund during 12 March 2018. In the two experiments, the simulated radar beams were directed at $100\ km$, $150 km$, $200\ km$, $250\ km$, $300\ km$, $350\ km$, and $400\ km$ ionospheric shell heights. Although the experiments were conducted for several days in March 2018, only the 3-D simulated design geometries of 12 March 2018 were included herein.

In the development and writing of the Experimental Language (ELAN) files originated from the CalSKY derived azimuth and elevation angles of GPS satellites for several days in March 2018, specific geometrical transformation stages were required. The stages involved to develop an ELAN file corresponding to a day used by either EISCAT or ESR are as follows:

a) Azimuth and elevation angles of GPS ray paths of relevance from a known geodetic GNSS receiver position in terms of latitude, longitude, and height courtesy of IGS at the selected ionospheric shell heights are transformed to corresponding Ionospheric Pierce Point (IPP) latitude, longitude, and height.
b) The known receiver position was calculated from a known approximate receiver position (X, Y, and Z coordinates) in Earth-centred Earth-fixed (ECEF) reference frame courtesy of RINEX observation file.
c) The coordinates of each of the IPP were then transformed to corresponding EISCAT UHF/ESR beams positions in terms of azimuth angle, elevation angle, and slant range from a known EISCAT UHF/ESR position in terms of geodetic latitude, longitude, and height.
d) The geodetic latitude, longitude, and height of EISCAT UHF/ESR antennas were extracted by means of the location of the EISCAT facilities (https://eiscat.se/scientist/document/location-of-the-eiscat-facilities).
e) The reference spheroid used in the coordinate transformation was WGS84 (World Geodetic System 1984), which is a reference frame coordinate used by GPS (https://gisgeography.com/wgs84-world-geodetic-system/).
f) The azimuth and elevation angles obtained in (c) corresponding to EISCAT UHF/ESR beams directions from EISCAT UHF/ESR antenna at the selected ionospheric shell heights were used to develop the ELAN files.
g) However, due to EISCAT UHF/ESR constraints (23°/30° elevation mask, respectively) and mechanical limitations of the radar antennas, the ELAN files were developed for only $150\,km, 250\,km$, and $350\,km$ ionospheric shell heights.
h) The ELAN files were developed and written in advance and sent to EISCAT before each day of experiment.
i) Thus, the EISCAT UHF/ESR experiments were conducted in accordance with the submitted ELAN files.

In the experiments, electron density profiles were measured transverse to GPS ray paths at these different shell heights by means of EISCAT UHF/ESR beams. The purpose of scanning radar beams at different shell heights was to determine the contribution of E and or F layer irregularities to fluctuations in TEC observed at the auroral and polar latitudes. Figure 6.3 shows a 2-D visualisation of the design geometry of the experiments with (a) EISCAT beams directed over auroral latitude and (b) ESR beams directed over polar latitude intersecting GPS ray paths of relevance, respectively. EISCAT UHF/ESR beams were alternated between different shell heights every 2 minutes to enable characterisation of irregularities in both E and F layer. This implies that the radar antenna stays stationary in a given pointing direction for 2 minutes and takes around 1 second to reposition the antenna in the subsequent pointing direction. This sequence is repeated as the radar beams scan transverse to the GPS ray paths of relevance at subsequent times and intersecting some of them. The GPS satellites (PRNs 26, 16, 21, and 27) used to design the geometry of the experiments were followed for a specific interval of time between 20:00 and 24:00 UT. Because of the movement of the GPS ray paths and the mechanical limitations of EISCAT UHF/ESR antennas, there was an offset between the radar beams and ray paths Ionospheric Pierce Points (IPPs) at the different shell heights. In these experiments, only GPS constellation was considered.

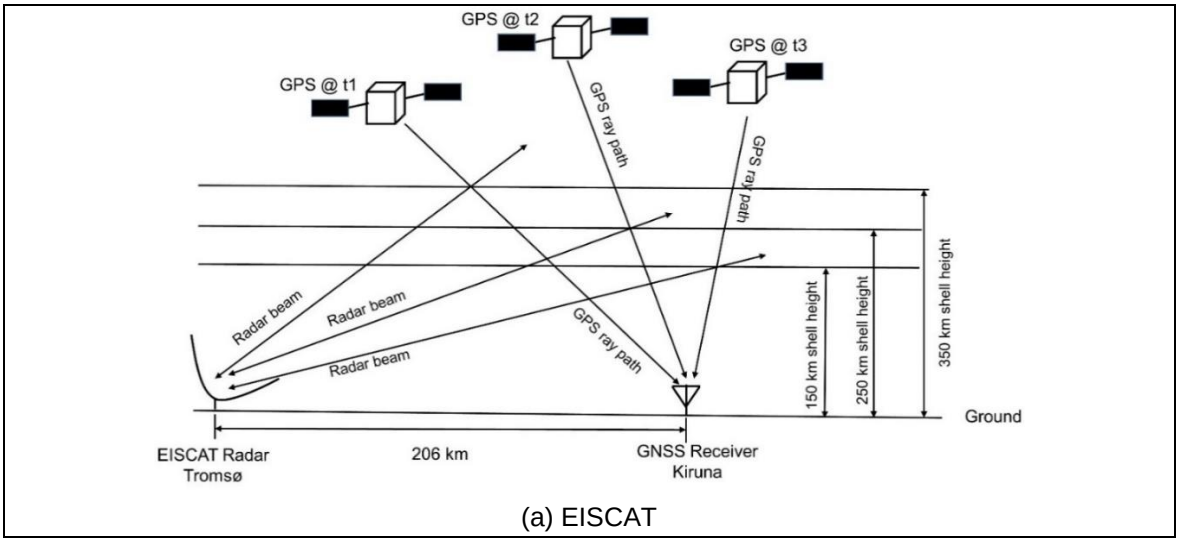

(a) EISCAT

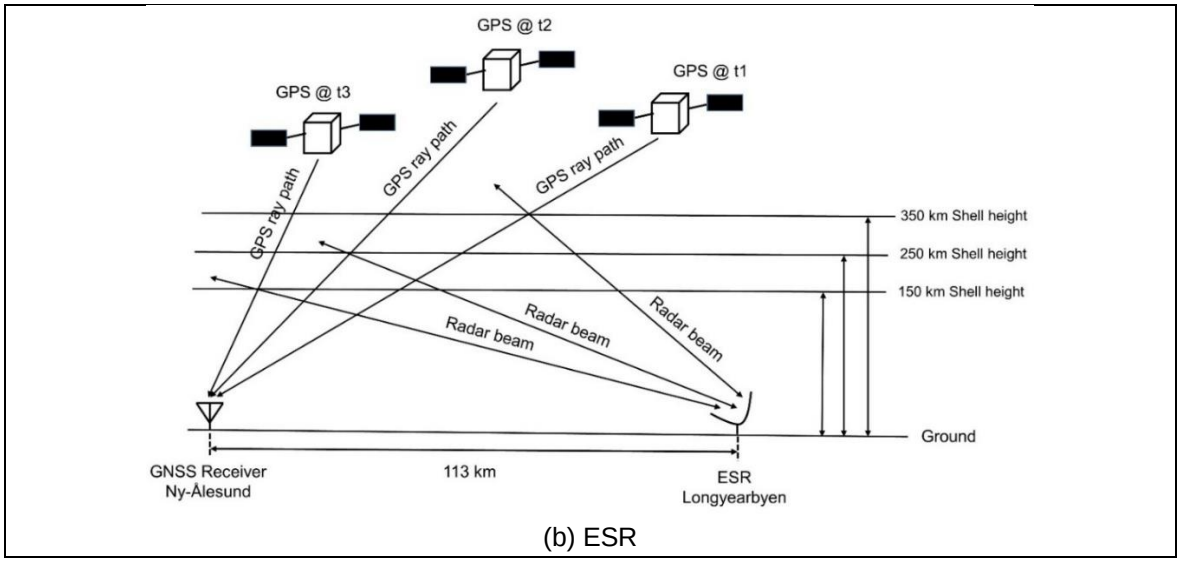

(b) ESR

Figure 6.3: 2-D description of March 2018 Experiments involving GPS ray paths theoretically and alternately intersected at $150\,km$, $250\,km$, and $350\,km$ shell heights over Kiruna and Ny-Ålesund between t1 and t3 by (a) EISCAT beams and (b) ESR beams, respectively. The experiments were funded by the Natural Environment Research Council (NERC), United Kingdom.

In order to minimise the effects of multipath and to overcome EISCAT UHF/ESR radars constraints, minimum elevation angles of 23° and 30° were considered in the design geometry of the experiments, respectively. Because auroral and polar irregularities are correlated with the night-time sector, the experiments were designed and conducted between 20:00 and 24:00 UT [*Aarons, 1982; Basu, 1975*]. To investigate the spatial distribution of auroral and polar irregularities and their effects on GPS signals, EISCAT UHF/ESR electron density profiles were compared with TEC fluctuations of specific GPS ray paths from geodetic GNSS stations surrounding EISCAT UHF/ESR antennas. Apart from the GPS satellites used to design the geometry of the experiments, TEC fluctuations from available GPS satellites in proximity to the ground-based GNSS station and with elevation angles meeting EISCAT UHF/ESR requirements were considered.

EISCAT UHF/ESR profiles of electron density, electron temperature, ion temperature, and ion drift velocity were measured to study the background ionospheric condition [*Beynon and Williams, 1978; Enell, 2016; Folkestad, 2016*]. Although several days were used to design and conduct the EISCAT UHF/ESR campaigns, however, only the results during 15 and 16 March 2018 are discussed. EISCAT UHF/ESR raw data were collected from EISCAT portal (http://portal.eiscat.se/schedule/schedule.cgi). These EISCAT UHF/ESR raw data

were analysed by means of GUISDAP courtesy of EISCAT. Errors observed in EISCAT UHF/ESR electron density profiles are inversely proportional to integration time but directly proportional to slant range [*Forte et al., 2013*]. In both experiments, the integration time of 1 minute was employed to the support comparison of electron density profiles with GPS TEC fluctuations and guarantee confidence in the measurements. The incoherent scatter radar measurement has a spatial resolution of about $2\ km$ on average in range [*Forte et al., 2017; and references therein*].

In this work, fluctuations in TEC $\left(\frac{\Delta TEC}{\Delta t}\right)$ [*Jacobsen and Dähnn, 2014; Luo et al., 2018; and references therein*] was calculated from a 30-s Receiver Independent Exchange Format (RINEX) observables (ftp://cddis.gsfc.nasa.gov/gnss/data/highrate). The RINEX observation data were collected through multi-frequency and multi-constellation geodetic GNSS receivers in the IGS network. The RINEX data from GNSS stations of relevance were downloaded via the Crustal Dynamics Data Information System (CDDIS) [*CDDIS, 2018*]. In addition, the 30-s RINEX data combined with ANTEX file as well as sources of orbit and clock were read and analysed by using gLAB GNSS positioning tool (https://gage.upc.edu/gLAB/) [*Hernandez-Pajares et al., 2010*]. gLAB is a software tool designed under ESA by the research group of Astronomy and Geomatics (gAGE), the Universitat Politecnica de Catalunya (UPC). It is an interactive multipurpose package designed to support education in the aspect of processing and analysis of GNSS data. On the other hand, Slant TEC (STEC) was calculated from carrier phase observables. Refer to equations (4.9 and 4.10) for details. Temporal TEC fluctuations $\frac{\Delta TEC}{\Delta t}$ were estimated as the difference in STEC between consecutive epochs [*Pi et al., 1997; Forte et al., 2013; Luo et al., 2018*] as shown in equation (4.11). Temporal TEC fluctuations ($\frac{\Delta TEC}{\Delta t}$) from 30-s observables are conveniently used to indicate the presence of large-scale electron density irregularities [*Keskinen and Ossakow, 1983; Pi et al., 1997*] in the auroral and polar ionospheres.

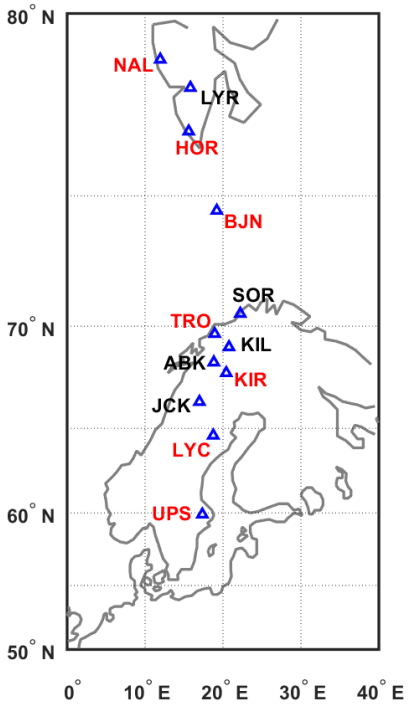

Figure 6.4: IMAGE magnetometer stations (blue triangles) at NAL (Ny-Ålesund), Hornsund (HOR), BJN (Bear Island), TRO (Tromsø), KIR (Kiruna), LYC (Lycksele), and UPS (Uppsala). The selected stations in red colour are along the geographic latitudinal chain.
[https://space.fmi.fi/image/www/index.php?page=user_defined].

To deduce the presence of particle precipitation in the auroral and polar ionosphere, measurements from several ground-based magnetometers distributed along a latitudinal chain courtesy of the IMAGE magnetometer network were considered. Figure 6.4 shows the locations of selected IMAGE magnetometers. Stations indicated in red colour represent magnetometers whose magnetograms were used to investigate the presence of substorms over auroral and polar latitudes. The Finnish Meteorological Institute (FMI) data repository was used to access the data https://space.fmi.fi/image/www/index.php?page=user_defined). Here, X (northward), Y (eastward), and Z (vertical) geographic components collected from FMI website were utilised to calculate the local geomagnetic field components H (horizontal), D (declination), and Z [*Schunk and Nagy, 2009; Jiao and Morton, 2015*] expressed as:

$$H = \sqrt{X^2 + Y^2} \qquad [nT] \qquad (6.1)$$

$$D = \tan^{-1}\frac{Y}{X} \qquad [nT] \qquad (6.2)$$

Whereas, variations in H, D, and Z (ΔH, ΔD, and ΔZ, respectively) are written as:

$$\Delta H = H - \langle H \rangle \qquad [nT] \qquad (6.3)$$

$$\Delta D = D - \langle D \rangle \qquad [nT] \tag{6.4}$$

$$\Delta Z = Z - \langle Z \rangle \qquad [nT] \tag{6.5}$$

Where $\langle H \rangle$, $\langle D \rangle$, and $\langle Z \rangle$ are the temporal averages of H, D, and Z, calculated as $\langle H \rangle = \frac{1}{N}\sum_{i=1}^{N} H_i$, $\langle D \rangle = \frac{1}{N}\sum_{i=1}^{N} D_i$, $\langle Z \rangle = \frac{1}{N}\sum_{i=1}^{N} Z_i$, respectively. In this study, N is the number of observation ($N = 1440$) corresponding to 1-minute sampling and $\langle H \rangle$, $\langle D \rangle$, and $\langle Z \rangle$ are the averages computed over the 24 hours. Similarly, geomagnetic variations (ΔH, ΔD, and ΔZ) were obtained by subtracting the computed averages from geomagnetic field components ($H,\ D,$ and Z). It is important to note that in this work, 1-minute sampling interval was considered to compare magnetograms with EISCAT UHF/ESR integration time of 1-minute [*Carrano and Groves, 2007; Luo et al., 2018; and references therein*].

6.3 Results

The results of the experiments are discussed herein as EISCAT experiment and ESR experiment, respectively. EISCAT experiment discusses the case observed at auroral latitude while ESR experiment presents the case from polar latitude. Both experiments were designed and conducted with respect to EISCAT and ESR beams' spatial coverage. The incoherent scatter radars cover a range of about $2000\ km$ on average [*Tjulin, 2017*]. To guarantee the quality of EISCAT UHF/ESR measurements, the maximum range of profiles of electron density, electron temperature, ion temperature, and ion drift velocity was limited to 45% ($900\ km$) of the spatial range of the radars. This can also ensure low errors in electron densities.

6.3.1 EISCAT Experiment

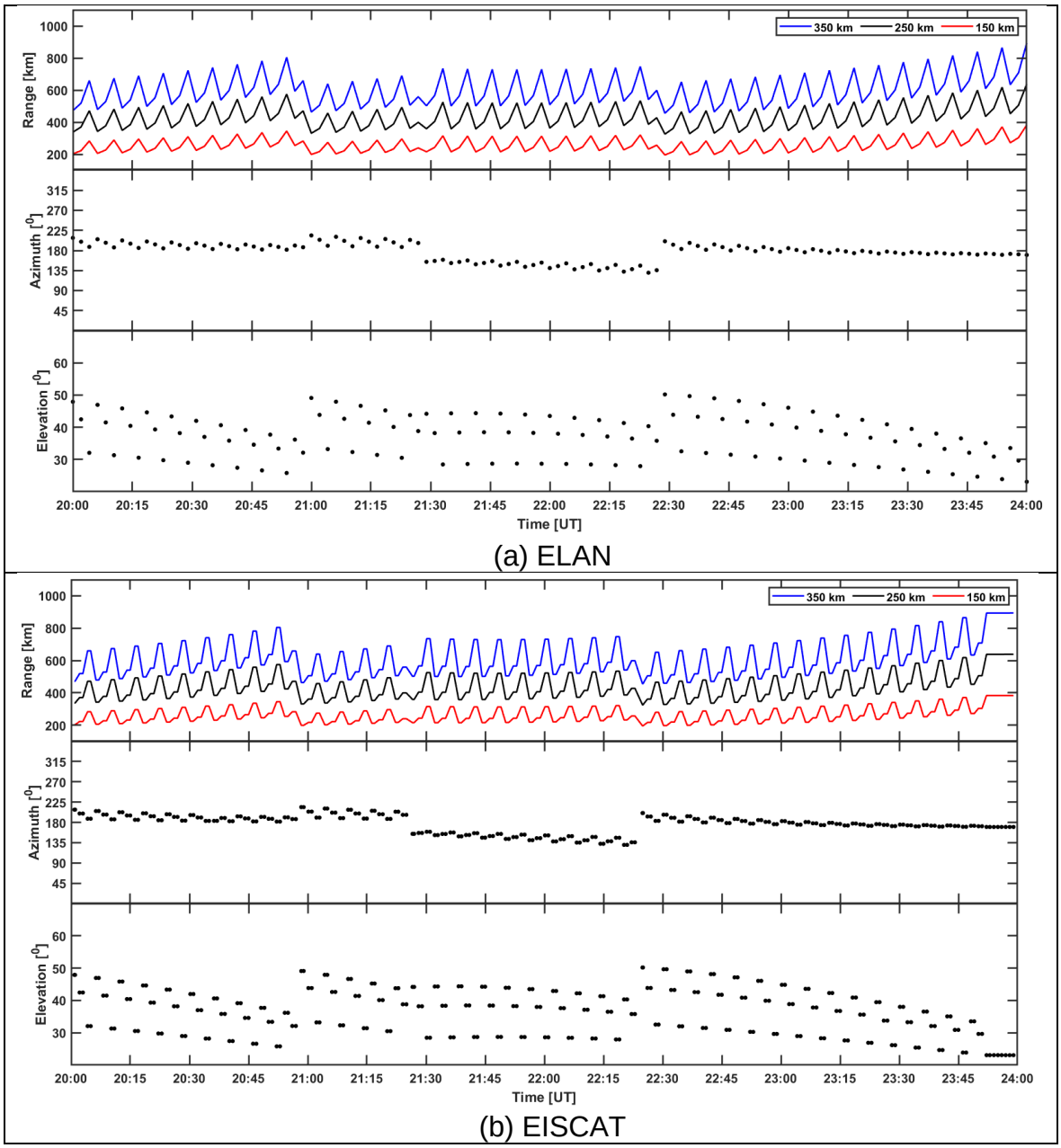

(a) ELAN

(b) EISCAT

Figure 6.5: From top to bottom shows slant ranges of EISCAT beams from EISCAT antenna to IPPs where the incoherent scatter radar alternately scans and follows GPS PRNs 26 (20:00-21:00 UT), 16 (21:00-21:30 UT), 21 (21:30-22:30 UT), and 27 (22:30-24:00 UT) ray paths at $150\ km$ (red line), $250\ km$ (black line), and $350\ km$ (blue line) ionospheric shell heights; azimuth angles; and elevation angles at these shell heights over Kiruna between 20:00 and 24:00 UT on 15 March 2018 from (a) ELAN and (b) EISCAT. The elevation angles were chosen because the mask of EISCAT UHF antenna is 23°.

This section describes EISCAT experiment during 15 March 2018. To appreciate and validate the accuracy of the theoretical design geometry of the experiment, ELAN and EISCAT spatial range, azimuth, and elevation data were compared. As

seen in Figure 6.5, the theoretical and experimental results were in good agreement. This increased the confidence of the design geometry. The red, black, and blue lines (top panels of Figures 6.5(a and b)) show EISCAT beams scan patterns at $150\ km$, $250\ km$, and $350\ km$ ionospheric shell heights, respectively. In Figures 6.5(a and b) (first panels from top), the wave-like patterns observed from the slant ranges at $350\ km$ (blue line), $250\ km$ (black line), and $150\ km$ (red line) were due to mechanical repositioning of EISCAT antennas as it scans each IPP for 2 minutes. The double points observed in Figure 6.5b were due to 1-minute integration time used during analysis of EISCAT raw data by GUISDAP. In Figure 6.5, the slant range, azimuth, and elevation angles corresponded to when EISCAT beams followed using GPS ray paths 26 (20:00-21:00 UT), 16 (21:00-21:30 UT), 21 (21:30-22:30 UT), and 27 (22:30-24:00 UT).

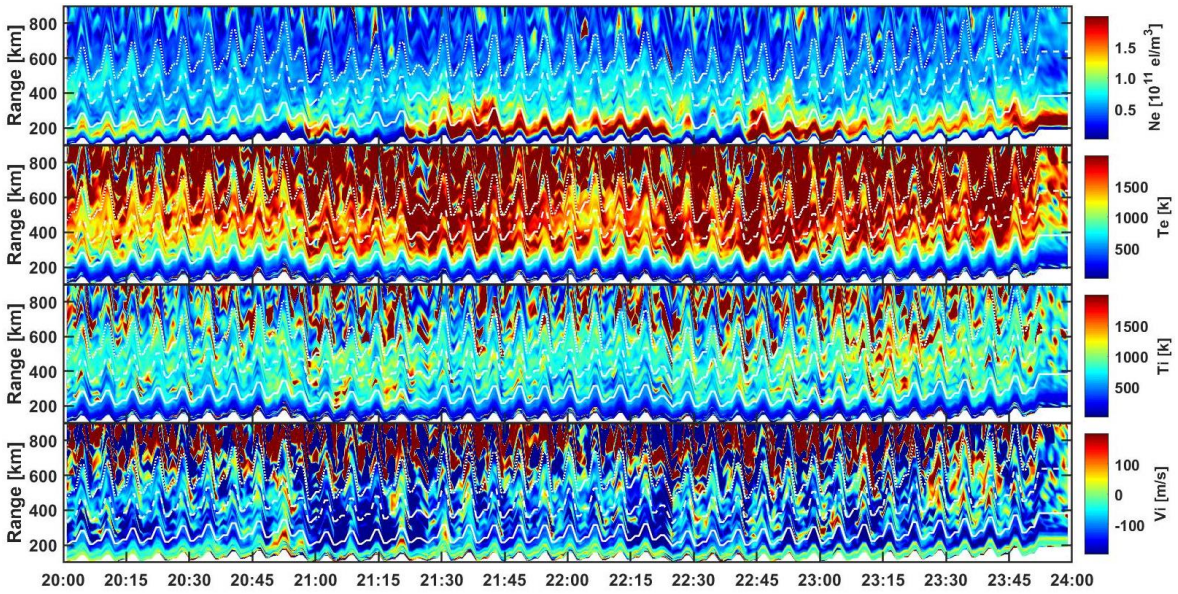

Figure 6.6: From top to bottom shows EISCAT profiles of electron density, electron temperature, ion temperature, and ion drift velocity, respectively over Kiruna between 20:00 and 24:00 UT on 15 March 2018. The solid, dashed, and dotted white lines on profiles correspond to $150\ km$, $250\ km$, and $350\ km$ ionospheric shell heights, respectively. EISCAT slant range is about $2000\ km$ but the profiles were pegged at $900\ km$ to guarantee reliability and quality of measurements. V_i ($\pm 200\ m/s$) is positive away from radar antenna.

EISCAT profiles of electron density, electron temperature, ion temperature, and ion drift velocity over Kiruna between 20:00 UT and midnight during 15 March 2018 provide insight into the ionospheric conditions as indicated in Figure 6.6. EISCAT profiles were pegged at $900\ km$ for the purpose of reliability and quality of

measurement. Where ion drift velocity (V_i) is negative (from green to blue colour), the ions flow towards the radar antenna. V_i can used as a convenient proxy to infer the magnitude and direction of plasma flow at a given ionospheric shell height. Ionisation structures were observed mainly in the E layer and these correspond to enhancement in electron temperature (low ion temperature). Ion velocity appears low when auroral structures were observed. The electron density profiles suggest a disturbed ionospheric condition indicative of the likely presence of auroral irregularities.

Figure 6.7, from top to bottom, shows EISCAT profiles of electron density at $150\ km$ (white solid line), $250\ km$ (white dashed line), and $350\ km$ (white dotted line) shell heights co-aligned with GPS TEC fluctuations for PRNs 08 (magenta), 16 (blue), 20 (cyan), 21 (green), 10 (yellow), 27 (red), and 26 (black); IPP distances between EISCAT beams and GPS ray paths of relevance at $150\ km$, $250\ km$, and $350\ km$ shell heights, respectively over (a) Tromsø (TRO1) and (b) Kiruna (KIRU). In Figure 6.7, d_{150}, d_{250}, and d_{350} are the calculated IPPs distances between EISCAT beams and GPS ray paths at $150\ km$, $250\ km$, $350\ km$ ionospheric shell heights, respectively. The analysis was performed between 20:00 and 24:00 UT on 15 March 2018. The IPPs of EISCAT beams at these shell heights were represented by a white line ($150\ km$), white dashed line ($250\ km$), and white dotted line ($350\ km$) superimposed on the electron density profiles as shown in the top panels of Figure 6.7.

Electron density intensified mainly below the $150\ km$ shell height as indicated in Figure 6.7. EISCAT observed E layer structures likely originating from auroral particle precipitation because of a corresponding increase in electron temperature (T_e). TEC fluctuations intensification was observed in general on GPS signals of relevance from TRO1 and KIRU geodetic GNSS stations during the entire time of measurements. Where intensification in electron density extended between $150\ km$ and $250\ km$ shell heights, a corresponding increase in TEC fluctuations was observed. In the figure, auroral structures localised around the $150\ km$ shell height were not in agreement with intensification in TEC fluctuations observed from TRO1 and KIRU ground stations. However, TEC fluctuations caused by ionisation structures extending between $150\ km$ and $250\ km$ shell heights were seen to

increase simultaneously at both stations and from multiple satellites during 21:20-21:50 UT and 22:40-22:50 UT.

In general, the bulk of auroral structures within the $150\,km$ shell height originating TEC fluctuations intensification appeared to distribute over a spatial distance below approximately $300\,km$ as indicated in the middle panels of Figure 6.7. Where structures were localised between $150\,km$ and $250\,km$, enhancement in TEC fluctuations was distributed over spatial distance below $500\,km$ on average as indicated in the 4th panels of Figure 6.7. Therefore, this suggests E and F layer auroral irregularities on average exist over spatial distances of several hundreds of kilometres. This further suggests a possible extension of the auroral oval.

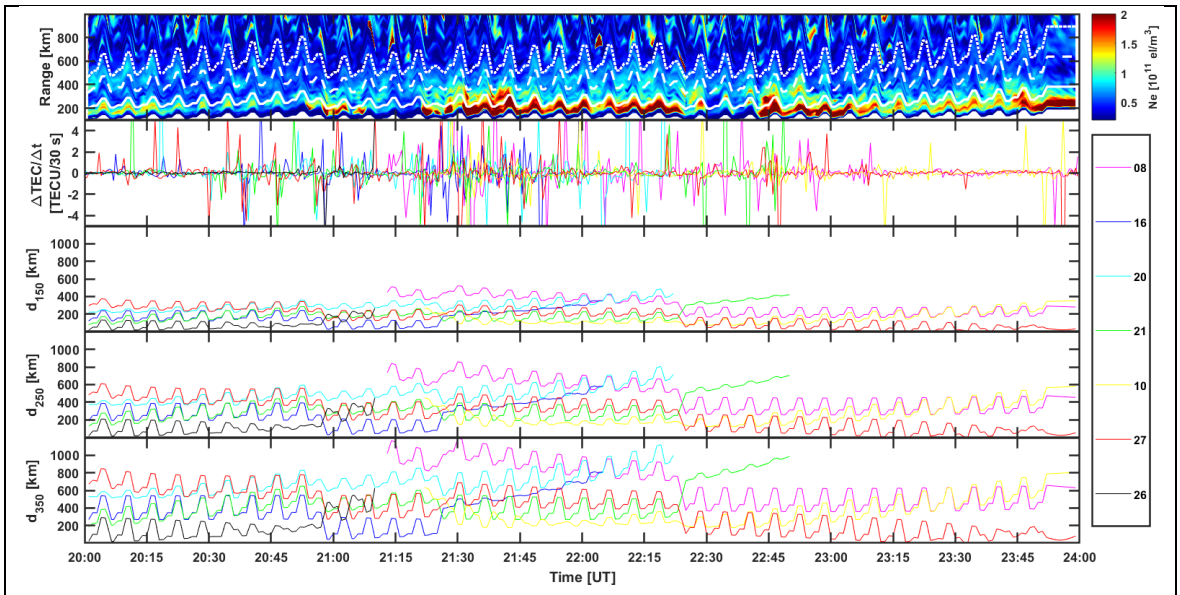

(a) TRO1

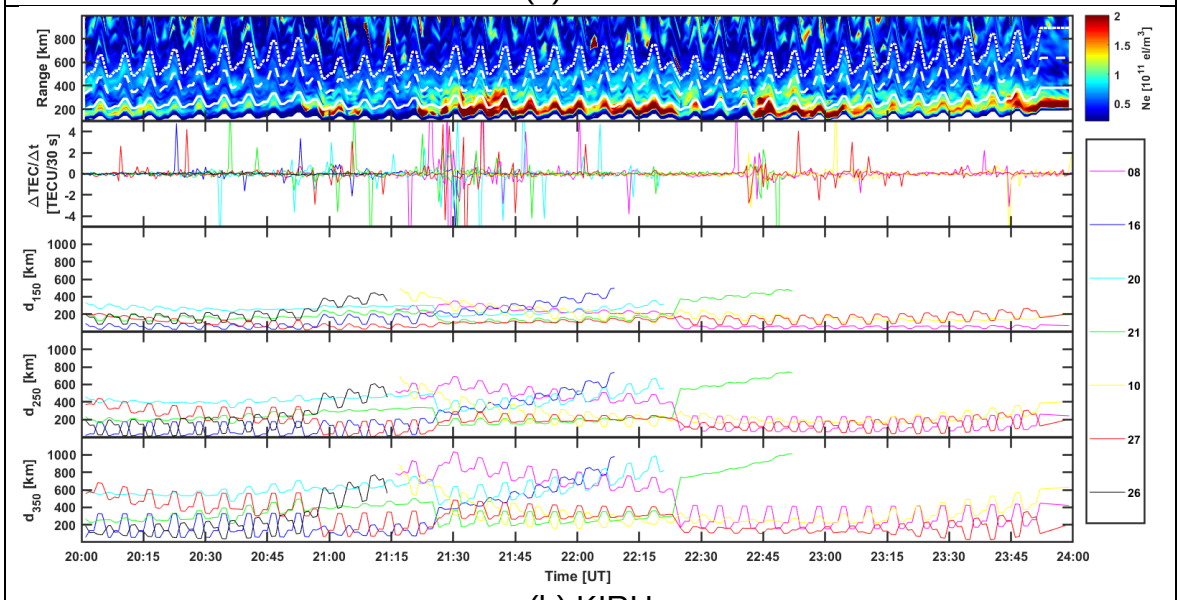

(b) KIRU

Figure 6.7: From top to bottom, EISCAT profiles of electron density at $150\ km$ (white solid line), $250\ km$ (white dashed line), and $350\ km$ (white dotted line) shell heights; 30-s RINEX TEC fluctuations for GPS PRNs 08 (magenta line), 16 (blue line), 20 (cyan line), 21 (green line), 10 (yellow line), 27 (red line), and 26 (black line) in view with elevation angle from 20°; distances between IPPs of EISCAT beams and GPS ray paths at $150\ km$, $250\ km$, and $350\ km$ shell height between 20:00 and 24:00 UT on 15 March 2018 over (a) TRO1 and (b) KIRU. The legend on the right-hand side shows the GPS PRNs used in the experiment.

Figure 6.8 presents north-south fluctuations in the H components over Ny-Ålesund (NAL, black line), Bear Island (BJN, blue line), Sørøya (SOR, green line), Tromsø (TRO, cyan line), Kiruna (KIR, red line), Lycksele (LYC, yellow line), and Uppsala (UPS, magenta line) magnetometer stations between 00:00 and 24:00 UT on 15 March 2018. The geomagnetic field varies between $\pm 600\ nT$ between 00:00 and 02:00 UT and 15:00 and 24:00 UT, respectively. The time of measurement is indicated by the shaded grey colour between 20:00 and 24:00 UT. Horizontal component of the geomagnetic field H over Kiruna (KIR, red line) varies between $+180\ nT$ and $-420\ nT$. K_p index value of 4 on average observed during the time of measurement (ftp://ftp.swpc.noaa.gov/pub/indices/old_indices/) suggests disturbed geomagnetic conditions. The K_p indices values are given for 3 hours interval. In addition, the negative variations in the H component after 21:00 UT over Kiruna indicated by red line shows multiple auroral substorms [*Wood et al., 2009*]. These negative H component fluctuations denote the presence of auroral particle precipitation in the E layer [*Forte et al., 2017*].

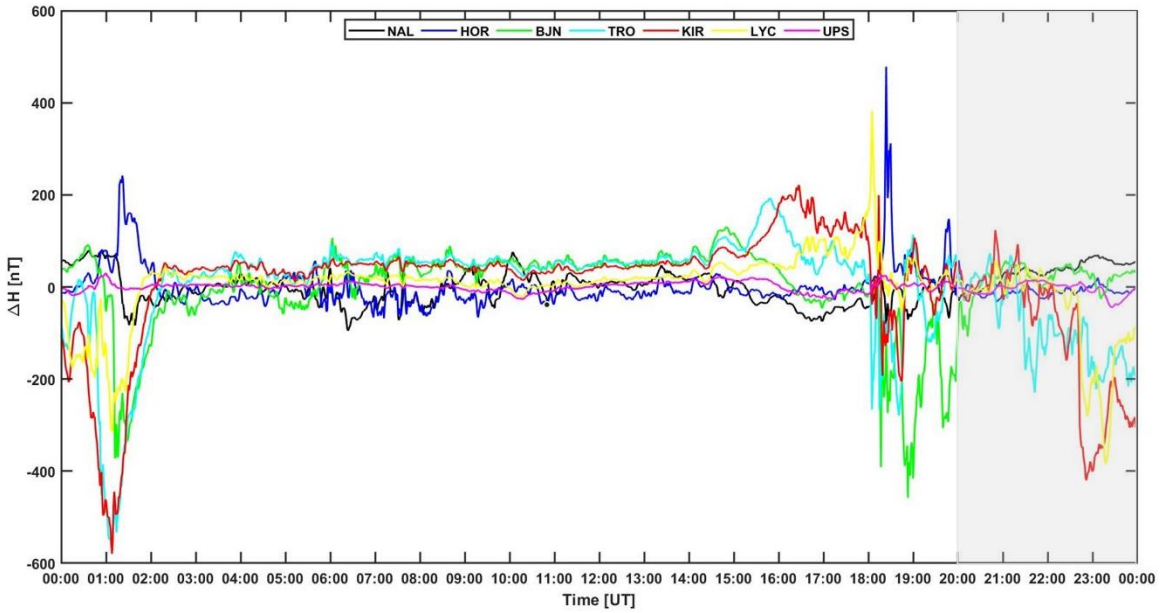

Figure 6.8: Magnetograms from the IMAGE network (H local geomagnetic field component variations) over Ny-Ålesund (NAL, black line), Hornsund (HOR, blue line), Bear Island (BJN, green line), Tromsø (TRO, cyan line), Kiruna (KIR, red line), Lycksele (LYC, yellow line), and Uppsala (UPS, magenta line), respectively between 00:00 and 24:00 UT on 15 March 2018. The time of measurement is indicated by the shaded light grey colour (right-hand side) between 20:00 and 24:00 UT.

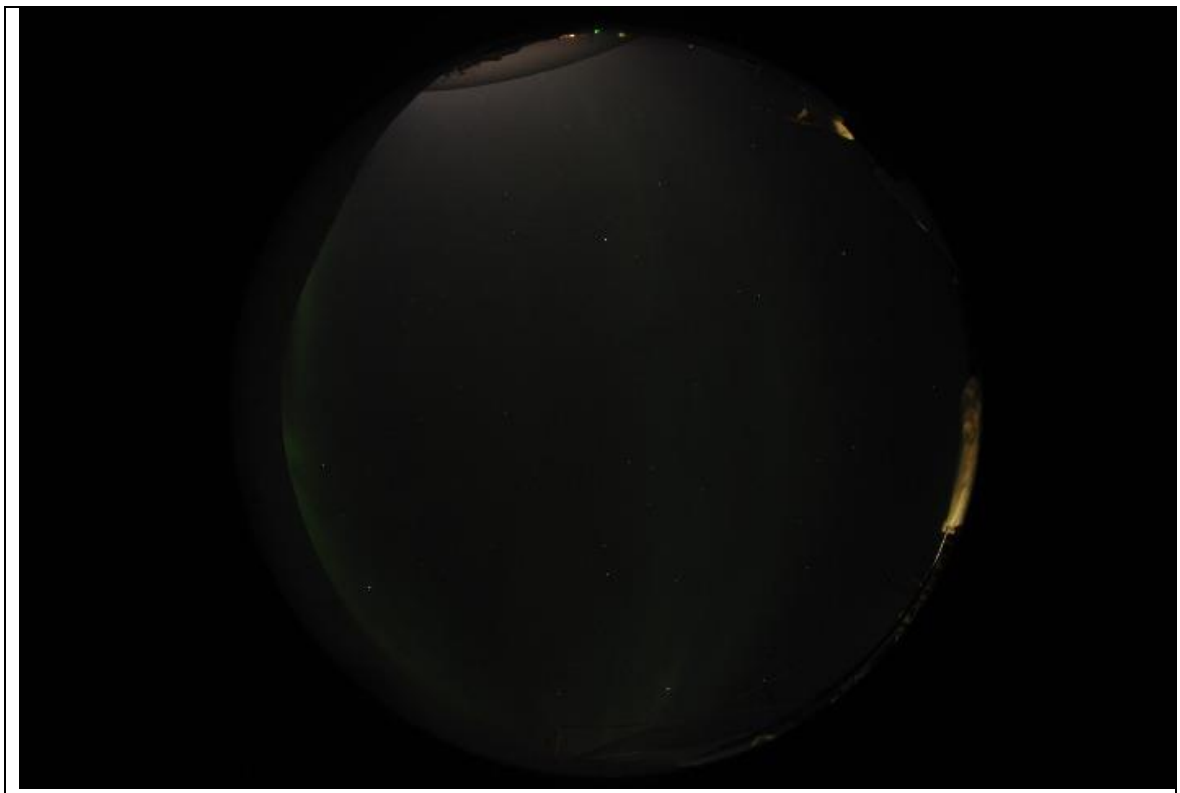

(a) 20:04 UT

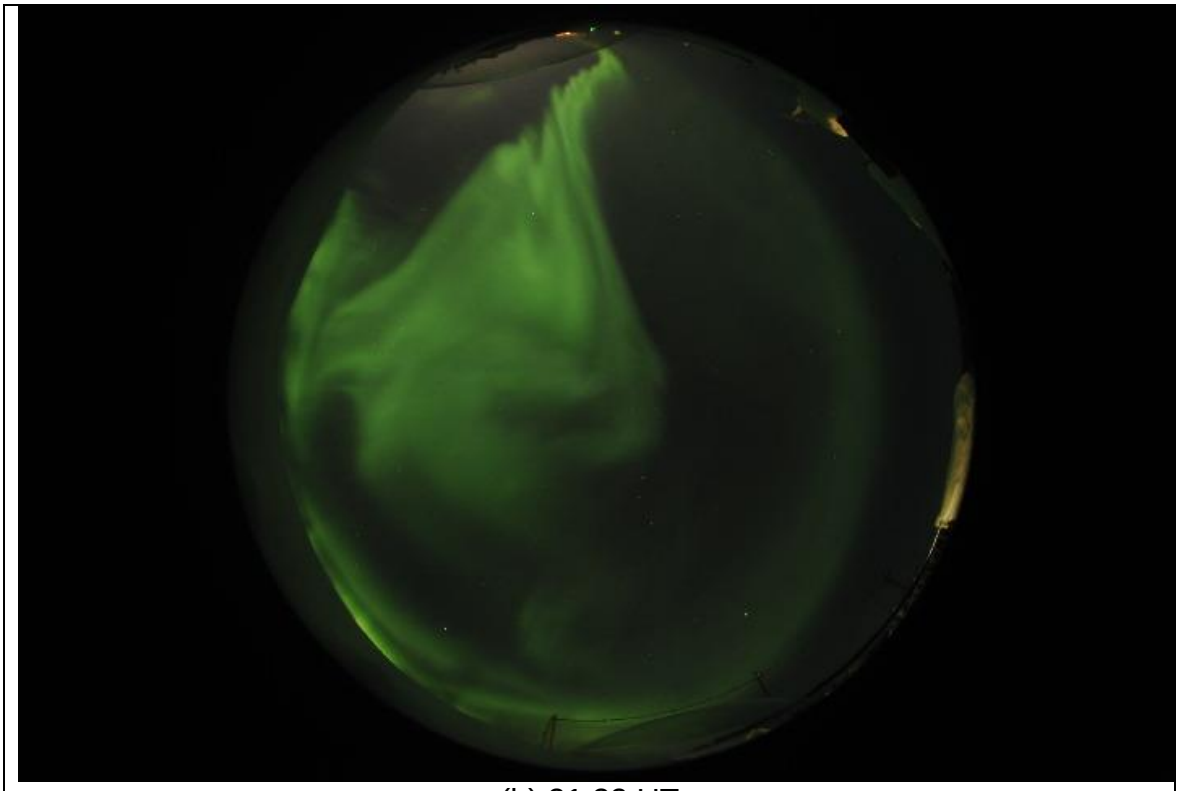

(b) 21:32 UT

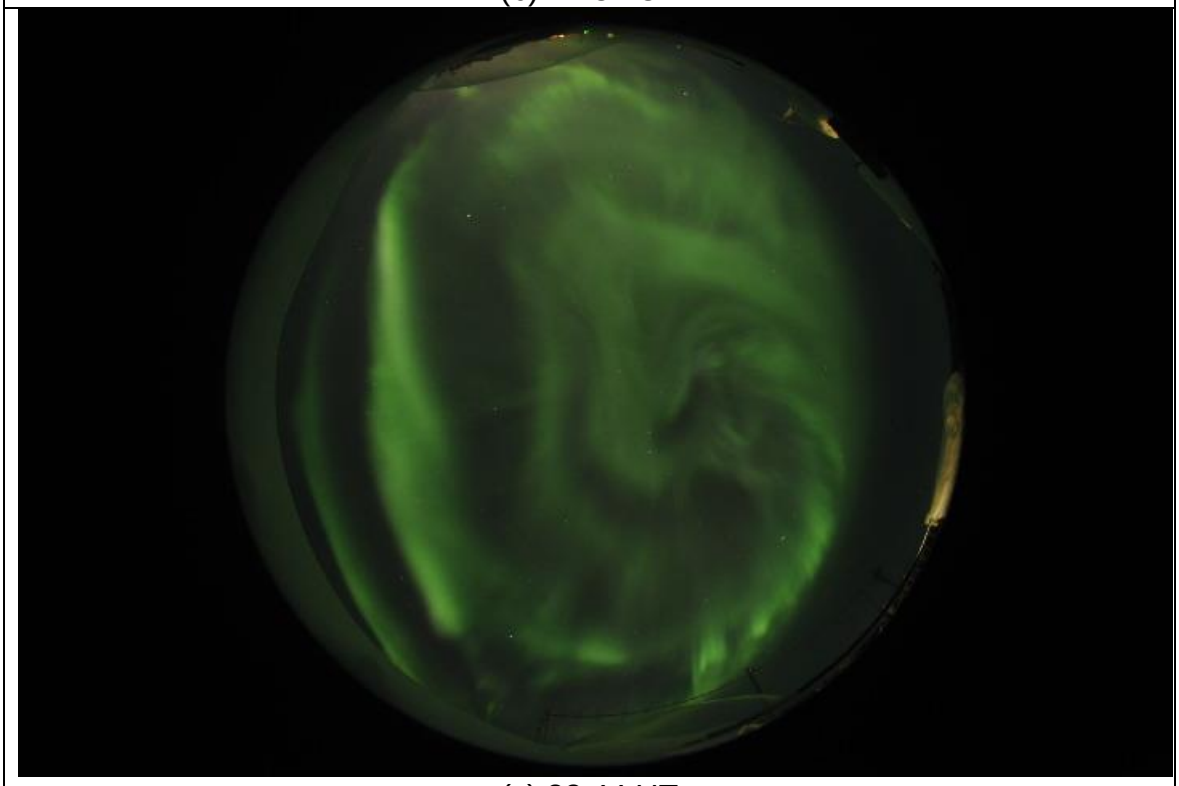

(c) 22:44 UT

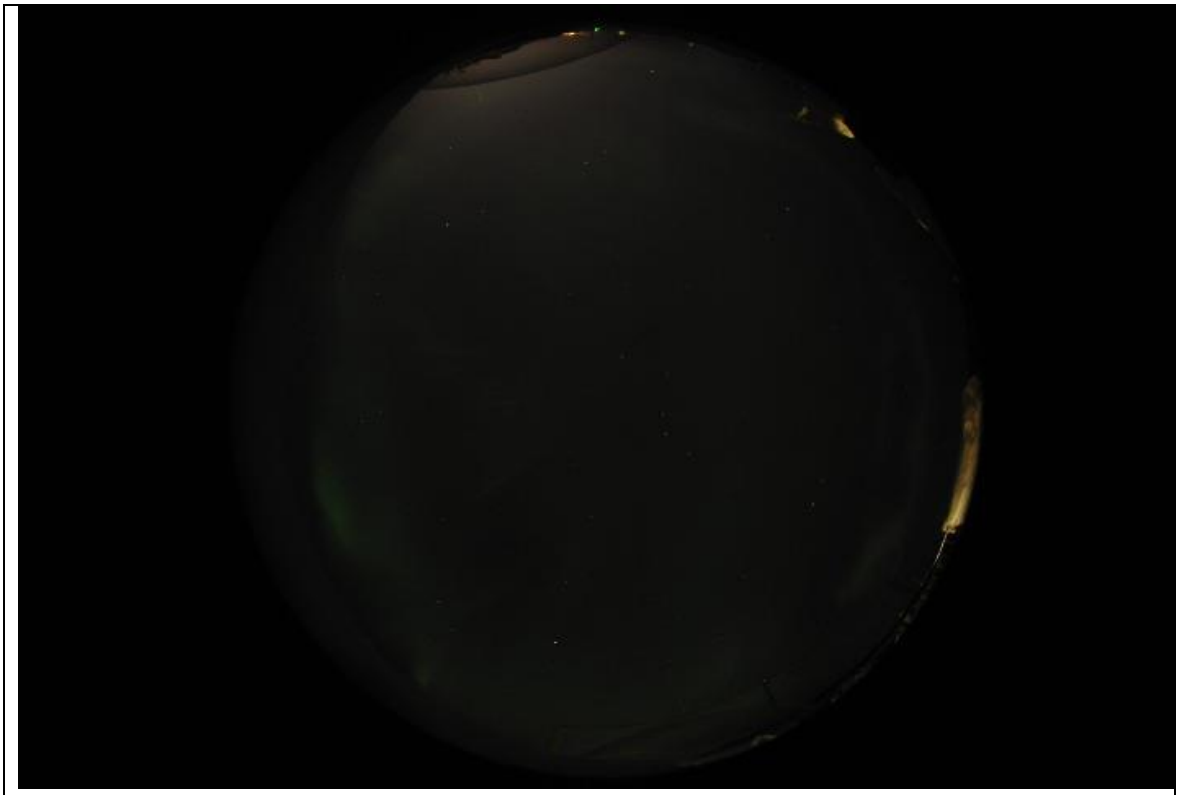

(d) 23:20 UT

Figure 6.9: ASC images collected from Kiruna ASC station during 15 March 2018. North is up and east is left of the image while the centre of the image is the zenith in this case Kiruna. EISCAT is on north-west of the ASC images at time intervals (a) 20:04 UT, (b) 21:32 UT, (c) 22:44 UT, and (d) 23:20 UT. Courtesy of the Swedish Institute of Space Physics (Swedish: Institutet för rymdfysik, IRF). (https://www2.irf.se/allsky/2018/20180315/jpgs/).

To validate the type of structure observed by means of EISCAT and the presence of particle precipitation, ASC images obtained from Kiruna ASC as shown in Figure 6.9 are included. Kiruna ASC is operated by the Swedish Institute of Space Physics (Swedish: Institutet för rymdfysik, IRF). IRF is a Swedish government agency which conducts research and education activities using related observatory activities in the fields of space technology, space physics, and atmospheric physics. For details on the Kiruna ASC refer to the IRF website (https://www.irf.se/en/observatory-activities/kiruna-all-sky-camera/). The ASC images have a diameter of $600\ km$ on average at $110\ km$ ionospheric shell height. Considering the north-west of images in Figure 6.9 because of EISCAT location with respect to Kiruna, the $557.7\ nm$ green emissions correspond to the presence of particle precipitation occurring at E layer ionospheric height. There was no presence of aurora in Figure 6.9(a and d, that is 20:04 UT and 23:20 UT) which correspond to intervals of time when there were no observed increased in TEC fluctuations as indicated in Figure 6.7. However, Figures

6.6(b and c, that is 21:32 UT and 22:44 UT) shows the likely presence of diffuse aurora and auroral arcslooking at north-west of images which correspond to intervals of time when there were observed increased in TEC fluctuations as indicated in Figure 6.7. Substorm onset observed by means of magnetograms is synchronous with the green optical emissions. The observed weaker emissions tend to show some patchiness over large distances whilst brighter emissions appeared more uniform over large distances. Similarly, irregularities forming in response to particle precipitation would then be distributed inhomogeneously and intermittently in space and time.

6.3.2 ESR Experiment

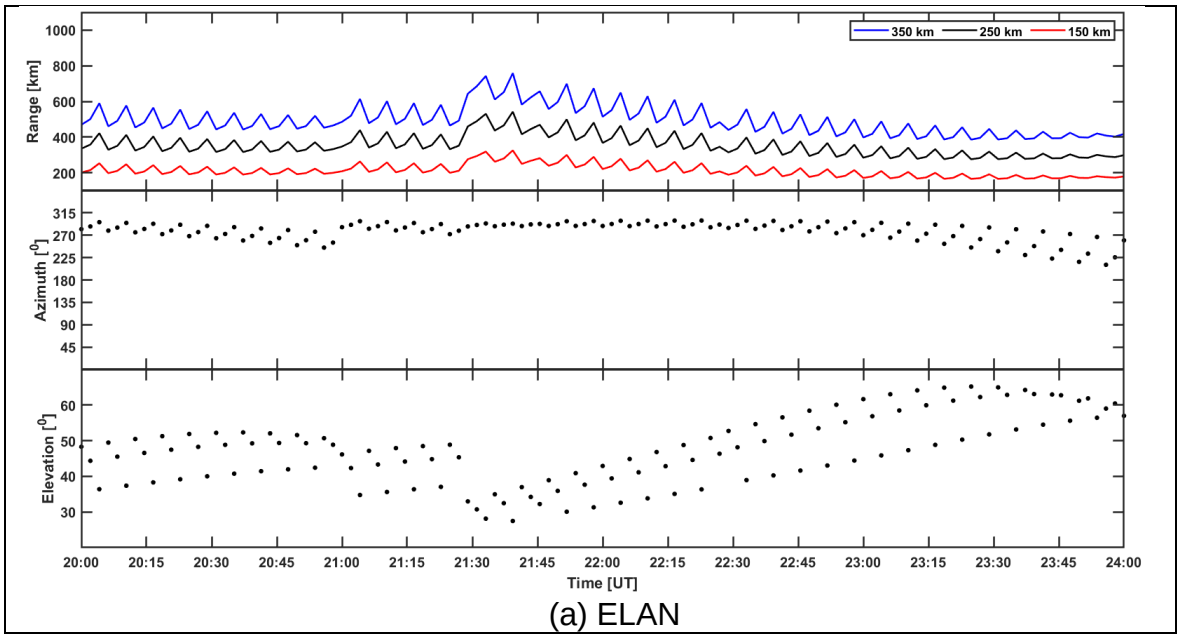

(a) ELAN

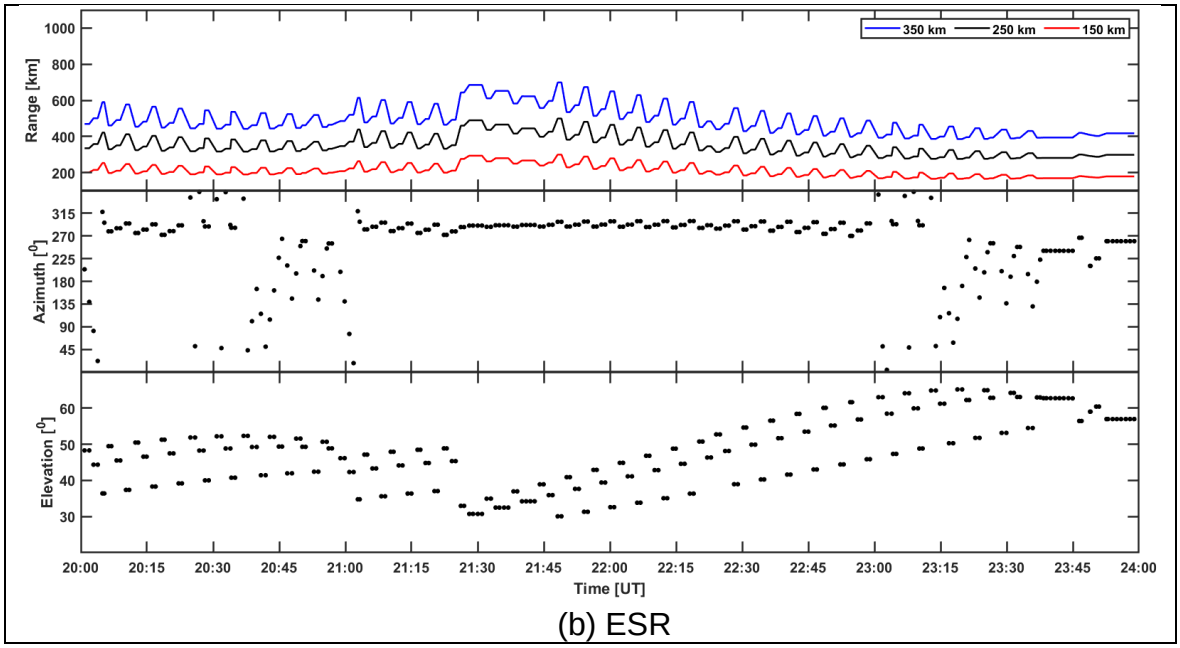

(b) ESR

Figure 6.10: From top to bottom shows slant ranges of ESR beams from ESR antenna to IPPs where the incoherent scatter radar alternately scans and follows GPS PRNs 26 (20:00-21:00 UT), 16 (21:00-21:30 UT), and 27 (21:30-24:00 UT) ray paths at $150\ km$ (red line), $250\ km$ (black line), and $350\ km$ (blue line) ionospheric shell heights; azimuth angles; and elevation angles at these shell heights over between 20:00 and 24:00 UT on 16 March 2018 from (a) ELAN and (b) ESR. The elevation angles were chosen because the mask of ESR UHF antenna is 30°.

As seen in EISCAT experiment (subsection 6.3.2), the accuracy of the design geometry of the ESR experiment was validated by comparing the slant range, azimuth angle, and elevation angle of ELAN (Figure 6.10a) and EISCAT (Figure 6.10b), respectively. As illustrated in Figure 6.10, the simulated (ELAN) and experiment (EISCAT) slant range, azimuth angle, and elevation angle showed a positive relation. However, exceptions were observed in intervals between 20:20 to 21:05 UT and 23:00 UT to midnight mainly when azimuth angles of from results of simulation and experiment were compared. Instead of ESR antenna pointing direction (essentially north-west) as indicated by the results of simulation, the antenna alternates in the north-east, south-east, and south-west directions as well. In most of this interval of time, the difference between the simulated azimuth angles and the experimental azimuth angles is 180°. This is likely caused by mechanical limitations of ESR antenna. ESR and EISCAT UHF antennas only have 2 degrees of freedom. This implies the antennas can only scan a given ionospheric shell height defined by azimuth and elevation angles. The radar antenna repositions to a pointing direction by aligning to a defined azimuth angle followed by a defined elevation angle or a defined elevation angle followed by a defined azimuth angle.

Figure 6.10 presents the simulated and experimental ESR beams in terms of slant range, azimuth angle, and elevation angle followed using GPS PRNs 26 (20:00-21:00 UT), 16 (21:00-21:30 UT), and 27 (21:30-24:00 UT) ray paths at three different ionospheric shell heights.

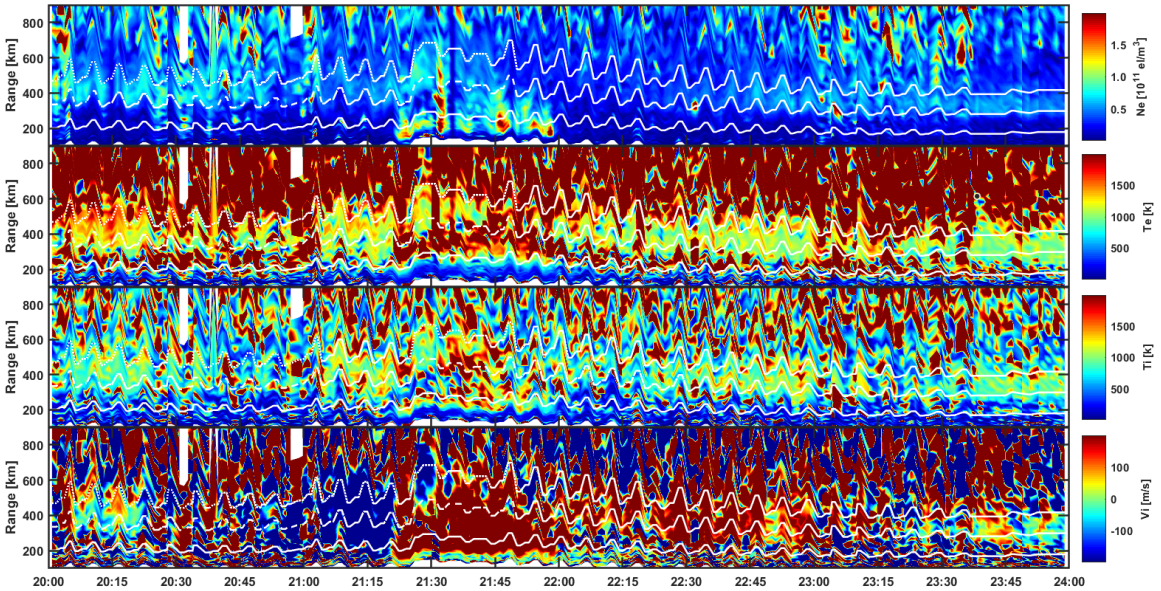

Figure 6.11: From top to bottom shows ESR profiles of electron density, electron temperature, ion temperature, and ion drift velocity, respectively over Ny-Ålesund between 20:00 and 24:00 UT on 16 March 2018. The solid, dashed, and dotted white lines on profiles correspond to $150\ km$, $250\ km$, and $350\ km$ ionospheric shell heights, respectively.

ESR profiles of electron density, electron temperature, ion temperature, and ion drift velocity as shown in Figure 6.12 suggest a disturbed ionospheric condition during 16 March 2018. Ionisation structures were observed between 21:15 and 22:00 UT extending between the E and F layers and these structures correspond to decrease and increase in electron and ion temperatures but with a markedly increase in ion drift velocity. The ion drift velocity can be used to infer plasma velocity.

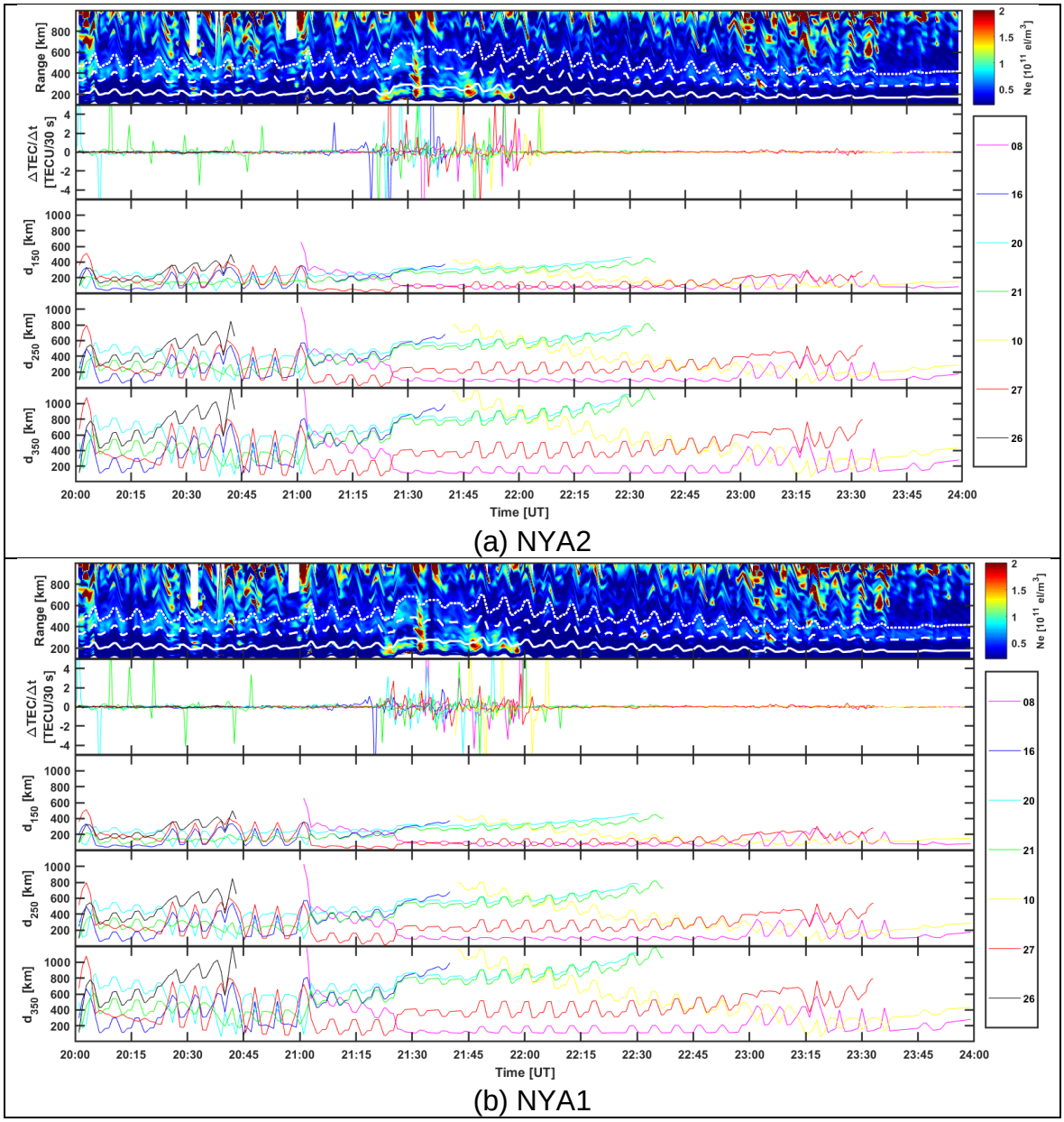

(a) NYA2

(b) NYA1

Figure 6.12: From top to bottom shows ESR profiles of electron density at $150\ km$ (white solid line), $250\ km$ (white dashed line), and $350\ km$ (white dotted line) shell heights; 30-s RINEX TEC fluctuations for GPS PRNs 08 (magenta line), 16 (blue line), 20 (cyan line), 21 (green line), 10 (yellow line), 27 (red line), and 26 (black line) in view with elevation angle from 20°; distances between IPPs of ESR beams and GPS ray paths at $150\ km$, $250\ km$, and $350\ km$ shell height between 20:00 and 24:00 UT on 16 March 2018 over (a) NYA2 and (b) NYA1.

Figure 6.12, from top to bottom, shows ESR profiles of electron density at $150\ km$ (white solid line), $250\ km$ (white dashed line), and $350\ km$ (white dotted line) shell heights co-aligned with GPS TEC fluctuations for PRNs 08 (magenta), 16 (blue), 20 (cyan), 21 (green), 10 (yellow), 27 (red), and 26 (black); IPP distances between ESR beams and GPS ray paths of relevance at $150\ km$, $250\ km$, and $350\ km$ shell heights, respectively over (a) Ny-Ålesund (NYA2) and (b) Ny-Ålesund (NYA1). The

only available ground-based GNSS stations were those in Ny-Ålesund. NYA2 and NYA1 GNSS receivers were separated by less than $200\ m$ on average. This implies the two receivers were close to each other. In figure 6.12 (2nd panels from top), TEC fluctuations from GPS PRNs considered were considerably enhanced consistently across both ground-based GNSS stations between 21:15 and 22:10 UT due to enhancements in the electron density between $150\ km$ and $350\ km$ shell heights. Polar structures were markedly observed below the $150\ km$ shell height (21:20-22:00 UT), between the $150\ km$ and $250\ km$ shell heights (21:30-21:40 UT) and between the $250\ km$ and $350\ km$ shell heights (21:30-21:35 UT).

Considering the 3rd, 4th, and 5th panels from top of Figure 6.12(a and b) between 21:20 and 22:00 UT when ESR observed ionisation structures with corresponding increase in TEC fluctuations ($\pm 5\ TECU/30\ s$), the spatial distance over which polar irregularities distribute at $150\ km$, $250\ km$, and $350\ km$ ionospheric shell heights are around 300 km, $500\ km$, and $800\ km$, respectively. This implies the spatial scale size of polar irregularities are likely of the order of several hundreds of kilometres.

Figure 6.13 shows the SuperDARN electric potential pattern between 20:30 and 22:32 UT on the evening of 16 March 2018. The intervals of time in Figure 6.12 were chosen to represent times when ESR does or does not observe ionisation structure. Figure 6.13(b and c) show the presence of a fast-moving plasma at a velocity of over $500\ m/s$ between 21:26 and 21:30 UT corresponding to when ESR observed ionisation structures. The fast-moving plasma coexisting with IMF B_z negative, the spatial scale size of polar irregularities of several hundreds of kilometres in the F layer, and the decrease in electron temperature (Figure 6.11) between $250\ km$ and $350\ km$ ionospheric shell heights indicate the presence of a polar patch intersected by the ESR beam originating enhancement in TEC fluctuations from GPS PRNs considered. However, the SuperDARN electric potential pattern at this time (Figure 6.13(a, d-f)) did not show evidence of ionospheric convection over Ny-Ålesund.

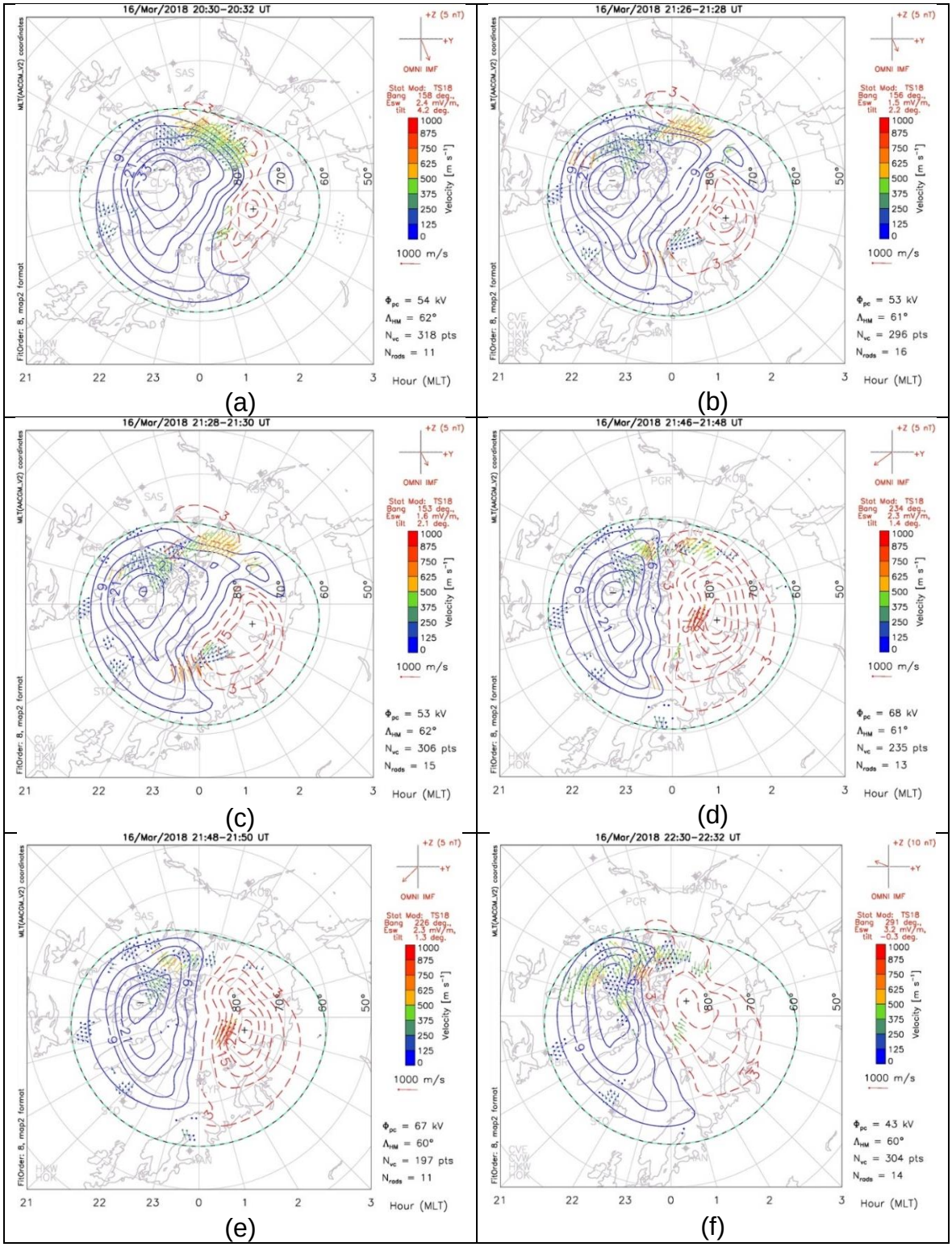

Figure 6.13: SuperDARN electric potential pattern of all Northern radars at a 2-minute window from (a) 20:30-20:32 UT, (b) 21:26-21:28 UT, (c) 21:28-21:30 UT, (d) 21:46-21:48 UT, (e) 21:48-21:50 UT, and (f) 22:30-22:32 UT on 16 March 2018 as a function of magnetic latitudes and magnetic local time (MLT). The green dashed curve represents the Heppner-Maynard Boundary. The intervals of time shown herein are representatives of times corresponding to when ESR does or does not observe ionisation structures.
[Courtesy of College of Engineering, VirginiaTech SuperDARN]

Southward variations of the H component of the geomagnetic field at approximately 21:20 UT (see Figure 6.14) suggest the presence of particle precipitation co-aligned with structures observed in the E layer height, whilst the irregularities occurring between the $250\ km$ and $350\ km$ (F layer altitude) shell heights appeared consistent with the presence of a polar patch traversing the ESR beams and the GPS ray paths of relevance.

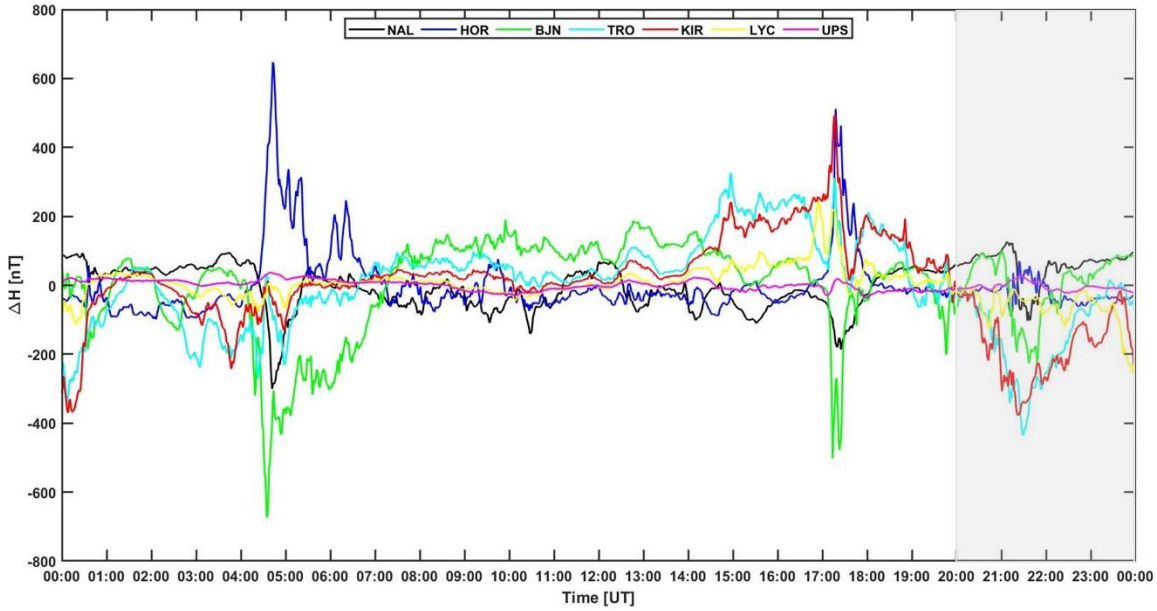

Figure 6.14: Magnetograms from the IMAGE network (H local geomagnetic field components variations) over Ny-Ålesund (NAL, black line), Hornsund (HOR, blue line), Bear Island (BJN, green line), Tromsø (TRO, cyan line), Kiruna (KIR, red line), Lycksele (LYC, yellow line), and Uppsala (UPS, magenta line), respectively between 00:00 and 24:00 UT on 16 March 2018. The time of measurement is indicated by the shaded light grey colour (right-hand side) between 20:00 and 24:00 UT.

6.4 Discussions

The origin of GPS phase fluctuations in the auroral and polar ionospheres was investigated through EISCAT UHF/ESR experiments aimed at characterising electron density distribution along profiles transverse to GPS ray paths of relevance. To appreciate how ionospheric irregularities in the E and F layer traverse GPS ray paths induce phase fluctuations, 3-D simulated geometries of the experiments were designed. Figures 6.1 and 6.2 showed the simulated geometry derived from CalSKY data from which $150\ km$, $250\ km$, and $350\ km$ shell heights were considered due to EISCAT UHF/ESR antennas mechanical limitations. The design geometry of EISCAT UHF/ESR experiments was validated by means of comparing the simulated

(ELAN) and experimental (EISCAT UHF/ESR) beams positions in terms of azimuth and elevation angles and confirmed to show good correlation (Figures 6.5 and 6.10).

In the auroral ionosphere, it seems plausible to conclude that temporal TEC fluctuations observed in the EISCAT experiment on the evening of 15 March 2018 were caused by electron density irregularities arising from auroral particle precipitation. The presence of particle precipitation was validated by intensification in electron temperature (2nd panel of Figure 6.6), substorms represented by negative H component of the geomagnetic field (Figure 6.8), and green optical emissions at $110\,km$ altitude (E layer) indicated in Figure 6.9. In the polar ionosphere, TEC fluctuations observed in the ESR experiment on the evening of 16 March 2018 were caused by electron density irregularities arising from both a polar cap patch and particle precipitation. Figure 6.11 shows decreased electron temperature mainly in the F layer (2nd panel from the top of Figure 6.11), increased ion drift velocity (bottom panel of Figure 6.11), and the presence of fast-moving plasma from SuperDARN electric potential pattern (Figure 6.13(b and c)) validate the presence of a patch. In Figure 6.11 (2nd panel from the top) mainly below the $150\,km$ altitude (E layer), electron temperature was high and negative deflection of H component of geomagnetic field representative of substorm (Figure 6.14) suggest the presence of particle precipitation.

Whilst the polar cap patch in the ESR experiment was drifting at a velocity of above $500\,m/s$ combined with IMF B_z negative (Figure 6.13(b and c)), no significant plasma drift was observed in the case of particle precipitation for both EISCAT experiment (not shown) and ESR experiment (Figure 6.13(a, d-f)) [http://vt.superdarn.org/tiki-index.php?page=DaViT+Map+Potential+Plot]. Yet, enhanced temporal TEC fluctuations were observed on GPS ray path considered for irregularities associated with the polar patch as well as particle precipitation. In the polar ionosphere, irregularities associated with particle precipitation were localised mainly in the E layer (Figures 6.11 and 6.12). On the other hand, irregularities associated with a patch were localised mainly in the F layer as indicated in Figures 6.11 and 6.12.

A possible explanation to the observed phase fluctuations on GPS ray paths considered are presented as follows:

a) The intermittent particle precipitation occurs inhomogeneously and is distributed unevenly over geomagnetic latitudes and longitudes (Figure 6.9). This intermittent and inhomogeneous precipitation originates in turn ionisation structures distributed inhomogeneously over large distances (that is, below $300\ km$ in the E layer and less than $500\ km$ in the F layer). When GPS ray paths scan through such an intermittent, inhomogeneous distribution of irregularities, they experience fluctuations on their carrier phases which manifested as intensification in TEC fluctuations as shown in Figures 6.4 and 6.8. When the phase fluctuations (TEC fluctuations) are estimated over time from 30-s RINEX observation data, large variations can be obtained as a consequence of the GPS ray paths scanning through a very low velocity inhomogeneities in the electron density distribution over time ($30\ s$ sampling time). This mechanism can originate intensified temporal TEC fluctuations observed associated with particle precipitation in the auroral and polar ionospheres. The supporting evidence to the observed mechanism is increased electron temperature, green optical emissions at $557.7\ nm$ wavelength, and substorms. The $557.7\ nm$ emissions correspond to the presence of particle precipitation at the E layer altitude. Following the recorded K_p value, intensity of enhancement of TEC fluctuations from GPS signals increases with disturbed geomagnetic conditions in response to higher particle fluxes (Figures 6.5 and 6.10) and higher particle energies.

b) In the polar ionosphere, in addition to intermittent and inhomogeneous particle precipitation, plasma patches can occur mainly in the F layer altitude, as well. Plasma patches convect at plasma drift velocities that are typically much faster (up to about $1\ km/s$) than the scan velocity of GPS ray paths at IPP heights ($21.24\ m/s$ in the E layer and $67.57\ m/s$ in the F layer). Here, E layer was estimated at $110\ km$ altitude while F layer was considered at $350\ km$ altitude whereas GPS satellite velocity at $20200\ km$ altitude was $3.9\ km/s$. When fast polar patches travel across GPS ray paths, carrier phase fluctuations can arise. In addition, as the phase fluctuations are estimated over time by means of temporal TEC fluctuations, large variations can be obtained as a consequence of gradients in the electron density distribution associated with patches (Figure 6.12).

In both EISCAT UHF/ESR experiments, the distance between the pierce points of GPS ray paths (showing enhanced TEC fluctuations simultaneously at various stations) and those of EISCAT UHF/ESR beams at several shell heights indicate that electron density irregularities distribute over spatial distances of up to approximately $300\ km$ in the E layer (Figures 6.4 and 6.12 middle panels) and up to approximately $800\ km$ in the F layer (Figures 6.4 and 6.12 bottom panels).

With respect to the case of ionospheric irregularities associated with the polar patch in the ESR experiment (Figure 6.12), this spatial distance also suggests the size of the patch. In Figure 6.12, the spatial distance corresponding to the observed patch was of the order of several hundreds of kilometres.

In Figures 6.4 and 6.12, whenever intensified TEC fluctuations are present on the GPS ray paths considered which are at a given spatial distance from EISCAT UHF/ESR beams in correspondence to intensified electron densities, then the irregularities are likely distributed over a spatial distance equal to or greater than the distances observed. However, suppose intensified TEC fluctuations are not present on GPS ray paths which are at a given distance from EISCAT UHF/ESR beams in correspondence to enhanced electron density, then the irregularities are likely distributed over a spatial distance less than the distances observed. Thus, simultaneous comparison of EISCAT UHF/ESR profiles of electron density combined with fluctuations in TEC from 30-s observables can provide insight into the type and spatial size of irregularities [*Keskinen and Ossakow, 1983*].

Therefore, EISCAT UHF/ESR profiles of electron density suggest that the irregularities occurring in both EISCAT UHF/ESR experiments are large-scale originating mainly phase fluctuations on GPS ray paths [*Forte et al., 2017*]. The presence of large-scale irregularities was supported by intensification of TEC fluctuations observed by means of 30-s observables in both EISCAT UHF/ESR experiments caused by particle precipitation events [*Keskinen and Ossakow, 1983*]. These large-scale irregularities forming in the auroral and polar ionosphere have a patchy (i.e. inhomogeneous and intermittent) spatial distribution over several hundreds of kilometres. Whilst irregularities forming in response to intermittent and inhomogeneous particle precipitation appear to be very low plasma flow, those forming in conjunction to plasma patches appear to drift with high plasma flow. In

addition, all these irregularities and structures are field-aligned [*Fejer and Kelley, 1980*; *Keskinen and Ossakow, 1983*]. Phase fluctuations (hence, temporal TEC fluctuations) are being produced in the auroral and polar ionospheres as follows:

a) the GPS ray paths scan through inhomogeneous and intermittent irregularities forming during particle precipitation in the E layer and/or
b) fast-moving plasma patches in the F layer traverse GPS ray paths considered.

6.5 Summary

For the first time, ionisation structures across GPS ray paths in the European auroral and polar ionospheres were investigated by using EISCAT UHF/ESR incoherent scatter radars in conjunction with geodetic GNSS receiver stations. Temporal TEC fluctuations were utilised to characterise phase fluctuations introduced by the observed ionisation structures in the auroral and polar ionospheres. In this investigation, only the events of 15 and 16 March 2018 during the evening corresponding to auroral and polar latitudes, respectively, were discussed.

At auroral and polar latitudes, intermittent and inhomogeneous particle precipitation distributed over geomagnetic latitudes and longitudes originated very low velocity electron density irregularities that induced enhanced temporal TEC fluctuations as GPS ray paths were scanning through them. Whereas at polar latitudes in addition to intermittent and inhomogeneous particle precipitation, polar cap patches drifting at a velocity much faster than the scan velocity of GPS ray paths at ionospheric heights, induced enhanced temporal TEC fluctuations on the GPS ray paths that were traversed.

In addition, the comparison between ionisation structures detected by means of EISCAT UHF/ESR profiles and intensification in TEC fluctuations on GPS ray paths in the proximity of EISCAT UHF/ESR beams suggests that these ionospheric irregularities were distributed over spatial distances of up to approximately $300\ km$ in the E layer and up to approximately $800\ km$ in the F layer. In both the auroral and polar ionospheres, EISCAT UHF/ESR electron density profiles suggest that the observed electron density structures were mainly large-scale and this was validated

by the observed intensification in the TEC fluctuations on GPS ray paths of relevance.

7 Performance of GPS Positioning in the Presence of Phase Fluctuations originated by Ionospheric Irregularities at High-latitudes

7.1 Introduction

This chapter is a follow up on Chapter 6 where EISCAT UHF/ESR incoherent scatter radars were used to investigate GPS phase fluctuations originating from auroral and polar irregularities in the auroral and polar ionospheres. In this chapter, the impact of auroral and polar irregularities on the performance of GPS positioning solutions was investigated. EISCAT UHF/ESR profiles of electron densities were co-aligned with TEC fluctuations and 3-D positioning solutions in Precise Static (PS) and Broadcast Kinematic (BK) to investigate the causal relationship. PS and BK solutions were used to understand the effects of irregularities on real-time and safety-critical applications. GPS positioning performance was investigated over auroral and polar latitudes by means of:

a) Measurements from different temporal resolution GNSS receivers (30-s and 1-s RINEX data).
b) Different geomagnetic conditions (quiet, moderately-active, and severe storm conditions).

Applications such as surveying, autonomous navigation, aviation, and precision agriculture increasingly rely on continuous and reliable GNSS positioning, navigation, and timing solutions [*Cosmen-Schortmann et al., 2008; Shagimuratov et al., 2012; Lee et al., 2017*]. However, ionospheric irregularities can originate temporal fluctuations on GNSS signals. Amplitude and phase fluctuations on GNSS signals can cause higher-order errors that cannot be removed by a combination of observables from different frequencies [*van den IJssel et al., 2016*]. Intensified errors in positioning solutions are a consequence of residual errors on the combination of observables at different frequencies [*Bhattacharyya et al., 2000; Skone, 2001; van den IJssel et al., 2016*]. In the presence of irregularities, positioning errors especially in the auroral and polar ionospheres can be significant and with intensified fluctuations.

Ionospheric irregularities can have spatial scale size between small-scale to large-scare irregularities originating from plasma instability mechanisms [*Kelley, 2009*]. Propagation of GNSS signals through large-scale irregularities is responsible for longer phase fluctuations whereas propagation through small-scale irregularities originates amplitude and phase fluctuations with shorter duration [*Xu et al., 2007; Prikryl et al., 2010; Forte et al., 2013; Forte et al., 2017*]. These rapid fluctuations with shorter duration of amplitude and phase is called scintillation. Phase fluctuations as a consequence of large-scale irregularities can be characterised by means of temporal fluctuations in TEC whilst intensity and phase fluctuations originating from small-scale irregularities can be identified and quantified in terms of scintillation indices (i.e. S_4 and σ_ϕ) [*Basu et al., 1988; Bhattacharyya et al., 2000; Xu et al., 2007; Prikryl et al., 2010*].

In the auroral and polar ionospheres, phase fluctuations are predominantly caused by large-scale irregularities. These large-scale irregularities originate from particle precipitation and polar patches in the polar ionosphere but mainly particle precipitation in the auroral ionosphere [*Fejer and Kelley, 1980; Kelley et al., 1982; Keskinen and Ossakow, 1983; Prikryl et al., 2010; John et al., 2020*]. In the region, the frequency and intensity of large-scale irregularities are directly proportional to geomagnetic conditions. Hence, phase fluctuations observed on GNSS signals are intensified during disturbed geomagnetic conditions manifesting as storms and substorms [*Aarons, 1982; Doherty el., 2003; Prikryl et al., 2010; Skone, 2001; Skone and Cannon, 1998*].

This chapter aimed to investigate the performance of GPS-only positioning in the presence of phase fluctuations in the auroral and polar ionospheres. To achieve this, phase fluctuations were characterised by means of residual errors on geometry-free (carrier phase observables) combination utilised in the processing of positioning solutions. Based on positioning applications, two positioning solutions were considered: single-point single-epoch positioning performed with dual-frequency L1 and L2 carrier phases and pseudoranges using broadcast ephemeris (BK) and precise ephemeris (PS). BK solution corresponds to real-time applications while PS solution is typical of post-processing PPP. 30-s and 1-s observables were read and analysed by means of gLAB tool during the positioning under different

geomagnetic conditions in March 2018 in conjunction with EISCAT UHF/ESR. The irregularities originating the observed TEC fluctuations on GPS signals were described by means of EISCAT UHF/ESR experiments.

7.2 Data and Methodology

The design geometry utilised in this investigation has been presented in Chapter 6. In EISCAT experiment, geodetic IGS station in Kiruna was considered, whilst in ESR experiment geodetic IGS station in Ny-Ålesund was considered [*John et al., 2020*]. Chapter 6 utilises measurements from only 30-s observables while this chapter combines measurements from both 30-s and 1-s observables to understand the performance of different temporal resolution GNSS receivers in the presence of ionospheric irregularities. 1-s observables concatenated from 15-minutes files to form a single 24-hour file and 30-s observables (24-hour file) were collected by means of RTKGET (http://www.rtklib.com/) software and downloaded through CDDIS website (https://cddis.nasa.gov/).

STEC was estimated from 1-s as well as 30-s carrier phase observables as given in equation (4.9) [*Correia et al., 2018; Rao and Dutt, 2017; Ward, 1997*] as stated in Chapter 6. In the same manner, temporal TEC fluctuations for each available GPS PRN were estimated as shown in equation (4.11) [*Carrano and Groves 2007; Forte et al., 2013; Luo et al., 2018*]. In view of this, Δt is $1\ s$ or $30\ s$ with respective to 1-s or 30-s observables, respectively. These TEC fluctuations were calculated simultaneously with EISCAT UHF/ESR measurements under different geomagnetic conditions. In addition, STEC is proportional to the geometry-free combination utilised in the processing of GPS positioning solutions. In this case, temporal fluctuations in $TEC(t)$ are proportional to residual errors in the geometry-free combination associated with positioning errors.

In this investigation, the different positioning solutions were calculated from 1-s and 30-s observables by means of gLAB available on-line at https://gage.upc.es/gLAB/ [*Dionisio et al., 2010; Hernandez-Pajares et al., 2010; Ibáñez et al., 2018*]. At the auroral latitude, the positioning solutions were calculated from Kiruna (KIRU) IGS station while at the polar latitude Ny-Ålesund (NYA2) IGS station was considered.

During this investigation, gLAB v5.4.4 developed by gAGE (research group of Astronomy and Geomatics) Technical University of Catalonia (UPC) on 10 June 2019 was used. This version of gLAB only reads and processes the GPS constellation. The initial screen of gLAB Graphic User Interface (GUI) is shown in Figure 7.1.

Figure 7.1: Initial screen of gLAB GUI. [Courtesy of gAGE/UPS]
Source: https://gage.upc.edu/gLAB/

BK and PS positioning solutions used in this investigation can be categorised into five sections. They are input, preprocess, modelling, filter, and output modules. Each of the positioning solutions is presented as follows:

a) The INPUT module.
   The INPUT module utilised in gLAB, either BK or PS solutions, is shown in Figure 7.1. It executes all the input reading capabilities such as RINEX observation, ANTEX, and orbit and clock source files.
b) The PREPROCESS module.
   This module processes the data before the MODEL stage.
c) The MODELLING module.
   This module is utilised to model the receiver measurements.
d) The FILTER module.
   This module implements the Extended Kalman Filter (EKF) to obtain estimations of the required parameters.
e) The OUTPUT module.

This module outputs the data obtained from the FILTER stage.

For details of how gLAB reads and processes GPS positioning solutions, refer to gLAB manual (https://gage.upc.edu/sites/default/files/gLAB/gLAB_SUM.pdf).

In each of the days during the investigation for auroral and polar ionospheres, positioning solutions in BK and PS were calculated. Here, pseudorange and carrier phase observables were used to compute the positioning solutions. For the detection of cycle slips, the Melbourne-Wübbena (geometry-free and ionosphere-free) and geometry-free (ionosphere-induced) combinations were used to process BK and PS positioning solutions through gLAB. Geometry-free is a cycle slip detection technique for dual frequency receivers using carrier phase measurements only. The detection is done by eliminating all geometry-related errors. Like geometry-free, ionosphere-free is a cycle slip detection which removes all ionosphere-related errors. On the other, Melbourne-Wübbena is a combination of geometry-free and ionosphere-free cycle slip detection techniques.

ANTEX files, which provide information on the antenna phase centre of GNSS satellites and the ground-based stations, were obtained from standard repositories through gLAB help tool [ftp://ftp.igs.org/pub/station/general/pcv_archive/]. While performing positioning in BK solution, orbit and clock sources were collected from RINEX navigation files corresponding to 1-s and 30-s observables. On the other hand, for positioning in PS solution, satellites orbit and clock sources were collected from SP3 and Clock sources (ftp://cddis.gsfc.nasa.gov/pub/gps/products). For the benefit of this investigation, BK and PS positioning solutions were considered because of their relevance to real-time and post-processing applications. Examples of real-time positioning applications are autonomous navigation, civil aviation, precision agriculture while geodesy and surveying are examples of post-processing applications.

Here, instantaneous 3-D positioning error E_{3D} was calculated by means of equation (7.1) [*Borre et al., 2007; Jacobsen and Dähnn, 2014; Vani et al., 2014*]:

$$E_{3D}(t) = \sqrt{(X(t) - X_0)^2 + (Y(t) - Y_0)^2 + (Z(t) - Z_0)^2} \qquad [m] \qquad (7.1)$$

Where $X(t)$, $Y(t)$, and $Z(t)$ are the ground-based station coordinates in the Earth-Centred, Earth-Fixed (ECEF) reference frame at each epoch t. X_0, Y_0, and Z_0 are

the receiver *a-priori* ECEF coordinates obtained from RINEX observation file for a given geodetic GNSS station [*Borre et al., 2007; Jacobsen and Dähnn, 2014; Vani et al., 2014; Vani et al., 2019*]. ECEF is the coordinate system that is used by most satellite systems especially GPS to designate an Earth position.

This $E_{3D}(t)$ was calculated at 1-s and 30-s rates from 30-s and 1-s observables in both the BK and the PS solutions and then compared with residual errors quantified through TEC fluctuations ($\frac{\Delta TEC}{\Delta t}$) at 1-s and 30-s respectively, in correspondence to the electron density structures detected on the EISCAT UHF/ESR profiles. Temporal fluctuations in TEC were considered for available GPS PRNs with elevation angle from 5°. This was to ensure consistency with the positioning solutions which were based on the same elevation angle mask (5°) to minimise errors due to low SNR (33 dB-Hz mask) and multipath [*Ibáñez et al., 2018*].

7.3 Results

Figure 7.2, from top to bottom, shows EISCAT profiles of electron density, electron temperature, ion temperature, and ion drift velocity over Kiruna between 20:00 and 24:00 UT during 12 March 2018. To support understanding of the design geometry of EISCAT experiment on 12 March 2018, refer to Figure 7.3. Figure 7.3 shows slant ranges of EISCAT beams from EISCAT antenna to ionospheric pierce points where ESR alternately scans and follows specific GPS PRNs ray paths at the chosen ionospheric shell heights; as well as azimuth angles; and elevation angles at these shell heights over Kiruna GNSS receiver station (KIRU) on the evening of 12 March 2018.

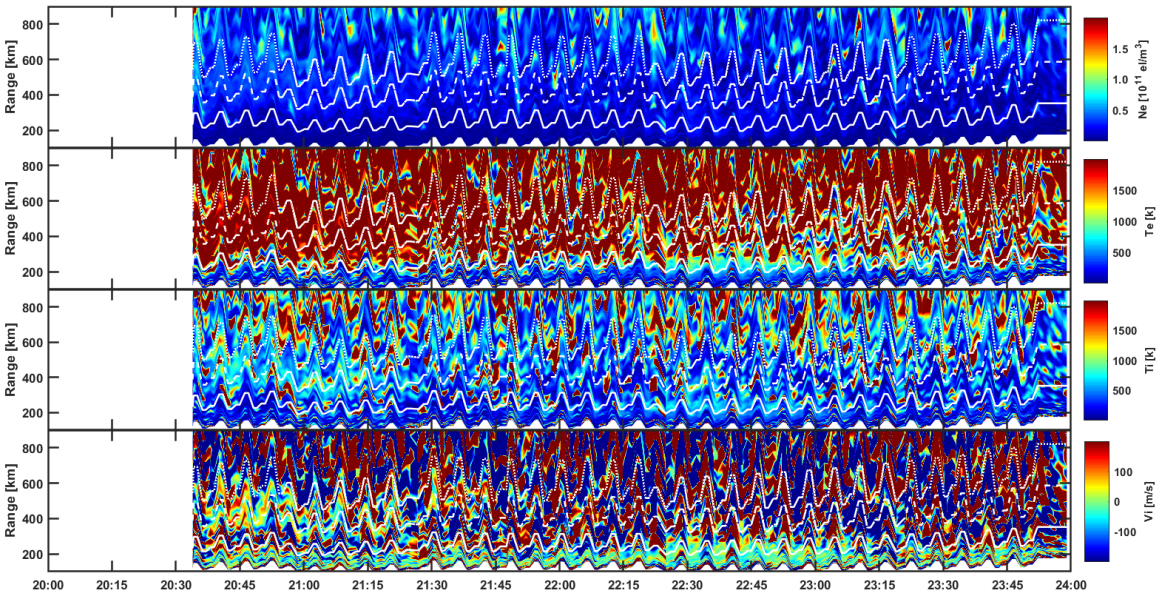

Figure 7.2: From top bottom shows EISCAT profiles of electron density, electron temperature, ion temperature, and ion drift velocity, respectively over Kiruna between 20:00 and 24:00 UT on 12 March 2018. The solid, dashed, and dotted white lines on the profiles correspond to $150\ km$, $250\ km$, and $350\ km$ ionospheric shell heights, respectively. The interval of time between 20:00 and 20:35 UT corresponds to when there was no measurement from EISCAT.

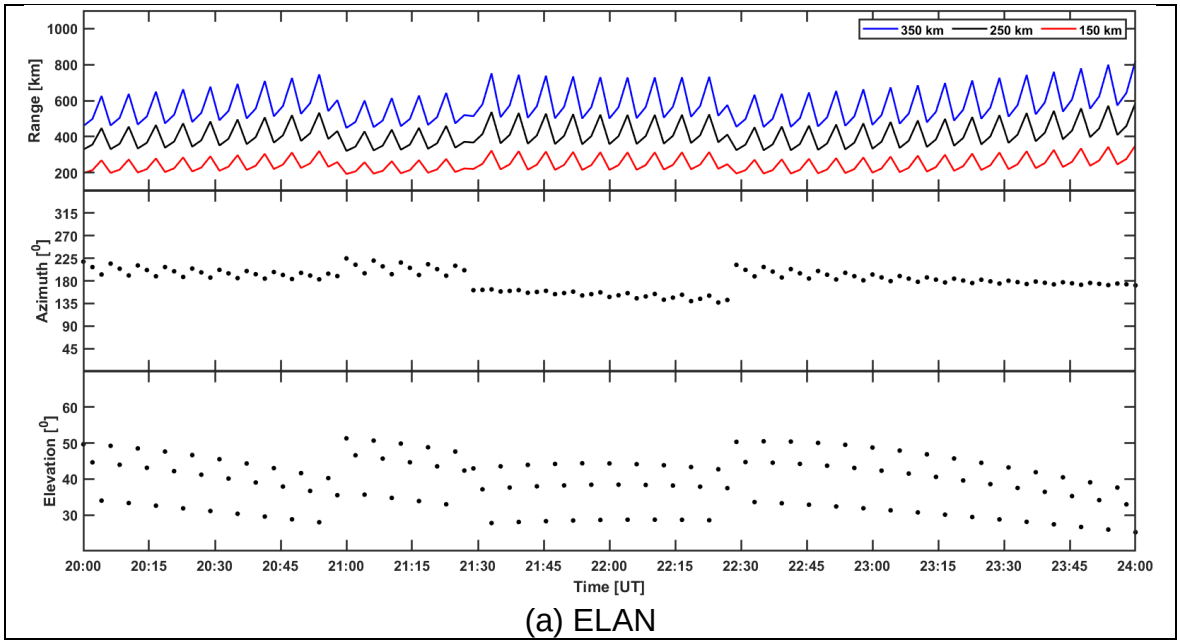

(a) ELAN

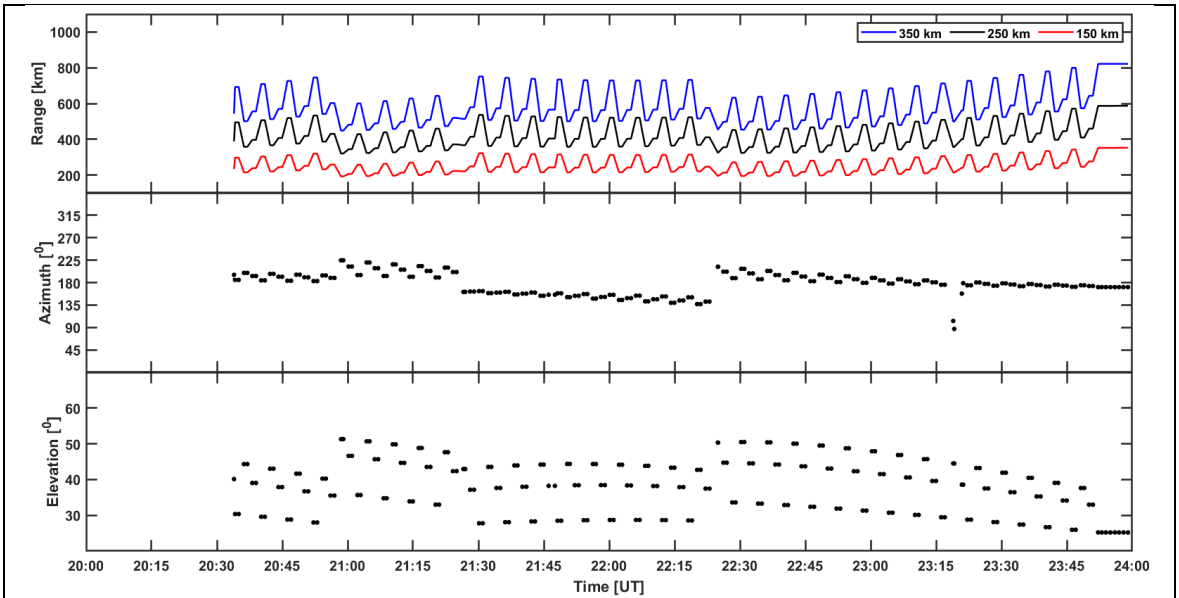

(b) EISCAT

Figure 7.3: From top to bottom shows slant ranges of EISCAT beams from EISCAT antenna to ionospheric pierce points where the incoherent scatter radar alternatively scans and follows GPS PRNs 26 (20:00-21:00 UT), 16 (21:00-21:30 UT), 21 (21:30-22:30 UT), and 27 (22:30-24:00 UT) ray paths at $150\ km$ (red line), $250\ km$ (black line), and $350\ km$ (blue line) ionospheric shell heights; azimuth angles; and elevation angles at these shell heights over Kiruna between 20:00 and 24:00 UT on 12 March 2018. The interval of time between 20:00 and 20:35 UT corresponds to when there was no measurement from EISCAT.

The slant range, azimuth, and elevation angles in Figure 7.3a were derived from simulated data by means of ELAN. The simulated slant range, azimuth, and elevation angles were compared with the same parameters obtained from the experiment (EISCAT) as indicated in Figure 7.3b. In Figure 7.3b, there were no measurements from EISCAT between 20:00 and 20:35 UT and 23:53 and 24:00 UT. Comparison of Figure 7.3a with Figure 7.3b showed a good agreement. The profiles provide insight into the auroral ionospheric condition indicative of a typical quiet day event with K_p value of 0 courtesy of the NOAA (ftp://ftp.swpc.noaa.gov/pub/indices/old_indices/).

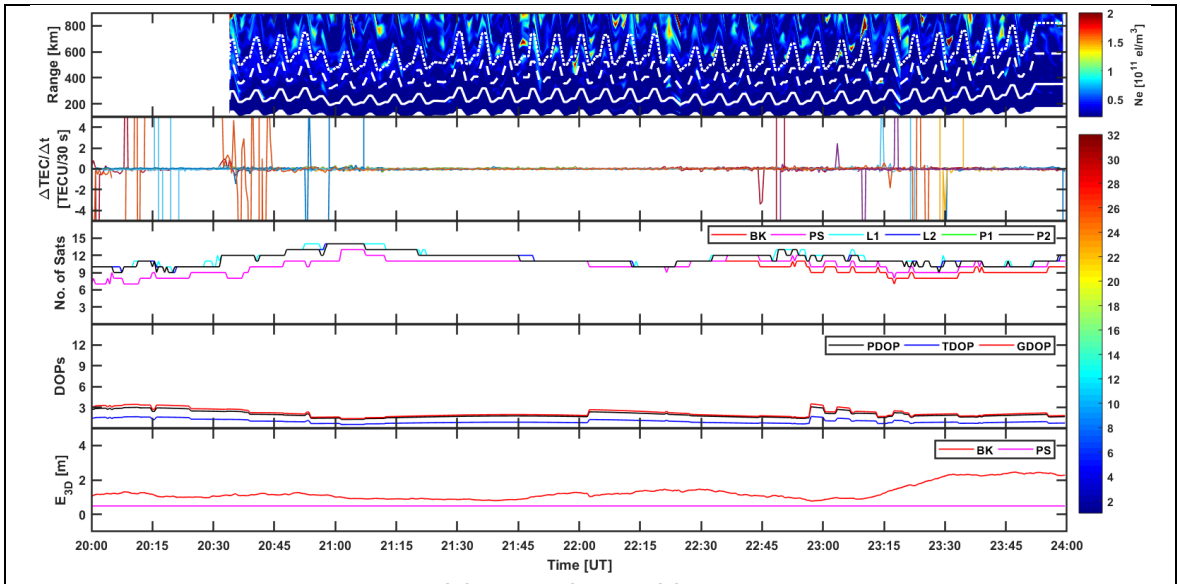

(a) 30-s observables KIRU

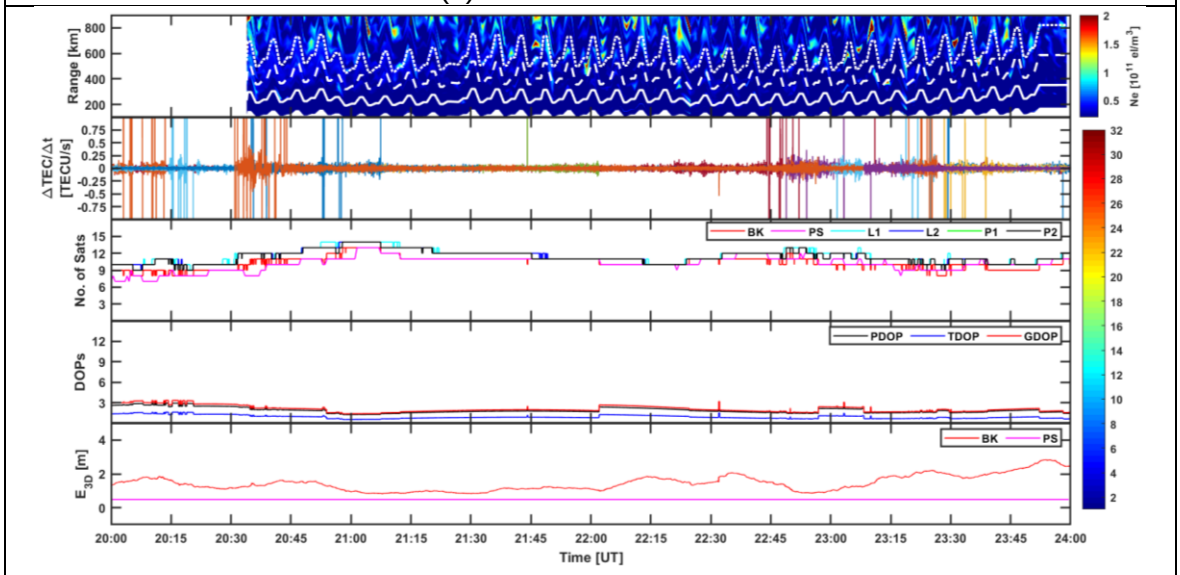

(b) 1-s observables KIRU

Figure 7.4: From top to bottom shows EISCAT profiles of electron density; temporal TEC fluctuations for GPS PRNs in view with elevation angle from 5°; number of available observables (L1 – cyan line, L2 – blue line, P1 – green line, and P2 – black line) from GPS PRNs in view together with the number of PRNs considered in the BK solution (red) and in the PS solution (magenta); DOPs (PDOP – black line, TDOP – blue line, and GDOP – red line); and the 3-D positioning error E_{3D} for the BK solution (red) and the PS solution (magenta). TEC fluctuations and positioning errors were calculated for the ground-based station KIRU (Kiruna) in conjunction with EISCAT profiles of electron density on the evening of 12 March 2018. (a) 30-s observables and E_{3D}, (b) 1-s observables and E_{3D}. L1 and L2 are carrier phase observables and P1 and P2 are pseudorange observables. The colour bar (right-hand side) indicates 1-32 GPS PRNs.

Figure 7.4 shows positioning results in conjunction with EISCAT measurements conducted on the evening of 12 March 2018. Figure 7.4a shows the results where 30-s observables were utilised to calculate $E_{3D}(t)$ at every $30\ s$. Similarly, Figure

7.4b shows the results where 1-s observables were used to calculate $E_{3D}(t)$ at every $1\,s$. Figures 7.4, from top to bottom, shows electron density profiles, TEC fluctuations, number of available observables from GPS PRNs in view together with the number of PRNs considered in the positioning solutions, DOPs, and the 3-D positioning error. The increased TEC fluctuations observed between 20:00 and 21:00 UT and between 22:45 and 23:45 UT are caused by low elevation satellites given the elevation mask of 5°. L1 and L2 are carrier phase observables and P1 and P2 are pseudorange observables obtained from RINEX observation files. In the middle panels of Figure 7.4, the values of BK and PS are comparable and the values of L1, L2, P1, and P2 are comparable. To plot the figure, BK, PS, L1, L2, P1, and P2 are listed starting from the first to the last item plotted. This implies at intervals of time where BK and PS have the same value(s), PS magenta line overrides the BK red line. Similarly, L2 blue line overrides L1 cyan line. P1 green line overrides L1 cyan line, and P2 black line overrides P1 green line, respectively. This explains why some colour lines are not visible in Figure 7.4 and subsequent figures in this Chapter where BK, PS, L1, L2, P1, and P2 appeared.

In Figure 7.4 (4th panel from top), DOP (Dilution of Precision), PDOP (Position Dilution of Precision), TDOP (Time Dilution of Precision), and GDOP (Geometric Dilution of Precision) provide insight into the positioning errors caused by the relative positions of GPS satellites with respect to, in this case, a ground-based GNSS receiver station. Smaller value means smaller positioning solution error otherwise larger positioning solution error. The more number of available GPS satellites and also spread apart in the sky, the GNSS receiver would have a smaller positioning error which is good for the performance of GPS positioning. This explanation applies to all figures in this Chapter were DOP, PDOP, TDOP, and GDOP are mentioned. For details on DOPs, refer to Langley (1999).

In Figure 7.4 (bottom panels), the BK solution (red line) varies between $0.4\,m$ and $3\,m$ because the orbit and clock data are obtained from the daily GPS broadcast ephemeris data combined with the relative movement of the GNSS receiver. On the other hand, the PS solution (magenta line) is constant on average because the orbit and clock data are obtained from precise sources (SP3 file and Clock) combined with static GNSS receiver. These precise orbit and clock sources have undergone reasonable error corrections to improve on data accuracy and precision. Thus, BK

solution is less accurate than PS solution in most instances. However, where BK solution is more accurate than PS solution which might occur at short intervals of time, this is likely caused by the random prediction of the orbit and clock data.

The geomagnetic conditions on 12 March 2018 were quiet with $K_p = 0$ and with no significant structures detected by EISCAT in the auroral ionosphere. Almost all available GPS PRNs were considered in the positioning solutions with only a very few of them showing larger residual errors, leading to low values with low variability for E_{3D} in both positioning solutions. In 2nd panels of Figure 7.4(a and b) from top between 20:00 and 21:00 UT and between 22:45 and 24:00 UT, intensification of TEC fluctuation of $\pm 5\, TECU/30\, s$ from 30 s observables and $\pm 1\, TECU/s$ from 1 s observables were observed. The increased TEC fluctuations are possibly caused by satellites with low elevation angles. There seems to be no significant difference between the 30-s and the 1-s positioning errors. As shown in Figure 7.4, the measurements indicate that the 12 March 2018 can be considered a quiet event. Comparisons with different geomagnetic conditions (moderate to severe) will be made to provide insight into the influence of geomagnetic activity on high-latitudes ionospheric activity.

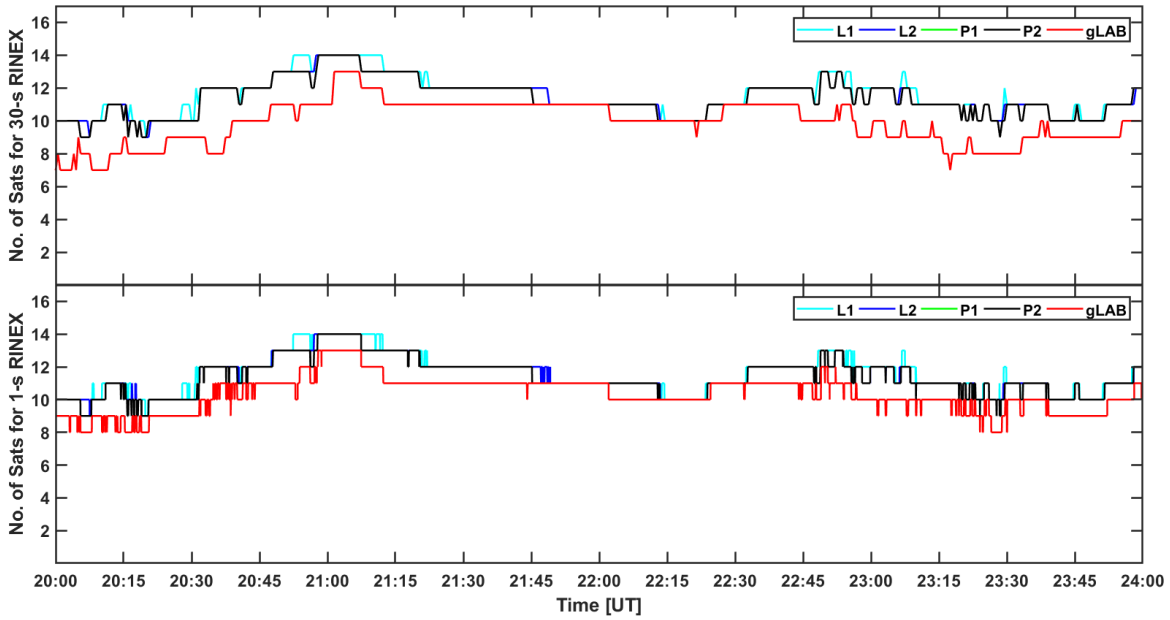

Figure 7.5: From top to bottom shows the number of available observables (L1 – cyan line, L2 – blue line, P1 – green line, and P2 – black line) from all available GPS PRNs in view together with the number of PRNs considered in the BK solution (gLAB, red line), respectively over Kiruna between 20:00 and 24:00 UT on 12 March 2018 using 30-s and 1-s RINEX observation data. L1 and L2 are carrier phase observables and P1 and P2 are pseudorange observables.

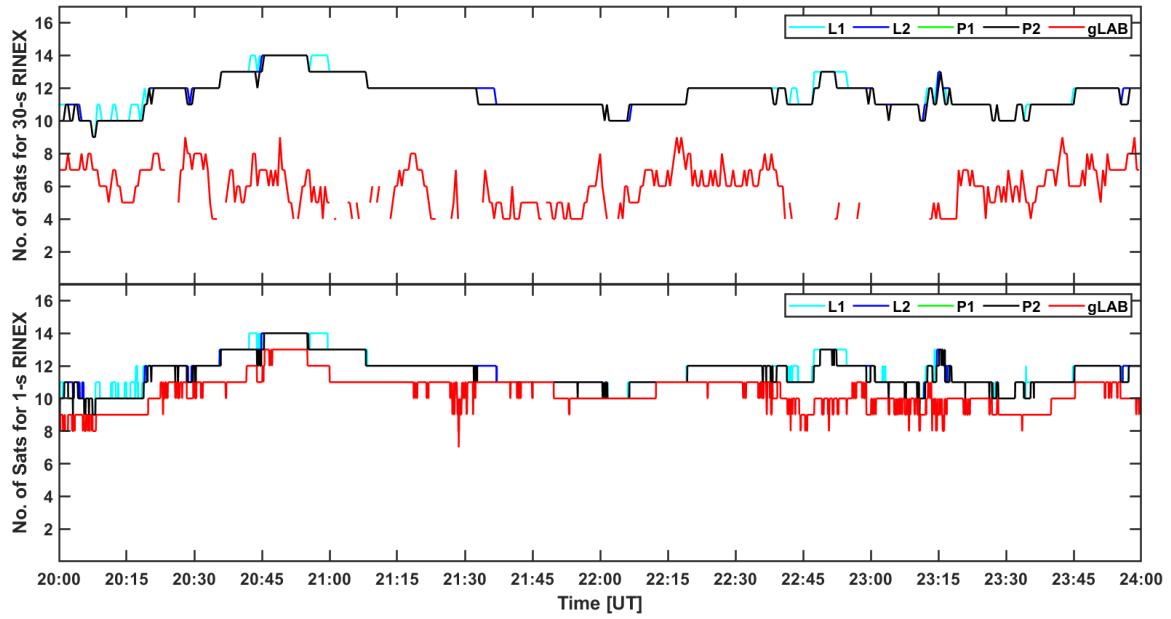

Figure 7.6: From top to bottom shows the number of available observables (L1 – cyan line, L2 – blue line, P1 – green line, and P2 – black line) from all available GPS PRNs in view together with the number of PRNs considered in the BK solution (gLAB, red line), respectively over Kiruna between 20:00 and 24:00 UT on 15 March 2018 using 30-s and 1-s RINEX observation data. L1 and L2 are carrier phase observables and P1 and P2 are pseudorange observables.

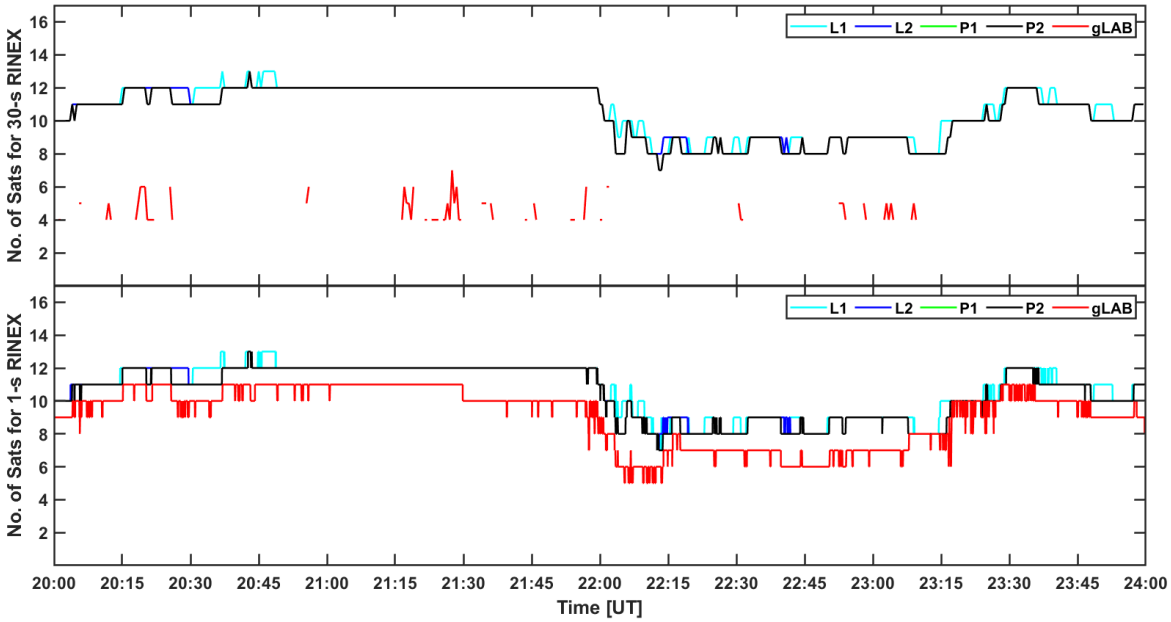

Figure 7.7: From top to bottom shows the number of available observables (L1 – cyan line, L2 – blue line, P1 – green line, and P2 – black line) from all available GPS PRNs in view together with the number of PRNs considered in the BK solution (gLAB, red line), respectively over Kiruna between 20:00 and 24:00 UT on 17 March 2015 using 30-s and 1-s RINEX observation data. L1 and L2 are carrier phase observables and P1 and P2 are pseudorange observables.

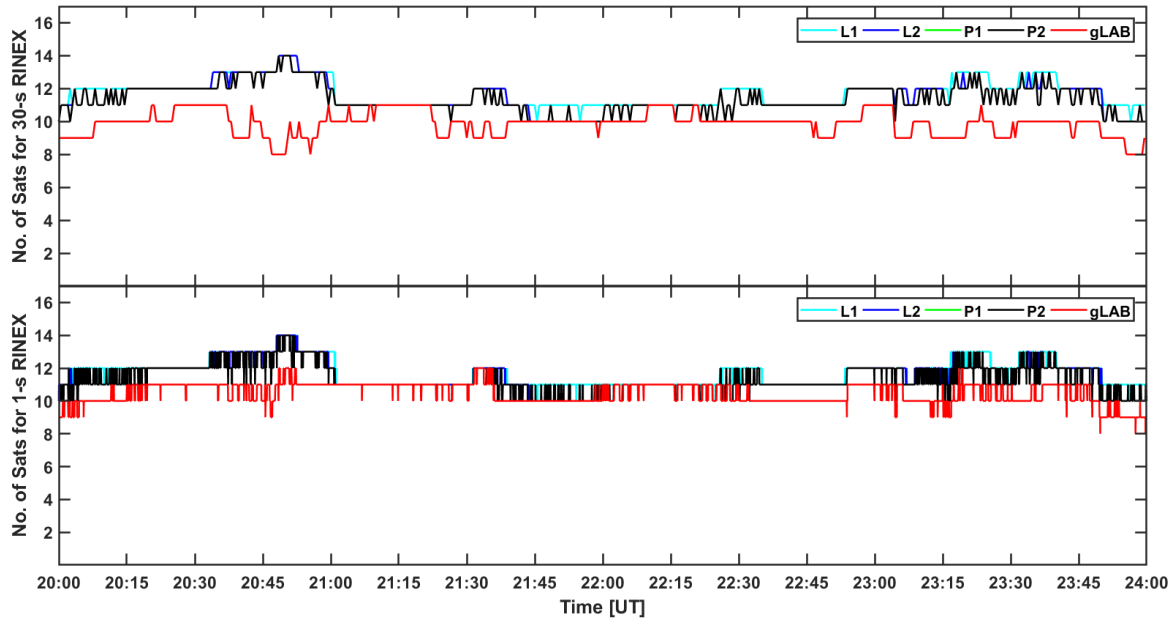

Figure 7.8: From top to bottom shows the number of available observables (L1 – cyan line, L2 – blue line, P1 – green line, and P2 – black line) from all available GPS PRNs in view together with the number of PRNs considered in the BK solution (gLAB, red line), respectively over Ny-Ålesund between 20:00 and 24:00 UT on 12 March 2018 using 30-s and 1-s RINEX observation data. L1 and L2 are carrier phase observables and P1 and P2 are pseudorange observables.

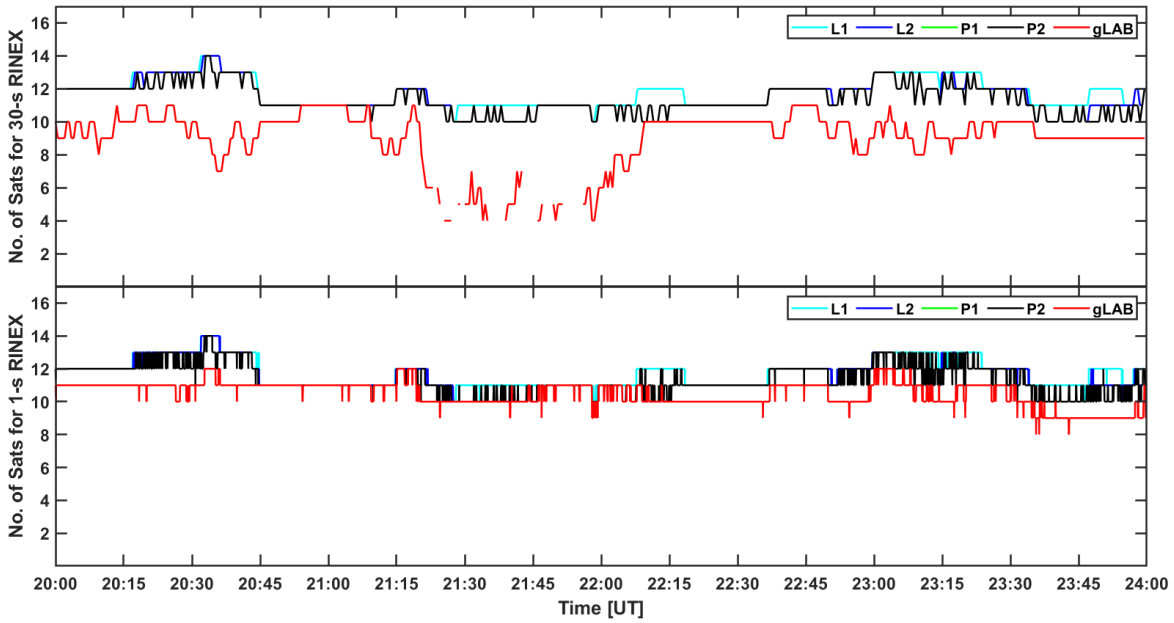

Figure 7.9: From top to bottom shows the number of available observables (L1 – cyan line, L2 – blue line, P1 – green line, and P2 – black line) from all available GPS PRNs in view together with the number of PRNs considered in the BK solution (gLAB, red line), respectively over Ny-Ålesund between 20:00 and 24:00 UT on 16 March 2018 using 30-s and 1-s RINEX observation data. L1 and L2 are carrier phase observables and P1 and P2 are pseudorange observables.

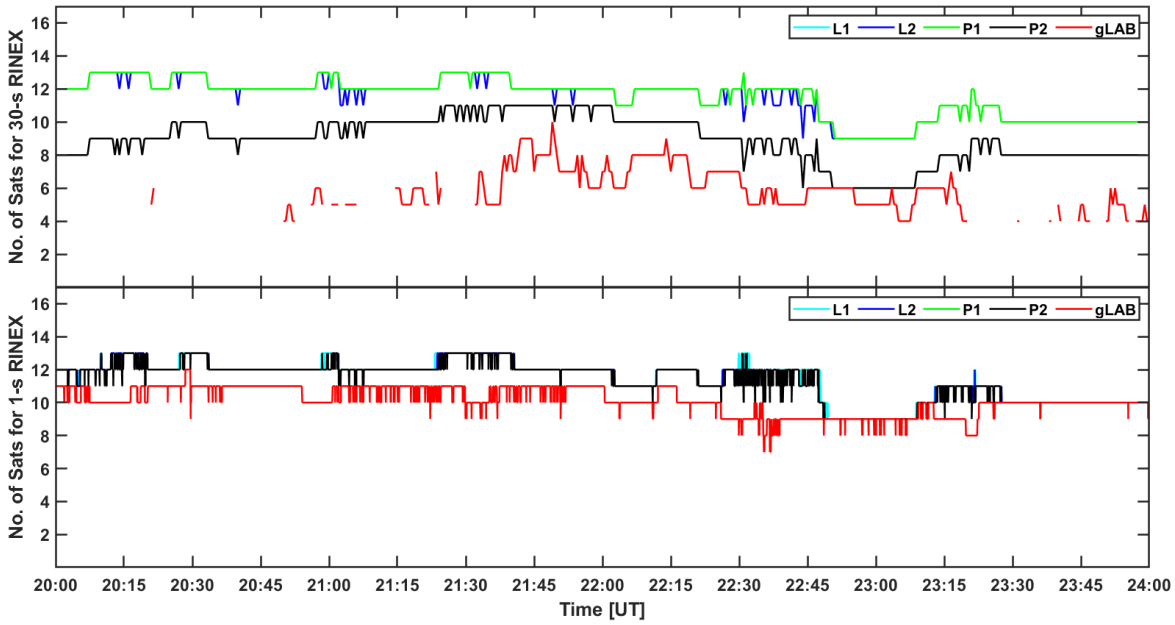

Figure 7.10: From top to bottom shows the number of available observables (L1 – cyan line, L2 – blue line, P1 – green line, and P2 – black line) from all available GPS PRNs in view together with the number of PRNs considered in the BK solution (gLAB, red line), respectively over Ny-Ålesund between 20:00 and 24:00 UT on 17 March 2015 using 30-s and 1-s RINEX observation data. L1 and L2 are carrier phase observables and P1 and P2 are pseudorange observables.

To appreciate the correlation between ionospheric condition with the number of GPS satellites used in the positioning solution on the evening of 12 March 2018, refer to Figure 7.5. In Figure 7.5, the number GPS observations available from raw RINEX data (30-s top panel and 1-s bottom panel) and the number GPS satellites used in the positioning solution (BK) by gLAB are of similar values on average. It was understood in Figures 7.4, 7.11-7.13, and7.17 middle panels that the number of satellites used to process positioning solution in BK (red line) was always less than or equal to the PS (magenta). In view of this, Figures 7.5-7.10 considered only the BK solution in both 30-s and 1-s measurements to show the worst-case scenario. As observed in the event of 12 March 2018, fewer satellites were discarded by gLAB due to cycle slips in the carrier phase observables. Figure 7.5 (top panel, 30-s observables) shows the number of satellites from 7 and above while Figure 7.5 (bottom panel, 1-s observables) shows the number of satellites from 8 and above.

Thus, the use of 1-s observables increases the number of satellites utilised to process the positioning solution. By extension, availability and accuracy performance requirements are improved. In the case of the polar ionosphere during

12 March 2018, Figure 7.8 shows a good agreement with Figure 7.4. Hence, the results indicated in Figure 7.8 inferred a typical quiet day as well.

Figure 7.11 shows the same quantities as in Figure 7.4 but for EISCAT measurements collected on the evening of 15 March 2018. Details of EISCAT profiles during 15 March 2018 were presented in Chapter 6. On the evening of March 2018, the geomagnetic conditions (K_p value of 4) were active which creates a good environment for particle precipitation in the auroral oval. Particle precipitation in the auroral ionosphere can originate inhomogeneous and intermittent ionisation irregularities (for details refer to *John et al., 2020*). In the 2nd panel (from top) of Figure 7.11a, intensified fluctuations in TEC implies larger residual errors on geometry-free combinations on the evening of 15 March 2018 responsible for fewer GPS PRNs used to process positioning solution. The intensified TEC fluctuations calculated at elevation mask of 5° (Figure 7.11a) are more compared to values in Figure 6.7b because the latter was calculated at elevation mask of 20°. Although 3-D positioning error in PS solution showed constant value on average, the BK solution showed higher variability as indicated in Figure 7.11a. In both BK and PS solutions, gaps were originated whenever the number of satellites used in the positioning solution was fewer than 4. However, in Figure 7.11b, the use of 1-s observables shows enhanced TEC fluctuations with shorter durations which suggest lower residual errors on the geometry-free combination. Dilutions of precision were below 6. While 3-D positioning error for PS solution was relatively constant, the BK solution showed lower variability during the time of measurements. In general, the use of 1-s observables removes gaps and reduces residual errors hence the observed improvement of accuracy performance requirement in both the BK and PS solutions.

In general, when both 30-s and 1-s observables were used to calculate the positioning solutions, intensification in TEC fluctuations were in agreement with the observed auroral structures except in instances where satellites with lower elevation angles were considered. The intensification in TEC fluctuations implies the occurrence of residual errors which are associated with the observed number of satellites both available from the raw RINEX observation file and the number of satellite utilised to process the positioning solutions.

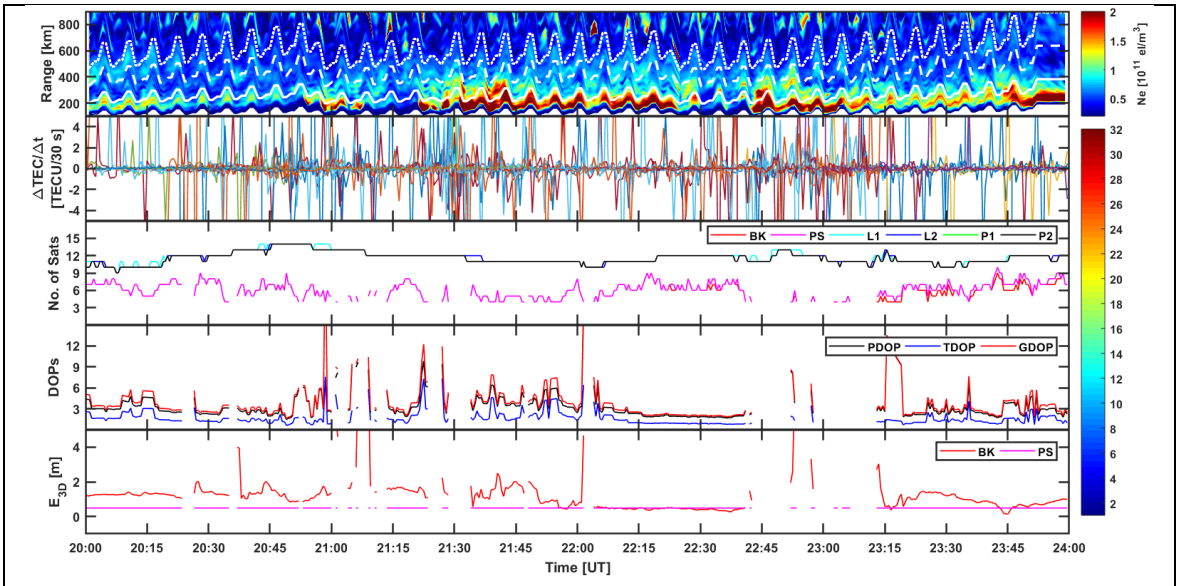

(a) 30-s observables KIRU

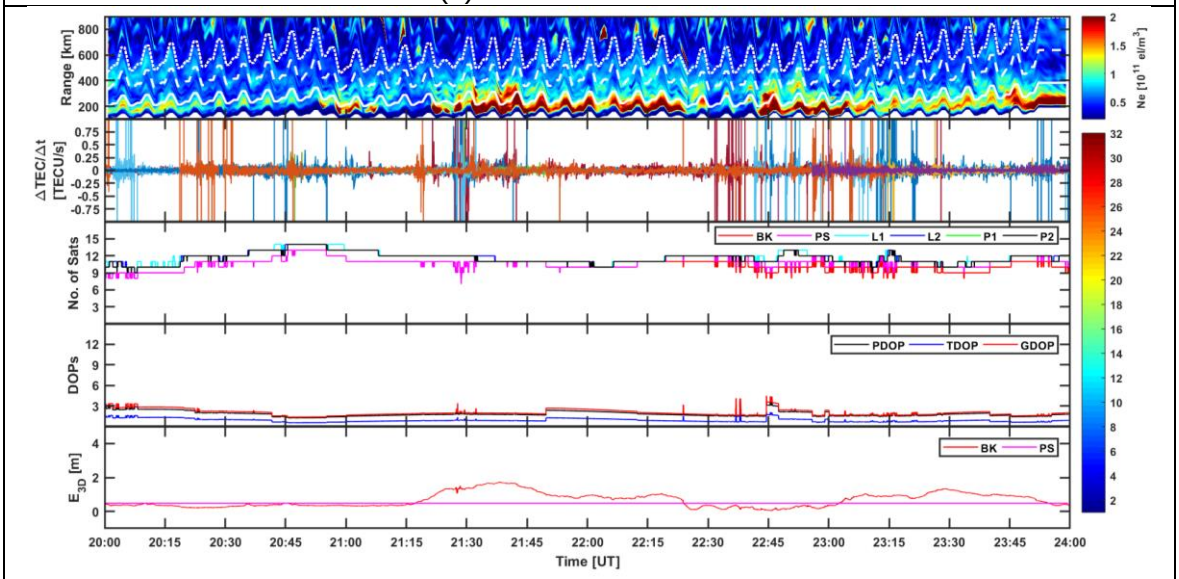

(b) 1-s observables KIRU

Figure 7.11: From top to bottom shows EISCAT profiles of electron density; temporal TEC fluctuations for GPS PRNs in view with elevation angle from 5°; number of available observables (L1 – cyan line, L2 – blue line, P1- green line, and P2 – black line) from GPS PRNs in view together with the number of PRNs considered in the BK solution (red) and in the PS solution (magenta); DOPs (PDOP – black line, TDOP – blue line, and GDOP – red line); and the 3-D positioning error E_{3D} for the BK solution (red) and the PS solution (magenta). TEC fluctuations and positioning errors were calculated for the ground-based station KIRU (Kiruna) in conjunction with EISCAT profiles of electron density on the evening of 15 March 2018. (a) 30-s observables and E_{3D}, (b) 1-s observables and E_{3D}. L1 and L2 are carrier phase observables and P1 and P2 are pseudorange observables.

As mentioned in the event of 12 March 2018, Figure 7.6 provides insight into the association between the ionospheric condition of 15 March 2018 with the number of GPS satellites utilised in the positioning solution using BK solution only. The top

panel of Figure 7.6 shows an increase in the difference between the number of GPS satellites available from 30-s RINEX data and the number of satellites utilised by gLAB in the positioning solution as opposed to the event of 12 March 2018. However, the bottom panel reveals improvement in the positioning solution due to an increase in the number of satellites used to process the positioning solutions by gLAB. No gaps and the number of satellites observed from both RINEX and gLAB was from 8 and above. In Chapter 6, the established source mechanism originating auroral irregularities on the evening of 15 March 2018 was particle precipitation.

Figure 7.12 shows the same quantities as in Figures 7.4 and 7.11 but for ESR measurements collected on the evening of 16 March 2018. As shown in Figure 7.12a, intensification in TEC fluctuations observed between 21:20 and 22:00 UT co-aligned with the observed polar structures by means of ESR. In this interval of time, enhancement in TEC fluctuations were associated with a fast-moving polar patch as well as particle precipitation [*John et al., 2020*]. Apart from this interval of time, enhancement in TEC fluctuations was observed corresponding to satellites with low elevation angles. The regular bands in TEC fluctuations from both 30 s and 1 s observables as indicated in Figure 7.12 between 21:45 and 22:15 UT and between 23:00 and 23:45 are due to low elevation satellites (elevation mask of 5°). More regular bands are observed in the 1 s observations than the 30 s observations because the former has higher temporal resolution than the latter. Hence, the use of 30-s observables enabled the detection of polar structures which are mostly large-scale structures. In Figure 7.12a, 3-D positioning error in BK solution and the dilutions of precision between 21:20 and 22:00 UT is characterised by larger values with larger variability and gaps. However, E_{3D} for the PS solutions shows a relatively constant value with gaps.

While Figure 7.12b (1-s observables) did not show good agreement between the observed polar structure by means of ESR and intensification in TEC fluctuations. Satellites with low elevation angles are responsible for the most observed intensification in TEC fluctuations and these are in agreement with the number of GPS satellites. DOPs were fewer than 6 and the number of satellites from both (RINEX and gLAB) was from 8 and above. E_{3D} for both BK and PS solutions did not show gaps. E_{3D} for PS solution was relatively constant but BK solution showed lower values and lower variability.

The effects of polar irregularities on GPS positioning is investigated as illustrated in Figure 7.9. The top panel of Figure 7.9 showed a considerable difference between the number of available satellites from raw RINEX observation file and the number of satellites used to process positioning solutions. Between 21:20 and 22:00 UT corresponding to when polar structures were observed by means of ESR, the difference was larger accompanied by gaps.

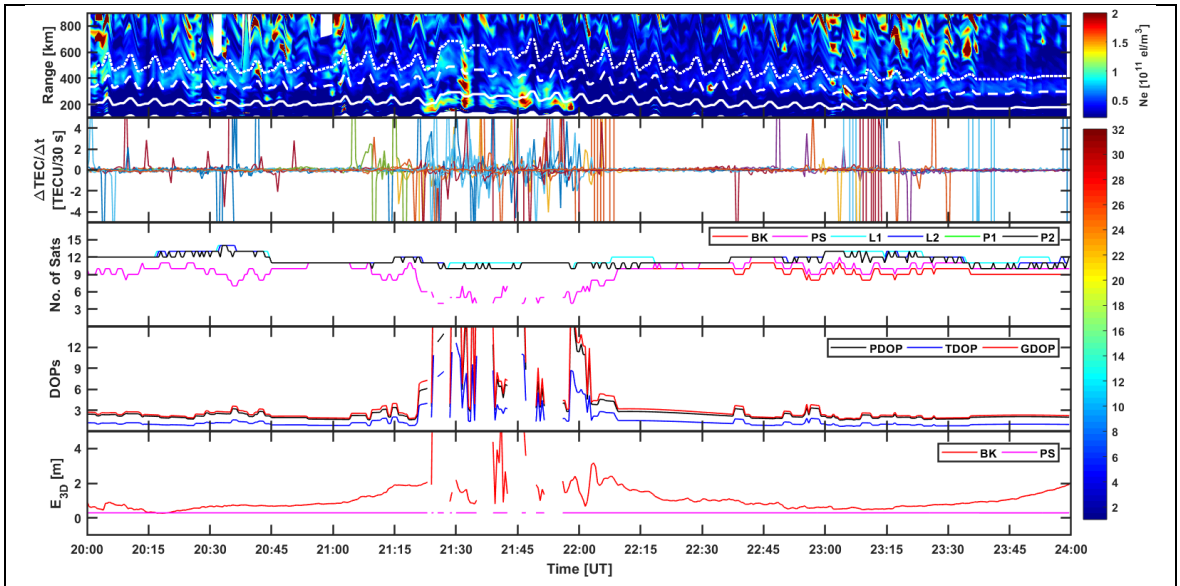

(a) 30-s observables NYA2

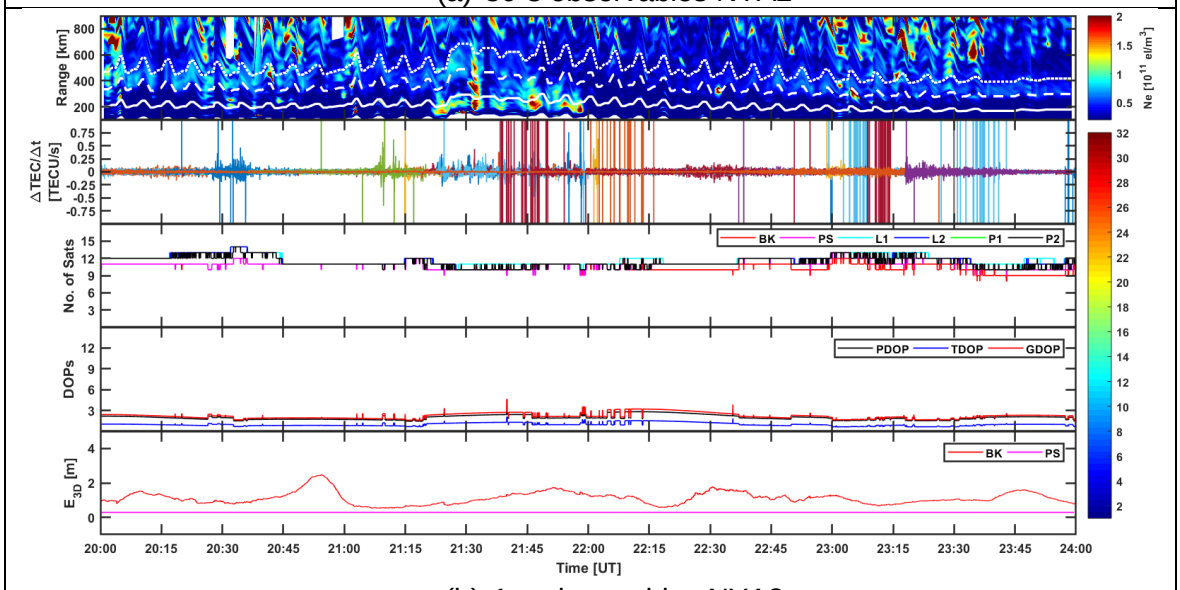

(b) 1-s observables NYA2

Figure 7.12: From top to bottom shows ESR electron density; temporal TEC fluctuations for GPS PRNs in view with elevation angle above 5°; number of available observables (L1 – cyan line, L2 – blue line, P1 – green line, and P2 – black line) from GPS PRNs in view together with the number of PRNs considered in the BK solution (red) and in the PS solution (magenta); DOPs(PDOP – black line, TDOP – blue line, and GDOP – red line); and the 3-D positioning error E_{3D} for the BK solution (red) and the PS solution (magenta). TEC fluctuations and positioning

errors were calculated for the ground-based station NYA2 (Ny-Ålesund) in conjunction with ESR profiles of electron density on the evening of 16 March 2018. (a) 30-s observables and E_{3D}, (b) 1-s observables and E_{3D}. L1 and L2 are carrier phase observables and P1 and P2 are pseudorange observables. The colour bar (right-hand side) indicates 1-32 GPS PRNs.

This implies more satellites were discarded due to ionospheric irregularities which induced cycle slips on the carrier phase observables. As observed in Figure 7.12b, the bottom panel of Figure 7.9 provides insight into the benefits of using 1-s observables in both BK and PS positioning solutions. On the evening of 16 March 2018 corresponding to the polar ionosphere measurements, the established source mechanisms responsible for the observed polar irregularities were polar patches combined with particle precipitation.

To appreciate the performance of GPS positioning at the auroral and polar latitudes during the geomagnetic storm and how this compares with the cases in both quiet and active geomagnetic conditions, case studies of St. Patrick's Day Storm on the evening of 17 March 2015 were considered. The auroral latitude station used is Kiruna (KIRU). In this way, the association of geomagnetic activity with ionospheric activity at high-latitudes is investigated. In this report, the case of the auroral ionosphere is first presented followed by the polar ionosphere.

In Figure 7.13a (30-s observables), enhanced TEC fluctuations were observed throughout the time of measurements. This enhancement in TEC fluctuations occurred over 70% of the time was observed on multiple satellites leading to a reduction in the number of satellites (maximum of 8) used in the positioning solution as well as data gaps.

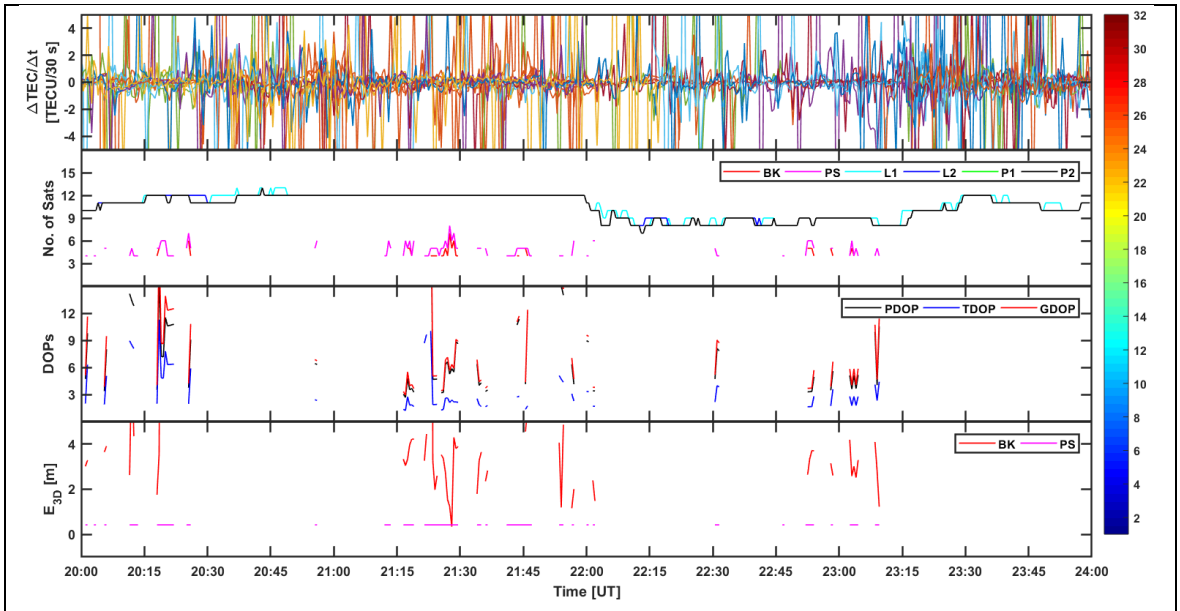

(a) 30-s observables KIRU

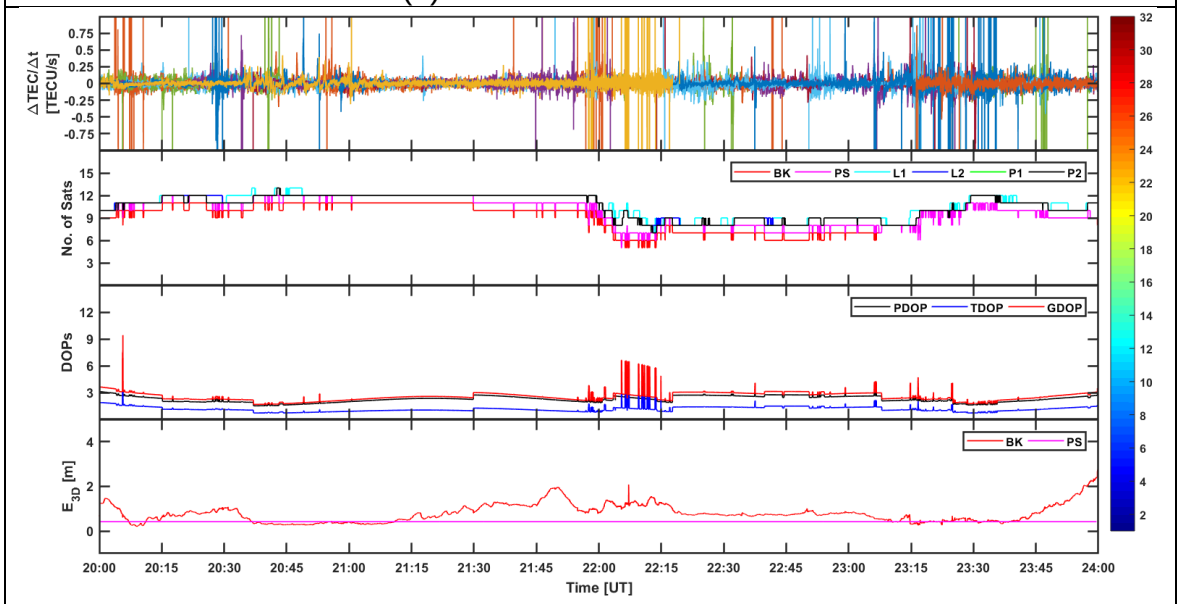

(b) 1-s observables KIRU

Figure 7.13: From top to bottom shows temporal TEC fluctuations for GPS PRNs in view with elevation angle above 5°; number of available observables (L1 cyan line, L2 – blue line, P1 – green line, P2 – black line) from GPS PRNs in view together with the number of PRNs considered in the BK solution (red) and the PS solution (magenta); the DOPs (PDOP – black line, TDOP – blue line, and GDOP – red line); and the 3-D positioning error E_{3D} for the BK solution (red) and the PS solution (magenta). TEC fluctuations and positioning errors were calculated for the ground-based station KIRU (Kiruna) on the evening of 17 March 2015 during St. Patrick's Day Storm. (a) 30-s observables and E_{3D}, (b) 1-s observables and E_{3D}. L1 and L2 are carrier phase observables and P1 and P2 are pseudorange observables. The colour bar (right-hand side) indicates 1-32 GPS PRNs.

Increase in TEC fluctuations which imply larger residual errors on the geometry-free combination for carrier phase observables almost throughout the time of measurements. DOPs and E_{3D} for BK solution were larger and larger variability

combined with gaps. Degraded DOPs means poor GPS satellites geometry as well. However, the E_{3D} for PS solution was constant on average combined with gaps. Unlike the cases in Figures 7.11a and 7.12a where the observed data gaps occurred below 40% of the time of measurements. Because of the disturbed ionospheric condition concurrent with the severe geomagnetic storm ($K_p = 8$), the overall accuracy and availability performance requirements were greatly impaired compared to the March 2018 events.

In Figure 7.13b (1-s observables), enhanced TEC fluctuations were observed between 20:00 and 21:10 UT and between 22:00 and 23:30 UT. The number of available GPS satellites from raw RINEX observation files and the number of GPS satellites used to process the positioning solutions was about the same throughout the time of measurements. As observed in Figures 7.11a and 7.12a, the number of satellites in the BK solution is fewer than that in the PS solution. The least number of satellite was around 5 on average and this did not lead to gaps caused by cycle slips on carrier phase observables. Although the observed errors were reduced significantly because of the use of 1-s observables as compared to Figure 7.13a, the E_{3D} for PS solution was about the same except for the absence of gaps.

To appreciate the impact of the disturbed ionospheric condition during severe geomagnetic condition on GPS positioning, refer to Figure 7.7. Figure 7.7, from top to bottom, shows the number of available GPS satellites from raw RINEX data and the number GPS satellites used to process the positioning solution by gLAB in BK solution over Kiruna between 20:00 and 24:00 UT during 17 March 2015 for 30-s and 1-s observables, respectively. In the top panel, the difference between the number of available satellites from 30-s observables (L1 – cyan line, L2 – blue line, P1 – green line, and P2 – black line) and the number of satellites used in the positioning solution (red line) was largely accompanied by gaps. As seen in other cases, the use of 1-s observables demonstrated the benefits of the use of higher temporal resolution measurements in the improvement of the performance of positioning.

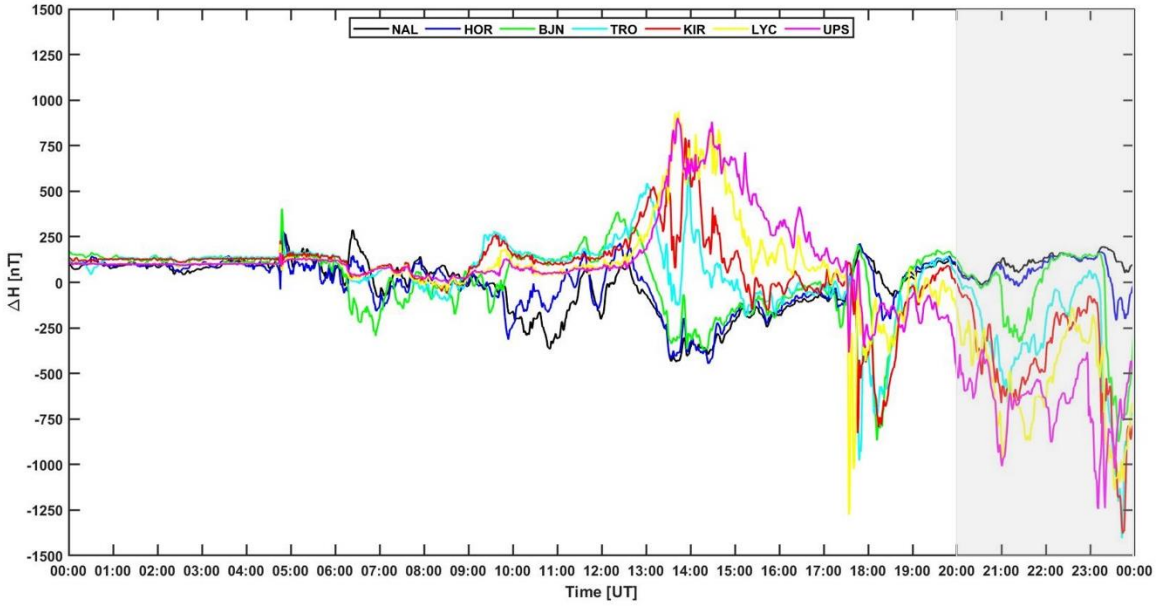

Figure 7.14: Magnetograms from the IMAGE network (H local geomagnetic field components variations) over Ny-Ålesund (NAL, black line), Hornsund (HOR, blue line), Bear Island (BJN, green line), Tromsø (TRO, cyan line), Kiruna (KIR, red line), Lycksele (LYC, yellow line), and Uppsala (UPS, magenta), respectively between 00:00 and 24:00 UT on 17 March 2015. The time of measurement corresponding to 2018 EISCAT UHF/ESR Campaigns is indicated by the shaded light grey colour (right-hand side) between 20:00 and 24:00 UT.

To appreciate the source mechanism responsible for auroral irregularities which manifested as increase in TEC fluctuations with values at some intervals outside $\pm 5\, TECU/30\, s$ (Figure 7.13a) and outside $\pm 1\, TECU/s$ (Figure 7.13b) occurring on multiple satellites on the evening of 17 March 2015 during St. Patrick's Day Storm, refer to Figure 7.14. Figure 7.14 shows magnetograms (H component variations) over Ny-Ålesund (NAL), Bear Island (BJN), Sørøya (SOR), Tromsø (TRO), Kiruna (KIR), Lycksele (LYC), and Uppsala (UPS), respectively during 17 March 2015. Here, the H component variations were about thrice the case on the evening of 15 March 2018 over the same latitudinal stations. In Figure 7.14 (KIR, red line), the H component was southward (negative) from about 20:20 UT on average to midnight. This southward component denotes substorms which indicate the presence of auroral particle precipitation in the E layer as the source mechanism inducing auroral irregularities [*Forte et al., 2017*].

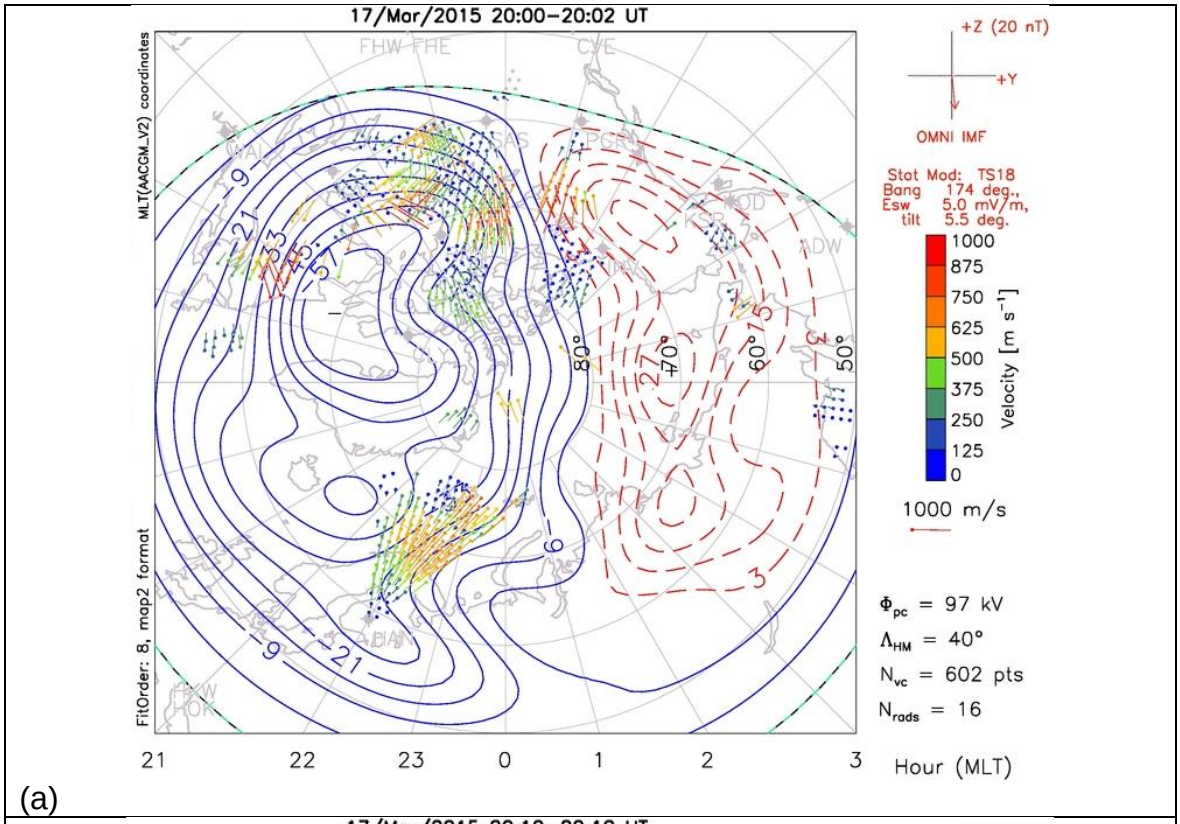
17/Mar/2015 20:00–20:02 UT
MLT(AACGM_V2) coordinates
FitOrder: 8, map2 format
+Z (20 nT)
+Y
OMNI IMF
Stat Mod: TS18
Bang 174 deg.,
Esw 5.0 mV/m,
tilt 5.5 deg.
1000
875
750
625
500
375
250
125
0
Velocity [m s⁻¹]
1000 m/s
Φpc = 97 kV
ΛHM = 40°
Nvc = 602 pts
Nrads = 16
21
22
23
0
1
2
3
Hour (MLT)

(a)

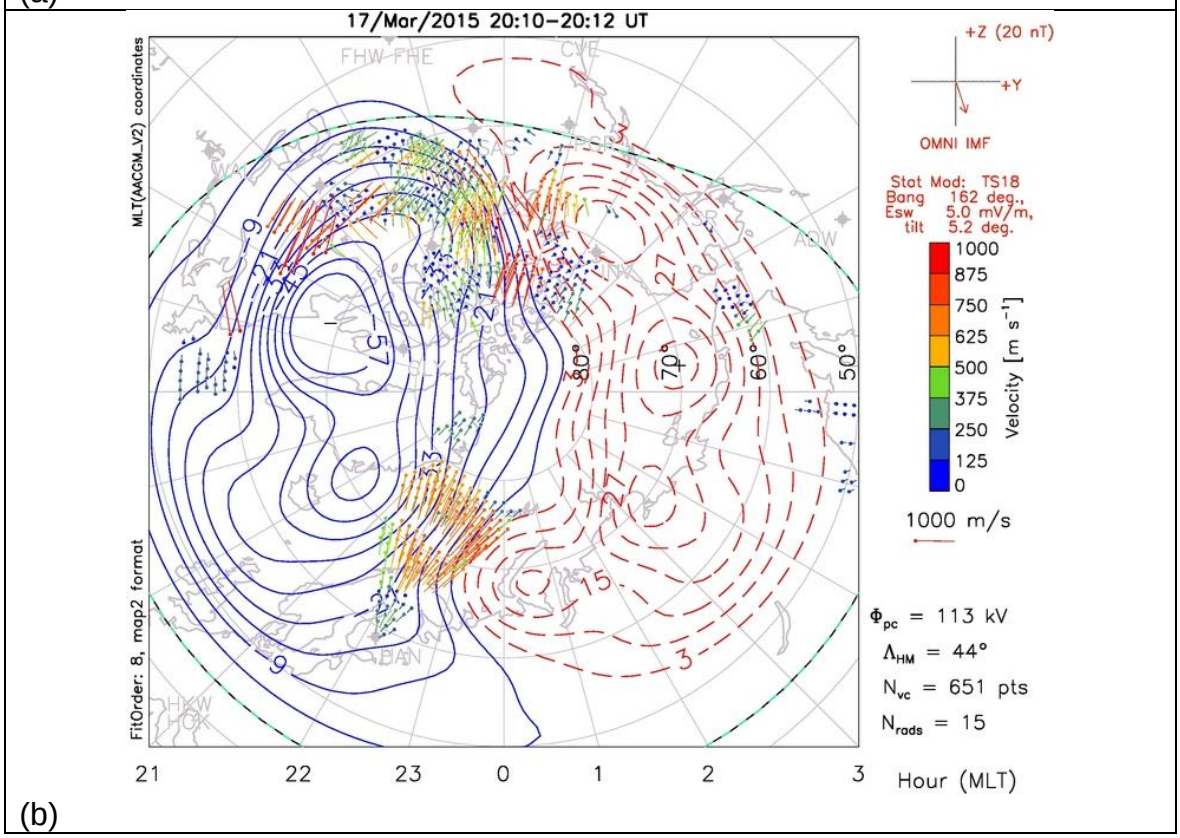
17/Mar/2015 20:10–20:12 UT
MLT(AACGM_V2) coordinates
FitOrder: 8, map2 format
+Z (20 nT)
+Y
OMNI IMF
Stat Mod: TS18
Bang 162 deg.,
Esw 5.0 mV/m,
tilt 5.2 deg.
1000
875
750
625
500
375
250
125
0
Velocity [m s⁻¹]
1000 m/s
Φpc = 113 kV
ΛHM = 44°
Nvc = 651 pts
Nrads = 15
21
22
23
0
1
2
3
Hour (MLT)

(b)

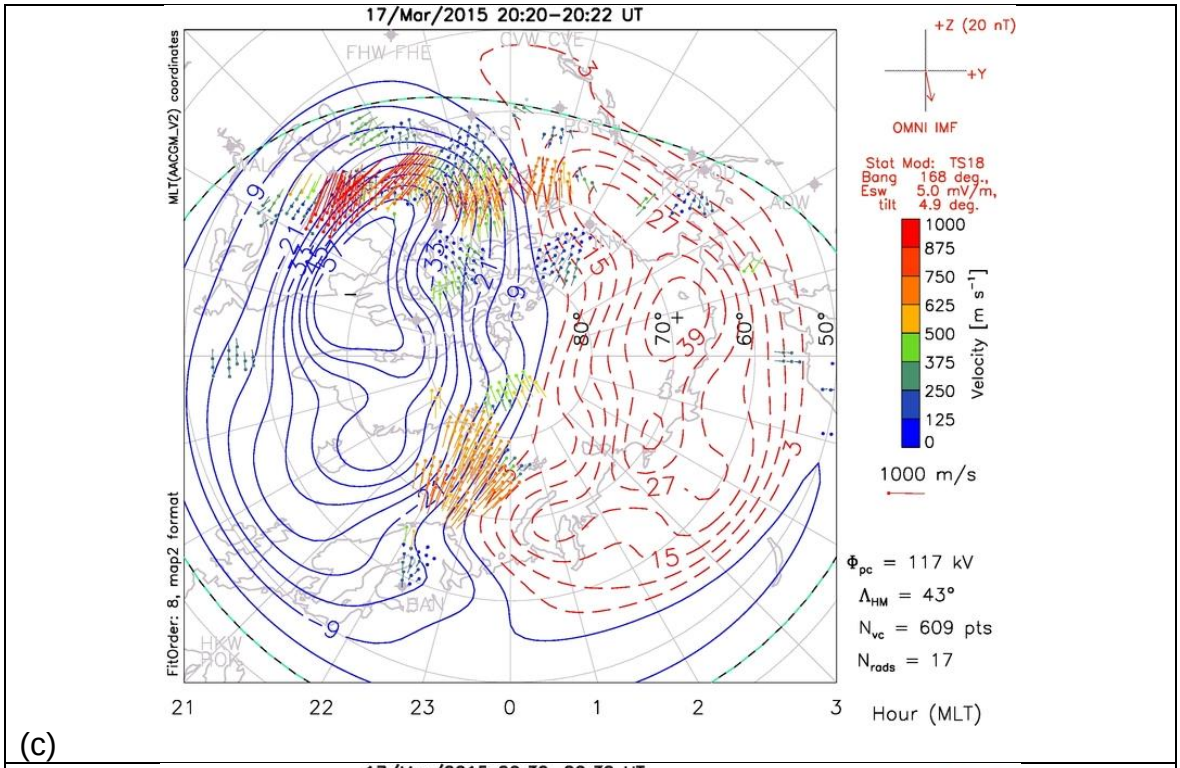

(c)

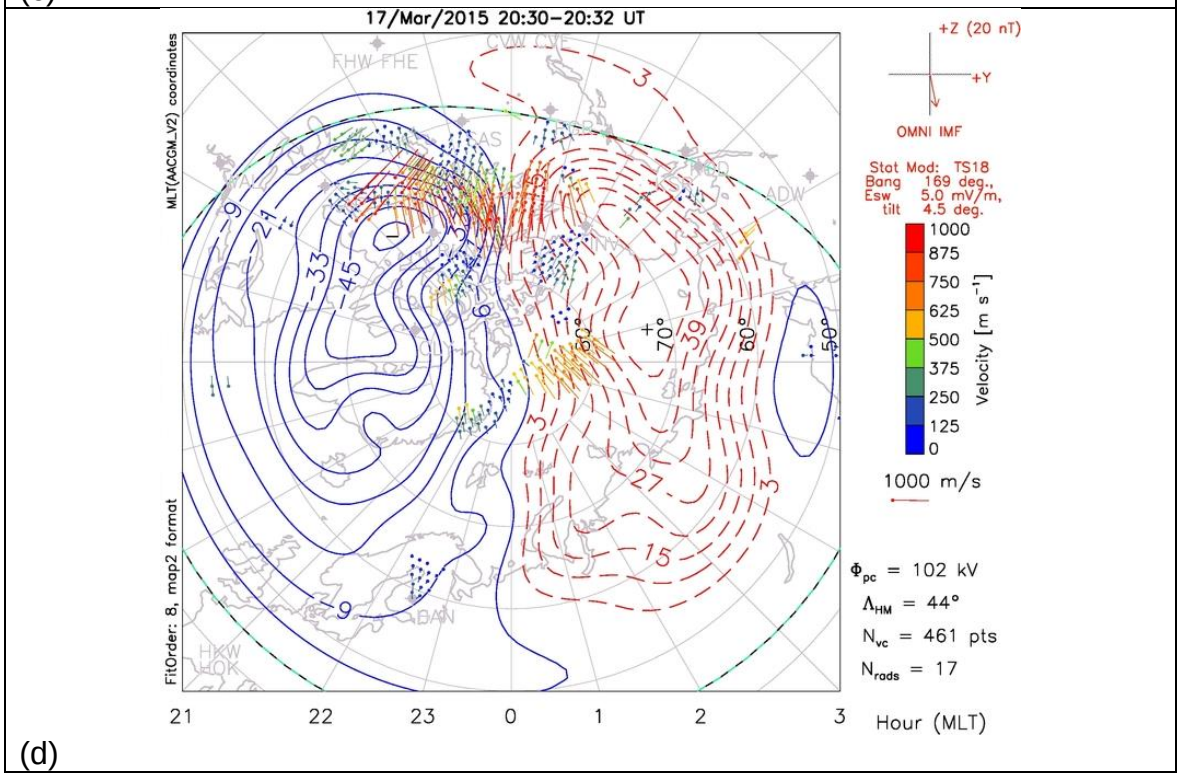

(d)

Figure 7.15: From top to bottom shows SuperDARN electric potential pattern at 2 min window (interval of 10 minutes) over Northern Hemisphere between (a) 20:00 and 20:02 UT, (b) 20:10 and 20:12 UT, (c) 20:20 and 20:22 UT, and (d) 20:30 and 20:32 UT on 17 March 2015 as a function of geomagnetic latitudes and magnetic local time (MLT). The magnetic noon is at the top of each panel with the dawn and dusk on the right- and left-hand sides, respectively. Green dashed line curve indicates the Heppner–Maynard Boundary (HMB) of ionospheric convection.
[Courtesy of College of Engineering, VirginiaTech SuperDARN]

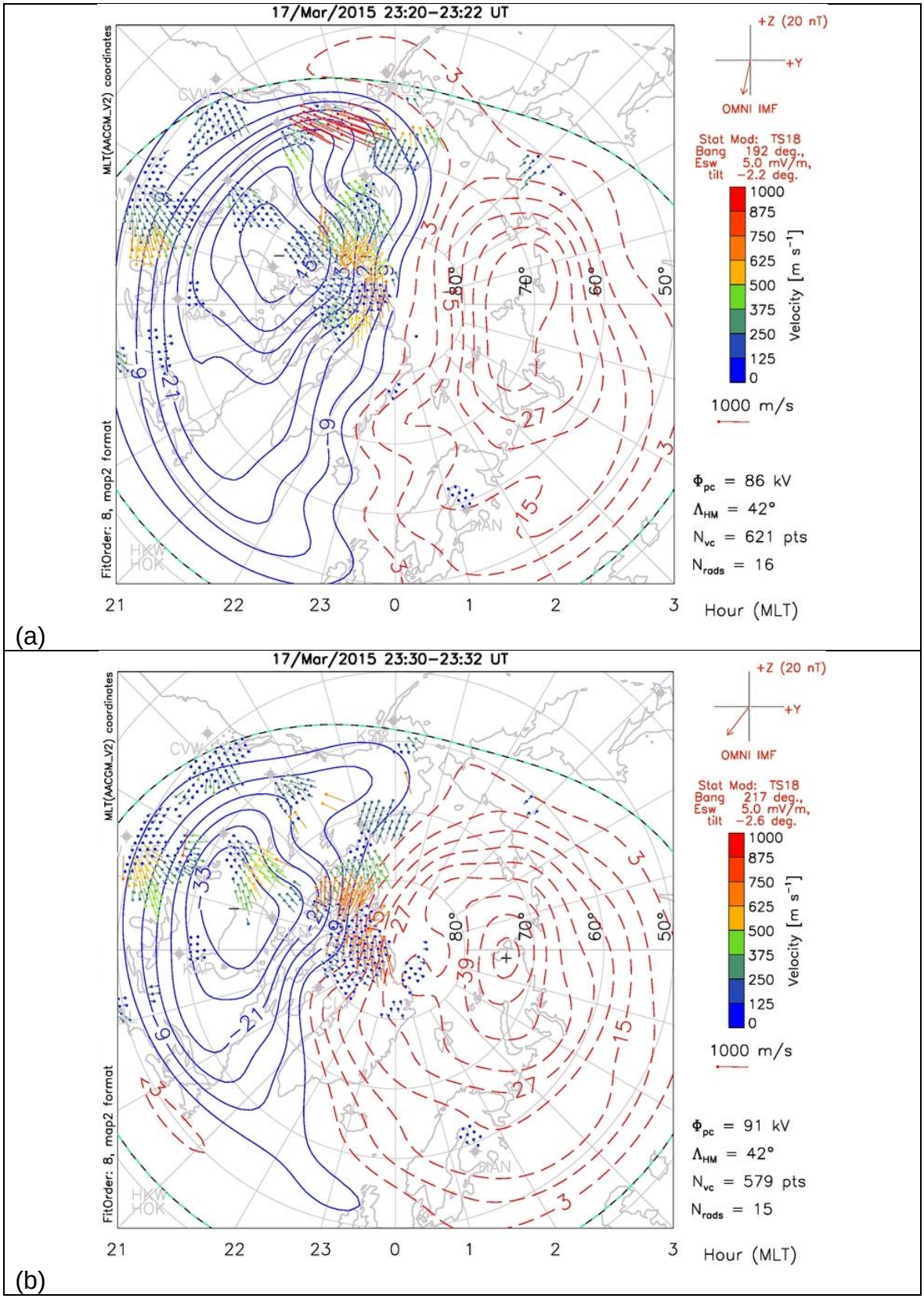
17/Mar/2015 23:20–23:22 UT
MLT(AACGM_V2) coordinates
FitOrder: 8, map2 format
+Z (20 nT)
+Y
OMNI IMF
Stat Mod: TS18
Bang 192 deg.,
Esw 5.0 mV/m,
tilt −2.2 deg.
1000
875
750
625
500
375
250
125
0
Velocity [m s⁻¹]
1000 m/s
Φpc = 86 kV
ΛHM = 42°
Nvc = 621 pts
Nrads = 16
80°
70°
60°
50°
21
22
23
0
1
2
3
Hour (MLT)
(a)
17/Mar/2015 23:30–23:32 UT
MLT(AACGM_V2) coordinates
FitOrder: 8, map2 format
+Z (20 nT)
+Y
OMNI IMF
Stat Mod: TS18
Bang 217 deg.,
Esw 5.0 mV/m,
tilt −2.6 deg.
1000
875
750
625
500
375
250
125
0
Velocity [m s⁻¹]
1000 m/s
Φpc = 91 kV
ΛHM = 42°
Nvc = 579 pts
Nrads = 15
80°
70°
60°
50°
21
22
23
0
1
2
3
Hour (MLT)
(b)

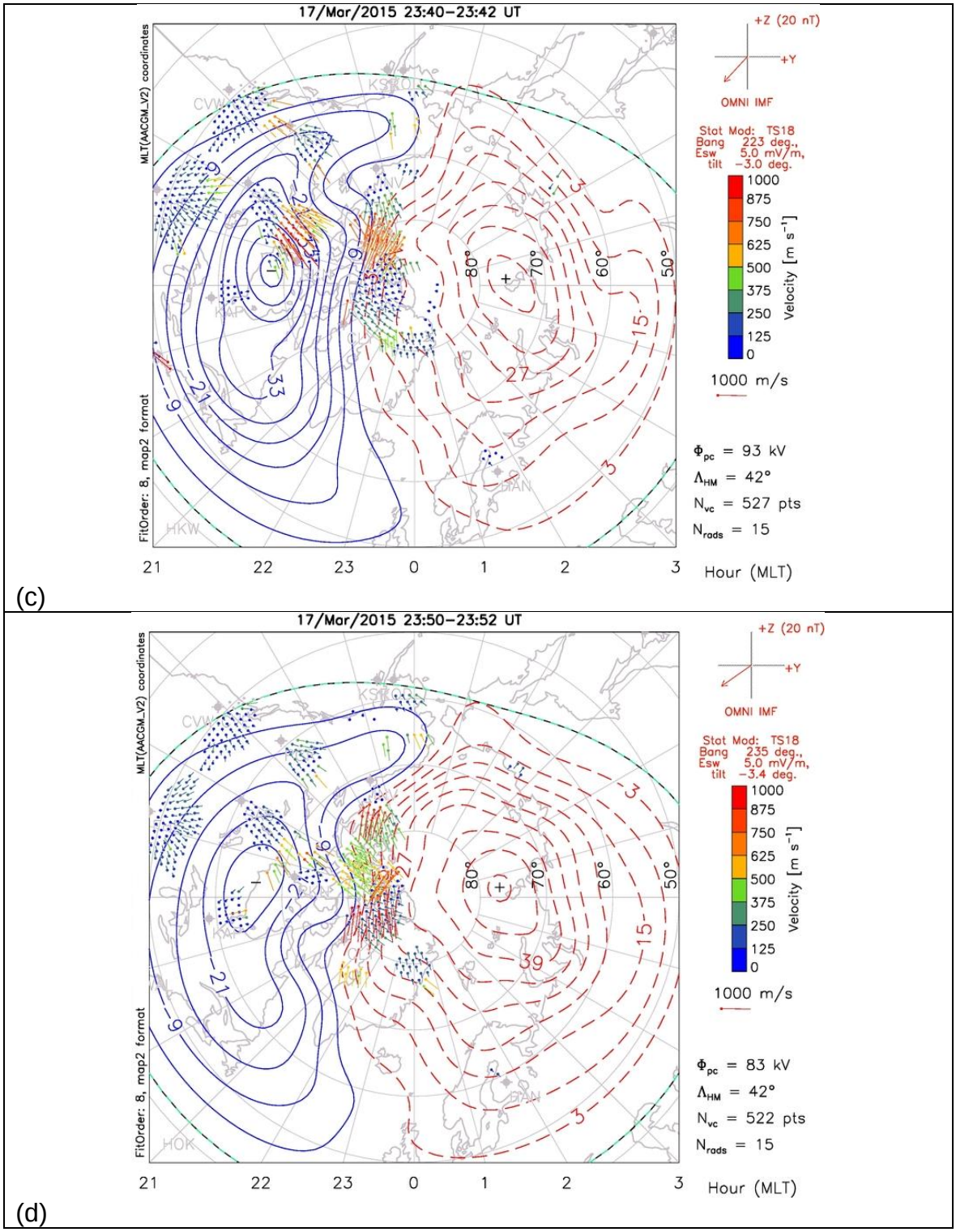

Figure 7.16: From top to bottom shows SuperDARN electric potential pattern at 2 min window (interval of 10 minutes) over Northern Hemisphere between (a) 23:20 and 23:22 UT, (b) 23:30 and 23:32 UT, (c) 23:40 and 23:42 UT, and (d) 23:50 and 23:52 UT on 17 March 2015 as a function of geomagnetic latitudes and magnetic local time (MLT). The magnetic noon is at the top of each panel with the dawn and dusk on the right- and left-hand sides, respectively. Green dashed line curve indicates the Heppner–Maynard Boundary (HMB) of ionospheric convection. [Courtesy of College of Engineering, VirginiaTech SuperDARN]

Similarly, to validate the ionospheric condition over the auroral latitude on the evening of 17 March 2015 during the St. Patrick's Day Storm, SuperDARN electric potential patterns as shown in Figures 7.15 and 7.16 were included. At intervals (20:00-20:32 UT and 23:20-23:52 UT) coinciding with enhanced errors and or data gaps as indicated in Figure 7.13, IMF B_z component was negative simultaneous with the expansion of ionospheric convection boundary (green curve) from auroral to middle latitudes as indicated in Figures 7.15 and 7.16. The expansion of ionospheric plasma from auroral latitudes to middle latitudes indicates the presence of geomagnetic storm which induced increase magnitude and duration of TEC fluctuations on several GPS PRNs and data gaps as observed in Figures 7.13 and 7.17 compared to Figures 7.4, 7.11, and 7.12. Figure 7.15((a) and (b)) shows evidence of slow-moving plasma over Kiruna.

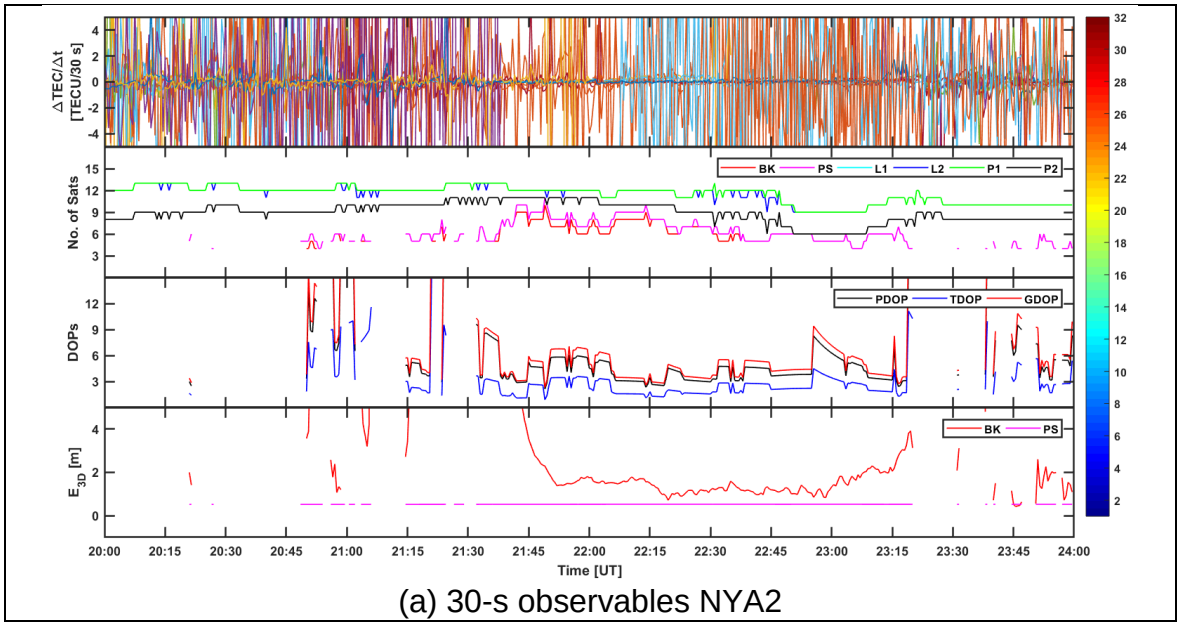

(a) 30-s observables NYA2

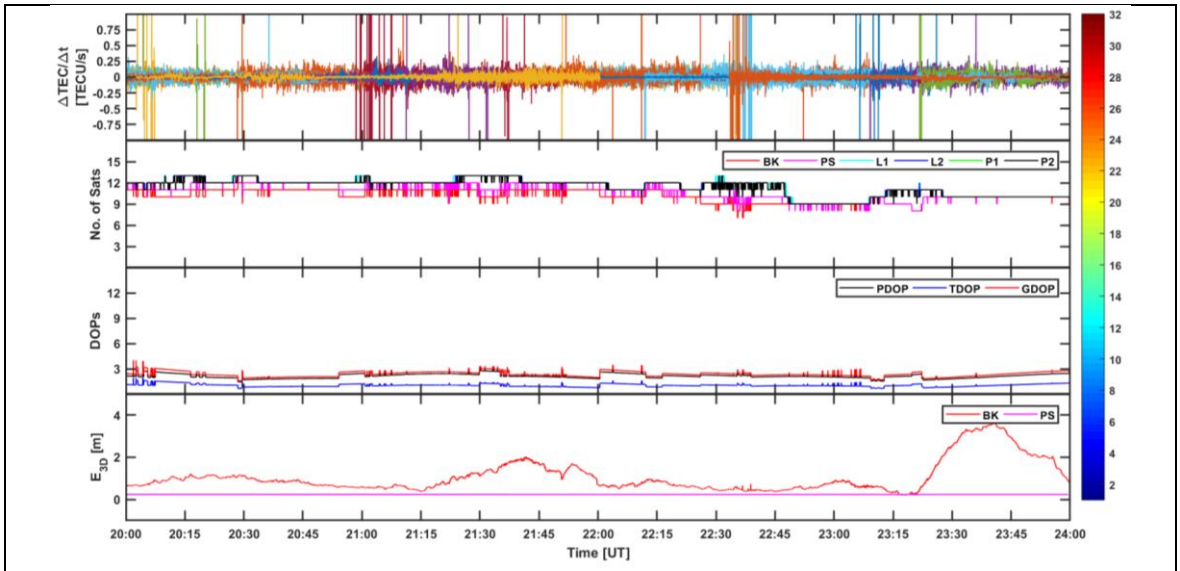

(b) 1-s observables NYA2

Figure 7.17: From top to bottom shows temporal TEC fluctuations for GPS PRNs in view with elevation angle above 5°; number of available observables (L1 – cyan line, L2 – blue line, P1 – green line, and P2 – black line) from GPS PRNs in view together with the number of PRNs considered in the BK solution (red) and in the PS solution (magenta); the DOPs (PDOP – black line, TDOP – blue line, and GDOP – red line); and the 3-D positioning error E_{3D} for the BK solution (red) and the PS solution (magenta). TEC fluctuations and positioning errors were calculated for the ground-based station NYA2 (Ny-Ålesund) on the evening of 17 March 2015 during St. Patrick's Day Storm. (a) 30-s observables and E_{3D}, (b) 1-s observables and E_{3D}. L1 and L2 are carrier phase observables and P1 and P2 are pseudorange observables. The colour bar (right-hand side) indicates 1-32 GPS PRNs.

This result suggests the positioning performance was strongly influenced by the level of geomagnetic activity and the temporal resolution of the GNSS receiver. Although the magnitude and duration of the observed impact on positioning vary from location to location, the use of higher temporal resolution GNSS receivers can improve the availability and accuracy of the positioning solution for applications at the auroral latitude.

As seen in the case of auroral latitude, this section presents the results obtained at the polar latitude on the evening of 17 March 2015 during St. Patrick's Day Storm. The polar latitude station used is Ny-Ålesund (NYA2). Figure 7.17a (30-s observables) shows enhancements in TEC fluctuations above 95% which implies larger residual errors on the geometry-free combination throughout the time of measurements. The occurrence of data gaps in most instances was when enhanced TEC fluctuations were observed on multiple satellites. In about 30% of the time of measurement, gaps were observed as illustrated in Figure 7a second panel from

the top. The use of precise products did not remove gaps but rather reduced the corresponding errors compared to the BK solution. These gaps are concurrent with when the number of satellites used to process the BK solution was fewer than 4 mainly caused by cycle slips on the carrier phase observables. Both the DOPs and BK solutions, in this case, were characterised by gaps with larger values and larger variabilities. Here, the use of precise products (as seen in other events) to process the PS positioning solution reduced the intensity and variability of errors but not gaps.

Whereas in Figure 7.17b (1-s observables), enhanced TEC fluctuations were observed at about 21:00-23:30 UT. Enhancement in TEC fluctuations observed at other intervals was due to satellites with low elevation angles. The observed residual errors, in this case, are of shorter duration and their occurrences were correlated with the number of satellites from both raw RINEX and gLAB. The number of available satellites for the BK solution was always less than the PS solution as seen in most of the time except in a few instances where the values are the same. The minimum number of satellites was about 7 on average during the time of measurement. No data gaps were observed, and the errors were significantly reduced. The DOPs observed were below 4. As demonstrated in Figures 7.4b, 7.11b, 7.12b, and 7.13b, the use of higher temporal resolution GNSS receivers increased the number of satellites used to process the positioning solution.

Similarly, to appreciate the effects of polar irregularities on the BK solution using 30-s and 1-s observables, refer to Figure 7.10. Figure 7.10, from top to bottom, shows the number of available GPS satellites derived from raw RINEX and the number of GPS satellites utilised to process the positioning solution over Ny-Ålesund between 20:00 and 24:00 UT during 17 March 2015 using 30-s and 1-s observables, respectively. In addition to this, Figure 7.14 (NAL, black line) shows positive H (north-south) variations from about 20:30 UT to midnight. While Figures 7.15 and 7.16 show the expansion of auroral oval to middle latitudes collocated with IMF B_z negative. The expansion of auroral oval to middle latitudes signifies the presence of ionospheric plasma convection in the north-south direction. The result further validates the impact of polar irregularities on positioning performance during severe geomagnetic storms.

7.4 Discussions

In both the case of the auroral and polar ionospheres, different geomagnetic conditions were considered to understand how ionospheric irregularities induced phase fluctuations on 30-s and 1-s observables and their impact on GPS positioning performance. EISCAT UHF/ESR incoherent scatter radars were used to investigate the background ionospheric conditions in the auroral and polar ionospheres through electron density profiles. The design geometry involves a simultaneous multi-instrument experiment in which EISCAT UHF/ESR combined with IGS stations (KIRU/NYA2) located at auroral and polar latitudes. Details of the design geometry of each experiment were discussed in Chapter 6. Signatures of ionospheric irregularities were characterised by means of TEC fluctuations observed from 30-s and 1-s observables.

Figures 7.2 and 7.4 on the evening of 12 March 2018 shows the absence of auroral structures as well as irregularities. Enhancement in TEC fluctuations observed on a few satellites did not affect the accuracy and availability of GPS positioning in terms of 30-s and 1-s observables in both BK and PS solutions. Figure 7.5 confirms not fewer than 7 satellites used to process positioning solution by gLAB. In the case of 15 March 2018, the presence of disturbed ionospheric condition suggests the existence of irregularities causing degradation and interruption of GPS positioning solution as indicated in Figure 7.4a and Figure 7.6 (top panel). Gaps were induced where fewer than 4 satellites were used in the positioning solution and this was associated with auroral irregularities. This fact was verified from gLAB report of Output Messages corresponding to the interval of time when gaps were induced due to discarded satellites caused by geometry-free combination. The geometry-free combination implies gaps were originated from ionospheric irregularities. Normally, GNSS positioning requires no fewer than 4 concurrently tracked satellites with good geometry [*Misra and Enge, 2006*]. Degraded DOPs suggests poor satellites geometry – a situation not favourable to GNSS positioning.

The performance of GPS positioning in the presence of phase fluctuations was also investigated during a severe geomagnetic storm. On the evening of 17 March 2015 during St. Patrick's Day Storm (Figures 7.7 and 7.13), increased errors and gaps

were recorded owing to the presence of severe geomagnetic storm. Figure 7.14 shows H (north-south) component variations of magnitude about thrice the case during 15 and 16 March 2018. Negative H signifies substorm onset responsible for energetic electron precipitation in the E layer. Figures 7.15 and 7.16 at intervals corresponding to enhanced errors and or data gaps are correlated with IMF B_z negative as well as expansion of auroral oval to middle latitudes. Variations of velocities of ionospheric convection at the polar and auroral latitudes owing to the expansion of the auroral oval were recorded by SuperDARN electric potential pattern between 20:00 and 20:22 UT (Figure 7.15) on average. The expansion of the auroral oval implies the response of the ionosphere to a geomagnetic storm. Here, geomagnetic storm in the auroral and polar ionospheres is correlated with disturbed ionosphere.

In the case of the polar ionosphere, there were no ESR measurements on 12 March 2018 owing to technical problems. However, 30-s and 1-s RINEX measurements as indicated in Figure 7.8 (top and bottom panels) show no fewer than 7 GPS satellites were available at all times to process the positioning solution. This was indicative of a quiet ionospheric condition over Ny-Ålesund.

On the evening of 16 March 2018 in the presence of active geomagnetic condition (Figures 7.9 and 7.12), the ionosphere was disturbed and this corresponds to enhanced errors and gaps observed between 21:15 and 22:00 UT as seen in the 30-s observables. In like manner, in the presence of severe geomagnetic storm during the 17 March 2015 event, more intensification in errors and gaps (poor availability) were recorded at the polar latitude due to irregularities. Enhancement in errors and gaps were a consequence of larger residual errors on the geometry-free combination of carrier phase observables originating from polar irregularities.

At both the auroral and polar latitudes, the 30-s BK solution was characterised by larger values of 3-D positioning errors accompanied by larger variability and several gaps. The use of precise products (PS solution) while processing positioning solution from 30-s observables lowered the 3-D positioning errors but gaps remained. However, the positioning solutions (BK and PS) from 1-s observables were characterised by lower values of 3-D positioning errors accompanied by lower variability and the absence of gaps. In general, gaps induced were a consequence

of fewer than 4 satellites to process positioning solution by means of gLAB. GPS satellites with larger residual errors characterised in terms of fluctuations in TEC and cycle slips were discarded by gLAB from the positioning algorithm in both BK and PS for 30-s observables [*Dionisio et al., 2010; Hernandez-Pajares et al., 2010; Ibáñez et al., 2018; Ramos Bosch et al., 2010*]. Whenever a threshold set by gLAB is exceeded, the 30-s BK and PS positioning solution are not performed for that particular satellite signal resulting in the observed gaps. In both cases, TEC fluctuations and cycle slips derived from 30-s observables showed a longer duration as opposed to 1-s observables. In view of this, the 3-D positioning errors in the case of 1-s BK solution showed a lower value and lower variability whereas in the case of 1-s PS solution it showed a lower and constant value. The absence of gaps from 1-s observables can be explained by the GPS ray paths scanning through, in this case, large-scale irregularities [*Forte and Radicella, 2004*]. However, at the equatorial latitudes, a higher temporal resolution receiver with a higher sampling rate is required due to the presence of small-scale irregularities [*Vani et al., 2019*].

In the auroral ionosphere (KIRU), GPS ray paths were scanning through field-aligned large-scale irregularities originating from particle precipitation on the evening (21:20-22:30 UT and 22:40-24:00 UT) of 15 March 2018. While in the polar ionosphere (NYA2) GPS ray paths were scanning through field-aligned large-scale irregularities caused by fast-moving polar patch and particle precipitation between 21:15 and 22:00 UT on 16 March 2018 [*John et al., 2020*]. Following the geometry of GPS satellites [*Forte and Radicella, 2004*] and the characteristics of auroral and polar irregularities [*Kelley, 1982; Keskinen and Ossakow, 1983; Forte et al., 2017; John et al., 2020*], the ray paths travel through auroral irregularities that were of a very low velocity on average arising from particle precipitation or through polar irregularities arising from fast-moving polar patches. In both events, the observed phase fluctuations inferred from TEC fluctuations over $1\ s$ were smaller and lasted shorter compared to phase fluctuations arising over $30\ s$. This is because the phase fluctuations (measured by TEC fluctuations) over $30\ s$ is higher than the phase fluctuations over $1\ s$ for typical GPS ray paths scan velocities at ionospheric heights (below $100\ m/s$ in both E and F layers). GPS ray path velocity in the E region is less than in the F region. This explains why fewer satellites showed larger values of residual errors and cycle slips for 1-s observables as opposed to 30-s observables.

In both cases, large-scale irregularities extending between the E and F layers by means of EISCAT UHF/ESR originate from particle precipitation (auroral ionosphere, Figure 7.11) and fast-moving polar patch (polar ionosphere, Figure 7.12) [*John et al., 2020*]. In the auroral ionosphere, irregularities formed across several magnetic latitudes and longitudes in the auroral oval were responsible for widespread intensification in TEC fluctuations over several satellites including those at lower elevation angles. Hence, smaller fluctuations in TEC were observed from irregularities in the E layer while irregularities localised in the E and F layers induced larger fluctuations in TEC as well as cycle slips.

Since 1-s observables minimised the impact of residual errors (enhanced TEC fluctuations) and cycle slips on the positioning solutions, this implies that 1-s observables experienced smaller phase changes happening at the edges of the large-scale irregularities whereas 30-s observables experience larger phase changes throughout the spatial scale of the irregularities. Figures 7.18-7.22 showed the spatial distances between consecutive IPPs at every $30\ s$ and $1\ s$ for GPS ray paths at 5° elevation angle mask over which these phase changes occurred calculated at $110\ km$ (Figures 7.18, 7.19, and 7.21) and $300\ km$ (Figure 7.20 and 7.22) corresponding to E and F layer ionospheric shell heights, respectively.

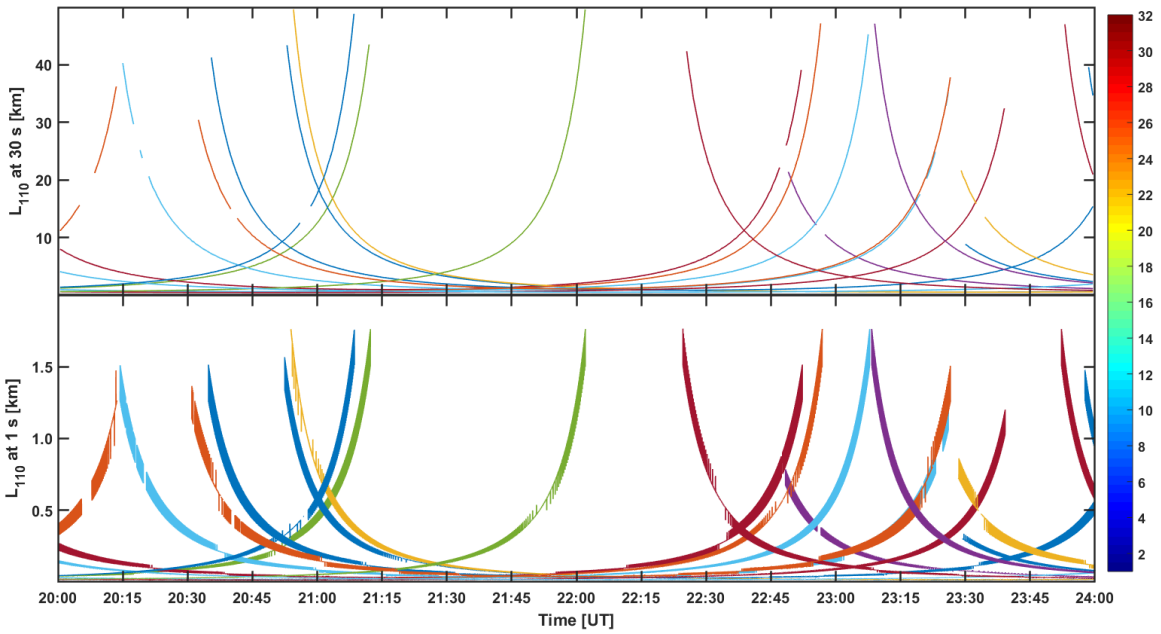

Figure 7.18: From top to bottom shows spatial distances between consecutive IPPs of available GPS PRNs ray paths at $110\ km$ shell height (E layer) every $30\ s$ (L_{110} at $30\ s$ $[km]$) and every $1\ s$ (L_{110} at $1\ s$ $[km]$), respectively. The calculations are at elevation angle mask 5° from Kiruna for the time interval between 20:00 and 24:00

UT during 12 March 2018. The colour scale (right) stands for GPS PRNs from 1 to 32 used to calculate the spatial distances.

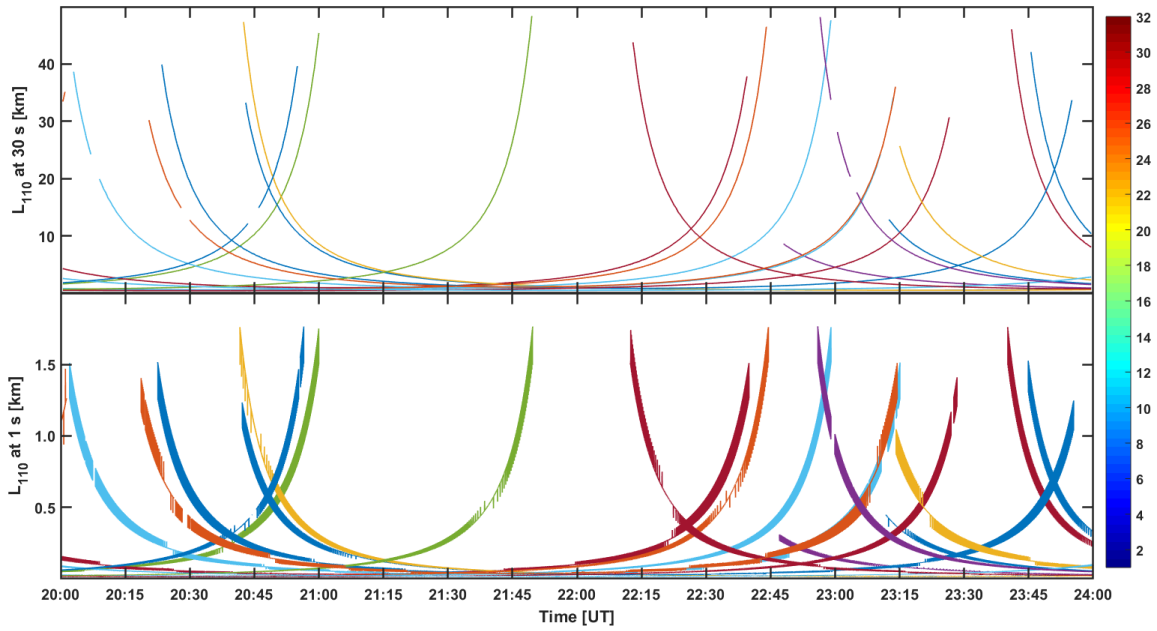

Figure 7.19: From top to bottom shows distances between consecutive IPPs of available GPS PRNs ray paths at $110\ km$ shell height (E layer) every $30\ s$ (L_{110} at $30\ s$ $[km]$) and every $1\ s$ (L_{110} at $1\ s$ $[km]$), respectively. The calculations are at elevation angle mask 5° from Kiruna for the time interval between 20:00 and 24:00 UT during 15 March 2018. The colour scale (right) stands for GPS PRNs from 1 to 32 used to calculate the spatial distances.

On the evening of 12 March 2018 typical of a quiet and benign ionosphere, only a few satellites experienced intensification in TEC fluctuations due to lower elevation angles as indicated in Figure 7.4 (2nd panel from top). However, on the evening of 15 and 16 March 2018 corresponding to active geomagnetic conditions (Figures 7.11 and 7.12, 2nd panels from the top), more satellites experienced intensification in TEC fluctuations at all elevation angles over $30\ s$ and $1\ s$. On the evening of 17 March 2015 during severe geomagnetic conditions over both auroral and polar latitudes, more satellites experienced enhancement in TEC fluctuations at all elevation angles over $30\ s$ and $1\ s$ compared to quiet and active geomagnetic conditions as indicated in Figures 7.13 and 7.17, respectively.

In the auroral ionosphere (Figures 7.18, 7.19, and 7.21), phase changes were experienced over spatial distances between $2\ km$ and $40\ km$ on average (top panels) for 30-s observables and below $2\ km$ (bottom panels) for 1-s observables in the E layer. The colour scale shows the GPS PRNs (1-32) used to compute the spatial distances between consecutive GPS ray paths at $110\ km$ ionospheric shell

height. Similarly, Figures 7.20 and 7.22 show that in the polar ionosphere, phase changes were experienced over spatial distances between $2\,km$ and $40\,km$ on average (top panels) for 30-s observables and below $2\,km$ (bottom panels) for 1-s observables in F layer. This implies phase changes have the same spatial distances over the auroral and polar latitudes as seen in both 30-s and 1-s observables.

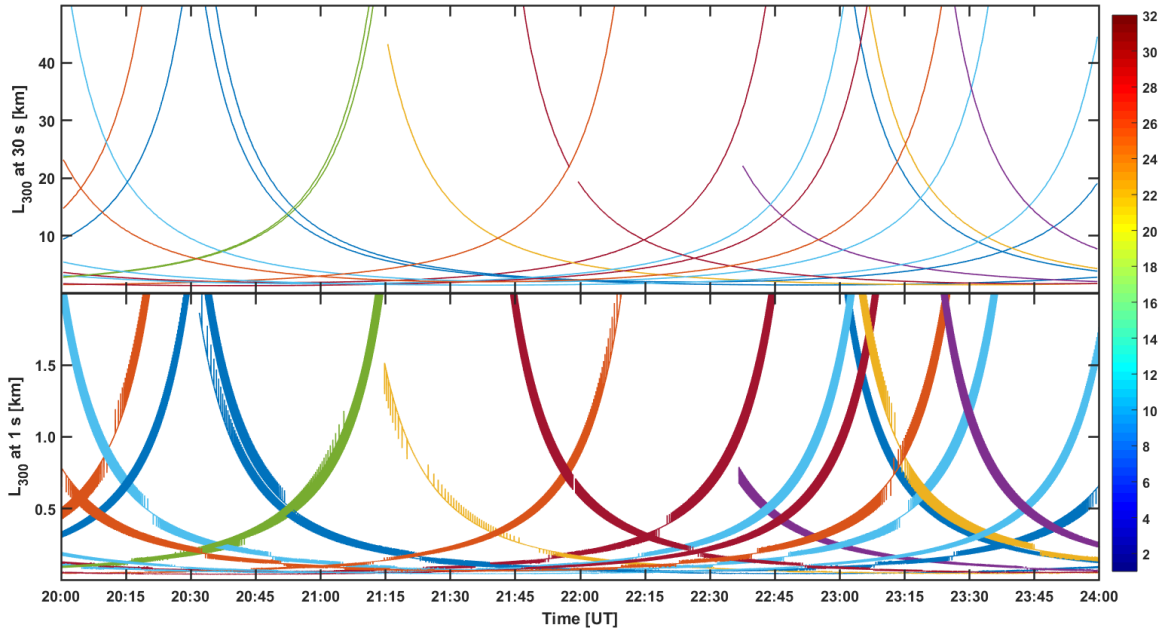

Figure 7.20: From top to bottom shows distances between consecutive IPPs of available GPS PRNs ray paths at $300\,km$ shell height (F layer) every $30\,s$ (L_{300} at $30\,s$ $[km]$) and every $1\,s$ (L_{300} at $1\,s$ $[km]$), respectively. The calculations are at elevation angle mask 5° from Ny-Ålesund for the time interval between 20:00 and 24:00 UT during 16 March 2018. The colour scale (right) stands for GPS PRNs from 1 to 32 used to calculate the spatial distances.

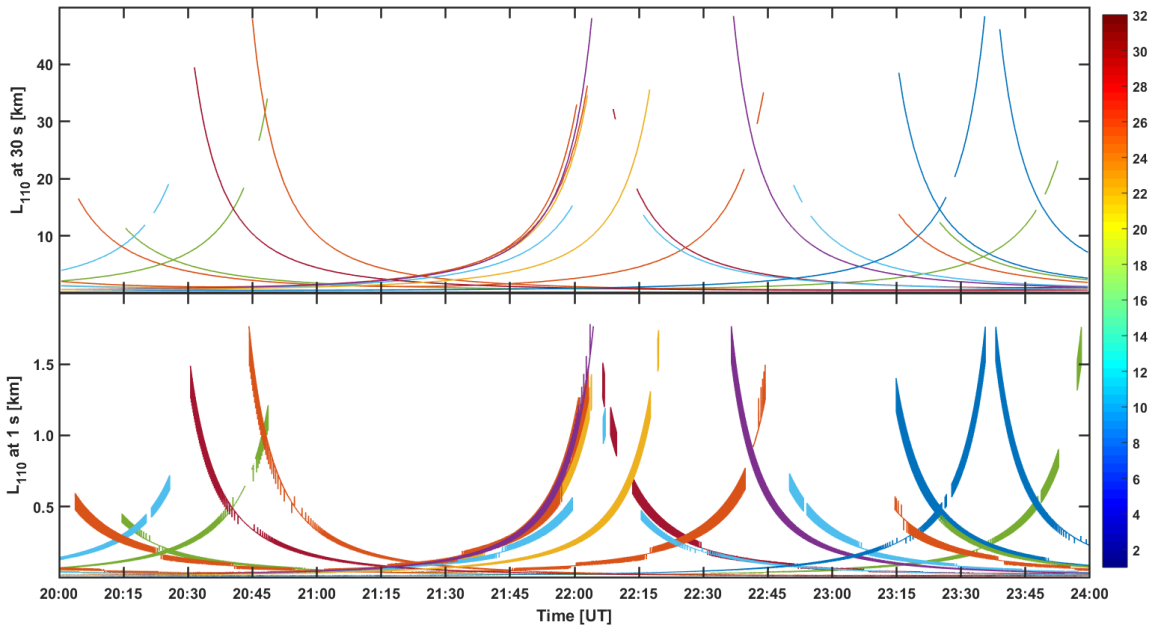

Figure 7.21: From top to bottom shows distances between consecutive IPPs of available GPS PRNs ray paths at 110 km shell height (E layer) every 30 s (L_{110} at 30 s [km]) and every 1 s (L_{110} at 1 s [km]), respectively. The calculations are at elevation angle mask 5° from Kiruna for the time interval between 20:00 and 24:00 UT during 17 March 2015. The colour scale (right) stands for GPS PRNs from 1 to 32 used to calculate the spatial distances.

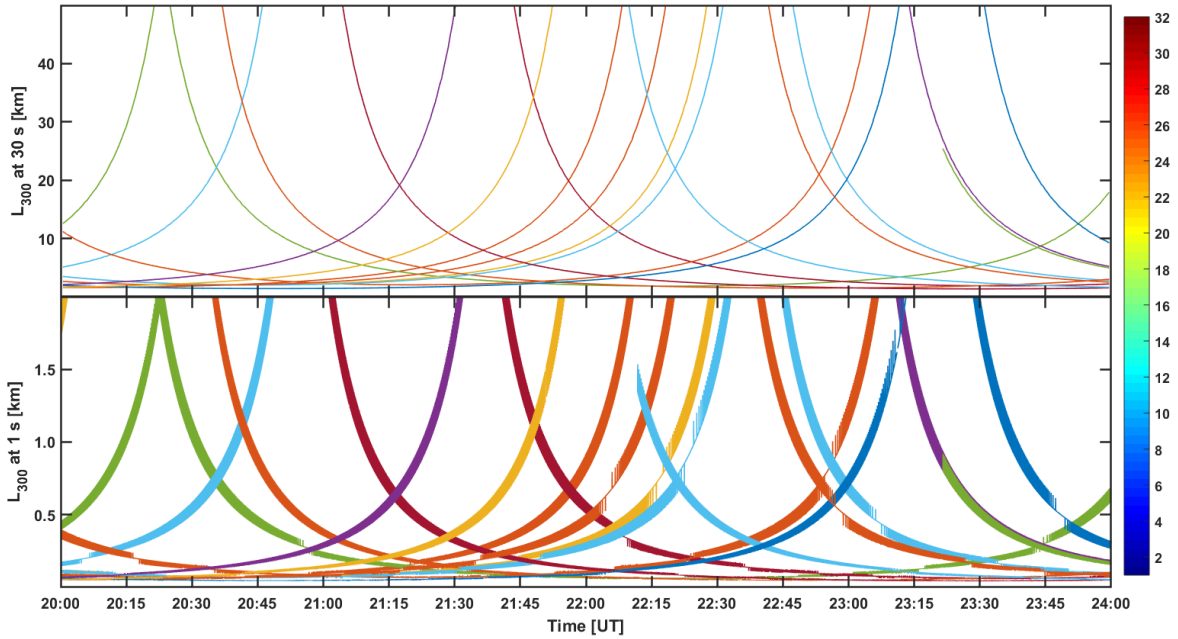

Figure 7.22: From top to bottom shows distances between consecutive IPPs of available GPS PRNs ray paths at 300 km shell height (F layer) every 30 s (L_{300} at 30 s [km]) and every 1 s (L_{300} at 1 s [km]), respectively. The calculations are at elevation angle mask 5° from Ny-Ålesund for the time interval between 20:00 and 24:00 UT during 17 March 2015. The colour scale (right) stands for GPS PRNs from 1 to 32 used to calculate the spatial distances.

Following the spatial resolution of EISCAT UHF/ESR ($2\ km$ on average) and the absence of amplitude scintillation inferred from 1-s observables in both auroral and polar observations, it can be inferred that irregularities have outer scale between $2\ km$ and $40\ km$ on average and are distributed over several hundreds of kilometres (as presented in Chapter 6). The spatial resolution of EISCAT UHF/ESR radars imply the type of ionospheric irregularities the radars can measure. The outer scale, calculated from the IPPs coordinates of consecutive GPS ray paths at $110\ km$ ionospheric shell height over auroral latitude and $300\ km$ ionospheric shell height over polar latitude, suggests the spatial scale over which electron density gradients distribute. The absence of amplitude scintillation, inferred from TEC fluctuations calculated from $1\ s$ observables (Figures 7.4, 7.11, 7.12, 7.13, and 7.17) since the observed increase in TEC fluctuations were caused by elevation mask of 5°, suggests the absence of energy cascade from larger to smaller scales as a result of low electron density gradients as opposed to equatorial irregularities.

7.5 Summary

In this chapter, the performance of GPS positioning in the presence of enhanced TEC fluctuations at the auroral and polar latitudes was investigated using EISCAT UHF/ESR experiments during different geomagnetic conditions. The investigation utilised a multi-instrument approach combining measurements collected through EISCAT UHF/ESR incoherent scatter radars and permanent geodetic GNSS receivers in the proximity of the radars. Depending on positioning applications (real-time and post-processing), two positioning solutions were implemented: BK and PS solutions using $30\ s$ and $1\ s$ observables. Geodetic IGS stations located at Kiruna and Ny-Ålesund representatives of auroral and polar latitudes respectively were used to investigate how auroral and polar irregularities impact on GPS positioning solutions. Several ionospheric shell heights, in this case, $150\ km$, $250\ km$, and $350\ km$ altitudes, were selected to simulate the design geometry of EISCAT UHF/ESR experiments. This was aimed at understanding the contribution of E and F layer irregularities in the auroral or polar ionosphere to the observed positioning performance by means of gLAB.

The results revealed that the intensity and variability of the 3-D positioning errors (E_{3D}) and the DOPs, as well as gaps, are functions of the sampling rate of the observables. E_{3D} showed higher values and higher variability for the case of 30-s BK solution when compared to 1-s BK solution. However, when precise products were used to process the positioning solution (PS) using 30-s and 1-s observables, E_{3D} showed a low but constant value through the time of measurements irrespective of the geomagnetic condition. During active and severe geomagnetic conditions at both the auroral and polar latitudes, both the 30-s BK and PS solutions were characterised by gaps induced by larger residual errors in terms of enhancement in TEC fluctuations and cycle slips concurrently on several satellites at all elevation angles. Contrary to this, the use of 1-s observables to compute BK and PS solutions was characterised by the absence of gaps following GPS ray paths scanning through field-aligned large-scale irregularities.

Phase changes observed in the E and F layer from both 30-s and 1-s observables are distributed over spatial IPP distances between $2\ km$ and $40\ km$ on average in the case of 30-s and below $2\ km$ in the case of 1-s at both the auroral and polar latitudes. As a consequence, fewer satellites experienced concurrent enhancement in TEC fluctuations and cycle slips from the 1-s observables as opposed to 30-s observables in both the auroral and polar ionospheres. The absence of amplitude scintillation in both auroral and polar observations implies the outer scale of irregularities was between $2\ km$ and $40\ km$ on average and these are distributed over several hundreds of kilometres. In addition, the absence of amplitude scintillation suggests the absence of energy cascade from larger to smaller scales as a result of low electron density gradients as opposed to equatorial irregularities.

8 Conclusions and Future Work

8.1 Introduction

This chapter presents the conclusions and future work of the research. To achieve this, the chapter is categorised into three parts. Part 1 presents the conclusions while Parts 2 and 3 are on future work. Part 2 presents the new design geometry of November 2019 EISCAT UHF/ESR campaigns. This was a follow up on the March 2018 EISCAT UHF/ESR campaigns presented in Chapters 6 and 7. EISCAT UHF/ESR campaigns of November 2019 were successfully designed and conducted. A completed analysis and results of the experiments will be submitted to a peer-reviewed journal for publication. Part 3 presents a potential research to be titled “Socio-economic assessment of the impact of ionospheric irregularities on applications of GNSS in Sub-Saharan Africa.” In Part 3, an overview of GNSS applications in Sub-Saharan Africa was presented followed by a brief description of the potential research.

8.2 Part 1: Conclusions

In this thesis the impact of ionospheric irregularities on GNSS at auroral and polar latitudes was investigated. The research utilised a multi-instrument experimental campaigns involving EISCAT UHF/ESR incoherent scatter radars combined with geodetic GNSS receivers located in the European northern hemisphere. To examine auroral and polar irregularities and their effects on GNSS operations and services, two different scenarios were considered. One, EISCAT experiment which represents the auroral ionosphere and second, ESR experiment which stands for the polar ionosphere. EISCAT UHF/ESR beams positions alternately and approximately intersected GPS ray paths of relevance at different ionospheric shell heights corresponding to the E and F layer altitudes. Towards this study, EISCAT UHF/ESR experiments were designed and conducted successfully on the evenings of March 2018 and November 2019 and the data collected from the study were used in this work.

Chapter 2 gives an overview on the ionosphere starting from adverse SW events. Adverse SW events can induce magnetospheric disturbances leading to plasma instabilities in the high-latitudes ionosphere. Instability mechanisms can act upon auroral and polar structures to produce auroral and polar irregularities. Particle precipitation and propagating polar cap patches were seen as source mechanisms for high-latitudes irregularities at the E and F layer latitudes. To characterise the presence of these irregularities, TEC fluctuations and scintillation are used as convenient proxies.

In Chapter 3, the literature was reviewed to provide insight into the impact of ionospheric irregularities on GNSS operations and services. Ionospheric measurements collected and analysed from ground-based and in situ instrumentations were considered. The results of investigation of the influence of irregularities on GNSS signals at equatorial, middle, and high-latitudes during varying geomagnetic conditions were reviewed. Several techniques were adopted to study the impact of irregularities on GNSS using, for example, incoherent scatter radars combined with other ionospheric instrumentations revealed that the performance of GNSS infrastructures can be degraded in disturbed ionospheres. The methods adopted in this research were considered based on the insight gained from existing knowledge.

Chapter 4 presented the effects of the ionosphere on propagation of GNSS signals. The influence of Ionospheric electron density irregularities on GNSS was quantified by means of TEC and TEC fluctuations using carrier phase measurements derived from multi-frequency GNSS receivers. Relevant theoretical equations required to support the understanding of the study were presented. The chapter discusses equatorial, middle, and high-latitudes scintillation. Scintillation activity especially in high-latitudes has been associated with geomagnetic activity. In general, the presence of ionospheric irregularities can degrade or interrupt GNSS navigation and positioning services operating in the regions.

While Chapter 5 gives the ionospheric instrumentations and measurements used in the research. To achieve the aim of the research, each instrumentation was presented along with the measurements so collected and analysed. Instrumentations such as ISRs (EISCAT, ESR, and AMISR), GNSS/GNSS receivers

(geodetic and scintillation), ASCs, IMAGE magnetometers, SuperDARN, and SGS were utilised as data sources. The purpose of using simultaneous multi-instrument campaigns was to enable interpretations and validations of results. Software used in the research was also discussed. 50-Hz GNSS data (both RINEX and HDF5 files) obtained from Kiruna station courtesy of DLR as well as keograms collected were not used due to noise in the form of spikes (in the case of 50-Hz data) originating from the GNSS receiver and the presence of cloud between the camera and the ionosphere (in the case of ASCs). In view of these observed challenges, TEC fluctuations derived from 30-s and 1-s observables were used to characterise the presence of auroral and polar irregularities since high-latitudes structures are mainly large-scales.

Chapter 6 investigated GPS phase fluctuations originating from ionospheric irregularities at the European auroral and polar latitudes by means of EISCAT UHF/ESR. Two representative case studies in the form of EISCAT (auroral ionosphere) and ESR (polar ionosphere) experiments were designed and conducted. The experiments examined the spatial distribution and scale size of auroral and polar structures responsible for phase fluctuations on GPS signals by measuring electron density profiles transverse to GPS ray paths of relevance. Since at high-latitudes GNSS signals experience higher phase fluctuations and lower amplitude fluctuations, phase fluctuations were quantified by means of fluctuations in TEC from 30-s observables. EISCAT UHF/ESR electron density profiles measured transverse to GPS ray paths revealed the type and location of auroral/polar irregularities whereas GPS observations provide insight into the spatial scale over which the observed irregularities are distributed. The results showed different source mechanisms inducing phase fluctuations on GPS signals in the auroral and polar ionospheres.

Chapter 7 studied the performance of GPS positioning in the presence of phase fluctuations caused by auroral and polar irregularities. Phase fluctuations were quantified by means of fluctuations in TEC which characterised residual errors on geometry-free combination utilised to process the positioning solutions. This was a follow up on March 2018 EISCAT UHF/ESR campaigns discussed in Chapter 6. BK (real-time applications) and PS (post-processing PPP application) solutions were used to estimate the positioning performance from 30-s and 1-s observables using

gLAB. The 3-D positioning errors were calculated from 30-s and 1-s observables during different geomagnetic conditions on the evenings of March 2015 and March 2018. The March 2018 events were computed concurrent with EISCAT UHF/ESR experiments providing insight into the irregularities inducing fluctuations in TEC and the positioning errors. The results obtained showed that the use of 1-s observables as opposed to 30-s reduces the errors and eliminates outages in terms of gaps for both the BK and PS solutions observed while GPS ray paths scan through auroral/polar irregularities.

Chapter 8 presented conclusions and future work. The future work was discussed in parts. First part presented a new design geometry of November 2019 campaign. Second part discussed GNSS applications in Sub-Saharan Africa and a potential research area following the experience acquired.

In summary, the key results of the research are as follows:

- For the first time, auroral and polar structures transverse to GPS ray paths in the European auroral and polar ionospheres were studied by means of EISCAT UHF/ESR ISRs simultaneously combined with permanent geodetic GNSS receiver stations. Temporal TEC fluctuations from 30-s observables were used as convenient proxies to characterise the presence of phase fluctuations originating from the observed auroral and polar structures.
- At both auroral and polar latitudes, intermittent and inhomogeneous particle precipitation distributed over geomagnetic latitudes and longitudes were responsible for a low velocity electron density irregularities inducing the observed intensification in TEC fluctuations as the GPS ray paths scan across the irregularities. However, in the polar latitudes, apart from the intermittent and inhomogeneous particle precipitation, polar patches moving with a velocity much greater than the scan velocity of the GPS ray paths at ionospheric heights originate intensification in TEC fluctuations on the GPS ray paths traverse.
- The source mechanism for the phase fluctuations at the auroral latitudes was particle precipitation. At the polar latitudes, phase fluctuations originated from a combination of particle precipitation and patches.

- Auroral and polar irregularities observed by means of EISCAT UHF/ESR combined with GNSS receivers are distributed over spatial distances of $300\ km$ and $800\ km$ on average in the E and F layer ionospheric heights, respectively.
- In both the auroral and polar ionospheres, the observed ionisation structures as inferred from EISCAT UHF/ESR electron density profiles and the concurrent enhancement in TEC fluctuations were mainly large-scale.
- The intensity and variability of 3-D positioning errors (E_{3D}), DOPs, and gaps depend on the temporal resolution of the GNSS observables ($30\ s$ or $1\ s$). At both auroral and polar latitudes, E_{3D} showed higher values and variability for the case of 30-s BK solution as opposed to the 1-s BK solution. For both 30-s and 1-s observables used to compute PS solution, the observed errors were lower and constant on average irrespective of the geomagnetic condition.
- At both auroral and polar latitudes, the observed increase in GPS positioning errors and gaps computed for both BK and PS solutions from 30-s observables were proportional to increasing geomagnetic activity.
- In disturbed ionosphere, the use of 30-s observables to compute BK and PS solutions was characterised by gaps which suggest poor availability and continuity performance of GPS positioning. However, the use of 1-s observables to compute both BK and PS solutions eliminates the presence of gaps.
- At both auroral and polar latitudes, phase changes observed in the E and F layers are distributed over spatial IPPs distances between $2\ km$ and $40\ km$ and below $2\ km$ on average in the case of 30-s and 1-s observables, respectively.
- The absence of amplitude scintillation at high-latitudes which was inferred from 1-s observation data implies the outer scale of the observed irregularities was between $2\ km$ and $40\ km$ and they are distributed over spatial distances of several hundreds of kilometres. This further suggests the absence of energy cascade from larger to smaller scales structures because of low electron density gradients compared to equatorial latitudes.

- A new design geometry of November 2019 experimental campaign was discussed following successful design and conduct of EISCAT UHF/ESR campaigns in 2019 with a view to use the data for research and publication purpose.
- A few applications of GNSS in Sub-Saharan Africa and a potential area of research were discussed.

8.3 Part 2: New Design Geometry of November 2019 EISCAT UHF/ESR Campaigns

8.3.1 Introduction

GNSS signals propagation traversing the ionosphere can suffer varying degree of scattering caused by refractive index fluctuations [*Forte, 2008 and references therein*]. This scattering of transionospheric radio signals can originate amplitude and phase fluctuations called amplitude and phase scintillation. Weak scattering is associated with low scintillation levels while strong scattering is correlated with high scintillation levels [*Rino, 1979a; Rino, 1979b*]. Scintillation activity depends on frequency of the electromagnetic wave, time of day, season of year, geomagnetic condition, and solar activity [*Aarons, 1982; Fortes et al., 2015*]. Scintillation has been observed to undermine the accuracy, continuity, availability, and reliability of GNSS-based infrastructure operating at the equatorial latitudes and the high-latitudes [*Basu et al., 1988; Guo et al., 2017*]. At auroral and polar latitudes, the ionosphere can be complex and dynamic during adverse Space Weather conditions due to transport of mass, energy, and momentum from the magnetosphere [*Aarons et al., 2000*]. Magnetosphere-ionosphere interactions and dynamics can cause impact ionisation originating from auroral particle precipitation and convecting polar cap patches. In addition, severe geomagnetic activity enhances inhomogeneities in the plasma density distributions. Such ionospheric instabilities can induce ionospheric irregularities responsible for scintillation events. The spatial scale size of the ionospheric irregularities in the plasma distribution determines the type of scintillation. For instance, refractive scintillation is cause by large-scale electron density irregularities whereas as diffractive scintillation originates from small-scale electron density irregularities [*Booker and Majidiahi, 1981; Forte, 2008*].

To understand the spatial distribution of electron density irregularities in given ionospheric layers, the plasma medium is treated as phase screens. Each phase screen is theoretically treated as a layer with uneven and irregular distribution of irregularities. To investigate how irregularities are distributed in a phase screen, a multi-instrument experiment involving EISCAT UHF/ESR radars combined with permanent geodetic GNSS receiver stations courtesy of IGS was designed and conducted between 20:00 and 24:00 UT in November 2019 (5 days). In the time of measurements, the observed K_p value was between 0 and 4 for all days with maximum value of 4 on 21 November 2019 corresponding to disturbed geomagnetic condition. In the auroral ionosphere, EISCAT beams intersected selected GPS ray paths along $110\ km$ altitude (phase screen height) at time interval of 5 minutes over Kiruna. While in the polar ionosphere, ESR beams intersected selected GPS ray paths along $300\ km$ altitude (phase screen height) at the same interval over Ny-Ålesund. Here, it is assumed that the contribution to the phase fluctuations originate from several ionospheric irregularities across the GPS ray paths [*Yeh and Liu, 1982 and references therein*]. Details of the experiment and the results obtained are presented and discussed in subsequent sections.

8.3.2 Data and Methodology

Table 8. 1: GPS PRNs ray paths intersected by EISCAT UHF/ESR beams during the November 2019 experimental campaign for both case studies.

13 November 2019		
Time [UT]	**Case Study 1**	**Case Study 2**
	GPS PRN	**GPS PRN**
20:00-21:00	32	19
21:00-22:00	14	12
22:00-24:00	31	25
20 and 21 November 2019		
20:00-21:00	32	19
21:00-22:00	14	12
22:00-23:20 22:00-23:00	31	 25
23:20-24:00 23:00-24:00	26	 29
27 and 28 November 2019		
20:00-21:00	14	12
21:00-23:00	31	25
23:00-24:00	26	29

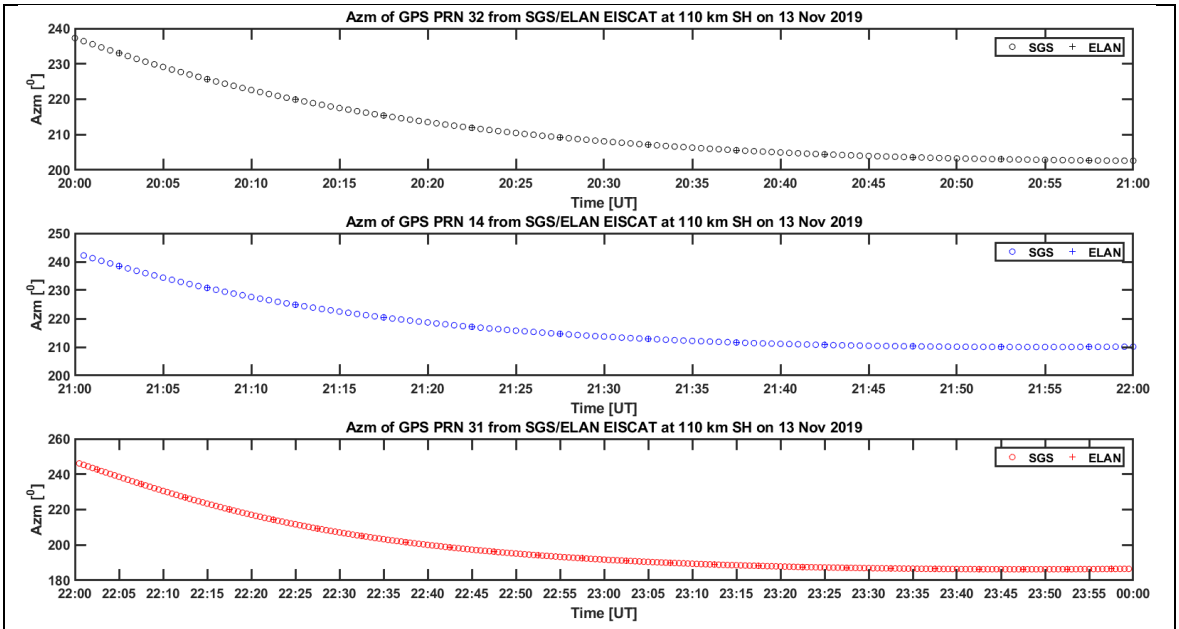

(a) Azimuth of GPS PRNs intersected by EISCAT beams from SGS/ELAN.

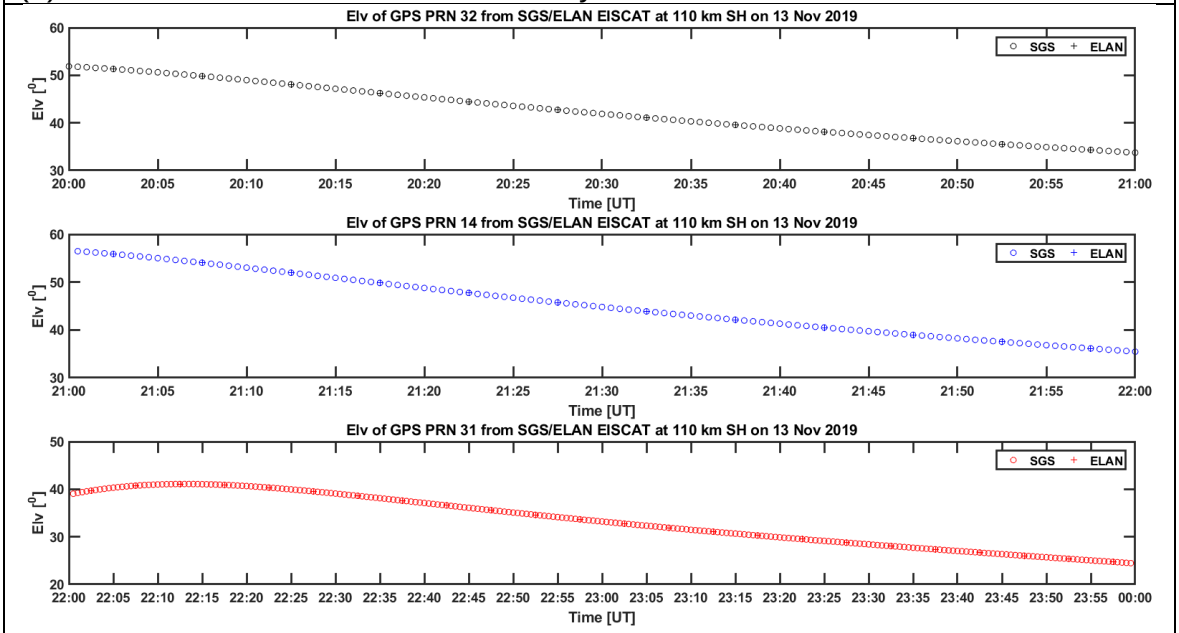

(b) Elevation of GPS PRNs intersected by EISCAT beams from SGS/ELAN.

Figure 8.1: From top to bottom shows simulated description of EISCAT experiment with GPS PRNs ray paths intersected by EISCAT beams at a step of 5 minutes at 110 km shell height. PRNs 32 (black circle line, 20:00 and 21:00 UT), 14 (blue circle line, 21:00 and 22:00 UT), and 31 (red circle line, 22:00 and 24:00 UT) from SGS were followed by black, blue, red, and green plus lines from ELAN respectively (a) azimuth and (b) elevation on 13 November 2019.

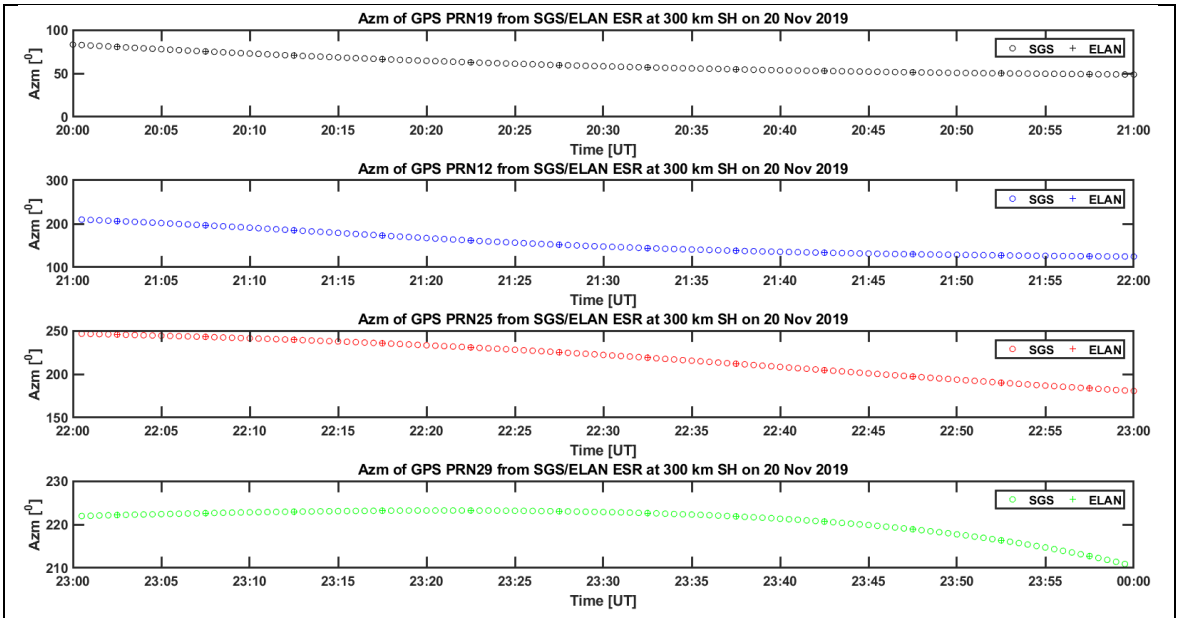

(a) Azimuth of GPS PRNs intersected by ESR beams from SGS/ELAN.

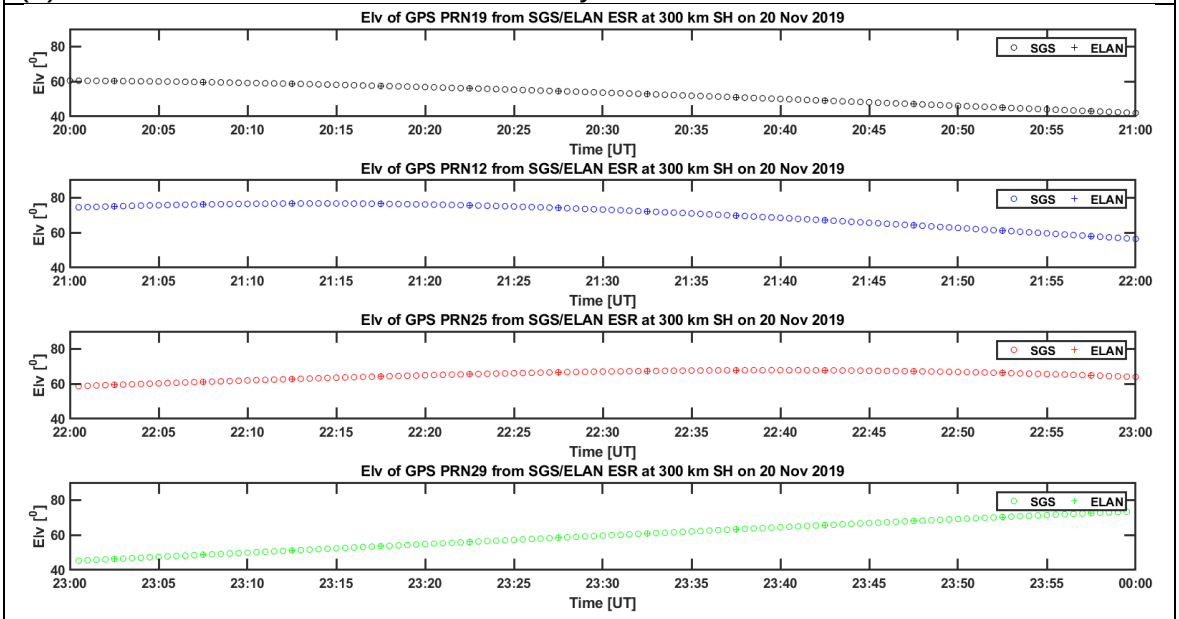

(b) Elevation of GPS PRNs intersected by ESR beams from SGS/ELAN.

Figure 8.2: From top to bottom shows simulated description of ESR experiment with GPS PRNs ray paths intersected by ESR beams at a step of 5 minutes at $300\ km$ shell height. PRNs 19 (black circle line, 20:00, 21:00 UT), 12 (blue circle line, 21:00 and 22:00 UT), 25 (red circle line, 22:00 and 23:00 UT), and 29 (green circle line, 23:00 and 24:00 UT) from SGS were followed by black, blue, and red plus lines from ELAN respectively (a) azimuth and (b) elevation on 20 November 2019.

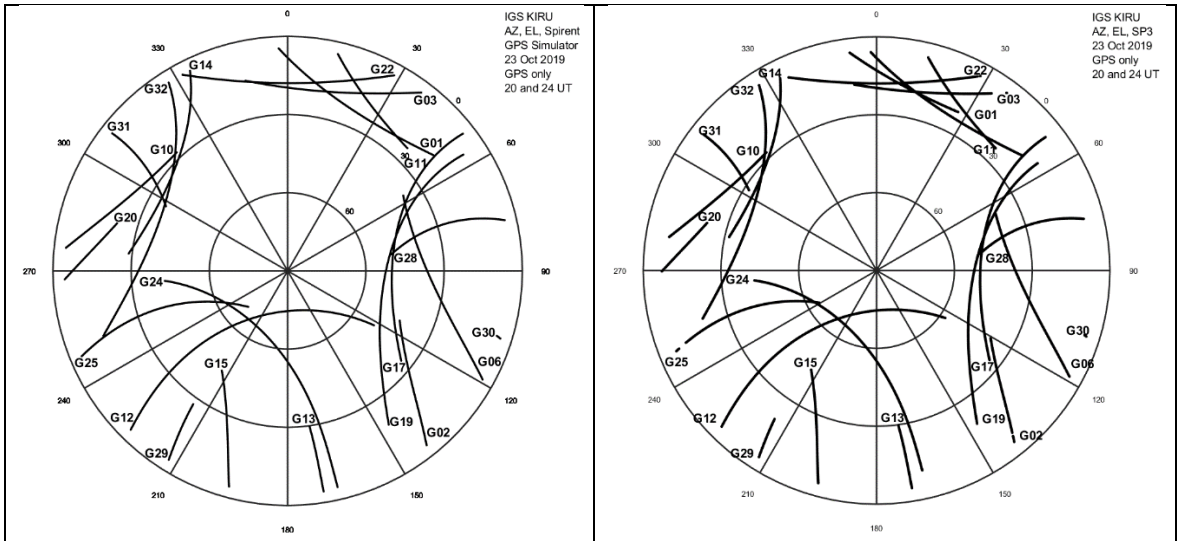

(a) Simulated GPS PRNs orbits over Kiruna (KIRU) from Spirent GPS Simulator.

(b) Actual GPS PRNs orbits over Kiruna (KIRU) from SP3 Data.

Figure 8.3: GPS PRNs orbits from azimuth and elevation data (elevation mask of 5°) over Kiruna between 20:00 and 24:00 UT on 23 October 2019 obtained from (a) Spirent GPS Simulator and (b) SP3 Data.

EISCAT UHF facilities located at Tromsø (EISCAT) and Longyearbyen (ESR) were used to collect measurements over Kiruna (auroral ionosphere) and Ny-Ålesund (polar ionosphere) between 20:00 and 24:00 UT in November 2019. Receiver Independent Exchange format (RINEX) observation and navigation (SP3) data over Kiruna (KIRU) and Ny-Ålesund (NYA2) were obtained courtesy of IGS. In this report, only 30-s RINEX data were used to process positioning solutions in RTK and PPP modes using gLAB. The idea was to investigate the impact of ionisation structures on positioning and timing applications at the auroral and polar latitudes. In this report, Case Study 1 is the EISCAT experiment while ESR experiment is Case Study 2. A summary of the November 2019 campaign is given in Table 8.1. SGS was used to obtained azimuth and elevation data over KIRU and NYA2 using known geodetic GNSS receiver locations courtesy of IGS.

The azimuth and elevation data were used to simulate the design geometry of the experiment in advance (Figures 8.1 and 8.2). Figure 8.1 shows the simulated azimuth and elevation angles of EISCAT beams over Kiruna GNSS receiver location using SGS derived ELAN file used in the design geometry of EISCAT experiment (Table 8.1: Case Study 1) between 20:00 and 24:00 UT on 13 November 2019. Figure 8.1a shows the azimuth of GPS ray paths intersected by EISCAT beams. EISCAT beams scan a given position for 5 minutes at $110\ km$ ionospheric shell

height, then aligned to a new scanning position defined by azimuth and elevation angles. The sequence continuous until the end of the time of measurement. In Figure 8.1, black circle line (20:00-21:00 UT), blue circle line (21:00-22:00 UT), and red circle line (22:00-24:00 UT) represent azimuth and elevation angles of PRNs 32, 14, and 31, respectively. The same explanation applies to Figure 8.1b but in terms of elevation angles.

Figure 8.2 shows the simulated azimuth and elevation angles of ESR beams over Ny-Ålesund GNSS receiver location using SGS derived ELAN file used in the design geometry of ESR experiment (Table 8.1: Case Study 2) between 20:00 and 24:00 UT on 20 November 2019. Figure 8.2a shows the azimuth of GPS ray paths intersected by ESR beams. ESR beams scan a given position for 5 minutes at $300\ km$ ionospheric shell height, then aligned to a new scanning position defined by azimuth and elevation angles. The sequence continuous until the end of the time of measurement. In Figure 8.2, black circle line (20:00-21:00 UT), blue circle line (21:00-22:00 UT), red circle line (22:00-23:00 UT), and green circle line (23:00-23:00 UT) represent azimuth and elevation angles of PRNs 19, 12, 25, and 29, respectively. The same explanation applies to Figure 8.2b except for elevation angles instead of azimuth angles. For more information on EISCAT UHF/ESR 2019 Experimental Campaigns, refer to Table 8.1.

Figure 8.3 shows a comparison between the simulated GPS PRNS orbital trajectories obtained from SGS (Figure 8.3a) and the measured GPS PRNs trajectories obtained from SP3 (Figure 8.3b) between 20:00 and 24:00 UT on 23 October 2019 over Kiruna.

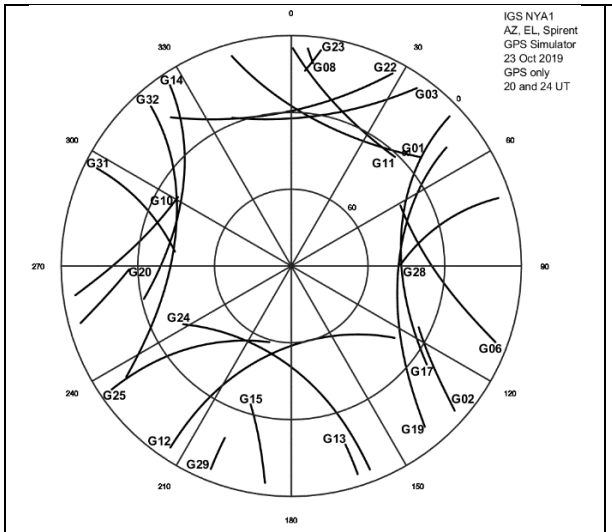

(a) Simulated GPS PRNs orbits over Ny-Ålesund (NYA2) from SGS data.

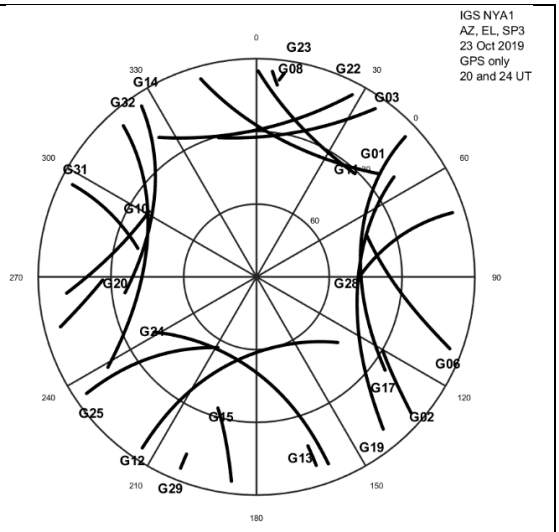

(b) Actual GPS PRNs orbits over Ny-Ålesund (NYA2) from SP3 data.

Figure 8.4: GPS PRNs orbits from azimuth and elevation data (elevation mask of 5°) over Ny-Ålesund between 20:00 and 24:00 UT on 23 October 2019 obtained from (a) SGS and (b) SP3 data.

To further check the accuracy and integrity of the simulated GPS PRNs trajectories over Ny-Ålesund, the simulated result was compared to the measured result. Figure 8.4a shows the simulated sky view while Figure 8.2b presents the measured visible satellites sky view between 20:00 and 24:00 UT on 23 October 2019. Figures 8.3 and 8.4 confirmed a reasonable agreement between the two measurements and this gave the confidence on the data source (SGS) used for prediction of the GPS satellites positions.

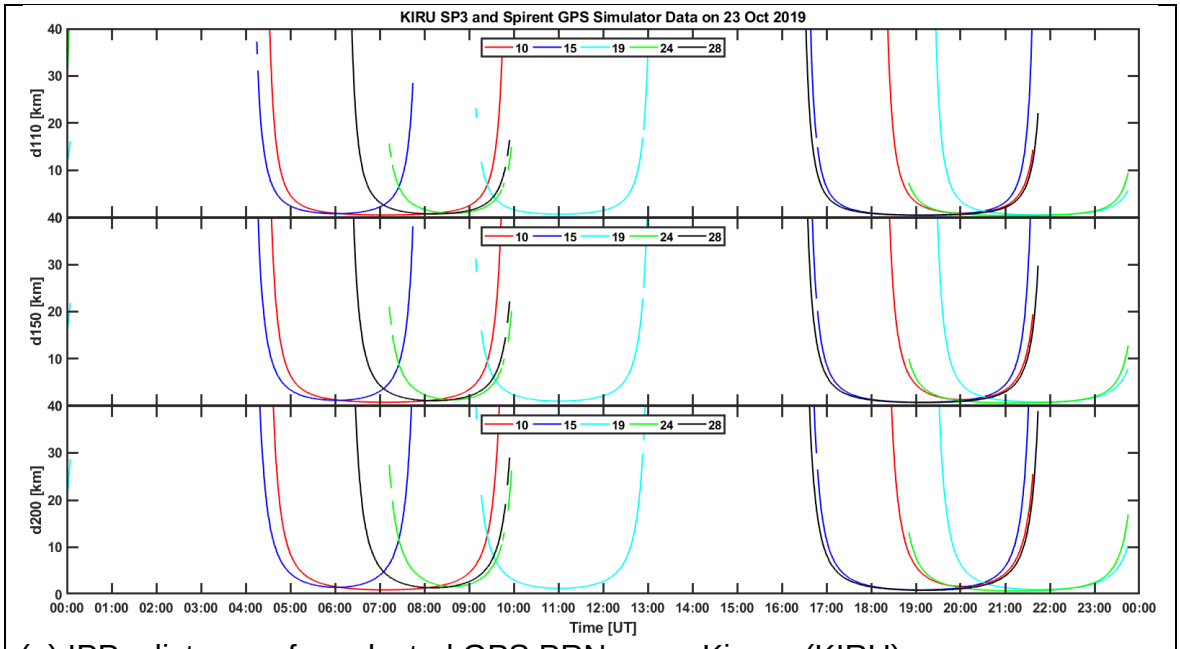

(a) IPPs distances for selected GPS PRNs over Kiruna (KIRU).

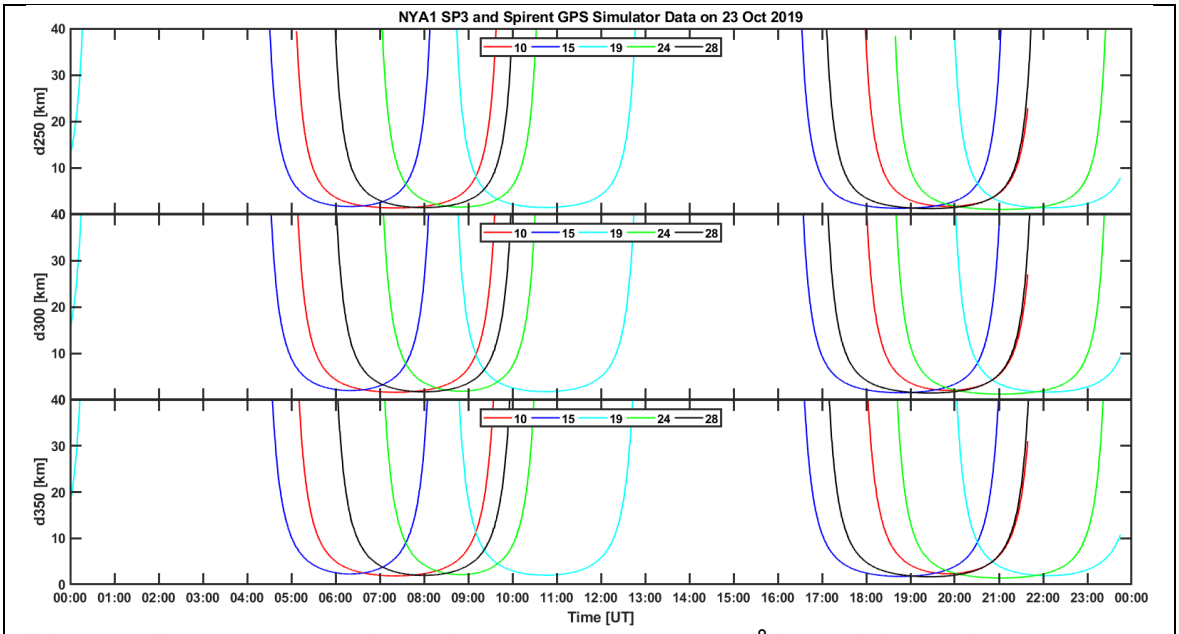

(b) IPPs distances for selected GPS PRNs over Ny-Ålesund (NYA2).

Figure 8.5: IPPs spatial distances of GPS PRNs 10 (red line), 15 (blue line), 19 (cyan line), 24 (green line), and 28 (black line) obtained from SGS and SP3 data at elevation mask of 5° between 00:00 and 24:00 UT on 23 October 2019 over (a) Kiruna (KIRU, IGS) at $110\ km$, $150\ km$, and $200\ km$ altitude from top to bottom panels and (b) Ny-Ålesund (NYA2, IGS) at $250\ km$, $300\ km$, and $350\ km$ altitude from top to bottom panels.

In Figure 8.5, distances between the simulated (SGS) GPS ray paths IPP coordinates and the experimental or actual (SP3) IPP coordinates at selected shell heights were calculated and presented. Figure 8.5a, from top to bottom, shows the calculated IPP distances of selected GPS PRNs (10 – red line, 15 – blue line, 19 – cyan line, 24 – green line, and 28 – black line) at $110\ km$, $150\ km$, and $200\ km$ shell heights over Kiruna whereas Figure 8.5b shows the IPP distances of the same PRNs at $250\ km$, $300\ km$, and $350\ km$ shell heights over Ny-Ålesund. In Figure 8.5, for satellites above 20° elevations, the calculated IPP distances were below $2\ km$ on average. Since the spatial resolution of EISCAT UHF/ESR radars is $2\ km$, therefore the design geometry was within acceptable tolerance [*Forte et al., 2017*]. This check was necessary to ensure accurate and reliable design geometry during the November 2019 campaign. Figures 8.6-8.8 present the design geometry of EISCAT experiment in the evenings of 13 November 2019 corresponding to the auroral ionosphere.

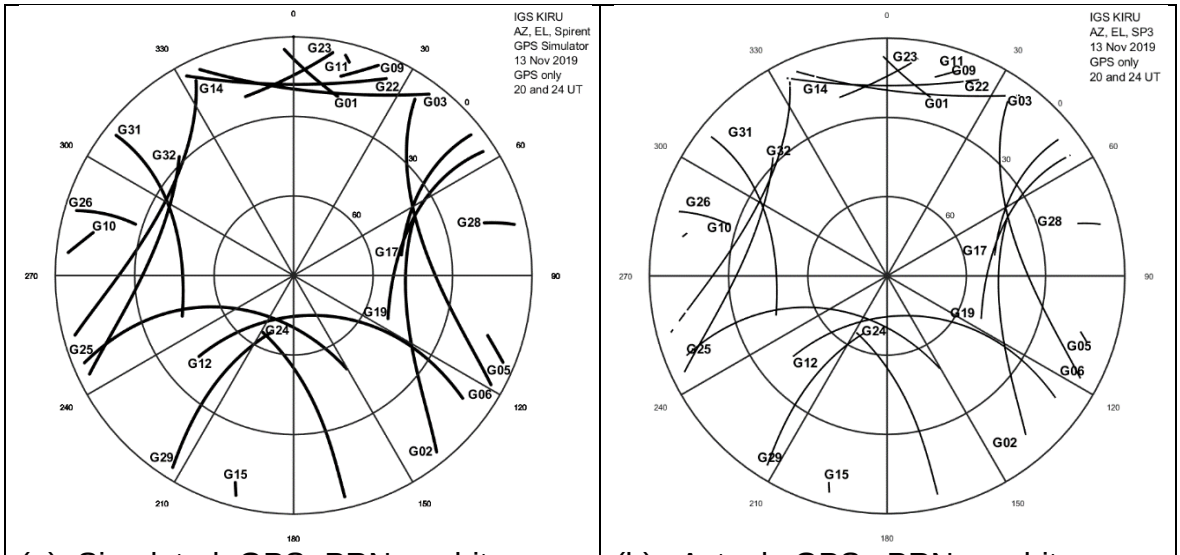

(a) Simulated GPS PRNs orbits over Kiruna from SGS data.

(b) Actual GPS PRNs orbits over Kiruna from SP3 data.

Figure 8.6: GPS PRNs orbits over Kiruna at elevation mask of 5° between 20:00 and 24:00 UT on 13 November 2019 obtained from (a) SGS and (b) SP3 data.

Figure 8.6 shows GPS PRNs orbits from (a) SGS and (b) SP3 data over Kiruna at elevation mask of 5° between 20:00 and 24:00 UT on 13 November 2019. Figure 8.6a shows the simulated GPS PRNs orbits in terms of azimuth and elevation angles. G stands for GPS will the numeric represents the PRN visible over Kiruna GNSS receiver station (KIRU). The GPS PRNs available are G31, G32, G14, G23, G11, G09, G22, G01, G03, G28, G17, G19, G05, G06, G02, G24, G12, G15, G29, G25, G10, and G26. The satellites orbits were predicted in advance by using azimuth and elevation data collected from SGS. To confirm the accuracy and reliability of SGS measurements, the results were compared to azimuth and elevation data derived from SP3 data indicated in Figure 8.6b. There was a good agreement between the simulated (SGS) and measured (SP3) satellites orbits.

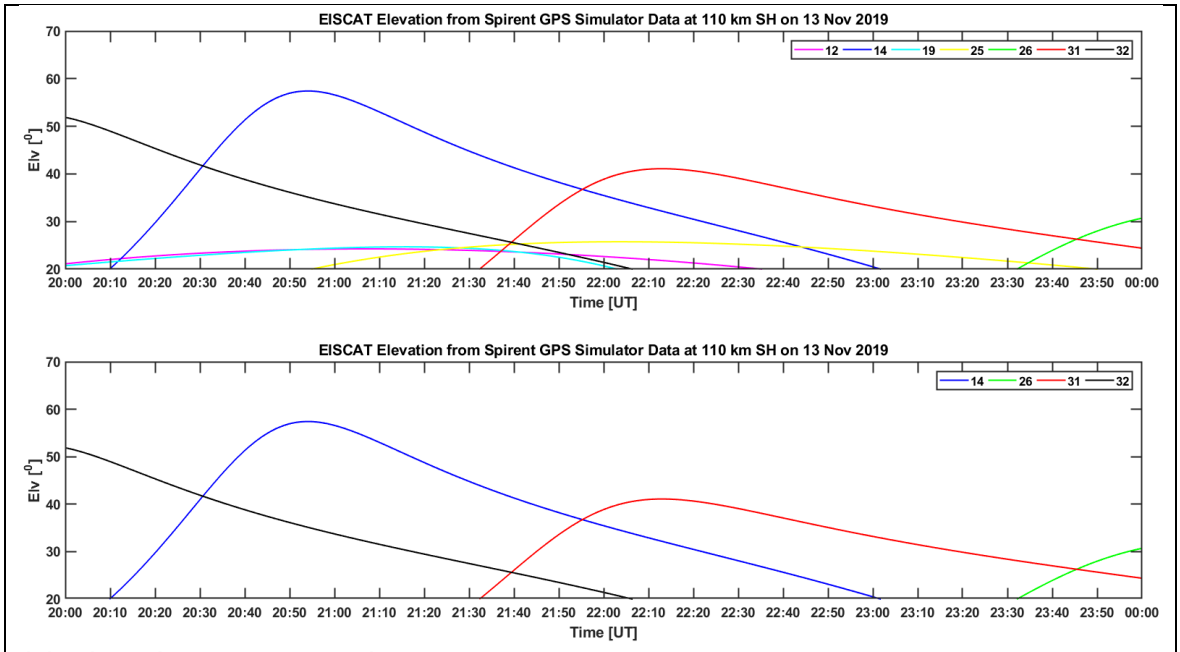

(a) Elevation of EISCAT beams from SGS.

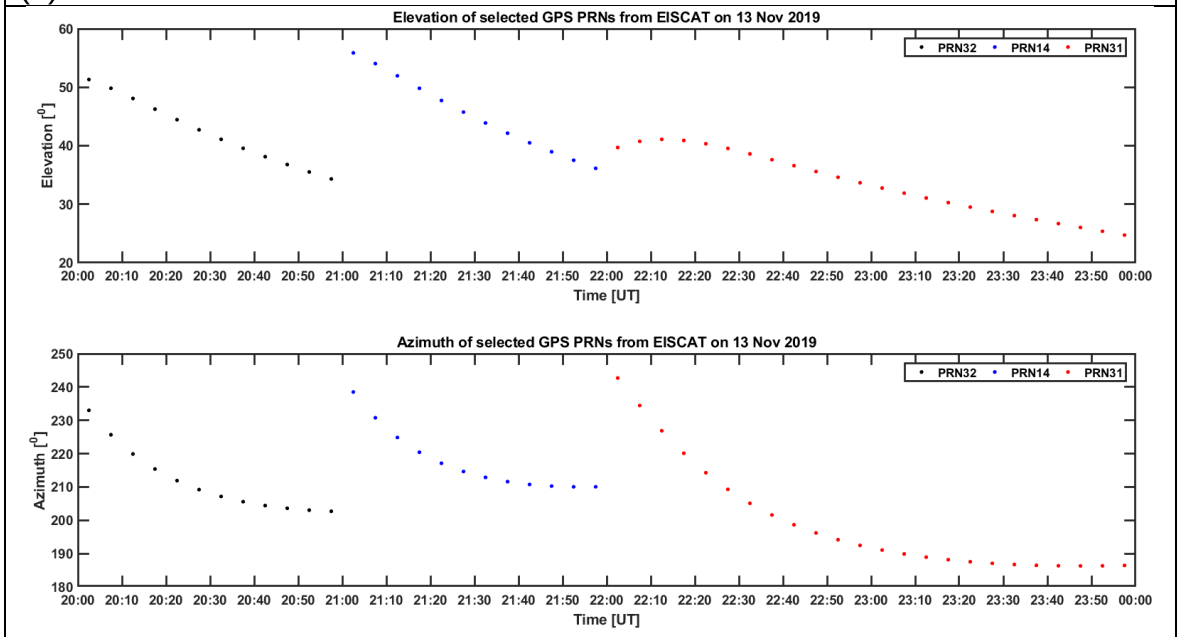

(b) Elevation and azimuth from EISCAT

Figure 8.7: From top to bottom shows (a) the elevation of EISCAT beams intersected by selected GPS PRNs ray paths over Kiruna at 110 km shell height and (b) the elevation and azimuth of EISCAT beams intersected by GPS PRNs 32 (black dotted line, 20:00-21:00 UT), 14 (blue dotted line, 21:00-22:00 UT), and 31 (red dotted line, 22:00-24:00 UT) ray paths over Kiruna at 110 km shell height between 20:00 and 24:00 UT on 13 November 2019.

Figure 8.7, from top to bottom, shows the elevations of GPS PRNs 12 (magenta line), 14 (blue line), 19 (cyan line), 25 (yellow line), 26 (green line), 31 (red line), and 32 (black line) at 110 km shell height between 20:00 and 24:00 UT on 13 November 2019 as indicated in Figure 8.7a. The selected PRNs 32, 14, and 31 (26 excluded) were used to design the experiment because their elevation angles were above 23°

(EISCAT minimum requirement). Figure 8.7b, from top to bottom, shows the elevation and azimuth from EISCAT at interval of 5 minutes of the selected PRNs 32 (black dotted line, 20:00-21:00 UT), 14 (blue dotted line, 21:00-22:00 UT), and 31 (red dotted line, 22:00-24:00 UT) on 13 November 2019. Here, EISCAT beams were repositioned after 5 minutes of scanning in a fixed location to continue with the process of collecting backscattered power until the end of time of measurements (applied to all days and both case studies). The elevation and azimuth data in Figure 8.7b were used to write the Experimental Language (ELAN) file used by EISCAT (applied to all days and both case studies). To better appreciate Figure 8.7b, the azimuth and elevation angles of SGS derived ELAN file EISCAT beams repositioned at every 5 minutes when the GPS ray paths of relevance were followed were simulated as indicated in Figure 8.1 during 13 November 2019. The same method was used for the design geometry of 20, 21, 27, and 28 November 2019 Case Study 1.

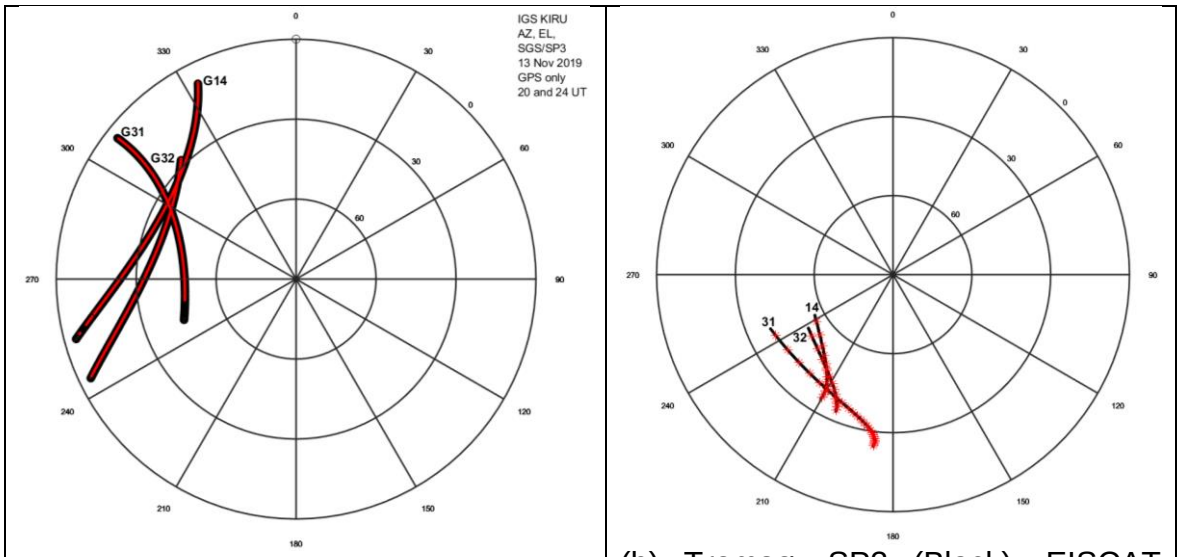

(a) Kiruna: SGS (Black), SP3 (Red).

(b) Tromsø: SP3 (Black), EISCAT beams (Red)

Figure 8.8: GPS PRNs 14, 31, and 32 orbits obtained between 20:00 and 24:00 UT on 13 November 2019 over (a) Kiruna from SGS (Black) co-aligned with SP3 (Red) data and (b) Tromsø from SP3 (Black) co-aligned with EISCAT beams (Red) data. The red colour is used to superimposed the black colour.

Figure 8.8 shows the selected PRNs (32, 14, and 31) trajectories over (a) Kiruna and (b) EISCAT (Tromsø). In Figure 8.8a, the simulated PRNs trajectories from SGS (black lines) were superimposed by trajectories from SP3 (red lines). On the other hand, Figure 8.8b shows the selected PRNs trajectories over Tromsø from SP3 (black lines) superimposed by EISCAT beams (red asterisk lines) between 20:00

and 24:00 UT on 13 November 2019. The EISCAT beams as indicated in Figure 8.8b were obtained from the experimental azimuth and elevation data after being analysed with GUISDAP. In both cases, there were good agreements in the different data sources (SGS, SP3, and EISCAT).

In addition, Figures 8.9-8.11 show the design geometry of ESR experiment in the evening of 20 November 2019 with respect to the polar ionosphere.

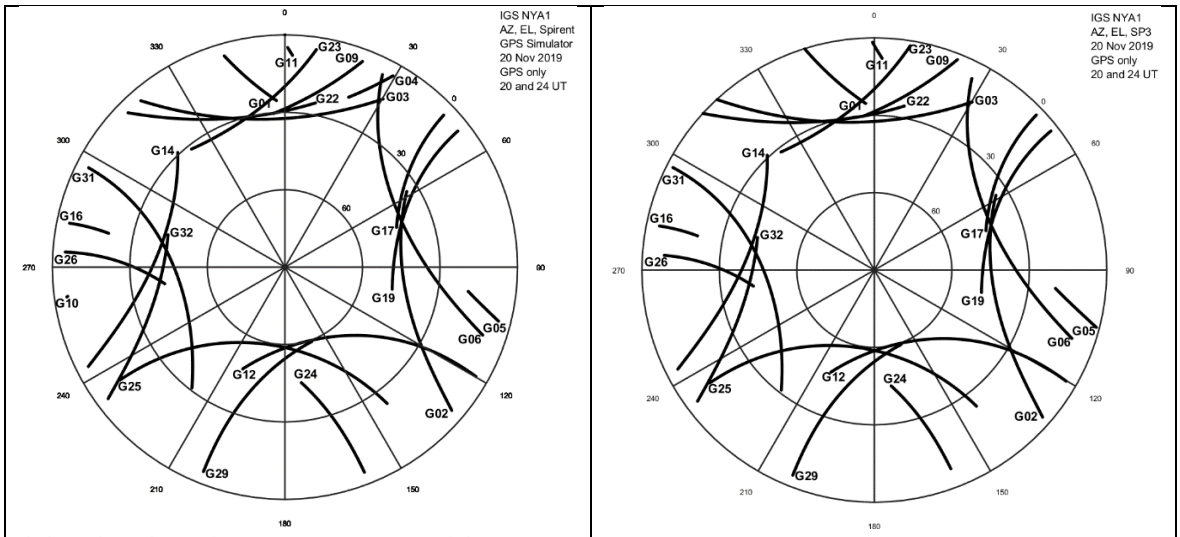

(a) Simulated GPS PRNs orbits over Ny-Ålesund from SGS data.

(b) Actual GPS PRNs orbits over Ny-Ålesund from SP3 data.

Figure 8.9: GPS PRNs orbits over Ny-Ålesund at elevation mask of 5° between 20:00 and 24:00 UT on 20 November 2019 obtained from (a) SGS and (b) SP3 data.

Figure 8.9 shows GPS PRNs orbits from (a) SGS and (b) SP3 data over Ny-Ålesund GNSS receiver station (NYA2) at elevation mask of 5° between 20:00 and 24:00 UT on 20 November 2019. Figure 8.9a presents the simulated GPS PRNs orbits in terms of azimuth and elevation angles. The GPS PRNs available are G31, G32, G14, G01, G11, G23, G09, G22, G04, G03, G17, G19, G05, G06, G02, G24, G12, G15, G29, G25, G10, G26, and G16. The satellites orbits were predicted in advance by using azimuth and elevation data collected from SGS. To confirm the accuracy and reliability of SGS measurements, the results were compared to the azimuth and elevation data derived from SP3 data indicated in Figure 8.9b. There was a reasonable similarity between the simulated (SGS) and measured (SP3) satellites orbits.

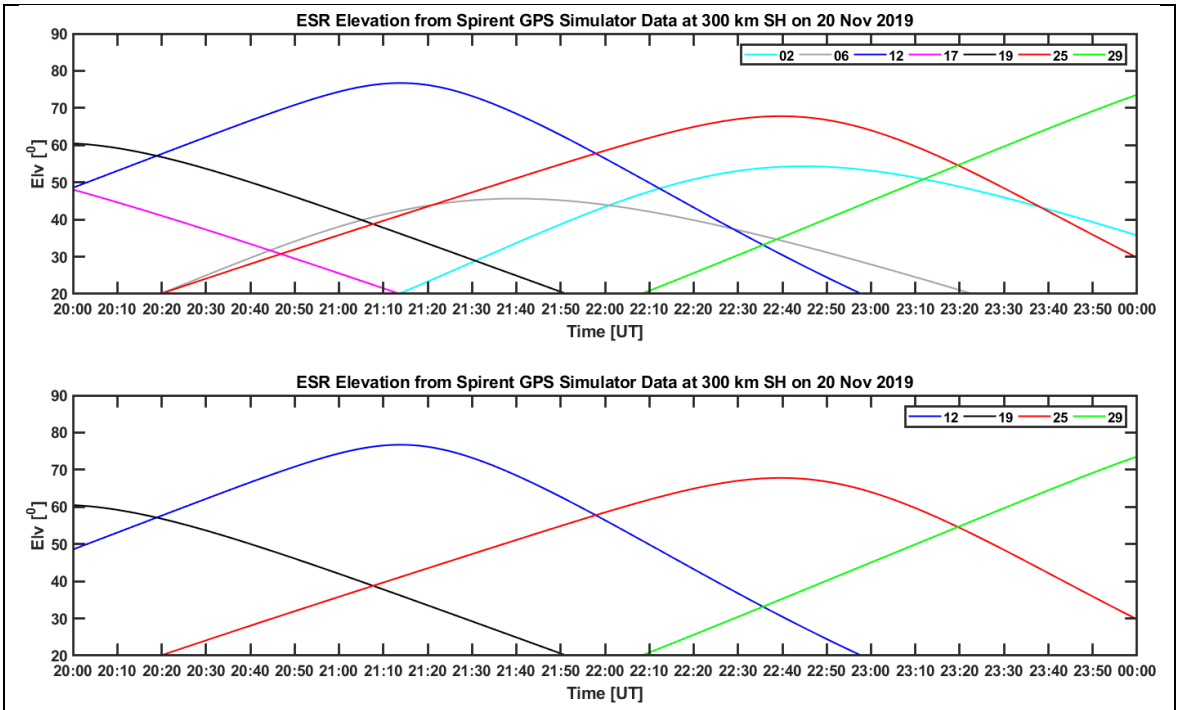

(a) Elevation of EISCAT beams from SGS.

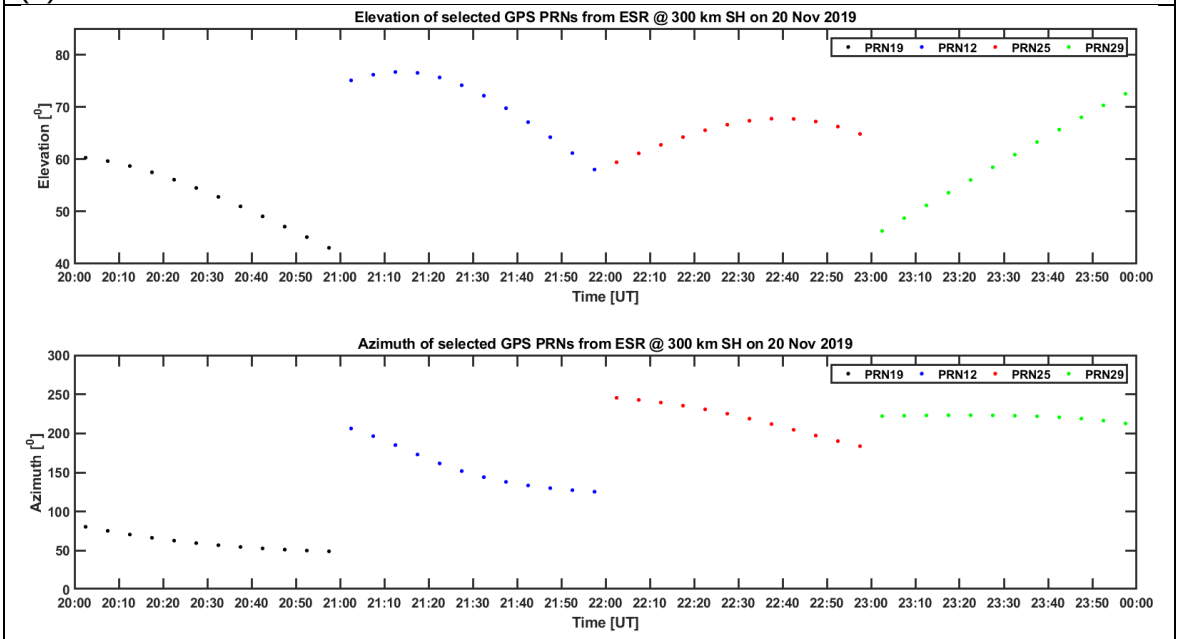

(b) Elevation and azimuth from EISCAT.

Figure 8.10: From top to bottom shows (a) the elevation of ESR beams intersected by selected GPS PRNs ray paths over Ny-Ålesund at $300\ km$ shell height and (b) the elevation and azimuth of ESR beams intersected by GPS PRNs 19 (black dotted line, 20:00-21:00 UT), 12 (blue dotted line, 21:00-22:00 UT), 25 (red dotted line, 22:00-23:00 UT), and 29 (green dotted line, 23:00-24:00 UT) ray paths over Ny-Ålesund at $300\ km$ shell height between 20:00 and 24:00 UT on 20 November 2019.

Figure 8.10a, from top to bottom, shows the elevations of GPS PRNs 02 (cyan line), 06 (grey line), 12 (blue line), 17 (magenta line), 19 (black line), 25 (red line), and 29 (green line) at $300\ km$ shell height between 20:00 and 24:00 UT on 20 November

2019. The selected PRNs 12, 19, 25, and 29 were used to design the experiment. Figure 8.10b, from top to bottom, shows the elevation and azimuth from ESR of the selected PRNs 19 (black dotted line, 20:00-21:00 UT), 12 (blue dotted line, 21:00-22:00), 25 (red dotted line, 22:00-23:00 UT), and 29 (green dotted line, 23:00-24:00 UT) on 20 November 2019. As mentioned in Case Study 1, to better appreciate the design geometry of ESR beams following GPS ray paths of relevance using azimuth and elevation derived from SGS, Figure 8.2 is included.

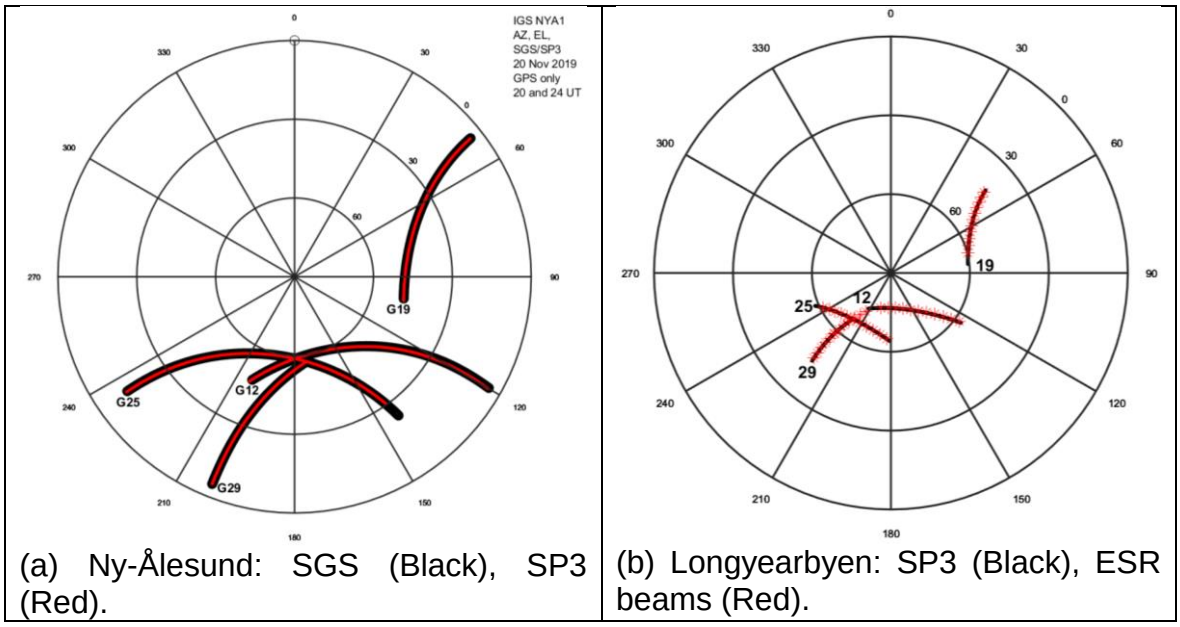

(a) Ny-Ålesund: SGS (Black), SP3 (Red).

(b) Longyearbyen: SP3 (Black), ESR beams (Red).

Figure 8.11: Shows GPS PRNs 12, 19, 25, and 29 orbits obtained between 20:00 and 24:00 UT on 20 November 2019 over (a) Ny-Ålesund from SGS (Black) co-aligned with SP3 (Red) data and (b) Ny-Ålesund from SP3 (Black) co-aligned with ESR beams (Red) data.

Figure 8.11 shows the selected PRNs trajectories in terms of azimuth and elevation angles over (a) Ny-Ålesund (NYA2) and (b) Longyearbyen (ESR). Figure 8.11a shows the simulated selected PRNs trajectories from SGS (black lines) superimposed by trajectories from SP3 (red lines). Figure 8.11b shows the selected PRNs trajectories over Longyearbyen from SP3 (black lines) superimposed by ESR beams (red asterisk lines) between 20:00 and 24:00 UT on 20 November 2019. The ESR beams were obtained as explained in Figure 8.8. The results obtained are in good agreement.

8.4 Part 3: GNSS and Sub-Saharan Africa

8.4.1 Introduction

Figure 8.12: Map of Sub-Saharan Africa.
Source: https://en.wikipedia/wiki/Sub-Saharan_Africa

Sub-Saharan Africa as shown in Figure 8.12 is a geographical area located south of the Sahara. Areas in dark and light green on the map are regarded as Sub-Saharan Africa. Over 50% of Sub-Saharan Africa are directly or indirectly employed in agriculture industry. Africa has a population of over 850 million people, which is greater than 14% of the total number of people in the world [*Rabiu, 2013*]. The population in this part of the world is growing at an alarming rate and thus the need to improve agricultural production, water, and land management has become a major concern. Insecurity, hunger, poverty, and disease have continued to rise in the region possibly due to inability of government and organised institutions to meet the increasing demand for food, clean water, energy, etc. for its populace. Water and land are limited resources, which must be used sustainably to ensure balance in the ecosystem and wellbeing of peoples. The present way of doing things has not helped current realities and therefore need to change with new but sustainable methods [*O'Keeffe, 2016*]. Appropriate data management can assist in delivering the basic change required for a sustainable community [*Blanco, 2016*]. To achieve sustainable (precision) agriculture, efficient water and land management; sustainable search and rescue; productive oil and gas exploration; accurate surveying and mapping; safety of civil aviation; effective use of mobile devices,

GNSS technology is a useful tool. This can support food security, environmentally friendly activity, and sustainable communities in the end. *Zarco-Tejada et al.,* [2014], for example, defines precision agriculture as a technologically informed decision-making for agricultural management to enhance agricultural activities through accurate management of every step of the processing chain.

8.4.2 Applications of GNSS

GNSS is a satellite-based navigation system with global coverage. During the time of writing this report, there are three GNSS with full operational and commercial capability used for civil and military applications. They are GPS designed and implemented by the U.S. Department of Defence and GLONASS built by the Russian Federation [*Oxford Economics, 2012*]. BeiDou or COMPASS (China) and Galileo (European Union) are two other GNSS but full operational availability is achieved by 2020 [*Pérez Ruiz and Upadhyaya, 2012*]. China Aerospace Science and Technology corporation reported a recent successful BeiDou launch on 9 March 2020. ESA hopes to complete the constellation in 2020 to have a global coverage (https://www.esa.int/Applications/Navigation/Four_new_Galileos_join_Europe_s_largest_satellite_constellation). However, this projection was not achieved in 2020.

GNSS is becoming an integral part of every aspect of today's life. Satellite navigation systems have been and will continue to be an enabling technology with widespread applications. Following a report for Science and Technology Facilities Council (STFC) November 2012, from 2011 to 2020 there is an estimated growth of 10% a year in the global market of services and products supported by GNSS. The deployment of a specific technology depends on equipment specifications in terms of the degree of precision (low, high, and very high). Thus, the applications [*Hofgartner, 2008 and Morton, 2017*] of GNSS include but not limited to the following: precision agriculture, water management, land management, road transport, maritime, aviation, search and rescue, military, oil and gas, location-based services, mobile phones, surveying and mapping, disaster prevention and management, health, climate and weather, Global Earth Observation System of Systems (GEOSS).

Figure 8.13: Applications of GNSS. Courtesy of GUIDE Geolocation Testing Laboratory.

As suggested in the preceding paragraph, the applications of GNSS are beyond the list provided. In the thesis, attention was on how GNSS can be utilised in precision agriculture, water and land management, oil and gas, aviation, surveying and mapping, search and rescue, mobile phones in Sub-Saharan Africa. Figure 8.13 depicts some areas of applications of GNSS.

8.4.3 GNSS and Precision Agriculture

In 2015 [United Nations], the world population was estimated to be above 7.3 billion. The growth rate shows an exponential pattern and that 16% of the growth is attributed to Sub-Saharan Africa. By 2019, the world's population was projected to grow to about 7.7 billion on average indicative of a potential socio-economic implication [*United Nations, 2019*]. The rapid growth rate in population will mean increased demand for food. The existing methods of food production (non-precision agriculture) in Africa cannot meet current let alone future demand. Thus, a sustainable and efficient method needs to be strategised to achieve food sufficiency in quantity and quality within the 47 member nations in the Sub-Saharan Africa. An example is precision agriculture. Precision agriculture can be regarded as gathering geospatial information on the requirements of soil, plant and animal, defining and distributing site-specific variables to achieve enhanced agricultural productivity and environmental protection [*GPS.GOV*]. Precision agriculture is correlated with smart agriculture which requires the use of internet of Things (IoT) combined with Data

Analytics (DA). IoT is the interconnection of computing devices embedded in objects by means of Internet to send and receive data. IoT and DA support smart agriculture to deliver high operational efficiency and productivity to guarantee food security [*Elijah et al., 2018; Goyal et al., 2020*].

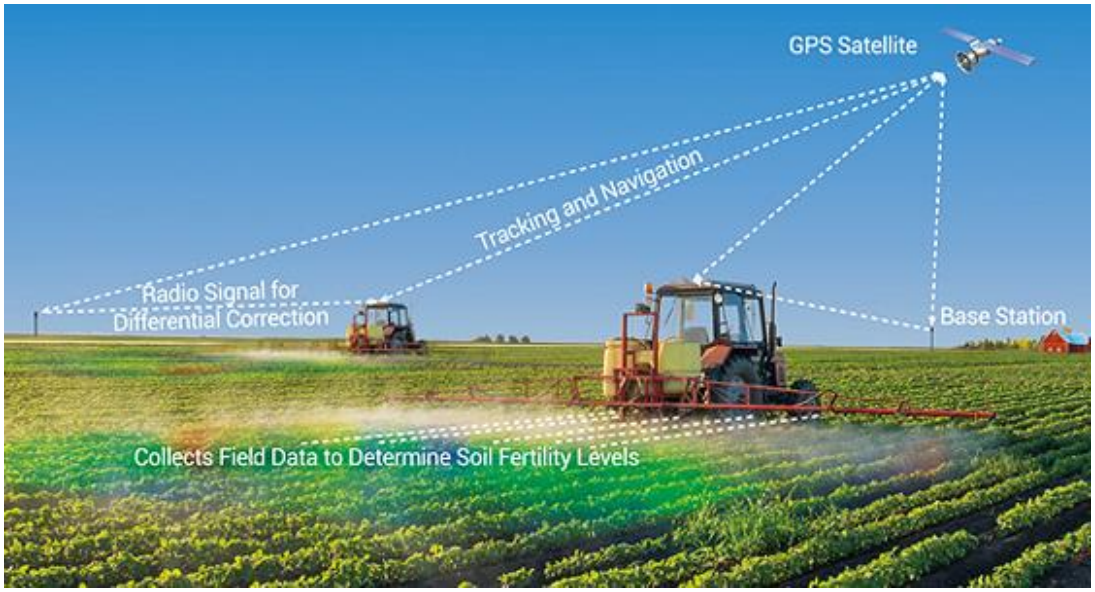

Figure 8.14: Precision agriculture. Courtesy of NEXCOM.
Source: http://www.nexcom.co.uk/news/Detail/nexcom-vehicle-mount-computers-increase-efficiency-of-precision-agriculture-in-asia

GNSS has enabled the design and deployment of precision agriculture systems, which makes farming interestingly cost-effective and easy to farmers. Figure 8.14 presents applications of GNSS and related technologies in precision agriculture. GNSS is applicable in precision agriculture in areas such as sensing of compaction profile, RTK-based plant mapping, precise weed management system, monitoring of yield, robotic equipment [*Fubara, 2009; Pérez Ruiz and Upadhyaya, 2012*]. In ACIL ALLEN report June 2013, precision agriculture contributes to environmental benefits in terms of water use efficiency, reduction in quantity of chemicals or fertilisers in the environment and improved management of disease. Apart from environmental benefits, precision agriculture offers economic benefits. In *Adekunle*, [2013], agricultural research and efficient implementation would enhance food security, sustainable production and development and increased productivity with an attendant profit margin when compared to traditional agriculture. There are also savings in time and energy, which is an addition to economic benefits. Notwithstanding, there are challenges with the adoption and application of this technology in terms of lack of political will, poor policy framework, acceptability of

new technology by farmers and inadequate funding. However, if these challenges are properly addressed, Sub-Saharan Africa can be a hub for agricultural production and food export.

8.4.4 GNSS and Water Management

Out of the amount of water available in the world, only about 2% is freshwater the rest is saltwater, which has no direct usage to human consumption. Furthermore, only half of the 2% of the freshwater is available for use [*Donkor, 2006*]. In the report, over 30% of nations of the world are classified under water stress (between 1000 and $1500\ m^3$ per capita). Most nations are facing development problems following water scarcity both in quality and quantity. Sub-Saharan Africa is not an exception. About 40% of its population are experiencing water scarcity and thus development in the region is being hampered. This implies efficient and reliable methods are necessary to define, regulate, and control water withdrawals for agriculture, sanitation, industry, and domestic supply purposes. In this region, it is necessary to promote the application of water resources management to address the increasing water inadequacy challenge. Water is an important ingredient in achieving global food security and quality of life. This can be realised for instance through effective application of GNSS technology in water use efficiency and precision agriculture. Figure 8.15 shows a local community approach to water management for use in irrigation farming. A local way of meeting local farming demand in Sub-Saharan Africa.

Figure 8.15: Water Management in Sub-Saharan Africa.
Source: www.scidev.net/objetcs_store/thumb

For instance, a project called “Water in Africa” pursues a vision to secure the attainment of economic development through improved management of desertification, droughts, and floods [*Donkor, 2006*]. GNSS technology is core in achieving this goal. The vision intends to eradicate desertification, droughts, and floods by 2025 with an estimated budget of about $20 billion in a year. This will amount to about $400 billion between 2006 and 2025. According to USAID 2008 report on Sub-Saharan Africa (about 47 countries in Africa), economic losses due to treatment of water-related diseases and the collapse of business activities amount to a sum above $28 billion per year which is equivalent to 5% of cumulative Gross Domestic Product (GDP) of the entire region. The consequences can transcend beyond economic terms but of course, a threat to human existence. To achieve economic sustainability and provision of food to the ever-growing population in Sub-Saharan Africa, the region must as a matter of topmost priority, ensure timely and effective deployment of policies and programmes geared at achieving water use efficiency and agricultural productivity [*Gebrehiwot and Gebrewahid, 2016*].

8.4.5 GNSS and Land Management

Land, water, and agriculture are interwoven. Land and water are input variables to agriculture. Everywhere, the land is not the same in size, soil type, composition, or water content. Thus, the study of soil parameters can assist in the estimation of agricultural input requirements and the predicted produce at the end of farming. Land provides the platform for the growth of plants and animals. The same way water is considered as a scarce commodity, land is likewise scarce. Therefore, effective management of these scarce commodities is critical to food security and sustainability of the environment. Land area estimation is a major factor in agricultural measurements and analysis [*Carletto et al., 2015*]. Effective land management depends on effective land measurements and analysis. Contrary to this, land mismeasurement can lead to misreporting and hence agricultural productivity is likely to dwindle. GNSS technology has been used as a very effective tool in land surveying and mapping and Geographic Information System (GIS) applications as indicated in Figure 8.16 [*Hofgartner, 2008*].

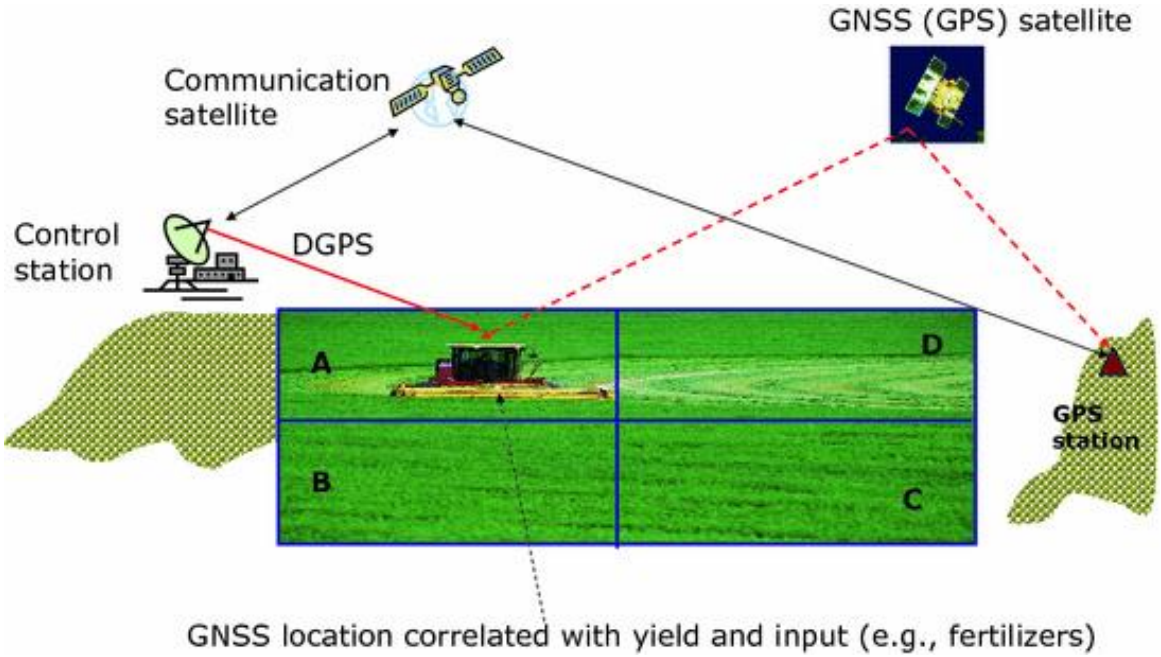

Figure 8.16: GNSS and land management [*Awange, 2018*].

The network of GNSS infrastructure can assist in land administration and development in Sub-Saharan Africa. *Gebrehiwot and Gebrewahid*, [2016] in "The need for agricultural water management in Sub-Saharan Africa" supports the projection of the World Bank in the need to enlarge agricultural land for irrigation to enhance growth in agricultural production. The information generated can support government, farmers and other users of GNSS technology in making informed decision. Augmented GNSS services can support monitoring of land with potential for natural disasters, which include but not limited to floods, droughts, earthquakes, volcanic eruptions, erosions, and landslides. Early warning systems can minimise chances of loss of lives and property in disaster-prune locations. This would reduce, if not eliminate, cost of government spending in rescue and emergency response in the affected areas. Such limited funds can now be channelled towards essential development purposes that would translate to socio-economic benefits. Countries such as USA, UK, Germany, Japan, and Israel where land and water resources are managed efficiently have attained food sufficiency. Augmented GNSS technology and workable policy framework can support the achievement of desired goals. Sub-Saharan Africa can borrow a leaf from these countries and do things differently to improve the standard of living of its teeming population.

8.4.6 GNSS and Oil and Gas

Africa is rich in oil and gas resources. However, because of lack of or inadequate use of GNSS technology in the aspect of oil and gas, Africa suffers a huge economic loss on a daily basis. Instead of harnessing these resources effectively and efficiently to address its apparent economic challenges, the continent operates far below its optimal capacity. This condition is evident in almost all regions with commercial oil and gas resources. GNSS can support all phases of oil and gas operation in Africa and this can translate to economic wealth as indicated in Figure 8.17. Geospatial data collected and used in the oil and gas industry can be obtained from precise measurements of GNSS [*Fubara, 2009*]. This information can be used by geoinformatics (field of activity that deals with the collection, processing, analysis, display, and management of geospatial information) engineers in the planning and execution of activities in the upstream, midstream, and downstream sector of the oil and gas industry [*Quaye-Ballard, 2013*]. Geospatial data, for example, in regions with prospect of commercial oil and gas resources can take advantage of GNSS precise measurements. Africa is one continent where lies a huge quantity of untapped natural resources. For government or any concerned authority to support sustainable exploration and production of oil and gas, geospatial data is useful. Hence, regions in Sub-Saharan Africa can benefit from GNSS technologies.

Figure 8.17: GNSS application in oil and gas courtesy of GNSS in Africa.
Source: http://www.gnss-africa.org/

8.4.7 GNSS and Aviation

GNSS augmentation systems (civil aviation) are beginning to gain considerable attention in Africa. This has been promoted because of the importance of GNSS as a primary means of navigation worldwide. One basic challenge of the use of ground-

based navigation and landing aids is the issue of poor coverage. For example, areas with difficult terrain can hinder the deployment of such infrastructures. Hence, the need for GNSS for civil aviation operation in Sub-Saharan Africa [*Fubara, 2009*]. Africa has so much to benefit from GNSS technology in civil aviation if the needed infrastructure is deployed [*Akala et al., 2016*]. To enhance the performance of GNSS in Safety of Life (SoL) applications, for example, aviation, augmentation systems are designed and deployed in several regions of the world [*Kaplan and Hegarty, 2005*]. Regions utilising this GNSS technology have recorded enhanced performance, hence safety of air travels, as well as reduced cost and time of travel, are achieved [*Sabatini et al., 2017*]. Controller-pilot workload has been significantly reduced while operations and services are optimised in all phases of flight. Almost all the continents of the world have regional augmentation systems (SBAS, ABAS, and GBAS) except Africa. Figure 8.18 shows a GBAS architecture. Because aviation is a global business, Africa cannot afford to lag. GNSS can support the development and implementation of Performance-Based Navigation (PBN), which can have safety, operational, and efficiency benefits, in Sub-Saharan Africa [*Akala et al., 2014; Doc, I.C.A.O., 2008*]. PBN uses area navigation based on performance requirements (accuracy, integrity, continuity, and availability) for all phases of flight including en route, terminal, approach, and final approach to the runway.

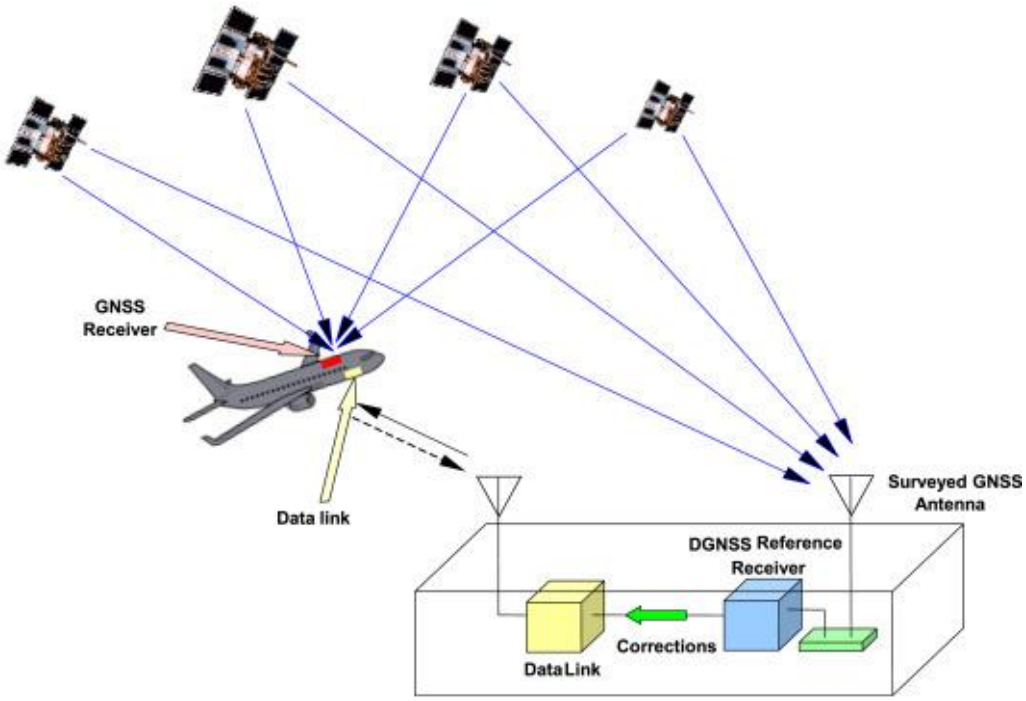

Figure 8.18: Ground-Based Augmentation System architecture [*Sabatini et al., 2017*].

Therefore, this part of the world must, as a matter of urgency and importance, design, develop, and deploy its augmentation system for the benefit of its citizens. Africa can collaborate with the International Civil Aviation Authority (ICAO) to develop a Regional Satellite Augmentation System (RSAS) that covers the whole of Africa and parts of Europe, Asia, South America, and Antarctica. When this is achieved, the GNSS augmentation system can support Air Traffic Control (ATC) and Air Traffic Management (ATM) for civil aviation safety and security.

8.4.8 GNSS and Surveying and Mapping

Africa is a rich continent, for example, in terms of human population, natural resources, favourable environmental condition, and landmass. The regional or cross-border developmental programme, which requires geospatial information in Africa, can be achieved with GNSS [*Wonnacott, 2008*]. The use of modern standard and uniform coordinate reference frames, for example, the African geodetic Reference Frame (AFREF), can support surveying and mapping design and development in Africa. AFREF uses geodetic data from permanent geodetic GNSS stations courtesy of IGS [*Dow et al., 2007*]. GNSS has been instrumental to the use of geospatial information in surveying and mapping applications.

However, majority of its population are poor, and this has negative consequences on the continent. Aerial mapping or surveying using drones (unmanned aerial vehicle, UAV) has been observed to be cost-effective, accurate, and efficient as indicated in Figure 8.19. Africa can achieve much more when these enabling GNSS technologies are deployed in applications, which require surveying and mapping [*Fubara, 2009*]. Apart from growing its economy through effective use of GNSS, Africa can provide jobs opportunity to its teeming young population. Requisite knowledge, skill, and attitude can be acquired through training and re-training of its population [*Kaplan and Hegarty, 2005*].

Figure 8.19: The use of GNSS in a drone mapping surveying Courtesy of 3DroneMapping.
Source: https://www.3dronemapping.com/

8.4.9 GNSS and Search and Rescue

Search and rescue operations involve locating and helping people in distress. During a natural disaster, people can be in a distress condition and so will need to be located and helped as indicated in Figure 8.20. GNSS can help to achieve this condition. In war-prone zones, for example, it becomes difficult to locate and reach out to those affected. Because of this, humanitarian assistance may be difficult to reach to the affected zones and the vulnerable may end up losing their lives. It is a commonplace where a prompt response to disaster prevention, management, and reduction in Africa is becoming a recurring challenge [*Momoh and Akinyede, 2008*]. According to *Momoh and Akinyede*, [2008], although GNSS has been widely accepted and used across the world, Africa is still struggling to key in. To minimise loss of lives and property in a distress-characterised environment, the use of GNSS technology in search and rescue operation can offer a great solution. African countries, like the developed countries, can take advantage of the opportunities offered in the effective and efficient use of GNSS, for example, Galileo, for disaster management [*Cinar and Ince, 2005; Fubara, 2009*]. Apart from support for search and rescue operation in the region, the use of GNSS can improve on safety and security of its population.

Figure 8.20: The use of GNSS in a helicopter Search and Rescue (SAR) Operation. Source: https://galileognss.eu/gricas-solution-for-aeronautical-search-rescue/

8.4.10 GNSS and Mobile Phone

In modern days, GNSS technology has a wide range of applications including mobile phones. Manufacturers of this device have developed mobile applications for specific and general applications to meet the growing demands of its customers. GNSS raw measurements can be obtained from an Android mobile phone for positioning and navigation. Once the Android application is downloaded and enabled on a mobile phone, the user can determine locations from the GNSS raw data. Similarly, electronic voting (e-voting), as opposed to traditional voting, can help redefine voting, which is an integral part of a democratic process using GNSS. GNSS technologies and Information and Communication Technology (ICT) can be deployed during voting in Sub-Saharan Africa because of its attendant benefits [*Kogeda and Mpekoa, 2013*]. Mobile phones offer a wide range of applications and owing to its ease of operation and affordability, the device can be used for e-voting. Once a user-friendly application is designed, eligible voters can download the application on their mobile device. In this way, citizens who are qualified to vote can do so at their comfort and security in the exercise of their franchise. Apart from e-

voting, GNSS has been used in both in-door and out-door navigation and positioning [*Pei et al., 2010*]. The smart devices are manufactured to contain embedded systems used to achieve the desired objective.

Figure 8.21: Topographic map from a mobile phone courtesy of Topo GPS. Source: https://www.topo-gps.com

Given this, Africa can take advantage of opportunities available in the effective and efficient use of GNSS. GNSS has the potential to support and enhance socio-economic activities in Africa. Safety and security can be improved with the proper use of GNSS-based applications. GNSS data such as clock, navigation, pseudorange, and carrier phase can be collected from GNSS receiver embedded in mobile phone. GNSS positioning, navigation, and timing applications can be derived from the raw GNSS data through the power of android software applications. Since majority of the young population in Africa are interested in the use of mobile phones, the potentials of the device can be harnessed for socio-economic development as indicated in Figure 8.21 [*Africa Renewal Magazine, 2013*]. Jobs can be created through mobile applications, which can improve the living standard of these young people who make up reasonable percent of the African population. Crimes and other social vices going on in this region can be significantly reduced through the effective use of GNSS technologies [*Fubara, 2009*].

8.4.11 Part 3: Socio-economic Assessment of the Impact of Ionospheric Irregularities on Applications of Precise GNSS in Sub-Saharan Africa

GNSS has great potentials to support and enhance socio-economic activities in Sub-Saharan Africa as shown in section 8.4.1. However, the presence of ionospheric irregularities particularly at the equatorial latitudes has negative consequences on these potential areas of applications. Future work will investigate the socio-economic impact of equatorial irregularities on GNSS precise applications in the region. To achieve this, ionospheric data during solar cycle 24 (Figure 8.22c) will be collected from geodetic GNSS stations courtesy of IGS and then analysed. To appreciate the distribution of geodetic IGS stations in Sub-Saharan Africa and surroundings, a selection of GNSS receivers is presented in Figure 8.22a. GNSS observation data availability from the selected IGS stations at the equatorial (black lines) and middle latitudes (blue lines) during solar cycle 24 is indicated in Figure 8.22b.

The presence of ionospheric irregularities will be characterised using TEC fluctuations (30-s observables) and scintillation indices collected from specialised GNSS receivers [*Aarons et al., 1996; Pi et al., 1997*]. Herein, only 30-s observations from geodetic GNSS stations will be utilised because of data availability. Supporting evidence to determine the presence of irregularities will largely depend on the availability of instruments and data in the region. Data from SCINDA, C/NOFS, and AMBER will be considered. Since irregularities responsible for scintillation as well as TEC fluctuations in the equatorial ionosphere are correlated with solar activity, geomagnetic condition, season of year, time of day, longitude, and frequency, the data to be collected will be informed by these factors [*Akala et al., 2014; Mungufeni et al., 2016; Olwendo et al., 2013; Paznukhov et al., 2012; Yizengaw et al., 2012*].

In view of this, ionospheric data will be collected from select stations for a few days post-sunset within the EIA sector during the declining phase of the solar maximum of solar cycle 24 [*Anderson and Haerendel, 1979*]. The maximum sunspot number of solar cycle 24 occurred on April 2014 while the minimum was recorded on December 2008 (https://www.swpc.noaa.gov/products/solar-cycle-progression).

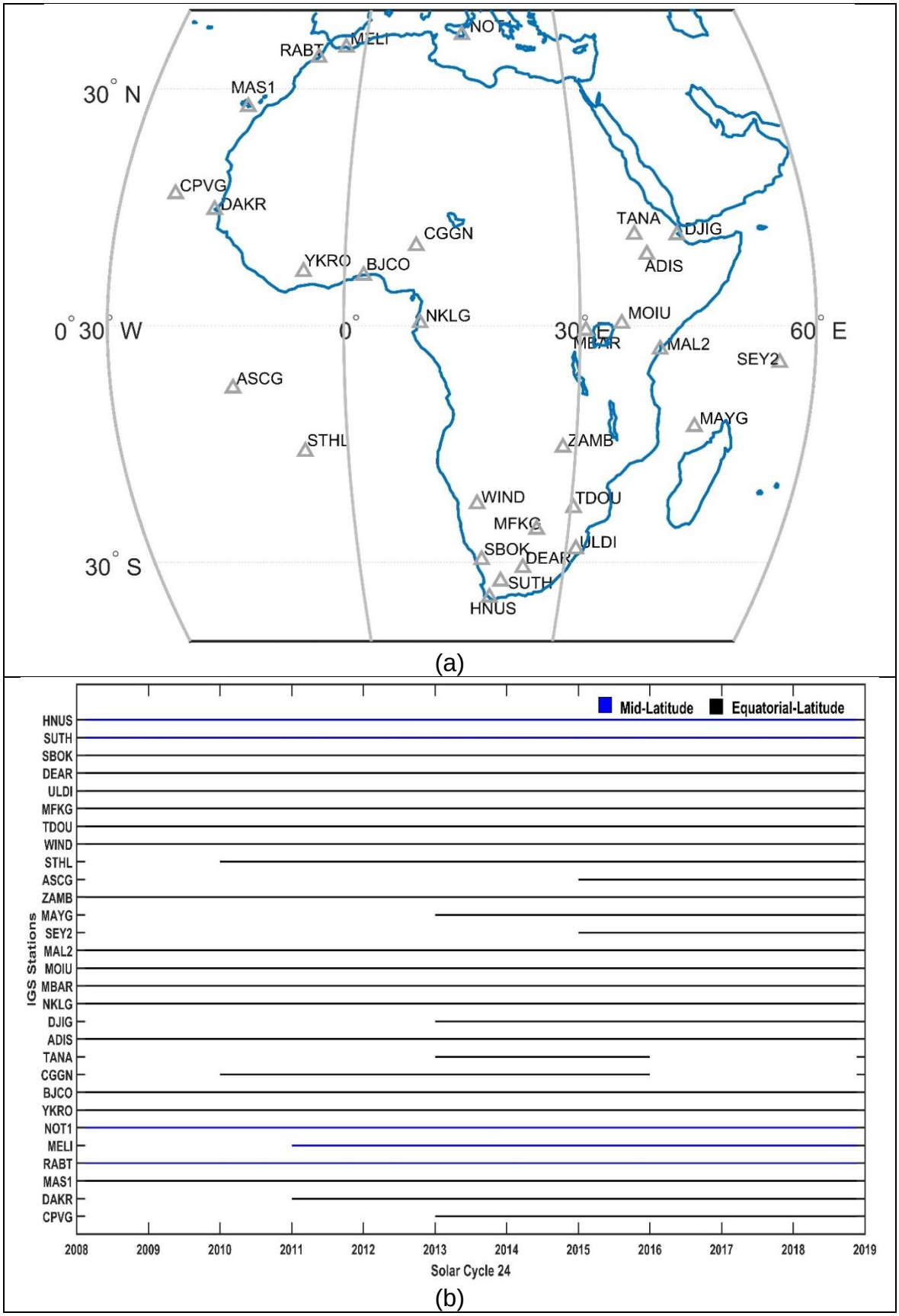
30° N
30° S
0° 30° W
0°
30° E
60° E
NOT1
MELI
RABT
MAS1
CPVG
DAKR
CGGN
YKRO
BJCO
NKLG
TANA
DJIG
ADIS
MOIU
MBAR
MAL2
SEY2
ASCG
MAYG
STHL
ZAMB
WIND
TDOU
MFKG
ULDI
SBOK
DEAR
SUTH
HNUS
(a)
Mid-Latitude
Equatorial-Latitude
IGS Stations
HNUS
SUTH
SBOK
DEAR
ULDI
MFKG
TDOU
WIND
STHL
ASCG
ZAMB
MAYG
SEY2
MAL2
MOIU
MBAR
NKLG
DJIG
ADIS
TANA
CGGN
BJCO
YKRO
NOT1
MELI
RABT
MAS1
DAKR
CPVG
2008
2009
2010
2011
2012
2013
2014
2015
2016
2017
2018
2019
Solar Cycle 24
(b)

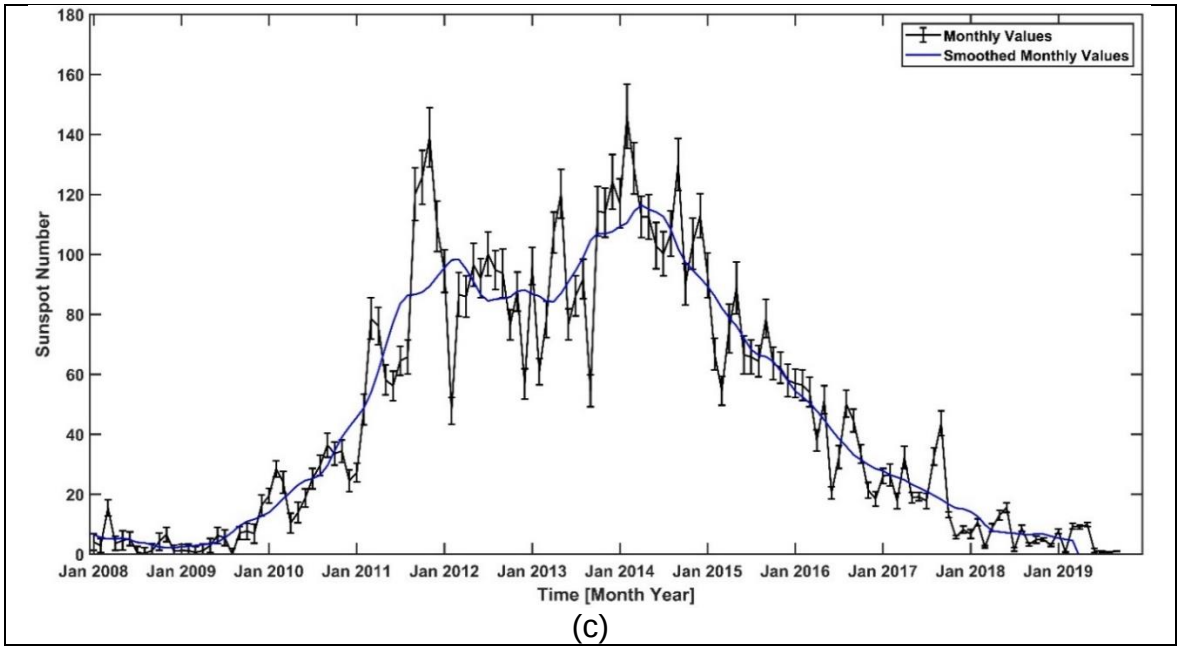

(c)

Figure 8.22: Selection of geodetic IGS stations distributed in and around African middle latitude (blue line) and equatorial-latitude (black line) indicated as HNUS (Hermanus, South Africa), SUTH (Sutherland, South Africa), SBOK (Springbok, South Africa) DEAR (De Aar, South Africa), ULDI (Ulundi, South Africa), MFKG (Mafikeng, South Africa), TDOU (Thohoyandou, South Africa), WIND (Windhoek, Namibia), STHL (Longwood, United Kingdom), ASCG (Ascension Island, Saint Helena, Ascension and Tristan da Cunha), ZAMB (Lusaka, Zambia), MAYG (Dzaoudzi, Mayotte), SEY2 (La Misère, Seychelles), MAL2 (Malindi, Kenya), MOIU (Eldoret, Kenya), MBAR (Mbarara, Uganda), NKLG (Libreville, Gabon), DJIG (Observatoire Geophysique dÂ'Arta, Djibouti), ADIS (Addis Ababa, Ethiopia), TANA (Bahir Dar, Ethiopia), CGGN (Toro, Nigeria), BJCO (Cotonou, Benin), YKRO (Yamoussoukro, Cote d'ivoire), NOT1 (Noto, Italy), MELI (Melilla, Spain), RABT (Rabat Morocco), MAS1 (Maspalomas, Spain), DAKR (Dakar, Senegal), and CPVG (Espargos, Cape Verde) with (a) map of the selected IGS stations and (b) data availability in solar cycle 24 (2008-2019). (c) Monthly sunspot number from January 2008 to September 2019 indicating monthly mean total sunspot number with associated errors (black line) and smoothed monthly total sunspot number (blue line) of the solar cycle 24 courtesy of Sunspot Index and Long-term Solar Observations (SILSO). The minimum sunspot number was recorded in December 2008 while the maximum was observed in April 2014.
Source: http://www.sidc.be/silso/datafiles

Since there exists a strong association between ionospheric irregularities and geomagnetic conditions, 1 December 2008 records the lowest K_p value of 0 while 7 October 2015 has K_p value of 6 (ftp://ftp.swpc.noaa.gov/pub/indices/old_indices/). Hence, 7 October 2015, corresponding to a declining phase of solar cycle 24, will be considered as a potential date to observe the presence of equatorial irregularities originating residual errors and or outages in GNSS observables. Irregularities in the

form of EPBs can negatively affect satellite communications signals and the performance of GNSS applications [*Conker et al., 2003; Srinivasu et al., 2018*].

Ionospheric irregularities calculated from select stations within EIA sector in the disturbed ionosphere will be quantified in terms of intensity and frequency. Socio-economic metrics corresponding to the ionospheric metrics (TEC fluctuations and scintillation indices) will be estimated. Depending on the GNSS application (oil and gas, precision agriculture, maritime, rail transport, civil aviation, etc.), the social-economic assessment of the impact of ionospheric irregularities will be investigated. It is important to mention here that this intended research will provide the opportunity to study the ionospheric irregularities in the African ionosphere impact on precise applications of GNSS in economic terms. The results obtained can provide insight into the possible socio-economic losses originating from the presence of irregularities on GNSS precise applications in the Sub-Saharan Africa region of relevance.

References

Aarons, J., 1982. Global morphology of ionospheric scintillations. Proceedings of the IEEE, 70(4), pp.360-378.

Aarons, J., Mendillo, M., Yantosca, R. and Kudeki, E., 1996. GPS phase fluctuations in the equatorial region during the MISETA 1994 campaign. Journal of Geophysical Research: Space Physics, 101(A12), pp.26851-26862.

Adekunle, I.O., 2013. Precision agriculture: Applicability and opportunities for Nigerian agriculture. Middle-East Journal of Scientific Research, 13(9), pp.1230-1237.

Africa Renewal Magazine, 2013. Africa's mobile youth drive change, [Online]. Available at: https://www.un.org/africarenewal/magazine/may-2013/africa%E2%80%99s-mobile-youth-drive-change# [Accessed 18 August 2020].

Aikio, A., Hector, L.G. and Schultz, H.L., 2011. Introduction to the ionosphere. The Dielectric Constant of Air at Radiofrequencies, 7(4), pp.133-136.

Akala, A.O., Amaeshi, L.L.N., Doherty, P.H., Groves, K.M., Carrano, C.S., Bridgwood, C.T., Seemala, G.K. and Somoye, E.O., 2014. Characterization of GNSS scintillations over Lagos, Nigeria during the minimum and ascending phases (2009–2011) of solar cycle 24. Advances in Space Research, 53(1), pp.37-47.

Akala, A.O., Awoyele, A. and Doherty, P.H., 2016. Statistics of GNSS amplitude scintillation occurrences over Dakar, Senegal, at varying elevation angles during the maximum phase of solar cycle 24. Space Weather, 14(3), pp.233-246.

Akala, A.O., Oyeyemi, E.O., Arowolo, O.A. and Doherty, P.H., 2019. Characterization of GPS and EGNOS amplitude scintillations over the African equatorial/low-latitude region. Advances in Space Research, 63(9), pp.3062-3075.

Akinyede, J. O., 2012. Capacity Building in Space Science and Technology: Achievements of African Regional Centre for Space Science and Technology Education in English (ARCSSTE-E). United Nations Office for Outer Space Affairs (UN-OOSA). Committee on the Peaceful Uses of Outer Space, Scientific and Technical Subcommittee, 49th Session, Vienna, Austria, [Online]. 1-43. Available at: http://www.unoosa.org/pdf/pres/stsc2012/tech-02E.pdf [Accessed 3 July 2017].

AMISR in Africa Workshop Report, 2012. Sponsored by the National Science Foundation and Boston College, Massachusetts, U.S.A., [Online]. Available at: https://www.bc.edu/content/dam/files/sites/amisr/presentations/AMISR_workshop_report.pdf [Accessed 20 September 2019].

Andalsvik, Y.L. and Jacobsen, K.S., 2014. Observed high-latitude GNSS disturbances during a less-than-minor geomagnetic storm. Radio Science, 49(12), pp.1277-1288.

Anderson, D. and Fuller-Rowell, T., 1999. Space environment topics: the ionosphere.

Anderson, D.N. and Haerendel, G., 1979. The motion of depleted plasma regions in the equatorial ionosphere. Journal of Geophysical Research: Space Physics, 84(A8), pp.4251-4256.

Arnold Barmettler, www.calsky.com

Awange, J., 2018. GNSS environmental sensing. Springer International Publishers. DOI, 10, pp.978-3.

Aylward, A., 2012. Introduction to the Ionosphere. Atmospheric Physics Laboratory, UCL. Summer School, [Online]. 4-5. Available at: http://star.arm.ac.uk/summerschool2012/Aylward.pdf [Accessed 8 July 2017].

Balan, N., Liu, L. and Le, H., 2018. A brief review of equatorial ionization anomaly and ionospheric irregularities. Earth and Planetary Physics, 2(4), pp.257-275.

Barona Mendoza J, Quiroga Ruiz C, Pinedo Jaramillo C. Implementation of an Electronic Ionosonde to Monitor the Earth's Ionosphere via a Projected Column through USRP. Sensors. 2017 May;17(5):946.

Baker, D.N., Li, X., Pulkkinen, A., Ngwira, C.M., Mays, M.L., Galvin, A.B. and Simunac, K.D.C., 2013. A major solar eruptive event in July 2012: Defining extreme space weather scenarios. Space Weather, 11(10), pp.585-591.

Basu, S., 1975. Universal time seasonal variations of auroral zone magnetic activity and VHF scintillations. Journal of Geophysical Research, 80(34), pp.4725-4728.

Basu, S. and Basu, S., 1981. Equatorial scintillations—A review. Journal of Atmospheric and Terrestrial Physics, 43(5-6), pp.473-489.

Basu, S., Kudeki, E., Basu, S., Valladares, C.E., Weber, E.J., Zengingonul, H.P., Bhattacharyya, S., Sheehan, R., Meriwether, J.W., Biondi, M.A. and Kuenzler, H., 1996. Scintillations, plasma drifts, and neutral winds in the equatorial ionosphere after sunset. Journal of Geophysical Research: Space Physics, 101(A12), pp.26795-26809.

Basu S, MacKenzie E, Basu Su (1988a) Ionospheric constrains on VHF/UHF communications links during solar maximum and minimum periods. Radio Sci 23:363–378.

Basu S, Basu S, Weber EJ, Coley WR (1988b) Case study of polar cap scintillation modeling using DE 2 irregularity measurements at 800 km. Radio Sci 23:545–553.

Beer, T., 1973. The equatorial ionosphere. Contemporary Physics, 14(4), pp.319-327.

Béniguel, Y., Cherniak, I., Garcia-Rigo, A., Hamel, P., Hernández-Pajares, M., Kameni, R., Kashcheyev, A., Krankowski, A., Monnerat, M., Nava, B. and Ngaya, H., 2017, March. MONITOR ionospheric network: two case studies on scintillation and electron content variability. In Annales Geophysicae (Vol. 35, No. 3, pp. 377-391). Copernicus GmbH.

Béniguel, Y., Forte, B., Radicella, S.M., Strangeways, H.J., Gherm, V.E. and Zernov, N.N., 2004. Scintillations effects on satellite to Earth links for telecommunication and navigation purposes. Annals of geophysics, 47(2-3 Sup.).

Béniguel, Y. and Hamel, P., 2011. A global ionosphere scintillation propagation model for equatorial regions. Journal of Space Weather and Space Climate, 1(1), p.A04.

Béniguel, Y., Forte, B., Radicella, S.M., Strangeways, H.J., Gherm, V.E. and Zernov, N.N., 2004. Scintillations effects on satellite to Earth links for telecommunication and navigation purposes. Annals of geophysics, 47(2-3 Sup.).

Bernhardt, P.A., Siefring, C.L., Briczinski, S.J., McCarrick, M. and Michell, R.G., 2016. Large ionospheric disturbances produced by the HAARP HF facility. Radio Science, 51(7), pp.1081-1093.

Beynon, W.J.G. and Williams, P.J.S., 1978. Incoherent scatter of radio waves from the ionosphere. Reports on Progress in Physics, 41(6), p.909.

Bhattacharyya, A., Beach, T.L., Basu, S. and Kintner, P.M., 2000. Night-time equatorial ionosphere: GPS scintillations and differential carrier phase fluctuations. Radio Science, 35(1), pp.209-224.

Blanco, M., 2016. Accelerating SMART Water: Challenges for Smart Water Services in Resilient Cities. 6th Annual Conference, FCC Aqualia, London, [Online]. 1-21. Available at: https://www.swan-forum.com/wp-content/uploads/sites/218/2016/05/Keynote_SWAN-2016-FCC-Aqualia_Mariano-Blanco.pdf [Accessed 2 February 2017].

Bob, R., 2001. The Advanced Modular Incoherent Scatter Radar (AMISR) Historical Perspectives". National Science Foundation.

Booker, H.G. and Wells, H.W., 1938. Scattering of radio waves by the F-region of the ionosphere. Terrestrial Magnetism and Atmospheric Electricity, 43(3), pp.249-256.

Borre, K., Akos, D.M., Bertelsen, N., Rinder, P. and Jensen, S.H., 2007. A software-defined GPS and Galileo receiver: a single-frequency approach. Springer Science & Business Media.

Bowman, G.G., 1990. A review of some recent work on mid-latitude spread-F occurrence as detected by ionosondes. Journal of geomagnetism and geoelectricity, 42(2), pp.109-138.

Briggs, B.H. and Parkin, I.A., 1963. On the variation of radio star and satellite scintillations with zenith angle. Journal of Atmospheric and Terrestrial Physics, 25(6), pp.339-366.

Bruzek, A. and Durrant, C.J. eds., 2012. Illustrated glossary for solar and solar-terrestrial physics (Vol. 69). Springer Science & Business Media.

Butler, T.W., Semeter, J., Heinselman, C.J. and Nicolls, M.J., 2010. Imaging F region drifts using monostatic phased-array incoherent scatter radar. Radio Science, 45(05), pp.1-15.

Cander, L.R. and Mihajlovic, S.J., 1998. Forecasting ionospheric structure during the great geomagnetic storms. Journal of Geophysical Research: Space Physics, 103(A1), pp.391-398.

Cannon, P., Angling, M., Barclay, L., Curry, C., Dyer, C., Edwards, R., Greene, G., Hapgood, M., Horne, R.B., Jackson, D. and Mitchell, C.N., 2013. Extreme space weather: impacts on engineered systems and infrastructure. Royal Academy of Engineering.

Carrano, C.S. and Groves, K.M., 2007, April. TEC gradients and fluctuations at low-latitudes measured with high data rate GPS receivers. In Proceedings of the 63rd annual meeting of the Institute of Navigation, Cambridge, MA (pp. 156-163).

Carrano, C., Bridgwood, C. and Groves, K., 2009, January. Impacts on Ionospheric Scintillation on GPS Positioning Accuracy. In Proc. AMS Sixth Symposium on Space Weather.

Carletto, C., Gourlay, S. and Winters, P., 2015. From guesstimates to GPStimates: Land area measurement and implications for agricultural analysis. Journal of African Economies, 24(5), pp.593-628.

Chartier, A., Forte, B., Deshpande, K., Bust, G. and Mitchell, C., 2016. Three-dimensional modelling of high-latitude scintillation observations. Radio Science, 51(7), pp.1022-1029.

Chen, F.F., 1984. Introduction to plasma physics and controlled fusion (Vol. 1, pp. 19-51). New York: Plenum press.

Coker, C., Hunsucker, R. and Lott, G., 1995. Detection of auroral activity using GPS satellites. Geophysical research letters, 22(23), pp.3259-3262.

Conker, R.S., El-Arini, M.B., Hegarty, C.J. and Hsiao, T., 2003. Modeling the effects of ionospheric scintillation on GPS/satellite-based augmentation system availability. Radio Science, 38(1), pp.1-1.

Correia, E., Muella, M., Alfonsi, L., Prol, F. and Camargo, P., 2018. GPS scintillations and total electron content climatology in the southern American sector. In *Accuracy of GNSS Methods*. IntechOpen.

Cosmen-Schortmann J, Azaola-Sáenz M, Martinez-Olague MA, Toledo-López M. Integrity in urban and road environments and its use in liability critical applications. In2008 IEEE/ION Position, Location and Navigation Symposium 2008 May 5 (pp. 972-983). IEEE.

Crustal Dynamics Data Information System (CDDIS DAAC). 2014. International GNSS Service (IGS), 15-min 1-s RINEX observation and daily (24-hour) 30-s RINEX observation data.

Dabas, R.S. and Dabas, R.S., 2000. Ionosphere and its influence on radio communications. Resonance, 5(07).

Dabove, P., Linty, N. and Dovis, F., 2019. Analysis of multi-constellation GNSS PPP solutions under phase scintillations at high latitudes. Applied Geomatics, pp.1-8.

Dahlgren, H. and Whiter, D., 2007. Observing and Analysing Structures in Active Aurora with the ASK Optical Instrument and EISCAT Radar. EISCAT Summer School Part I, 31 July 2007, [Online]. Available at: https://www.eiscat.se/wp-content/uploads/2016/12/Aurora.pdf [Accessed 25 September 2019].

D'Angelo, N., 1973. Type III spectra of the radar aurora. Journal of Geophysical Research, 78(19), pp.3987-3990.

DASI2 - Digital All-Sky Imager Mark 2. Department of Physics, Lancaster University, [Online]. Available at: http://spears.lancs.ac.uk/dasi2/ [Accessed 8 May 2017].

Denardini, C.M., Dasso, S. and Gonzalez-Esparza, J.A., 2016. Review on space weather in Latin America. 3. Development of space weather forecasting centers. Advances in Space Research, 58(10), pp.1960-1967.

Dey, A., Reddy, K.S. and Dashora, N., 2016, March. Low latitude ionospheric effects on GNSS performance: A case study of GPS positioning. In 2016 IEEE International Conference on Engineering and Technology (ICETECH) (pp. 437-442). IEEE.

Doc, I.C.A.O., 2008. 9613. Performance-based Navigation (PBN) Manual, 999.

Doherty, P., Coster, A.J. and Murtagh, W., 2004. Space weather effects of October–November 2003. *GPS Solutions*, *8*(4), pp.267-271.

Doherty, P. H., 2009. Ionospheric Effects on GNSS. Satellite Navigation Science and Technology for Africa, [Online]. 1-19. The Abdus Salam International Centre for Theoretical Physics, Italy. Available at: http://indico.ictp.it/event/a08148/session/82/contribution/51/material/0/0.pdf [Accessed 15 June 2017].

Doherty, P.H., Delay, S.H., Valladares, C.E. and Klobuchar, J.A., 2003. Ionospheric scintillation effects on GPS in the equatorial and auroral regions. Navigation, 50(4), pp.235-245.

Donkor, S., 2006. Water in Africa: management options to enhance survival and growth. Economic Commission for Africa.

Dow, J.M., Neilan, R.E. and Rizos, C., 2007, September. The International GNSS Service (IGS): Preparations for the coming decade. In 20th International Technical Meeting of the Satellite Division of the US Institute of Navigation (pp. 2136-2144).

Eastwood, J.P., 2008. The science of space weather. *Philosophical Transactions of the Royal Society A: Mathematical, Physical and Engineering Sciences*, *366*(1884), pp.4489-4500.

Elijah, O., Rahman, T.A., Orikumhi, I., Leow, C.Y. and Hindia, M.N., 2018. An overview of Internet of Things (IoT) and data analytics in agriculture: Benefits and challenges. IEEE Internet of Things Journal, 5(5), pp.3758-3773.

Enell, C.; 2016. Introduction to GUISDAP: How to Analyse EISCAT Data. Incoherent Scatter Radar School 2016, Sodankylä, pp 1-17, [Online]. EISCAT Scientific Association. Available at: https://eiscat3d.se/drupal/sites/default/files/ISRSchool2016/19-Enell-GUISDAP_lecture.pdf [Accessed 1 October 2018].

Fallows, R.A., Bisi, M.M., Forte, B., Ulich, T., Konovalenko, A.A., Mann, G. and Vocks, C., 2016. Separating Nightside Interplanetary and Ionospheric Scintillation with LOFAR. The Astrophysical Journal Letters, 828(1), p.L7.

Fejer, B.G., 2011. Low latitude ionospheric electrodynamics. Space Science Reviews, 158(1), pp.145-166.

Fejer, B.G. and Kelley, M.C., 1980. Ionospheric irregularities. *Reviews of Geophysics*, *18*(2), pp.401-454.

Fejer, B. G., 2015. The Equatorial Ionosphere: A Tutorial. CEDAR Meeting, Seattle, WA, [Online]. 1-41. Available at: https://cedarweb.vsp.ucar.edu/wiki/images/2/22/2015CEDAR_Tutorial_Fejer_b.pdf [Accessed 1 July 2017].

Feldstein, Y.I., 1986. A quarter of a century with the auroral oval. Eos, Transactions American Geophysical Union, 67(40), pp.761-767.

Folkestad, K.; 2016. Use of the EISCAT Radar as a Supplement to Rocket Measurements. EISCAT Technical Note, pp 1-26, Kiruna, Sweden, [Online]. EISCAT Scientific Association. Available at: https://www.eiscat.se/wp-content/uploads/2016/06/Use-of-the-EISCAT-Radar-as-a-Supplement-to-Rocket-Measurements.pdf [Accessed 1 October 2018].

Forte, B., Coleman, C., Skone, S., Häggström, I., Mitchell, C., Da Dalt, F., Panicciari, T., Kinrade, J. and Bust, G., 2017. Identification of scintillation signatures on GPS signals originating from plasma structures detected with EISCAT incoherent scatter radar along the same line of sight. Journal of Geophysical Research: Space Physics, 122(1), pp.916-931.

Forte B, Radicella SM. Geometrical control of scintillation indices: What happens for GPS satellites. Radio Science. 2004 Oct;39(5):1-3.

Forte, B., Smith, N.D., Mitchell, C.N., Da Dalt, F., Panicciari, T., Chartier, A.T., Stevanovic, D., Vuckovic, M., Kinrade, J., Tong, J.R. and Häggström, I., 2013, April. Comparison of temporal fluctuations in the total electron content estimates from EISCAT and GPS along the same line of sight. In Annales Geophysicae (Vol. 31, No. 4, p. 745). Copernicus GmbH.

Foster, J.C., Coster, A.J., Erickson, P.J., Holt, J.M., Lind, F.D., Rideout, W., McCready, M., Van Eyken, A., Barnes, R.J., Greenwald, R.A. and Rich, F.J., 2005.

Multiradar observations of the polar tongue of ionization. Journal of Geophysical Research: Space Physics, 110(A9).

Fubara, D.M. and Yakubu, T.A., 2009, July. Applications of GNSS in West Africa. In 2009 IEEE International Geoscience and Remote Sensing Symposium (Vol. 5, pp. V-453). IEEE.

Gebrehiwot, K.A. and Gebrewahid, M.G., 2016. The need for agricultural water management in sub-Saharan Africa. Journal of Water Resource and Protection, 8(09), p.835.

Ghafoori, F. and Skone, S., 2015. Impact of equatorial ionospheric irregularities on GNSS receivers using real and synthetic scintillation signals. *Radio Science*, *50*(4), pp.294-317.

Gondarenko, N.A. and Guzdar, P.N., 2004. Plasma patch structuring by the nonlinear evolution of the gradient drift instability in the high-latitude ionosphere. Journal of Geophysical Research: Space Physics, 109(A9).

Gordon, W.E., 1958. Incoherent scattering of radio waves by free electrons with applications to space exploration by radar. Proceedings of the IRE, 46(11), pp.1824-1829.

Goyal, P., Sahoo, A.K., Sharma, T.K. and Singh, P.K., 2020. Internet of Things: Applications, security and privacy: A survey. Materials Today: Proceedings.

GUIDE. Geolocation Testing Laboratory. GNSS Simulation and Live Testing. Available at: http://www.guide-gnss.net/ [Accessed 19 June 2019].

Guo, K., Liu, Y., Zhao, Y. and Wang, J., 2017. Analysis of ionospheric scintillation characteristics in sub-Antarctica region with GNSS data at Macquarie Island. Sensors, 17(1), p.137.

Habarulema, J. B., 2014. An Overview of using Multiple Data Sources to Study Ionospheric Dynamics over the African Sector. Journal of South African National Space Agency (SANSA), Hermanus, South Africa, [Online]. 1-61. University of Rwanda, College of Science and Technology, Kigali, Rwanda. Available at: http://indico.ictp.it/event/a13251/session/6/contribution/41/material/0/0.pdf [Accessed 9 December 2016].

Hargreaves, J.K., 1979. The upper atmosphere and solar-terrestrial relations-An introduction to the aerospace environment. *New York, Van Nostrand Reinhold Co., 1979. 312 p.*

Hargreaves, J.K., 1992. The solar-terrestrial environment: an introduction to geospace-the science of the terrestrial upper atmosphere, ionosphere, and magnetosphere. Cambridge University Press.

Henderson, S.B., Swenson, C.M., Christensen, A.B. and Paxton, L.J., 2005. Morphology of the equatorial anomaly and equatorial plasma bubbles using image subspace analysis of Global Ultraviolet Imager data. Journal of Geophysical Research: Space Physics, 110(A11).

Hernández-Pajares, M., Juan, J.M., Sanz, J., Aragón-Àngel, À., García-Rigo, A., Salazar, D. and Escudero, M., 2011. The ionosphere: effects, GPS modeling and the benefits for space geodetic techniques. Journal of Geodesy, 85(12), pp.887-907.

Hernandez-Pajares, M., Juan, J.M., Sanz, J., Ramos-Bosch, P., Rovira-Garcia, A., Salazar, D., Ventura-Traveset, J., Lopez-Echazarreta, C. and Hein, G., 2010, December. The ESA/UPC GNSS-lab tool (glab). In Proc. of the 5th ESA Workshop on Satellite Navigation Technologies (NAVITEC'2010), ESTEC, Noordwijk, The Netherlands.

Hickey, D.A., Martinis, C.R., Rodrigues, F.S., Varney, R.H., Milla, M.A., Nicolls, M.J., Strømme, A. and Arratia, J.F., 2015. Concurrent observations at the magnetic equator of small-scale irregularities and large-scale depletions associated with equatorial spread F. Journal of Geophysical Research: Space Physics, 120(12), pp.10-883.

Hofgartner, K., 2008. Economic Benefits of Global Positioning System (GPS) Technology in Developing Countries for Land Management, Geographic Information and Agriculture. Trimble Navigation Limited, [Online]. Available at: https://www.fig.net/resources/proceedings/2008/verona_am_2008_comm7/ppt/12_sept/7_6_hofgartner.pdf [Accessed 9 February 2017].

Horne, R.B., 2003. Rationale and requirements for a European space weather programme. In *Space Weather Workshop: Looking Towards a European Space Weather Programme* (pp. 139-144). European Space Agency, Estec Nordwijk, the Netherlands.

Hunsucker, R.D. and Hargreaves, J.K., 2007. The high-latitude ionosphere and its effects on radio propagation. Cambridge University Press.

Hunt, S.M., Close, S., Coster, A.J., Stevens, E., Schuett, L.M. and Vardaro, A., 2000. Equatorial atmospheric and ionospheric modeling at Kwajalein missile range. Lincoln Laboratory Journal, 12(1), pp.45-64.

Hysell, D., Larsen, M., Fritts, D., Laughman, B. and Sulzer, M., 2018. Major upwelling and overturning in the mid-latitude F region ionosphere. Nature communications, 9(1), pp.1-11.

ICAO. 2012. Ionospheric Effects on GNSS Aviation Operations. First Meeting of Ionospheric Studies Task Force (ISTF/1), [Online]. 1-54. Tokyo, Japan. Available at: https://www.icao.int/APAC/Meetings/Pages/2012-ISTF-1.aspx [Accessed 30 June 2017].

ICAO Doc 9849 AN/457. 2012. Global Navigation Satellite System (GNSS) Manual. Second Edition, [Online]. Available at: http://www.icao.int/Meetings/anconf12/Documents/Doc.%209849.pdf [Accessed 10 February 2017].

ICAO. 2011. GNSS for Aviation: A Brief Background. Ionospheric Data Collection, Analysis and Sharing Workshop, [Online]. 1-11. Available at: https://www.icao.int/APAC/Meetings/2011_WKSHP_GNSS/SP01_ICAO%20GNSS%20for%20Aviation.pdf [Accessed 30 June 2017].

Ibáñez D., Rovira-García A., Sanz J., Juan JM., Gonzalez-Casado G., Jimenez-Baños D., López-Echazarreta C., Lapin I. The GNSS Laboratory Tool Suite (gLAB) updates: SBAS, DGNSS and Global Monitoring System. 9th ESA Workshop on Satellite Navigation Technologies (NAVITEC 2018), Noordwijk, The Netherlands. December 5 - 7, 2018. DOI: 10.1109/NAVITEC.2018.8642707.

IMAGE.; 2018. Geographic Cartesian Coordinates (X, Y, Z) Data Request Form. IMAGE through Finnish Meteorological Institute (FMI) Data Website, [Online]. Available at: http://space.fmi.fi/image/www/index.php?page=request [Accessed 28 September 2018].

Ionospheric Monitoring and Prediction Centre (IMPC). JAVAD GNSS Scintillation Receiver (50 Hz) courtesy of DLR. Available at: https://impc.dlr.de/products/ionospheric-perturbations/local-scintillation-measurements/kiruna/ [Accessed 10 September 2019].

Jacobsen, K.S. and Andalsvik, Y.L., 2016. Overview of the 2015 St. Patrick's Day storm and its consequences for RTK and PPP positioning in Norway. Journal of Space Weather and Space Climate, 6, p.A9.

Jacobsen, K.S. and Dähnn, M., 2014. Statistics of ionospheric disturbances and their correlation with GNSS positioning errors at high-latitudes. *Journal of Space Weather and Space Climate*, *4*, p.A27.

Jeffrey, C., 2010. An introduction to GNSS: GPS, GLONASS, Galileo and other global navigation satellite systems. NovAtel.

Jiao, Y. and Morton, Y.T., 2015. Comparison of the effect of high-latitude and equatorial ionospheric scintillation on GPS signals during the maximum of solar cycle 24. *Radio Science*, *50*(9), pp.886-903.

Jiao, Y., Morton, Y.T., Taylor, S. and Pelgrum, W., 2013. Characterization of high-latitude ionospheric scintillation of GPS signals. Radio Science, 48(6), pp.698-708.

Jin, Y., Moen, J.I. and Miloch, W.J., 2014. GPS scintillation effects associated with polar cap patches and substorm auroral activity: Direct comparison. Journal of Space Weather and Space Climate, 4, p.A23.

John H. M., B. Forte, I. Astin, T. Allbrook, A. Arnold, B. C. Vani, I. Häggström, and H. Sato (2020), An experiment based on EISCAT UHF/ESR measurements to understand how ionospheric irregularities induce GPS phase fluctuations in the European auroral and polar latitudes, to be submitted to a peer-reviewed Journal.

Kaplan, E. and Hegarty, C., 2005. Understanding GPS: principles and applications. Artech house.

Kataoka, R., Miyoshi, Y., Shigematsu, K., Hampton, D., Mori, Y., Kubo, T., Yamashita, A., Tanaka, M., Takahei, T., Nakai, T. and Miyahara, H., 2013, September. Stereoscopic determination of all-sky altitude map of aurora using two ground-based Nikon DSLR cameras. In Annales Geophysicae (Vol. 31, No. 9, pp. 1543-1548). Copernicus GmbH.

Kelley, M.C., Vickrey, J.F., Carlson, C.W. and Torbert, R., 1982. On the origin and spatial extent of high-latitude F region irregularities. Journal of Geophysical Research: Space Physics, 87(A6), pp.4469-4475.

Kelley et al., 2005. The Advanced Modular Incoherent Scatter Radar (AMISR). Project Review and Initial Results. Workshop Cornell University, USA, [Online]. 1-18. Available at: http://cedarweb.vsp.ucar.edu/workshop/tutorials/2005/kelley05.pdf [Accessed 16 June 2017].

Kersley, L., Pryse, S.E. and Wheadon, N.S., 1988. Small scale irregularities associated with a high latitude electron density gradient: scintillation and EISCAT observations. Journal of atmospheric and terrestrial physics, 50(6), pp.557-563.

Keskinen, M.J. and Ossakow, S.L., 1983. Theories of high-latitude ionospheric irregularities: A review. *Radio science*, *18*(6), pp.1077-1091.

Kintner, P.M., Humphreys, T. and Hinks, J., 2009. GNSS and ionospheric scintillation. Inside GNSS, 4(4), pp.22-30.

Kintner, P.M., Ledvina, B.M. and De Paula, E.R., 2007. GPS and ionospheric scintillations. *Space weather*, *5*(9).

Kivelson, A., 1995. Introduction to space physics. Cambridge university press.

Klobuchar, J.A., 1991. Ionospheric effect on GPS. GPS world, 2(4), pp.48-51.

Kogeda, O.P. and Mpekoa, N., 2013, June. Model for A Mobile Phone Voting System for South Africa. In 2013 Conference.

Langley, R.B., 1999. Dilution of precision. GPS world, 10(5), pp.52-59.

Lasisi, E.D.L.S., 2018. UPDATE ON NIGERIAN SATELLITE AUGMENTATION SYSTEM.

Ledvina, B.M., Makela, J.J. and Kintner, P.M., 2002. First observations of intense GPS L1 amplitude scintillations at mid-latitude. Geophysical Research Letters, 29(14), pp.4-1.

Lehtinen, M.S. and Huuskonen, A., 1996. General incoherent scatter analysis and GUISDAP. Journal of Atmospheric and Terrestrial Physics, 58(1-4), pp.435-452.

Liu, J., Nakamura, T., Liu, L., Wang, W., Balan, N., Nishiyama, T., Hairston, M.R. and Thomas, E.G., 2015. Formation of polar ionospheric tongue of ionization during minor geomagnetic disturbed conditions. Journal of Geophysical Research: Space Physics, 120(8), pp.6860-6873.

Luo, X., Gu, S., Lou, Y., Cai, L. and Liu, Z., 2020. Amplitude scintillation index derived from C/N 0 measurements released by common geodetic GNSS receivers operating at 1 Hz. Journal of Geodesy, 94(2), pp.1-14.

Luo, X., Gu, S., Lou, Y., Xiong, C., Chen, B. and Jin, X., 2018. Assessing the Performance of GPS Precise Point Positioning Under Different Geomagnetic Storm Conditions during Solar Cycle 24. Sensors, 18(6), p.1784.

Luo, X., Lou, Y., Xiao, Q., Gu, S., Chen, B. and Liu, Z., 2018. Investigation of ionospheric scintillation effects on BDS precise point positioning at low-latitude regions. GPS solutions, 22(3), p.63.

Marques, H.A.S., Monico, J.F.G. and Marques, H.A., 2016. Performance of the L2C civil GPS signal under various ionospheric scintillation effects. GPS solutions, 20(2), pp.139-149.

Martin, E. and Aarons, J., 1977. F layer scintillations and the aurora. Journal of Geophysical Research, 82(19), pp.2717-2722.

Misra, P. and Enge, P., 2006. Global position systems: Signals, measurements and performance. Ganga-Jamuna Press.

Moen, J., Oksavik, K., Alfonsi, L., Daabakk, Y., Romano, V. and Spogli, L., 2013. Space weather challenges of the polar cap ionosphere. *Journal of Space Weather and Space Climate*, *3*, p.A02.

Momoh, J.A. and Akinyede, J.O., 2008. African regional challenges in space-based disaster management and reduction. African skies, 12, p.57.

Moraes, A.D.O., Vani, B.C., Costa, E., Abdu, M.A., de Paula, E.R., Sousasantos, J., Monico, J.F., Forte, B., de Siqueira Negreti, P.M. and Shimabukuro, M.H., 2018. GPS availability and positioning issues when the signal paths are aligned with ionospheric plasma bubbles. GPS Solutions, 22(4), p.95.

Morton, J., 2017. High Latitude Ionospheric Scintillations Studies using Multi-Constellations Multi-Band GNSS Receivers. GPS Laboratory, [Online]. 1-46. Colorado State University, Colorado, USA. Available at: https://community.apan.org/wg/afosr/m/kathy/189656/download [Accessed 3 July 2017].

Mungufeni, P., Habarulema, J.B. and Jurua, E., 2016. Trends of ionospheric irregularities over African low latitude region during quiet geomagnetic conditions. Journal of Atmospheric and Solar-Terrestrial Physics, 138, pp.261-267.

National Science Foundation. 2012. AMISR in Africa Workshop. Boston College, Chestnut Hill, Massachusetts, United States, [Online]. 1-20. Available at: http://www.bc.edu/content/dam/files/sites/amisr/presentations/AMISR_workshop_report.pdf [Accessed 25 May 2017].

Nava, B., Coïsson, P., Amarante, G.M., Azpilicueta, F. and Radicella, S.M., 2005. A model assisted ionospheric electron density reconstruction method based on vertical TEC data ingestion. Annals of Geophysics, 48(2).

Ngcofe, L. and Gottschalk, K., 2013. The growth of space science in African countries for Earth observation in the 21st century. South African Journal of Science, 109(1-2), pp.1-5.

Nicolls, M.J., 2014. Space Debris Measurements using the Advanced Modular Incoherent Scatter Radar. In Proceedings of the Advanced Maui Optical and Space Surveillance Technologies Conference.

Nishitani, N., Ruohoniemi, J.M., Lester, M., Baker, J.B.H., Koustov, A.V., Shepherd, S.G., Chisham, G., Hori, T., Thomas, E.G., Makarevich, R.A. and Marchaudon, A., 2019. Review of the accomplishments of mid-latitude Super Dual Auroral Radar Network (SuperDARN) HF radars. Progress in Earth and Planetary Science, 6(1), p.27.

Norsuzila, Y., Abdullah, M., Ismail, M., Ibrahim, M. and Zakaria, Z., 2010. Total Electron Content (TEC) and estimation of positioning error using Malaysia data. ionosphere, 7, p.8.

O'Keeffe, J., 2016. Water Management Challenges in the Indo-Gangetic Plain. NERC Science of the Environment, [Online]. Imperial College London. Available at: http://www.gewexevents.org/wp-content/uploads/Day1_OKeeffe_IWMinLSMs.pdf [Accessed 2 February 2017].

Oxford Economics. 2012. The Economic Impact of Physics Research in the UK: Satellite Navigation Case Study. *A Report for STFC*, [Online]. 1-24. Available at: https://www.stfc.ac.uk/files/satellite-navigation-case-study/ [Accessed 11 December 2016].

Olwendo, O.J., Baluku, T., Baki, P., Cilliers, P.J., Mito, C. and Doherty, P., 2013. Low latitude ionospheric scintillation and zonal irregularity drifts observed with GPS-SCINDA system and closely spaced VHF receivers in Kenya. Advances in Space Research, 51(9), pp.1715-1726.

Parker, E.N., 1958. Dynamics of the interplanetary gas and magnetic fields. The Astrophysical Journal, 128, p.664.

Paznukhov, V.V., Carrano, C.S., Doherty, P.H., Groves, K.M., Caton, R.G., Valladares, C.E., Seemala, G.K., Bridgwood, C.T., Adeniyi, J., Amaeshi, L.L.N. and Damtie, B., 2012, April. Equatorial plasma bubbles and L-band scintillations in Africa during solar minimum. In Annales Geophysicae (Vol. 30, No. 4, pp. 675-682). Copernicus GmbH.

Pei, L., Chen, R., Liu, J., Chen, W., Kuusniemi, H., Tenhunen, T., Kröger, T., Chen, Y., Leppäkoski, H. and Takala, J., 2010, September. Motion recognition assisted indoor wireless navigation on a mobile phone. In Proceedings of the 23rd International Technical Meeting of the Satellite Division of the Institute of Navigation (pp. 3366-3375).

Perkins, F.W., 1975. Ionospheric irregularities. Reviews of Geophysics, 13(3), pp.884-884.

Pérez Ruiz, M. and Upadhyaya, S., 2012. GNSS in precision agricultural operations. Intech.

Pestana, A., 2015. Reading RINEX 2.11 Observation Data Files.

Pi, X., Mannucci, A.J., Lindqwister, U.J. and Ho, C.M., 1997. Monitoring of global ionospheric irregularities using the worldwide GPS network. Geophysical Research Letters, 24(18), pp.2283-2286.

Prikryl, P., Jayachandran, P.T., Mushini, S.C. and Chadwick, R., 2011, February. Climatology of GPS phase scintillation and HF radar backscatter for the high-latitude ionosphere under solar minimum conditions. In Annales Geophysicae (Vol. 29, No. 2, pp. 377-392). Copernicus GmbH.

Prikryl, P., Jayachandran, P.T., Mushini, S.C., Pokhotelov, D., MacDougall, J.W., Donovan, E., Spanswick, E. and St-Maurice, J.P., 2010. GPS TEC, scintillation and cycle slips observed at high latitudes during solar minimum. Annales Geophysicae (09927689), 28(6).

Pestana, A., 2015. Reading RINEX 2.11 Observation Data Files.

Priyadarshi, S., 2015. A review of ionospheric scintillation models. Surveys in geophysics, 36(2), pp.295-324.

Priyadarshi, S. and Singh, A.K., 2011, August. Study of equatorial low-latitude ionospheric irregularities during a recent geomagnetic storm of 03 August 2010 using GPS Receiver. In 2011 XXXth URSI General Assembly and Scientific Symposium (pp. 1-4). IEEE.

Quaye-Ballard, J.A., An, R., Andam-Akorful, S.A. and Quaye-Ballard, N.L., 2013. Role of Geoinformatics for Ghana oil and gas industry. decision making, 1, p.6.

Rabiu, B., 2013. GNSS in Africa: Applications, Infrastructures, Research Implications and Prospects. Centre for Atmospheric Research, National Space Research and Development Agency, NASRDA, Anyigba, Nigeria. African Leadership Conference Space Science and Technology, Session 7, Accra, Ghana, [Online]. Available at: http://www.unoosa.org/pdf/icg/2013/ALC/2.pdf [Accessed 2 February 2017].

Rana, G. and Yadav, M.K., 2014. The ionosphere and radio propagation. Journal Impact Factor, 5(11), pp.09-16.

Rao, K.D. and Dutt, V.S.I., 2017. An Assessment of Mapping Functions for VTEC Estimation using Measurements of Low-Latitude Dual Frequency GPS Receiver. Int. J. Appl. Eng. Res, 12(4), pp.422-427.

Rino, C.L., Livingston, R.C. and Matthews, S.J., 1978. Evidence for sheet-like auroral ionospheric irregularities. Geophysical Research Letters, 5(12), pp.1039-1042.

Rishbeth, H. and Garriott, O.K., 1969. Introduction to ionospheric physics (Vol. 14). New York: Academic press.
Rishbeth, H. and Williams, P.J.S., 1985. The EISCAT ionospheric radar-The system and its early results. Quarterly Journal of the Royal Astronomical Society, 26, pp.478-512.

Rizos, C., 2003. Trends in GPS Technology & Applications. In 2nd International LBS Workshop.

Roettger, J., 1989. The instrumental principles of MST radars and incoherent scatter radars and the configuration of radar system hardware.

Romano, V., Spogli, L., Aquino, M., Dodson, A., Hancock, C. and Forte, B., 2013. GNSS station characterisation for ionospheric scintillation applications. Advances in Space Research, 52(7), pp.1237-1246.

Sabatini, R., Moore, T. and Ramasamy, S., 2017. Global navigation satellite systems performance analysis and augmentation strategies in aviation. Progress in Aerospace Sciences, 95, pp.45-98.

Sastri, J.H., 1990. Equatorial anomaly in F-region—a review.

Sato, H., Kim, J.S., Jakowski, N. and Häggström, I., 2018. Imaging high-latitude plasma density irregularities resulting from particle precipitation: spaceborne L-band SAR and EISCAT observations. Earth, Planets and Space, 70(1), p.163.

SBAS-IONO Working Group, 2012. Ionospheric scintillations: How irregularities in electron density perturb satellite navigation systems. GPS World, 23(4), pp.44-50.

Schunk, R. and Nagy, A., 2009. Ionospheres: physics, plasma physics, and chemistry. Cambridge university press.

Seo, J., Walter, T., Marks, E., Chiou, T.Y. and Enge, P., 2007, June. Ionospheric scintillation effects on GPS receivers during solar minimum and maximum. In Proceedings of the International Beacon Satellite Symposium (pp. 11-15).

Shagimuratov, I.I., Krankowski, A., Ephishov, I., Cherniak, Y., Wielgosz, P. and Zakharenkova, I., 2012. High latitude TEC fluctuations and irregularity oval during geomagnetic storms. Earth, planets and space, 64(6), pp.521-529.

Shanmugam, S. and MacLeod, R., 2013, July. GNSS ionospheric scintillation and TEC monitoring using GPStation-6. In 2013 IEEE International Conference on Space Science and Communication (IconSpace) (pp. 207-212). IEEE.

Skone, S. and Cannon, M.E., 1998. Auroral zone ionospheric considerations for WADGPS. Navigation, 45(2), pp.117-127.

Skone, S.H., 2001. The impact of magnetic storms on GPS receiver performance. Journal of Geodesy, 75(9-10), pp.457-468.

Someswar, G.M., Rao, T.P.S.C. and Chigurukota, D.R., 2013. Global navigation satellite systems and their applications. International Journal of Software and Web Sciences, 3(1), pp.17-23.

Srinivasu, V.K.D., Dashora, N., Prasad, D.S.V.V.D., Niranjan, K. and Krishna, S.G., 2018. On the occurrence and strength of multi-frequency multi-GNSS Ionospheric Scintillations in Indian sector during declining phase of solar cycle 24. Advances in Space Research, 61(7), pp.1761-1775.

Susnik, A. and Forte, B., 2011, August. Ionospheric scintillation activity measured in the African sector. In 2011 XXXth URSI General Assembly and Scientific Symposium (pp. 1-3). IEEE.

Tanaka, Y., Ogawa, Y., Kadokura, A., Partamies, N., Whiter, D., Enell, C.F., Brändström, U., Sergienko, T., Gustavsson, B., Kozlovsky, A. and Miyaoka, H., 2015. Eastward-expanding auroral surges observed in the post-midnight sector during a multiple-onset substorm. Earth, Planets and Space, 67(1), p.182. https://doi.org/10.1186/s40623-015-0350-8.

Tariku, Y.A., 2015. Patterns of GPS-TEC variation over low-latitude regions (African sector) during the deep solar minimum (2008 to 2009) and solar maximum (2012 to 2013) phases. Earth, Planets and Space, 67(1), p.35.

Teunissen, P. and Montenbruck, O. eds., 2017. Springer handbook of global navigation satellite systems. Springer.

Theerapatpaiboon, P., Leelaruji, N., Hemmakorn, N. and Supnithi, P., 2005, December. The Effects of Sumatra-Andaman Earthquake on Total Ionospheric Electron Content (TEC) and Ionospheric Scintillation of GPS Signal in Thailand. In 2005 5th International Conference on Information Communications & Signal Processing (pp. 1183-1186). IEEE.

Tjulin, A., 2017. EISCAT Experiments. EISCAT Scientific Association, (March).

Tsai, L.C., Su, S.Y., Liu, C.H., Schuh, H., Wickert, J. and Alizadeh, M.M., 2018. Global morphology of ionospheric sporadic E layer from the FormoSat-3/COSMIC GPS radio occultation experiment. *GPS Solutions*, *22*(4), p.118.

United Nations, 2019. *World Population Prospects 2019*. Department of Economic and Social Affairs, pp 1-46, Online. Available at: https://population.un.org/wpp/Publications/Files/WPP2019_Highlights.pdf [Accessed 4 September 2019].

United Nations, 2015. The World Population Prospects: 2015 Revision. Department of Economics and Social Affairs, [Online]. Available at:

https://esa.un.org/unpd/wpp/Publications/Files/Key_Findings_WPP_2015.pdf [Accessed 21 June 2017].

United Nations Office for Outer Space Affairs (UN-OOSA). 2009. United Nations and GNSS: Global in Space and in Time. International Committee on Global Navigation Satellite Systems (ICG). Workshop on the Applications of Global Navigation Satellite Systems, Baku, Azerbaijan, [Online]. 1-13. Available at: http://www.unoosa.org/documents/pdf/psa/activities/2009/azerbaijan/presentations/2.pdf [Accessed 30 June 2017].

United Nations Office for Outer Space Affairs (UN-OOSA). 2008. Capacity Building in Space Science and Technology. Regional Centres for Space Science and Technology Education Affiliated to the United Nations, [Online]. 1-26. United Nations, New York. Available at: http://www.unoosa.org/pdf/publications/st_space_41E.pdf [Accessed 2 July 2017].

Valentic, T., Buonocore, J., Cousins, M., Heinselman, C., Jorgensen, J., Kelly, J., Malone, M., Nicolls, M. and Van Eyken, A., 2013, October. AMISR the advanced modular incoherent scatter radar. In 2013 IEEE International Symposium on Phased Array Systems and Technology (pp. 659-663). IEEE.

Van, D. A. J.; 2009. GPS Ionospheric Scintillation and TEC Monitor (User's Manual). Satellite Navigation Science and Technology for Africa, 23 March – 9 April 2009, pp 2025-33, [Online]. The Abdus Salam International Centre for Theoretical Physics. Available at: http://indico.ictp.it/event/a08148/session/90/contribution/56/material/0/0.pdf [Accessed 17 September 2018].

van den IJssel, J., Forte, B. & Montenbruck, O. Impact of Swarm GPS receiver updates on POD performance. *Earth Planet Sp* 68, 85 (2016). https://doi.org/10.1186/s40623-016-0459-4.

Van Dierendonck, A.J., Klobuchar, J. and Hua, Q., 1993, September. Ionospheric scintillation monitoring using commercial single frequency C/A code receivers. In proceedings of ION GPS (Vol. 93, pp. 1333-1342).

Vani, B.C., Shimabukuro, M.H. and Monico, J.F.G., 2017. Visual exploration and analysis of ionospheric scintillation monitoring data: the ISMR query tool. *Computers & Geosciences*, *104*, pp.125-134.

Vani, B.C., Ivánová, I., Monico, J.F. and Shimabukuro, M.H., 2014, January. Visualizing the Quality of GNSS Multivariate Data. In GeoInfo (pp. 95-106).

Varney, R. H., 2016. Advanced Modular Incoherent Scatter Radar. Centre for Geospace Studies, [Online]. 1-40. AMISR Technology. AMISR Science. SRI International. Available at: https://eiscat3d.se/drupal/sites/default/files/ISRSchool2016/24-Varney-AMISR_open_me_in_adobe_for_movies.pdf [Accessed 11 July 2017].

Von Engeln, A., Andres, Y., Marquardt, C. and Sancho, F., 2011. GRAS radio occultation on-board of Metop. Advances in space research, 47(2), pp.336-347.

Walter, T., 2010. Effect of ionospheric scintillations on GNSS—a white paper. SBAS Ionospheric Working Group.

Ward, N., 1997. Understanding GPS—Principles and Applications. Elliott D. Kaplan (Editor). £75. ISBN: 0-89006-793-7. Artech House Publishers, Boston & London. 1996. The Journal of Navigation, 50(1), pp.151-152.

Wernik, A.W., Alfonsi, L. and Materassi, M., 2004. Ionospheric irregularities, scintillation and its effect on systems. *Acta geophysica polonica*, *52*(2), pp.237-249.

Wernik, A.W., Secan, J.A. and Fremouw, E.J., 2003. Ionospheric irregularities and scintillation. Advances in Space Research, 31(4), pp.971-981.

Wonnacott, R., 2008. GNSS as a multi-disciplinary tool for Africa's development. African Skies, 12, p.81.

Wood, A.G., Pryse, S.E. and Moen, J., 2009. Modulation of nightside polar patches by substorm activity. In Annales Geophysicae (Vol. 27, No. 10, pp. 3923-3932). Copernicus Publications on behalf of the European Geosciences Union.

Xu, J.S., Zhu, J. and Li, L., 2007. Effects of a major storm on GPS amplitude scintillations and phase fluctuations at Wuhan in China. Advances in Space Research, 39(8), pp.1318-1324.

Yasyukevich, Y., Vasilyev, R., Ratovsky, K., Setov, A., Globa, M., Syrovatskii, S., Yasyukevich, A., Kiselev, A. and Vesnin, A., 2020. Small-Scale Ionospheric Irregularities of Auroral Origin at Mid-Latitudes during the 22 June 2015 Magnetic Storm and Their Effect on GPS Positioning. Remote Sensing, 12(10), p.1579.

Yeh, K.C. and Liu, C.H., 1982. Radio wave scintillations in the ionosphere. Proceedings of the IEEE, 70(4), pp.324-360.

Yizengaw, E., 2013. Space Science Instrumentation in Africa: Past, Present and Future. CAWSES-II TG4 Newsletter, [Online]. 12, 1-2. Available at: http://www.cawses.org/wiki/images/1/16/TG4_newsletter_issue12.pdf [Accessed 3 July 2017].

Yizengaw, E., Zesta, E., Moldwin, M.B., Damtie, B., Mebrahtu, A., Valladares, C.E. and Pfaff, R.F., 2012. Longitudinal differences of ionospheric vertical density distribution and equatorial electrodynamics. Journal of Geophysical Research: Space Physics, 117(A7).

Yokoyama, T., 2017. A review on the numerical simulation of equatorial plasma bubbles toward scintillation evaluation and forecasting. Progress in Earth and Planetary Science, 4(1), p.37.

Yue, X., Schreiner, W.S., Pedatella, N., Anthes, R.A., Mannucci, A.J., Straus, P.R. and Liu, J.Y., 2014. Space weather observations by GNSS radio occultation: From FORMOSAT-3/COSMIC to FORMOSAT-7/COSMIC-2. Space Weather, 12(11), pp.616-621.

Zarco-Tejada, P.J., Hubbard, N. and Loudjani, P., 2014. Precision Agriculture: An Opportunity for EU Farmers-Potential Support with the Cap 2014-2020. Joint Research Centre (JRC) of the European Commission; Monitoring Agriculture ResourceS (MARS) Unit H04.

Zolesi, B. and Cander, L. R., 2014. Chapter 2: The General Structure of the Ionosphere. Ionospheric Prediction and Forecasting. Springer Geophysics, [Online]. Berlin, Heidelberg: Springer-Verlag. Available at: www.springer.com/cda/content/document/cda.../9783642384295-c2.pdf?SGWID [Accessed 16 December 2016].

Zou, Y. and Wang, D., 2009. A study of GPS ionospheric scintillations observed at Guilin. Journal of atmospheric and solar-terrestrial physics, 71(17-18), pp.1948-1958.